博士論文

Unsteady Aerodynamic Characteristics of Compressor Oscillating Cascade in Transonic Flow with Shock Waves

（衝撃波を伴う遷音速流における圧縮機振動翼列の非定常空力特性に関する研究）

甘 久亮

Gan Jiuliang

Unsteady Aerodynamic Characteristics of Compressor Oscillating Cascade in Transonic Flow with Shock Waves

衝撃波を伴う遷音速流における圧縮機振動翼列の非定常空力特性に関する研究

By

甘 久亮

Gan Jiuliang

A Dissertation Submitted in Partial Fulfilment of the Requirements
for the Degree of Doctor of Philosophy
in Aeronautics and Astronautics Engineering

Abstract

In the field of commercial turbofan engine, the fan and compressor technology improves to satisfy the demands of high propulsive efficiency and energy saving, and the trend of increasing bypass ratio is obvious. Among the design solutions, more complex 3D structure and higher load cause the more complicated and unsteady flow field, while larger fan size and more weight saving cause blade rigidity decreasing. In such situation, blade vibration is more likely affected by the surrounding unsteady flow field, which can cause the aeroelastic instability. Among the aeroelastic phenomena, cascade flutter is a phenomenon of self-exciting vibration which affects the stability of the machine to great extent. It often has disastrous consequence and difficult to predict theoretically. In the fan and front compressor stages, the cascade is under transonic flow condition where the flutter phenomena are more complicated due to the interaction among blade motion, shock wave and flow separation. The deeper understanding and effective predicting method of cascade flutter phenomena are essential for engine performance promotion.

The knowledge of unsteady aerodynamic force and unsteady pressure distribution acting on the blade surface is significant for flutter interpretation. However, in past researches, only discrete pressure distribution can be acquired which is insufficient to understand the unsteady behaviors of 2D spatial flow phenomena, such as shock wave and flow separation. Therefore, the fast-response pressure-sensitive paint (PSP) is expected to be a powerful tool for obtaining detailed information of unsteady surface pressure due to its capability of non-contact, quantitative pressure measurement with fast time response and high spatial resolution for complex aerodynamic flows. CFD is another effective way for flutter research based on the verification by experimental results.

In view of above mentioned background, this research is aimed to conduct the unsteady aerodynamic characteristics analysis of compressor oscillating cascade in transonic flow with shock waves, and accumulate basic knowledge on the mechanism of transonic compressor flutter phenomena. Experimental object was a compressor cascade consisted of 7 DCA blades in a transonic flow with different shock pattern by changing the static pressure ratio (P.R.). The central blade 0 can be oscillated in translational mode. Anodized aluminum pressure-sensitive paint (AA-PSP) technique was applied to the measurement of steady and unsteady surface pressure on the transonic oscillating cascade. Then, 3D RANS simulation of the oscillating cascade was conducted for comparing with PSP results and obtaining more flow details. Finally, the flow phenomena and aerodynamic stability of the cascade were analyzed comprehensively.

The steady flow fields with different P.R. were measured and calculated. Pressure results obtained by PSP and CFD have good accordance with conventional methods. The shock wave structure in current transonic compressor cascade is classified into 4 types: choked flow/ double shocks/ merged shocks/ detached shock patterns with the P.R. increasing. The detailed pressure distribution on blade surface and more flow details were analyzed. Under lower P.R., the shock

pattern consists of an oblique shock wave induced by blade leading edge and a passage shock wave in flow passage. The two shock waves cause two low pressure areas on suction side (S.S.). With the increasing of P.R., the downstream low pressure area becomes small and finally disappears. The two shock waves also merge with each other gradually near S.S..

Then, based on the known steady flow field, the unsteady aerodynamic characteristics of oscillating cascade in translational mode were analyzed. Unsteady pressure on blade surface under double shocks pattern and merged shocks pattern were measured by PSP. The corresponding CFD calculations were also conducted by using the converged steady calculation results. The unsteady pressure phenomena are mainly caused by the oscillations of shock waves, and also affected by tip clearance flow and hub side separation. CFD shows a satisfactory accordance with the PSP results in capturing the dominant unsteady pressure induced by shock wave movement and interpreting the unsteady pressure change with P.R.. The shock wave moving direction in neighboring flow passages of oscillating blade is different between double shocks pattern and merged shocks pattern due to the different mass flowrate sensitivity. The blade oscillation has stronger influence on the downstream blade passages than upstream ones. The amplitude of unsteady aerodynamic force has a tendency of accelerated growth with P.R. increase, comparing to the linear increasing averaged aerodynamic force. The mechanism of unsteady pressure propagation were analyzed based on CFD results.

Finally, aerodynamic stability of transonic compressor oscillating cascade was analyzed by using influence coefficient method. Shock waves and 3D wall effects were considered as the dominant factors of aerodynamic instability. In low reduced frequency range, the oscillating cascade is possible to be aerodynamically unstable. The maximum positive unsteady aerodynamic work has an increasing tendency with P.R.. In low P.R. range (choked flow/ double shocks pattern), the maximum unsteady aerodynamic work is of relatively small value and sourced from two shock waves, tip clearance flow and P.S. supersonic area; in high P.R. range, the maximum unsteady aerodynamic work is of quite larger value and dominated by the work done by passage shock on blade pressure side. In detached shock case, P.S. is in subsonic condition and the leading edge also has server positive work influx. With the increasing of reduced frequency, the maximum unsteady aerodynamic work and the corresponding IBPA decrease. In high reduced frequency range, the cascade is stable in all IBPA range, while there are still some obvious positive work influx located in passage shock wave area at maximum unsteady aerodynamic work point. By considering all the working conditions of current cascade, the leading edge area (0-0.3x/c) is vulnerable to be affected by large unsteady aerodynamic force, which is also thinnest part of the airfoil.

As described above, the fast response PSP technique and CFD simulation were applied effectively to acquiring unsteady pressure distribution on blade surface of a transonic compressor oscillating cascade. The unsteady aerodynamic characteristics of oscillating cascade were illustrated by shock wave analysis. Moreover, the cascade stability of various working conditions was analyzed comprehensively.

Acknowledgement

It is my great honor to give thanks to all the people and organizations who have supported and inspired me during my Ph.D. studies.

I feel extremely grateful to my supervisor, Prof. T. Watanabe, for giving the opportunity to conduct this research and encouraging me to complete the studies. I would like to thank him for his patience and guidance in my research and during the tough times I endured. His profound knowledge and outstanding leadership in the field of gas turbine systems stimulate my enthusiasm and inspiration for my doctoral research. Furthermore, his kind personality and meticulous attitude have been influencing on my personal life and also future career.

I am also grateful to Assoc. Prof. T. Himeno for all the help he provided me throughout my Ph.D. course. He shared many important ideas and helped me to grow though the difficulties I encountered in my research. I am also thankful for his encouragement and faith in me throughout doctoral period. He never stints the time for doing academic discussions and answering academic questions, which inspire me a lot.

I am thankful to my doctoral supervising committee members, Doctor T. Nishizawa, Prof. K. Suzuki, Prof. S. Teramoto, for their kind feedback. I am equally grateful to Mr. S. Uzawa and Asst. Prof. Y. Sakuma, for their help in teaching me many experimental skills, giving me some effective ideas and fulfilling the wind-tunnel experiments. Without their help, it would be much tougher to obtain such experimental results. I am equally grateful to Ass. Prof. C. Inoue, Asst. Prof. A. Tatesihi and Asst. Prof. X. Nan, for their constructive suggestions and comments which helped the improvement of my research. I am also thankful to Prof. S. Teramoto and Assoc. Prof. K. Okamoto for their feedback and comments during the joint lab seminars. Also, the support from Miss. Y. Yamada for helping me in dealing with different office work is also highly appreciated.

In my daily research routine, I am blessed with friendly seniors, Dr. B. Javed. He was always kind to help me to solve some troubles. I am also thankful to the master's and bachelor's student from 2015 to 2019 for their kindness, especially K. Horimoto, Y. Koike, T. Ishii, Y. Iwasaki and T. Yasuda. I am thankful to Mr. R. Okamoto, Mr. K. Otofuji, Mr. T. Murata and Mr. R. Iwasaki for the collaboration in conducting the wind tunnel experiments. To say the least, all UTJPL members made my life in Japan enjoyable and amazing. I am also thankful to the members of Teramoto-Okamoto lab for their feedback in the joint lab seminars.

Lastly, and most importantly, I wish to thank my family members, my parents, my wife and my daughter. They raised me, supported me, taught me, and loved me. They have given me unconditional love and moral support.

Table of Contents

List of Figures

List of Tables

List of Symbols

Latin symbols

A	Blade oscillation amplitude	[m]
c	Chord length	[m]
F	Aerodynamic force	[N]
$\tilde{F}$	Unsteady aerodynamic force amplitude	[N]
I	Luminescent intensity	[0~1023]
i	Angle of incidence	[deg]
l	Span length	[m]
P	Static pressure	[Pa]
P^*	Total pressure	[Pa]
$\tilde{P}$	Unsteady pressure amplitude	[Pa]
U	Inlet velocity	[m/s]

Greek symbols

φ	Phase shift	[deg]
ω	Circular velocity	[rad/s]

Subscript

in	Cascade inlet
out	Cascade outlet

Superscript

$*$	Stagnation parameter

Dimensionless Number

C_F	Aerodynamic force coefficient	$C_F = \frac{F}{(P_{in}^* - P_{in})cl}$
$\tilde{C}_F$	Normalized unsteady aerodynamic force amplitude	$\tilde{C}_F = \frac{\tilde{F}}{(P_{in}^* - P_{in})Al}$
C_P	Static pressure coefficient	$C_P = \frac{P - P_{in}}{(P_{in}^* - P_{in})}$
$\tilde{C}_P$	Normalized unsteady pressure amplitude	$\tilde{C}_P = \frac{\tilde{P}}{(P_{in}^* - P_{in})h}$
$\tilde{C}_P(Re)$	Real part of $\tilde{C}_P$	

$\tilde{C}_P(Im)$	Imaginary part of $\tilde{C}_P$	
h	Normalized bending amplitude	$h = \frac{A}{c}$
k	Reduced frequency	$k = \frac{c\omega}{2U}$
Ma	Mach number	
$P.R.$	Static pressure ratio	$P.R. = \frac{P_{out}}{P_{in}}$
W	Unsteady aerodynamic work	
$\bar{\omega}$	Total pressure loss coefficient	$\bar{\omega} = \frac{P_{in}^* - P^*}{P_{in}^* - P_{in}}$
x/c	Normalized chordwise coordinate	

Abbreviations

AA-PSP	Anodized aluminum pressure-sensitive paint
CFD	Computational fluid dynamics
DCA	Double circular arc
DFT	Discrete Fourier transformation
L.E. / T.E.	Leading edge / Trailing edge
P.S. / S.S.	Pressure side / Suction side

Chapter 1 Introduction

1.1 Research Background

1.1.1 Development of Modern Fan/Compressor Component

Turbomachinery is an important energy conversion machine and widely utilized in various engineering fields, including gas turbine, steam turbine, turbofan engine, turbocharger, and so on. In commercial turbofan engine, fan/compressor and turbine are typical turbomachinery and key components for engine performance promotion. To achieve the targets of saving fuel, reducing operating expenses and reducing noise, the trend of higher bypass ratio and higher efficiency of fan/compressor component is continuous at present and in the future. The increasing of bypass ratio causes the size enlargement and structural complexity increasing of fan blade. For depressing the weight increasing of fan blades due to higher bypass ratio, the corresponding solutions include using lighter material, thinner structure and hollow structure. Figure 1.1 shows a representative high bypass ratio engine GE90-115B (bypass ratio: 9) with composite fan blades. Besides, increasing stage load is also considered as good approached in improving engine performance, which causes stricter blade shape design and more unsteady 3D flow field to appear.

For the above reasons, the risk of aeroelastic instability in fan/compressor component is increasing. Therefore, the evaluation of aeroelastic performance inside fan/compressor component becomes more and more important in order to keep the safety and stability of the machine. Among the unstable phenomena in turbomachinery, cascade flutter is a phenomenon of self-excited vibration and often has disastrous consequence and is difficult to be predicted. It is caused by the interaction between the unsteady aerodynamic force and the structural forces and occurs when the vibration induced by the unsteady aerodynamic force acting on the structure exceeds a condition of dynamic equilibrium. Figure 1.2 shows an example of cascade flutter occurrence in stator vanes in a bending mode. This kind of failure was violent, wide spread and didn't follow any pattern [2]. Cascade flutter in transonic flow is especially complicated due to the interaction of shock wave, flow separation and blade motion.

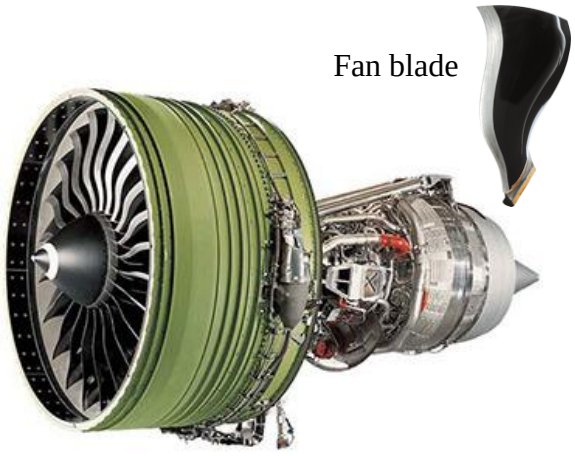

Figure 1.1 GE90-115B Engine [1]

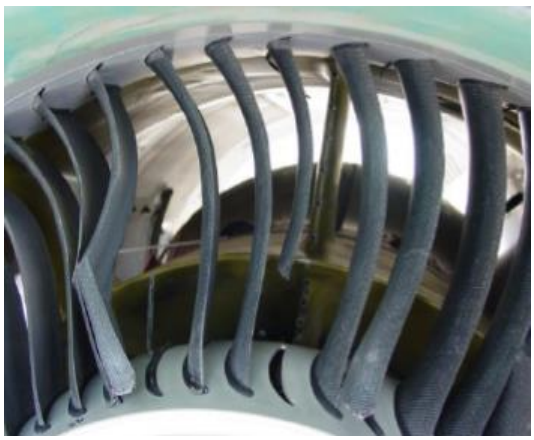

Figure 1.2 Catastrophic damage in stator [2]

Therefore, the design for aeroelastic stability is an important task in fan/compressor design. One of the design objectives is to ensure the aeroelastic stability over wide operation condition and guarantee the operation without flutter occurrence. It is of great significance to develop high-accurate theoretical and computational approaches in predicting the flutter boundary which can help to achieve high performance and adequate design margins.

1.1.2 Introduction of Aeroelastic Phenomena in Turbomachinery

The aeroelastic phenomena in turbomachinery are caused by the interaction among the unsteady aerodynamic force and the structural forces which is shown by the Collar's triangle in Figure 1.3. The forces include aerodynamic forces, elastic forces and inertial forces. When the inertial forces can be ignored, the aeroelasticity becomes static aeroelasticity, which appears in the phenomena of divergence and reversal of control. Conversely, it is dynamic aeroelasticity. The dynamic aeroelastic phenomena can be classified into forced response, flutter and other non-synchronous vibrations. These phenomena are explained in details as follows.

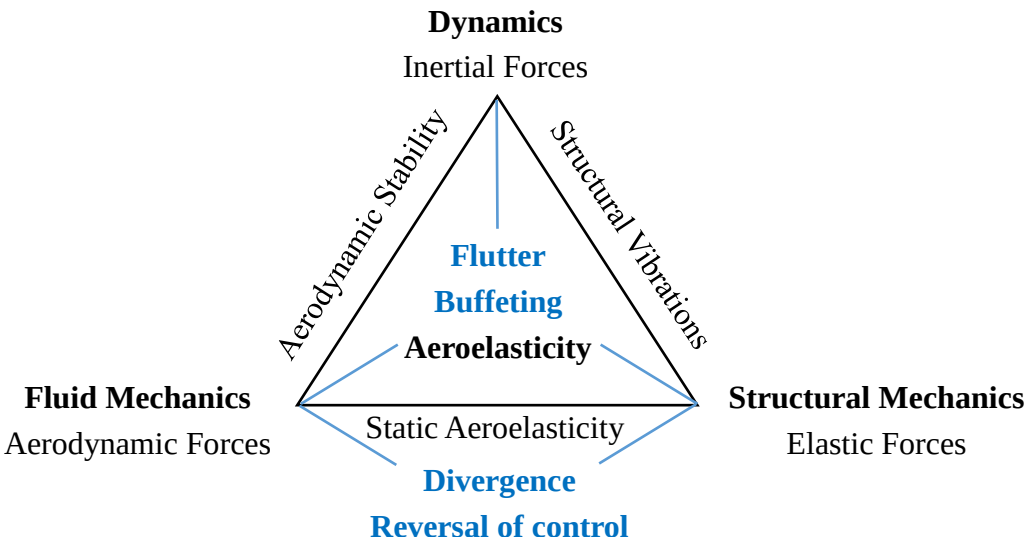

Figure 1.3 Collar's triangle of aeroelasticity

(1) Forced Response

Forced vibration occurs when an alternating force or motion is applied to a mechanical system, for example when a washing machine shakes due to an imbalance. Forced vibration is a type of vibration in which a force is repeatedly applied to a mechanical system and has no relation with blade vibration. In turbomachinery, the main reasons of forced response include:

1. Aerodynamic factors:

   ① Potential interference by static structure including inlet guide vane and strut; ② Inlet distortion; ③ Wake interference; ④ Rotating stall (non-synchronous); ⑤ Random vibration forces induced by flow separation (non-synchronous)

2. Structural factors

   ① Shaft imbalance; ② Friction with casing

(2) Self-Excited Vibration: Flutter

Flutter is aeroelastic instability phenomenon caused by the coupling of blade motion and unsteady aerodynamic forces (self-excited aerodynamic forces) induced by blade motion. It is generally non-synchronous with the shaft rotation. The damages caused by flutter will occur when the vibration induced by the unsteady aerodynamic force acting on the structure exceeds a condition of dynamic equilibrium. The aerodynamic reasons for flutter include: shock wave and its reflection, boundary layer separation, shock wave-boundary layer interference, secondary flow. These reasons are complex and interact with each other.

(3) Other Non-Synchronous Vibrations (NSV, SFV)

Non-synchronous vibrations (NSV) were also reported in previous researches, which is an aeromechanic phenomenon in which rotor blades are driven by a fluid dynamic instability [4]. Unlike flutter, NSV is primarily a fluid dynamic instability which can cause vibrations with large amplitude when the natural frequencies of the instability and rotor blade are close. Separated flow vibration (SFV) is a broad-band buffeting response of blades. The blades are not frequency or phase locked, and vibrate in first few vibration modes with moderate responses.

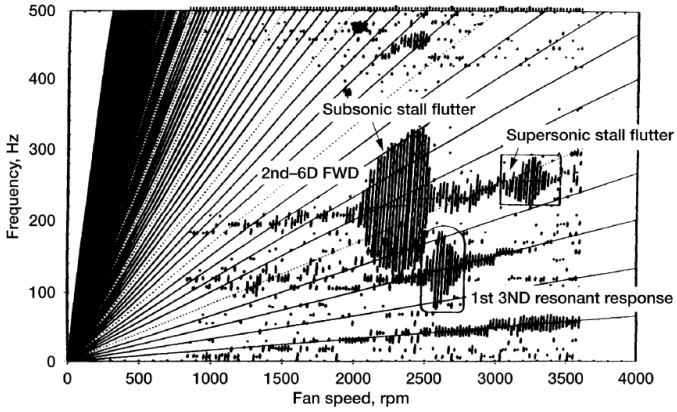

Figure 1.4 Experimental Campbell diagram [3]

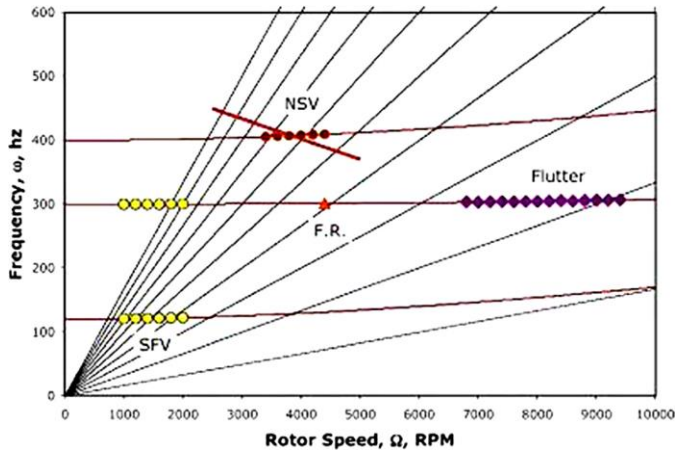

Figure 1.6 Campbell diagram of a typical integrally bladed rotor in modern aeroengine [5]

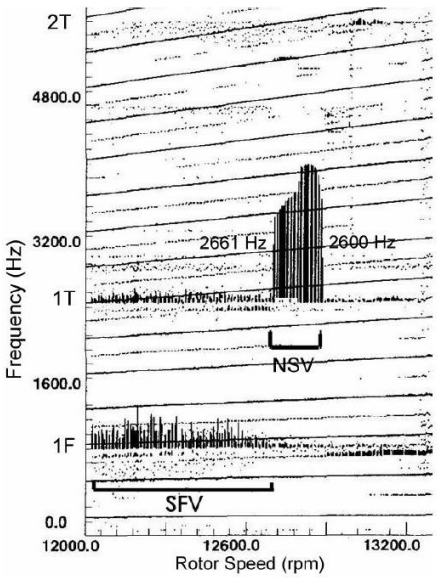

Figure 1.5 Strain gage response of first-stage rotor blades of compressor rig [4]

Figure 1.4 is a Campbell diagram in which the relationship between rotating speed and vibration mode is shown. Besides the large amplitude of 1st 3ND resonant response which is a forced response, there are two large vibration response which are considered to be the responses of blade vibration induced by flutter [3]. NSV was observed by monitoring the strain gauge response by Kielb and considered to be caused by a coupled suction side vortex unsteadiness and tip flow instability [4], as shown in Figure 1.5. As a summary, Figure 1.6 shows the characteristics of all these vibrations in Campbell diagram, including forced response, flutter, NSV and SFV. In this study, only the mechanisms of flutter phenomena are focused on.

1.2 Research Approaches of Cascade Flutter

1.2.1 Classification of Cascade Flutter

Flutter is primarily seen in fans, front and middle compressor blades, and high aspect ratio low pressure turbine stages. The general classification of flutter in turbo-machinery is shown on a compressor map in Figure 1.7.

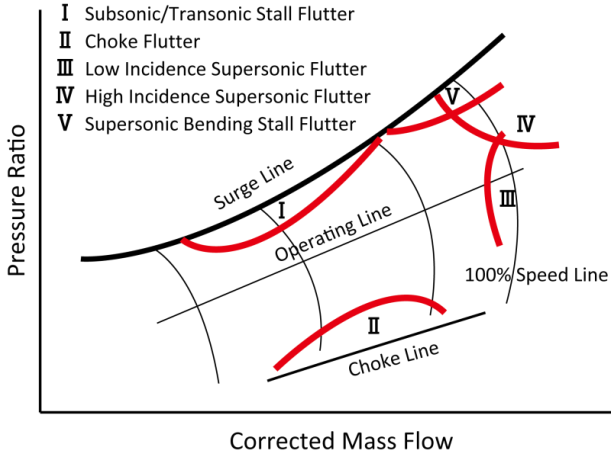

Figure 1.7 Classification of flutter in turbomachinery [6]

Stall flutter occurs under the high load condition near the surge line and is directly related with flow separation on blade suction side. It is usually seen in fans and front compressor stages. Supersonic unstalled flutter and choke flutter are considered to have no close relation with flow separation and effect of boundary layer. Supersonic unstalled flutter is commonly seen in shrouded fans. Choke flutter is a less common, low operating line type of flutter experienced by middle and rear compressor stages. In brief summary, inducing mechanisms of flutter are of high complicacy, and common stall flutter is related to large size separation vortices.

1.2.2 Analysis Method of Cascade Flutter

The equation of vibration used for aeroelastic study is written in eqn.(1.1).

$$\boldsymbol{M}\ddot{\boldsymbol{x}} + \boldsymbol{C}\dot{\boldsymbol{x}} + \boldsymbol{K}\boldsymbol{x} = \boldsymbol{F}, \qquad \boldsymbol{F} = \boldsymbol{A}\boldsymbol{x} + \boldsymbol{B}\dot{\boldsymbol{x}} \tag{1.1}$$

Here, $\boldsymbol{x}$ is the displacement vector of the blade. $\boldsymbol{M}$, $\boldsymbol{C}$ and $\boldsymbol{K}$ mean the global mass, structural damping and stiffness matrices. $\boldsymbol{F}$ is total aerodynamic force acting on blade surface which is determined by the matrix of unsteady aerodynamic force coefficient, $\boldsymbol{A}$ and $\boldsymbol{B}$.

(1) Empirical Method

The empirical methods were the earliest methods and are still used now. Due to lack of knowledge about the mechanism of flutter, the methods are based on large amount of experimental data to obtain empirical flutter boundary. In the early stage, the Campbell diagram was used to show the possibility of forced response. And parameters of reduced frequency, angle of attack and inlet relative Mach number are used for flutter prediction. As the newly designed blades have different shapes and flows, empirical methods are not adequate.

(2) Aerodynamic Method

Many researches on flutter are based on the method proposed by Carta [7] which is called energy method by Bendiksen [8]. This method is based on the assumption that flutter occurs in one normal mode and the prediction is obtained by calculating the energy transfer between flow and vibration under this mode.

If the blade starts to vibrate at natural frequency, the mechanical damping will consume the vibration energy. But the blades also exchange energy with surrounding flow. So, flutter occurrence is judged by the sum of mechanical damping work and aerodynamic damping work. The principles are shown as follows.

$$W_{aero} + W_{mech} < 0 \quad \Rightarrow \quad \text{Aeroelastic stable}$$
$$W_{aero} + W_{mech} = 0 \quad \Rightarrow \quad \text{Critical condition}$$
$$W_{aero} + W_{mech} > 0 \quad \Rightarrow \quad \text{Aeroelastic unstable}$$

This method can be summarized as Figure 1.8. It indicates that energy transfer is the essence of flutter, but sometimes neglects the influence of unsteady aerodynamic force on vibration. Research methods on aeroelastic problems include linearized model (small perturbation assumption) and nonlinear model. Energy method is widely used in flutter researches.

For the calculation of blade row, Lane [9] proposed “Travelling Wave Mode” to simplify the multiple degrees of freedom system in turbomachinery on the natural environment of flutter. An alternative solution is call “Influence Coefficient Method” proposed by Hanamura et al. [10] which is based on the decomposition of each blade contribution on aerodynamic unsteadiness.

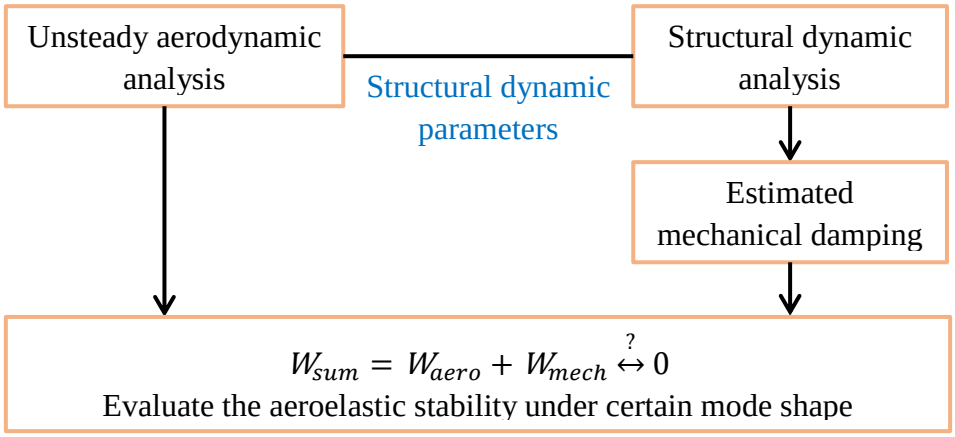

Figure 1.8 Schematic diagram of energy method

(3) Structural Method

Structural method emphasizes on the dynamic response of the blade under aerodynamic force and is based on vibration analysis equation. The aerodynamic stiffness matrix and damping matrix can be obtained by some linear assumptions so that flutter problem can be simplified as a problem about solving the eigenvalues of the matrix.

(4) FSI (Fluid-Structure Interaction) Method

Flutter phenomena in turbomachinery have some special characters as follows.

- ✧ Blades in one row are arranged closely.
- ✧ Mistuning phenomenon exists in the row.
- ✧ Flow field is affected by both aerodynamic and structural parameters.

So, flutter is decided by the interaction between blade and surrounding flow which is a typical fluid-structural coupling problem. So the real flutter phenomenon should be simulated by using FSI method. This method is near the actual process and being developed rapidly, while the computation is of relatively high cost.

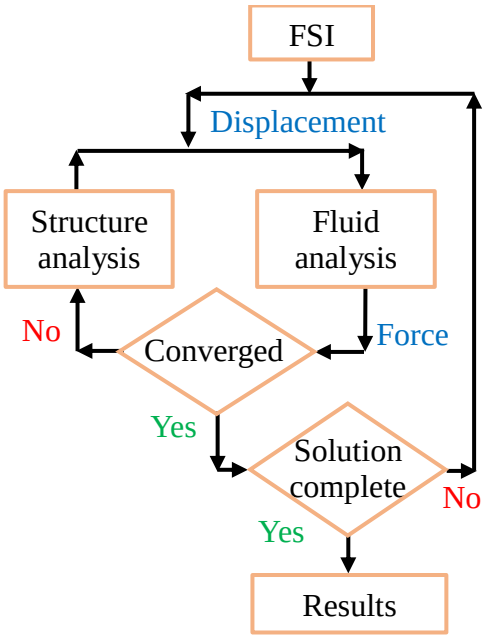

Figure 1.9 Flow chart of FSI method

1.3 Previous Researches on Cascade Flutter

Under transonic flow conditions, the shock waves occur in blade passages and move with the blade oscillation which causes the large pressure fluctuation on blade surface and influences the unsteady aerodynamic characteristics of cascade to great extent. Besides, in such operating conditions, the large separation vortices also have large impacts on flutter characteristics. Due to the existence of lots of unknown phenomena in cascade flutter, the integration of experimental measurement and numerical simulation is expected for research development and analysis method establishment [11].

1.3.1 Researches Based on Experimental Approaches

Many experiments based on compressor rig test and wind tunnel have been conducted for cascade flutter study. Flutter boundary obtained by rig test is very meaningful to interpret the occurrence of real flutter phenomena and verify the overall performance of CFD method. Besides, for the fundamental research of flutter phenomena, the wind tunnel experiment with oscillating cascade are also considered an appropriate and effective way to grasp real phenomena of unsteady aerodynamic forces caused by blade vibration.

Szechenyi et al. [12] measured the unsteady aerodynamic force under started flow condition in a linear cascade. Due to this study, the bending mode flutter doesn't occur under medium load, while it occurs under low and high load. The flutter occurrence under high load is related

with attachment point of lead edge shock wave on suction side, and under low load, it is related with attachment point of trailing edge shock wave on pressure side. By using a transonic compressor annular cascade, Kobayashi et al. [13] investigated the cascade stability under the inlet flow from high subsonic to supersonic conditions at IBPA=67.5deg. The bending mode flutter doesn't occur under subsonic inflow, while it occurs under supersonic inflow when the reduced frequency was less than 0.0786. Furthermore, the attachment point of lead edge shock wave on suction side is considered the main excitation source of flutter. However, the upper limit of inlet Mach number of 1.06 is relatively low blade loading condition.

Watanabe et al. [14][15][16] experimentally and theoretically studied the aerodynamic characteristics of an oscillating cascade with tip clearance in case of nonloaded and loaded cascades. They found that when steady aerodynamic loading acts on blades, the blade vibration is stabilized by the presence of tip clearance due to the appearance of tip vortices. When the blade oscillation becomes unstable, the tip side of blade changes to an unstable state prior to the hub side.

Shibata [17] investigated the cascade stability of bending mode flutter under various shock wave configurations by adjusting the static pressure ratio of cascade with inlet Mach number from 1.1 to 1.2. With the increase of pressure ratio, the cascade has a tendency to be unstable with the increase of the amplitude of unsteady aerodynamic force. Also, the influence of reduced frequency was illustrated. Aotsuka [18] investigated the oscillation characteristics of torsional mode flutter in transonic flow. At low reduced frequency, the instability is stronger under low pressure ratio due to the smaller phase delay.

Yang et al. [19] carried out an experiment on unsteady flow of a linear three-dimensional oscillating compressor cascade by use of off-board transducers and influence coefficient method. The results illustrated fully 3D unsteady behavior and the blades are aeroelastically destabilized as tip gap is increased.

In the field of flutter research on turbine cascade, the influence of oscillating frequency and tip clearance flow on flutter characteristics was clarified by Bell et al. [20] with a linear cascade and Vogt [21] with an annular sector cascade.

Since the unsteady pressure distribution on the blade surface is of great significance for prediction of blade flutter, the detailed information of unsteady aerodynamic force acting on the blade is strongly needed. Due to the previous researches, the steady pressure and unsteady pressure are conventionally measured by pressure transducers mounted on the surface, but there are still some limitations in some conditions, such as thin model parts, complex shape and high spatial resolution demand. Also, the past experimental investigations were still insufficient to show the relationship of flow phenomena and flutter occurrence based on the unsteady pressure distribution on the whole surface of an oscillating blade.

1.3.2 Unsteady Pressure Measurement in Transonic Flows with PSP Technique

Recently, Pressure-Sensitive Paint (PSP) has been widely used in the pressure measurement of various kinds of body surfaces which was introduced by Liu and Sullivan [22] and some new

trends was summarized by Gregory et al. [23]. PSP can realize non-contact, quantitative, high spatial resolution surface pressure measurement for various aerodynamic flows by using the images captured by high speed camera. Among the PSP methods, the anodized aluminum pressure-sensitive paint (AA-PSP) has fast time response of 34.8μs [24]. The performance of AA-PSP shows the capability of unsteady pressure measurement [25][26]. Due to the previous applications of PSP in various flows [27][28][29][30], the current applicability of PSP under different flow speed range was summarized as Table 1.1. The steady pressure measurement by PSP is relatively easier than unsteady pressure measurement, while measurement of transonic and supersonic flow can reach industrial level. For unsteady pressure measurement, the qualitative results can be expected in high speed range, while it is hard to get good result in low speed flow due to the limitation of pressure resolution.

Table 1.1 Current applicability of PSP under different flow speed

Speed range	Steady pressure	Unsteady pressure
Low speed flow	△	×
Transonic flow	○	△
Supersonic flow	○	△
Hypersonic flow	△	△

○ - industrial level; △ - academic level; × - challenging level

In the field of turbomachinery, PSP is capable of measuring the cascade blade surface with complex geometry including the leading edge and trailing edge. Gregory used porous PSP in resolving the unsteady wall pressure distributions on turbocharger blades, and porous PSP was considered to be potential in evaluations of rotor-stator interaction, flutter, inlet flow distortion, rotating stall and surge [31]. Kitamura et al. also measured unsteady pressure field in a turbocharger compressor and the temperature dependency was corrected by using symmetrical PSP-TSP coating [32]. As to the axial compressor cascade, Liu et al. conducted the steady pressure and temperature measurement on the rotor stage in a high-speed rotating compressor environment, and the shock wave at higher rotational speeds was indicated clearly in pressure maps [33].

Furthermore, in handling unsteady pressure on oscillating blade with periodic motion, PSP is also expected. Fonov et al. had studied the pressure measurement precision of an oscillating blade based on Fast Binary Pressure Sensitive Paint (FBPSP) in early years [34]. Okabe et al. captured the unsteady pressure distribution including the shock oscillation over an oscillating wing by using a motion-capturing two-color PSP system, which also agreed well to the Kulite measurements [35]. Watanabe et al. has adopted the fast-response PSP technique into cascade flutter study and realized qualitative unsteady pressure measurement in transonic oscillating cascade which is expected for flutter mechanism analysis [36].

Therefore, PSP is considered as an effective tool for obtaining detailed information of unsteady pressure on blade surface, so as to provide a reliable verification way for CFD methods.

1.3.3 Researches Based on CFD Methods

With the development of CFD technology, the numerical simulation of flutter is realized to great extent based on the verification by experimental results. CFD methods for flutter simulation mainly includes unsteady RANS method and FSI method. URANS method is simple and relatively costless which is capable of solving unsteady aerodynamic forces and helping understanding the influence of flow phenomena on cascade stability. It can be applied in the conditions of already known structure deformation, independency of vibration state on aerodynamic forces and ignorance of elastic and inertial forces. The time-domain RANS method is commonly used in general oscillating cascade simulation. Besides, some CFD simulations are conducted using a nonlinear frequency- domain, harmonic balance method [37] which is validated through some tests [38][39]. It has advantages of calculation speed, multi-row calculation and understanding of unsteady flow. As to FSI method, it is an essential analysis method for aeroelastic phenomena, which is able to grasp overall behavior of the system by one computation and is effective for coupled system which is difficult to estimate. Nevertheless, it still have some demerits that it is not suitable for parametric study of sensitivity analysis and easy understanding of complex phenomena by time domain analysis. It also takes higher cost and needs more complex programming. In handling with flutter simulation, the method should be selected according to characteristics of the phenomena to be illustrated. Under the condition of small amplitude when the blade deformation is known and can be evaluated linearly, URANS method is effective with enough accuracy.

Isomura and Giles [40] studied the mechanisms of transonic fan flutter in bending mode by quasi-3D thin-shear-layer Navier-Stokes (N-S) equations. Results showed that an oscillation of the passage shock rather than blade stall is the main source for flutter occurrence.

Srivastava et al. [41] conducted 3D simulation based on N-S equation with TURBO-AE code and showed that in transonic fan, the location and strength of shock wave have strong influence on blade stability. The accurate blade operating shape is important for accurate damping prediction, while the variations in vibration frequency are less significant to the stability.

Vahdati et al. [42] conducted a detailed wide-chord fan blade flutter analysis with emphasis on flutter bite by using three different intakes. Both stall flutter driven by flow separation and acoustic flutter driven by intake acoustics were identified.

Aotsuka and Murooka [43] numerically investigated the transonic stall flutter by calculating two types of fan blade (one with flutter bite and the other without flutter bite) with a 3D N-S CFD code. The results shows agreement with rig test results [44] in qualitative sense. A detached shock wave and separation due to the shock boundary layer interaction were considered to have significant impacts for flutter stability.

Tateishi [45] conducted the simulation of a compressor rig based on a FSI method with modal identification technique for predicting the flutter boundary of part-speed transonic stall flutter. The flutter boundary obtained by FSI simulations agrees well in a qualitative sense for the high speed lines, while it cannot reproduce the end of the flutter boundary for the low speed lines. The reason for the mismatch was concluded that highly complex and sensitive near-wall flow

phenomena are related to the shock position and flutter characteristics.

Duquesne et al. [46] investigated the choke flutter in an Ultra High Bypass Ratio fan using a time-linearized RANS solver. Main sources of flutter excitation were considered to be the shock-wave motion and the shock-wave / boundary layer interaction.

1.4 Research Motivation and Objectives

1.4.1 Research Motivation

Cascade flutter phenomena in transonic flow is of great complexity which are interactively influenced by many factors, including blade vibration, shock waves movement and flow separation. The shock waves and separated flows are with strong 3D characteristics which is affected by boundary layer development, and tip leakage flow. The 3D flow also causes 2D spatial unsteady pressure on blade surface which is the dominant factor of flutter occurrence in aerodynamic view. However, the reports on 2D spatial unsteady pressure distribution were hardly found in previous researches. The past researches were always based on unsteady pressure measurement on discrete points at blade middle span which was inadequate for understanding the spatial distribution and unsteady behavior of local details.

Under such situation, in this study, fast-response PSP technique is proposed and applied in measuring the unsteady surface pressure of an oscillating cascade, to acquire the fundamental results of unsteady pressure distribution and observe the movement of flow phenomena in 2D space, such as shock waves, tip leakage flow and corner separation. These results can provide important knowledge on spatial unsteady behaviors of 3D flow and evidences for verifying CFD methods.

1.4.2 Research Objectives and Approaches

In view of above mentioned background, this study is focusing on the basic flutter mechanisms of compressor oscillating cascade in transonic flow with shock waves. The research objectives with corresponding approaches are expressed as follows.

1. Understand the steady flow field inside a compressor cascade in transonic flow with different shock pattern and analyze the effect of 3D flow on surface pressure distribution on blade surface.
2. Obtain the unsteady pressure distribution on blade surface of oscillating cascade, so as to observe the unsteady behavior of the flow phenomena. Then, clarify the mechanisms of unsteady pressure propagation.
3. Based on energy analysis, illustrate the aerodynamic stability of oscillating cascade and the impact factors on stability. Finally, summarize the fundamental mechanisms of flutter occurrence in the transonic compressor oscillating cascade.

This study is based on both experimental and numerical approaches, and the overview of the methods is shown in Figure 1.10. A fast-response PSP technique is applied to realize the steady

and unsteady surface pressure measurements on oscillating cascade blades and the results are compared with some conventional pressure measurement and flow visualization methods. Then, the CFD method is validated by the experimental results and used to obtain more flow details and more results in wider operation range of the cascade. Based on the results, cascade stability is analyzed under different shock configurations.

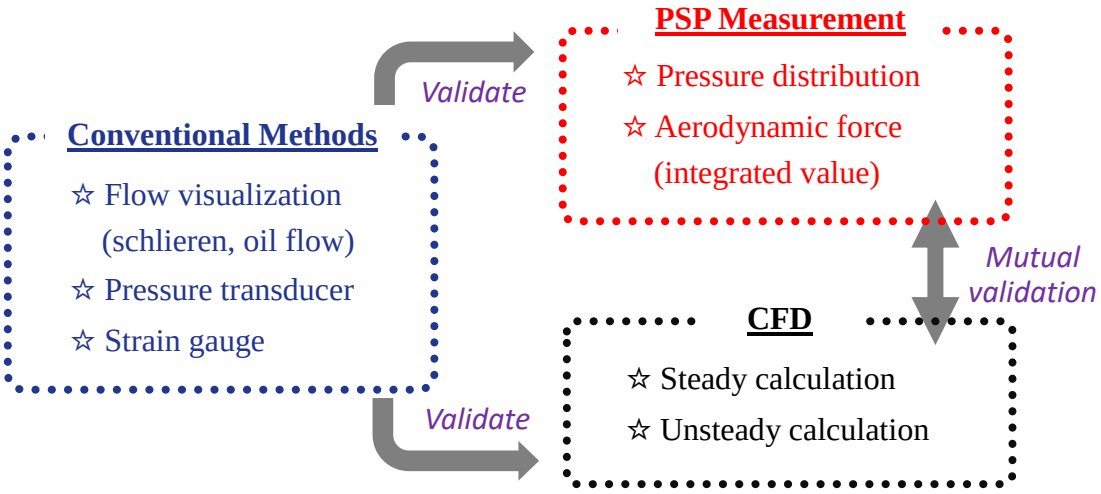

Figure 1.10 Diagram of research approaches

1.5 Overview of the Thesis

This thesis insists of 6 Chapters.

Chapter 2 and Chapter 3 explain the research approaches adopted in this research. Chapter 2 describes the stability analysis method of flutter, wind tunnel and measurement techniques. Chapter 3 explains the CFD schemes based on RANS equations for flutter simulation.

In Chapter 4, the steady flow fields with different P.R. are measured and calculated. The steady aerodynamic characteristics of the cascade are investigated. The shock waves structure in current transonic compressor cascade is classified into 4 types. Furthermore, the compressor characteristic line, total pressure loss and 3D characteristics of the cascade are analyzed.

In Chapter 5, based on the known steady flow field, the unsteady aerodynamic characteristics of oscillating cascade in translational mode are analyzed. Three central blade under double shocks pattern and merged shocks pattern are measured by PSP. The corresponding CFD calculations are also conducted by using the steady calculation results. The propagation mechanisms of unsteady pressure are clarified. Furthermore, aerodynamic stability of transonic compressor oscillating cascade is analyzed by using influence coefficient method. The impacts of pressure ratio variation and oscillating frequency variation on aerodynamic stability of oscillating cascade are investigated. The reasons and mechanisms of aerodynamic instability are summarized and clarified.

At last, conclusions are drawn and some prospects are suggested in Chapter 6.

Besides, more details including AA-PSP technique and characteristics of transonic wind tunnel are summarized in Appendix A and B.

Chapter 2 Experimental Approaches

2.1 Stability Analysis Method of Oscillating Cascade

For evaluating the aerodynamic stability of oscillating cascade, travelling wave mode method or influence coefficient method are widely used based on the energy analysis. The theory of travelling wave mode is by supposing all blades are same and vibrating with same amplitude and a constant inter blade phase angle (IBPA) from the neighbor blade. The unsteady aerodynamic force and unsteady aerodynamic work are investigated and used for stability analysis, while it is time-consumed and difficult to conduct experiment. In cases of small oscillating amplitude and linear supposing of superposition of unsteady aerodynamic forces, influence coefficient method is effective with less cost.

The description of influence coefficient method is expressed by the following equations and shown in Figure 2.1. The blades are named as –n~-1, 0, +1~+n in flow direction. The forced oscillation of central blade 0 is defined as eqn.(2.1). Blade oscillation causes unsteady aerodynamic forces on all the blades at oscillation frequency which is described as eqn.(2.2). C_n is the influence coefficient and φ_n means the phase shift from motion of central oscillating blade. Then, by supposing all blades are oscillating with amplitude A and IBPA σ, the displacement of each blade can be expressed as eqn.(2.3). In the periodic cascade, the aerodynamic force induced by blade n on blade 0 is equivalent to the aerodynamic force induced by blade 0 on blade –n which is written as eqn.(2.4). Then, we can summarize the aerodynamic forces induced by each blade on the central blade 0 into the aerodynamic force sum $F_{sum}(t)$ expressed as eqn.(2.5). Finally, the unsteady aerodynamic work is calculated as a function of IBPA expressed as eqn.(2.6). In this paper, unsteady aerodynamic work was calculated as W by eqn.(2.7), and the parameters C_n and φ_n of influence coefficient method used the amplitude $\tilde{C}_F$ and phase φ of unsteady aerodynamic force coefficient on each blade. When W is greater than 0, the system is considered to be aerodynamically unstable.

$$A_0(t) = Asin(\omega t) \tag{2.1}$$

$$F_{0\to n}(t) = |C_n| sin(\omega t + \varphi_n) \tag{2.2}$$

$$A_n(t) = Asin(\omega t + n\sigma) \tag{2.3}$$

$$F_{n\to 0}(t) = |C_{-n}| sin(\omega t + \varphi_{-n} + n\sigma) \tag{2.4}$$

$$F_{sum}(t) = \sum_{n=-\infty}^{\infty} |C_{-n}| sin(\omega t + \varphi_{-n} + n\sigma) \tag{2.5}$$

$$W'(\sigma) = \int_0^{\frac{2\pi}{\omega}} F_{sum}(t) \cdot \frac{dA_0(t)}{dt} dt = \pi A \sum_{n=-\infty}^{\infty} |C_{-n}| sin(\varphi_{-n} + n\sigma) \tag{2.6}$$

$$W(\sigma) = W'(\sigma)/(\pi A) \tag{2.7}$$

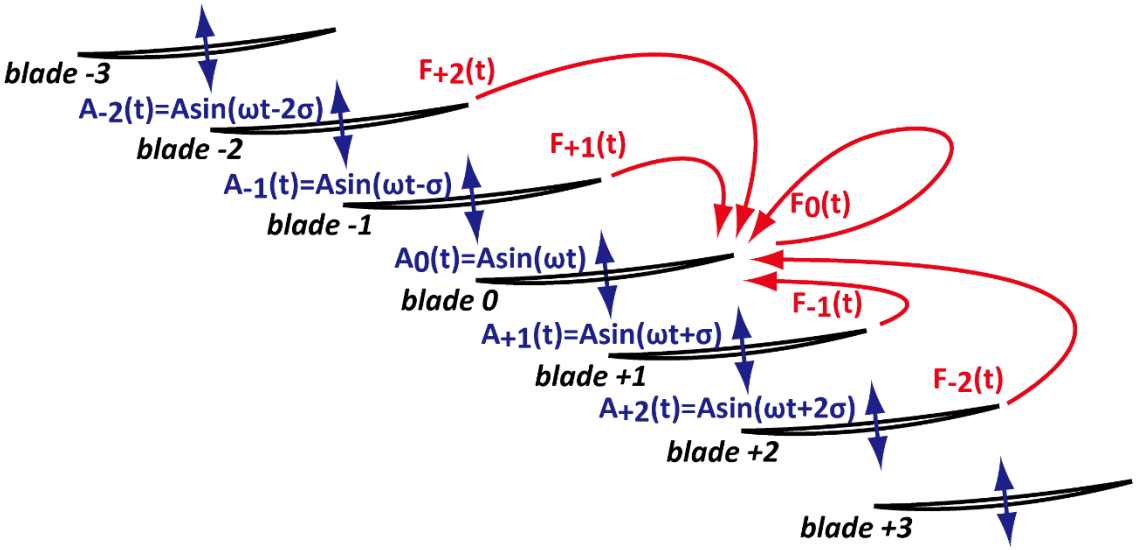

(a) Travelling wave mode method

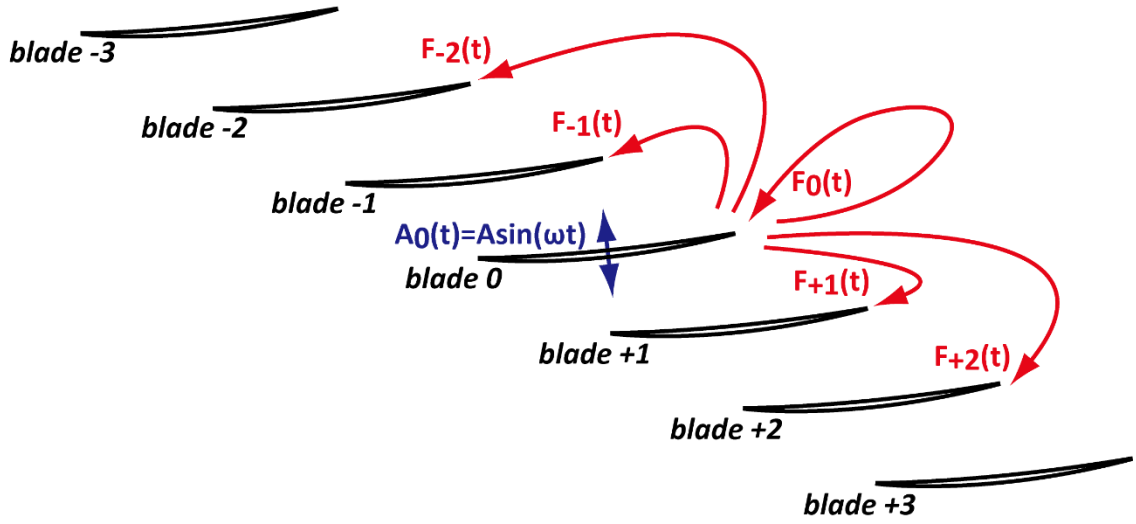

(b) Influence coefficient method

Figure 2.1 Study method for aerodynamic stability of oscillating cascade

In this study, the influence coefficient method was used for both experimental and numerical analysis. A transonic wind tunnel with a compressor cascade was adopted for establishing the experimental model.

2.2 Wind Tunnel Facility

A blow-down type transonic linear wind tunnel is used to conduct the experiment, and the overview of arrangement schematic is shown in Figure 2.2. The wind tunnel facility is mainly consisted of air supply facility, pressure regulator & air straightening device, transonic wind tunnel, and silencing & exhaust device. The details of these devices are introduced as follows.

2.2.1 Air Supply Device

The air supply device is shown in Figure 2.3. The air supply device is consisted of one air compressor, two air dryers and two air reservoirs. The air compressor is package-type 2-stage dry screw compressor SD-H1B and the specification is shown in Table 2.1. It can produce air flow with maximum pressure 0.83MPa and maximum flowrate 16.5m^3/min (atmospheric pressure converted). The air dryers use two PSD-1250 heatless dryers (Table 2.2) for continuous air drying by switching alternately every 5 minutes. They can be used for the air with the outlet dew point -40~-70℃ (atmospheric pressure converted). By using two 15m^3 air reservoirs, it takes 25 minutes for charging the air reservoirs from atmospheric pressure to maximum pressure. And it takes 10 minutes from 4atm to maximum pressure.

Table 2.1 Specification of air compressor

Air flowrate	16.5m^3/min
Discharge pressure	0.83MPa-G
Motor output power	132kW

Table 2.2 Specification of air reservoir

Capacity	15m^3
Max. design pressure	9.5kgf/cm^2-G
Number	2

2.2.2 Pressure Regulator and Air Straightening Device

The overview of pressure regulator and air straightening device is shown in Figure 2.4. It consists of pressure regulating valve, air straightening tube and quick open ball valve.

The self-acting pressure reducing valve P-26 (FUSHIMAN Co., LTD.) is used for pressure regulation with the improvement in secondary pressure detection unit and internal flow path. In addition, with the mechanism which can adjust the displacement and phase of feedback amount of secondary pressure, the pressure inside the regulating duct can be kept constant. The adjusting range of secondary side pressure is 0.35~5kg/cm^2-G and the maximum flowrate is 13000m^3/hour.

The air straightening duct consists of porous plate (aperture ratio 44%), porous cone, regulating honeycomb and two kinds of wire mesh. It is used to diffuse the flow, homogenize the flow and remove the flow turbulence. As a result, the turbulence intensity of static pressure inside the regulating duct is below 1%.

2.2.3 Transonic Wind Tunnel

The overview of transonic wind tunnel and the photo of wind tunnel insight view are shown in 0. The wind tunnel body can be divided into 4 parts: the nozzle part for adjusting inlet Mach

number, test section for installing cascade and doing measurement, boundary layer bleeding part for eliminating the influence of boundary layer development, and downstream part for adjusting outflow angle and back pressure.

(5) Nozzle

The transonic wind tunnel can be used for various inlet conditions with different inlet Mach number by applying a variable nozzle with an upper variable wall and a lower flat plate wall. The upper variable wall is made by bonding a neoprene rubber (thickness: 14mm) to a phosphor bronze plate (thickness: 1mm). There are 10 rods attached to the phosphor bronze plate. The shape of upper wall can be changed by adjusting the tightening heights of rods.

There are 13 pressure taps on the lower wall from nozzle throat to test section. By using the static pressure distribution results in nozzle and the knowledge of characteristic curve, the targeted Mach number and optimal shape can be approached. By adjusting the shape of upper wall, the angle of lower wall and the air bleeding amount, the range of inlet Mach number can be set to be 1.05~1.60. The bypass passages are set between the cascade and the upper wall or lower wall for separating the upper/lower wall induced boundary layer from the main flow, in order to improve the starting characteristic of wind tunnel.

(6) Test Section

The enlarged view of test section is shown in Figure 2.6. The test section measures 50mm×100mm rectangular cross section and 7 blades can be installed. The brass circular disk can be mounted on one side of the test section which is shown in Figure 2.7. There are rectangle holes on the circular disk where the blocks for fixing blades can be inserted into the holes and the blade is fixed by the blade fixing block. The wall static pressure can be measured by the static pressure taps on the disk surface to calculate the isentropic Mach number and static pressure ratio. The glass circular disk shown in Figure 2.8 can be mounted on the other side to realize optical access for observing, PSP measurement and schlieren visualization. The angle of incidence can be changed by rotating the circular plate with circumferential long holes.

(7) Boundary Layer Bleeding Device

The layout of boundary layer bleeding device is shown in Figure 2.9. The device consists of vacuum pump, $30m^3$ vacuum tank and quick open valve. The boundary layer bleeding is done through the porous side walls in the upstream of the test cascade in order to reduce boundary layer thickness and improve spanwise uniformity. Also, boundary layer bleeding is conducted through the bottom wall in the upstream of the test cascade to prevent the bottom wall boundary layer from developing.

When doing wind tunnel experiment, the quick open valve opens 0.5s after beginning the suction, then the bleeding begins by extracting the boundary layer into vacuum tank. Because pressure in the vacuum tank will increase with the bleeding being done, the vacuum pump is always working to keep the vacuum degree.

(8) Tailboard and Throttle Valve

The downstream structure of the wind tunnel is shown in Figure 2.10. Two tailboards are set behind the trailing edge of top-side blade and bottom-side blade, separately. The angle and height of the tailboards can be adjusted in wide range to realize better uniformity of the cascade by giving appropriate outflow angle. Besides, the fore-end of upper tailboard is designed as a pressure box with porous wall and hollow structure. The inner space of pressure box is used to alleviate the upper tailboard induced separation.

Furthermore, the throttle valve on the upper tailboard is used to adjust the back pressure by controlling the outlet area. Based on the change of cascade pressure ratio, various flow field with different shock patterns can be achieved.

2.2.4 Silencing and Exhaust Device

The high speed exhaustive air is leaded into silencing room by passing a special silencing duct to reduce noise level before exhausting into atmosphere. The configuration of silencing duct is shown in Figure 2.11. The duct wall has two-layer and the space between the two layers is filled with dry sand to prevent the vibration and sound from propagating. The silencing room shown in Figure 2.12. The partition wall is of 0.5m height and the internal flow space is 5m×7m×0.5m. The flow passage is designed with a splitter which also serves as guide vane, a partition wall and some narrow sections. The acoustic lining with glass wool is applied to all the walls. As a result, the reduction of exhaust air speed to the extent of several m/s and interacted silencing of exhaust sound are realized.

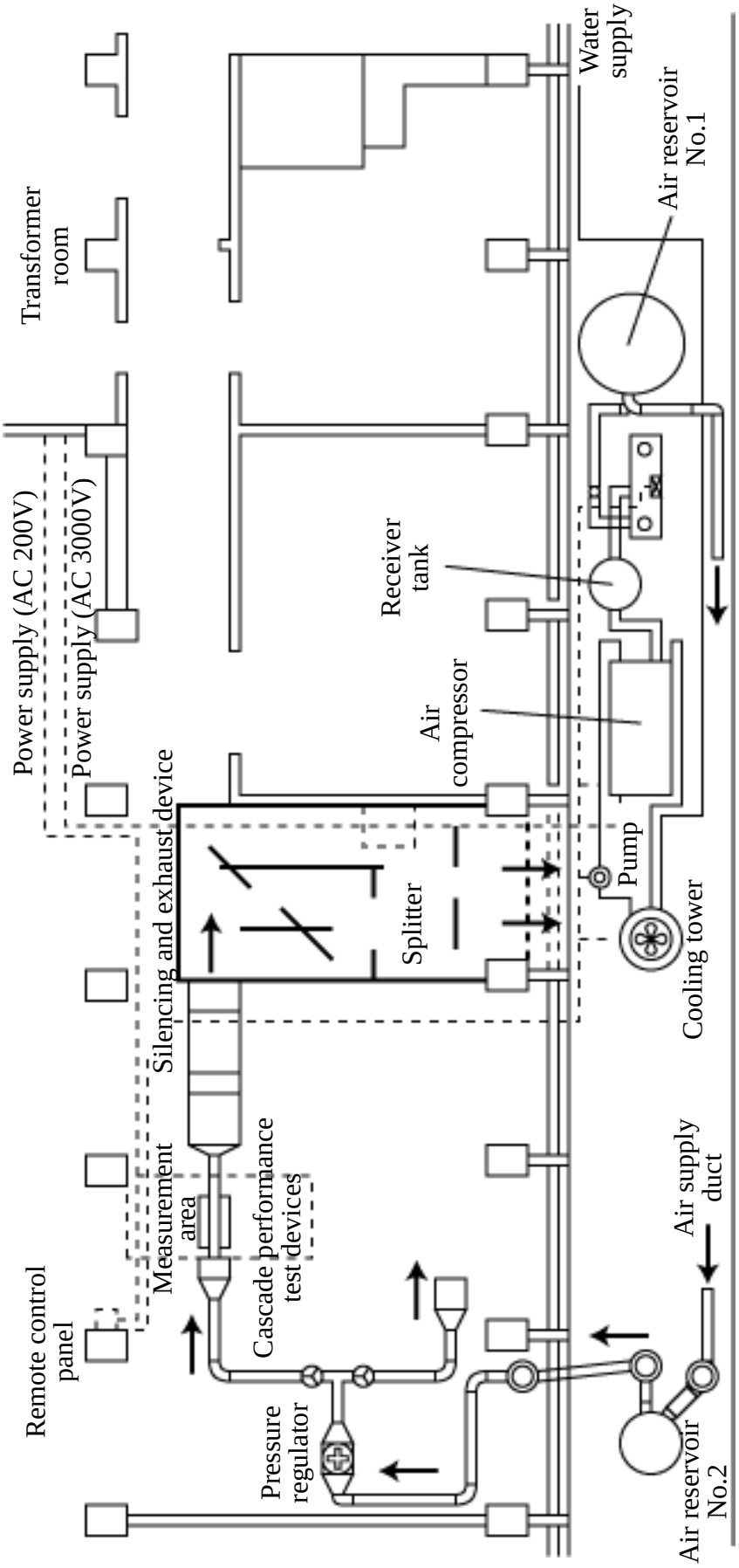

Figure 2.2 Overview of wind tunnel system

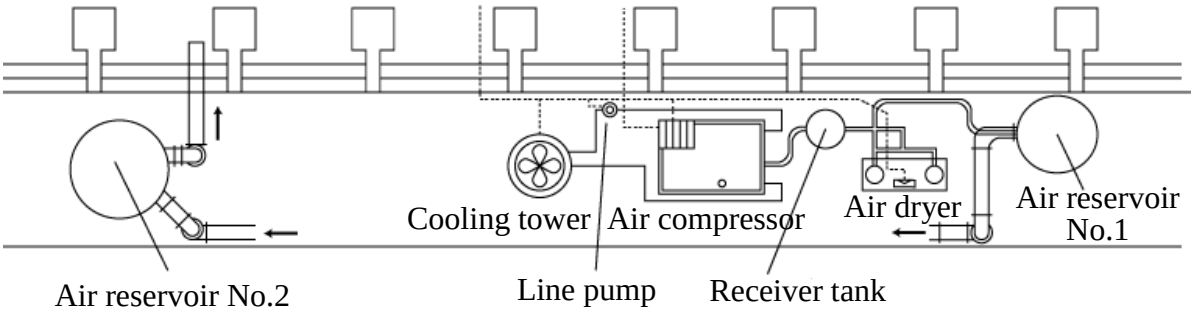

Figure 2.3 Overview of air supply facility

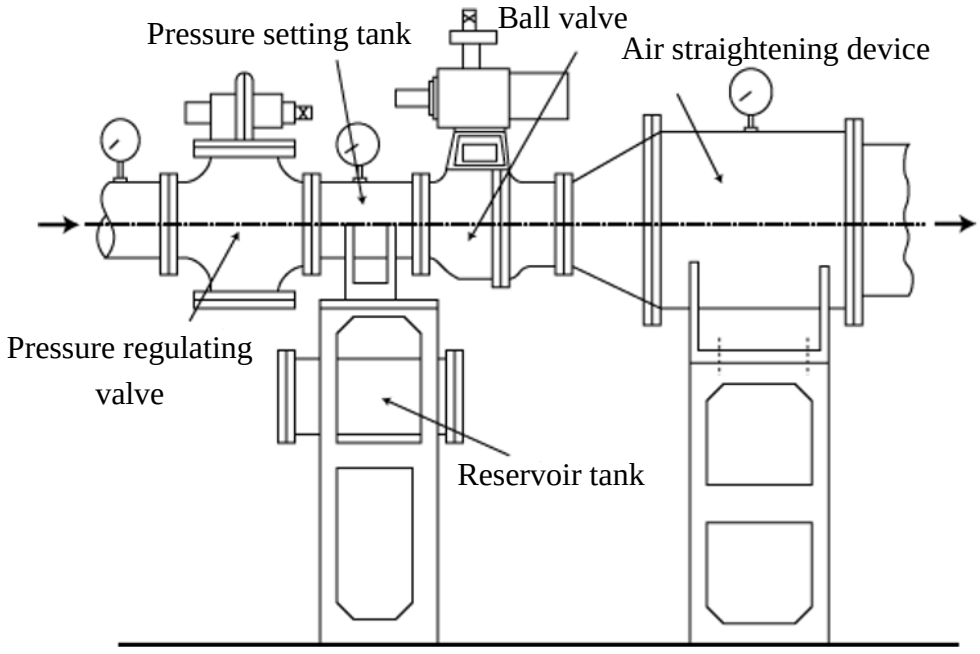

Figure 2.4 Pressure regulator and air straightening device

Inlet Mach number	1.2
Reynolds number	1.2×10^6
Static pressure ratio	1.15~1.45

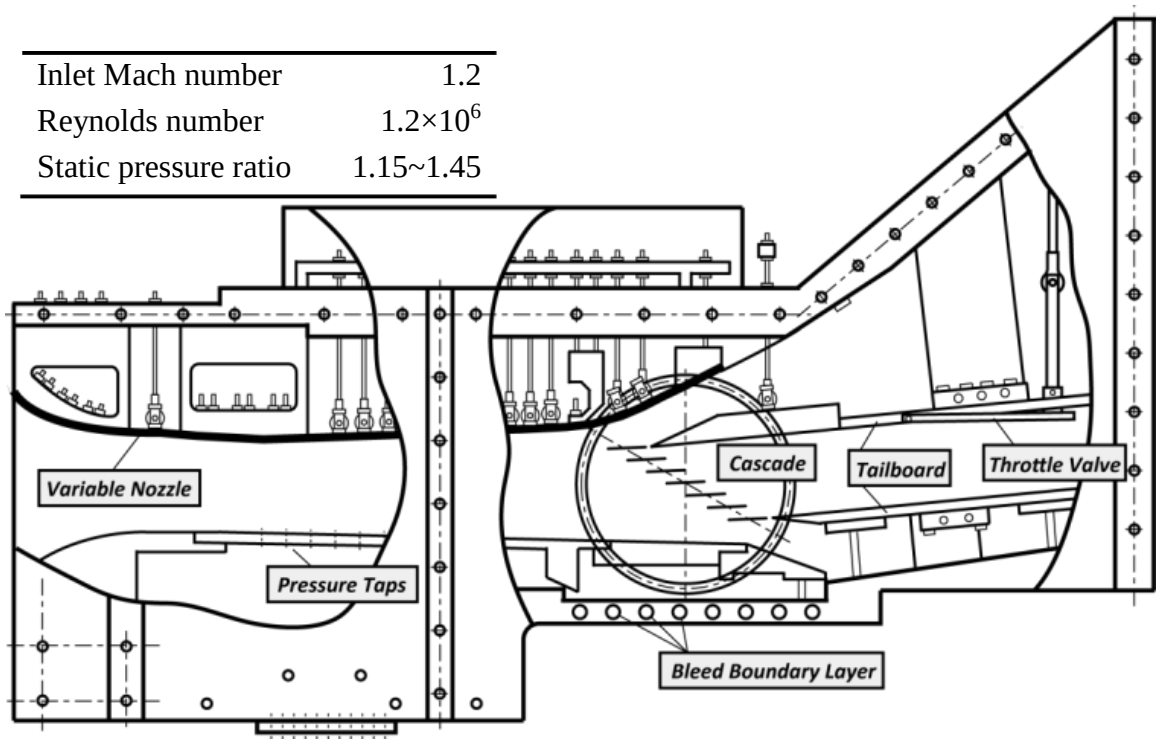

(a) Schematic of transonic linear cascade wind tunnel

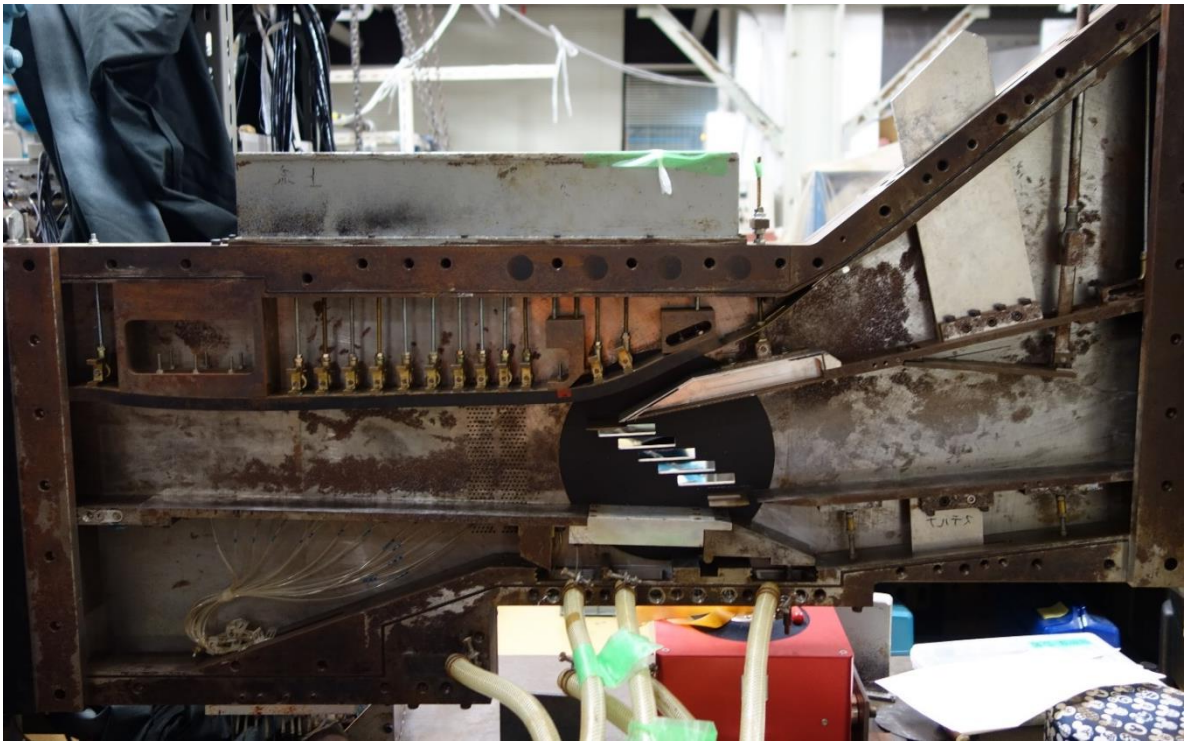

(b) Inside view of wind tunnel

Figure 2.5 Transonic wind tunnel

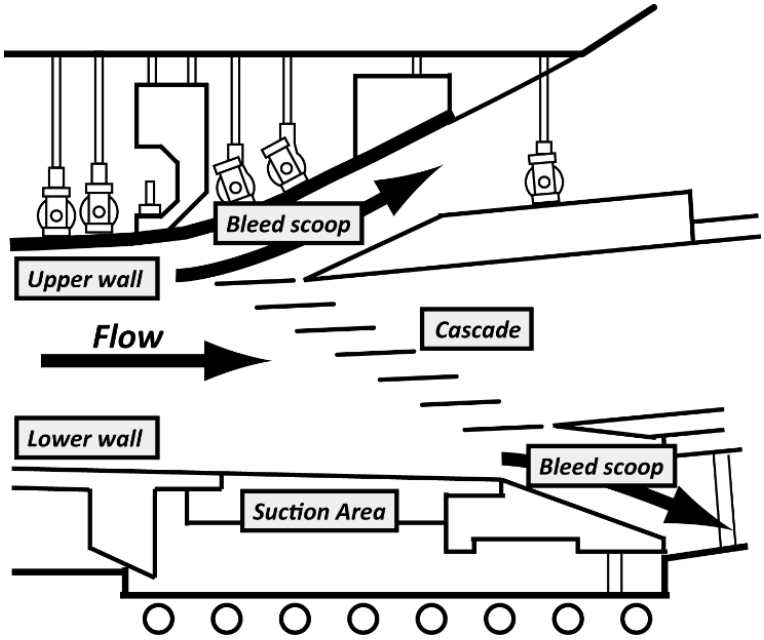

Figure 2.6 Test section

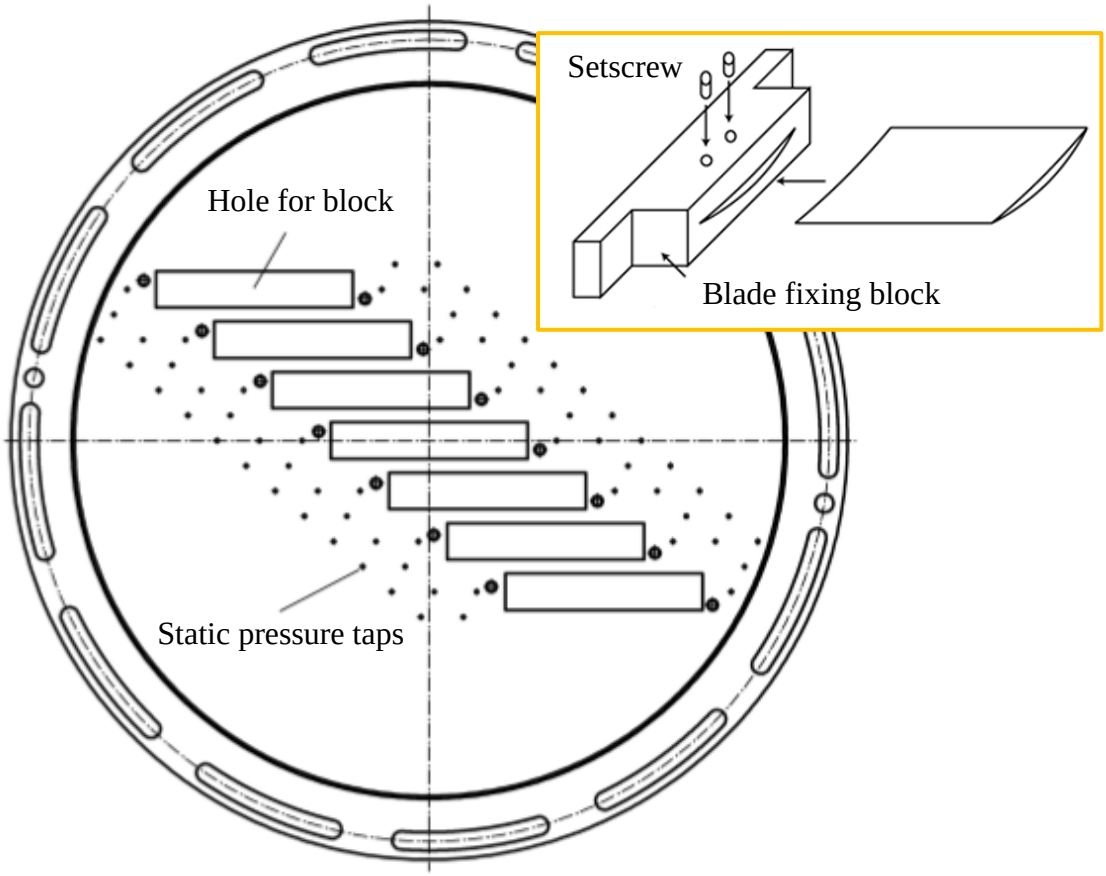

Figure 2.7 Circular disk for blade fixing with pressure taps

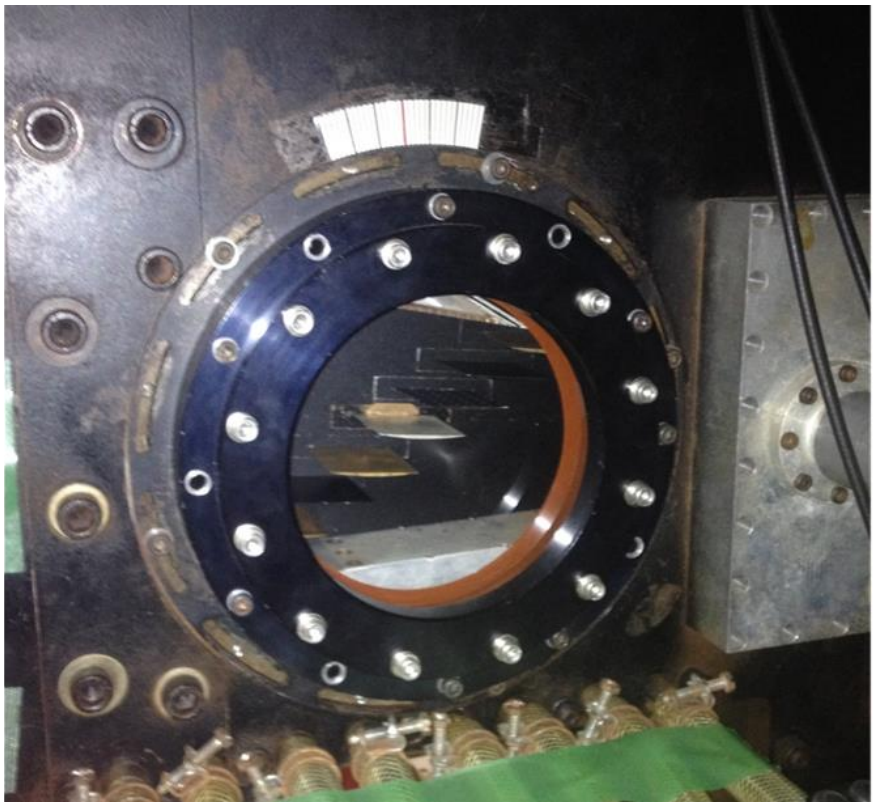

Figure 2.8 Glass disk

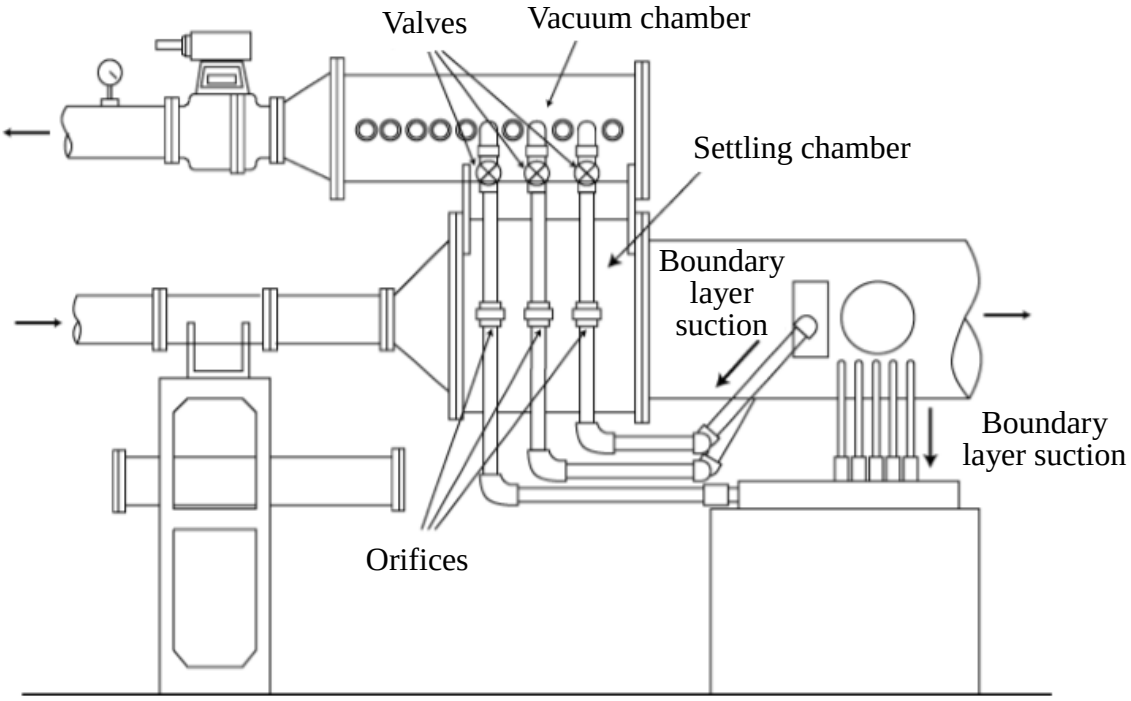

Figure 2.9 Boundary layer bleeding system

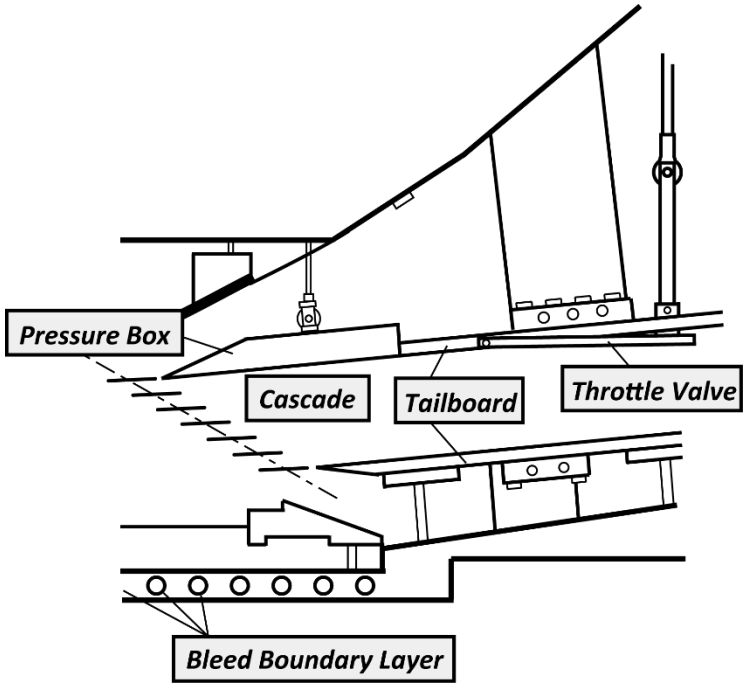

Figure 2.10 Downstream board and throttle valve

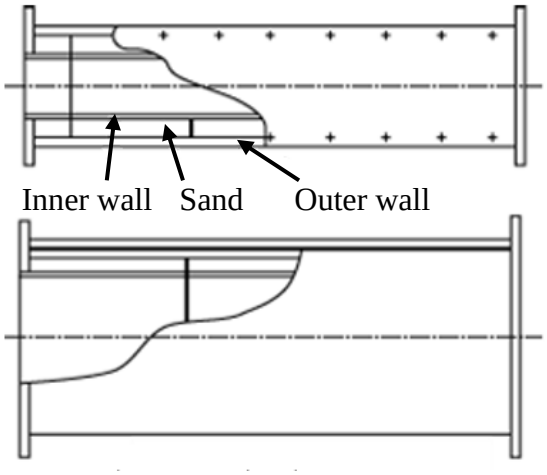

Figure 2.11 Silencing duct

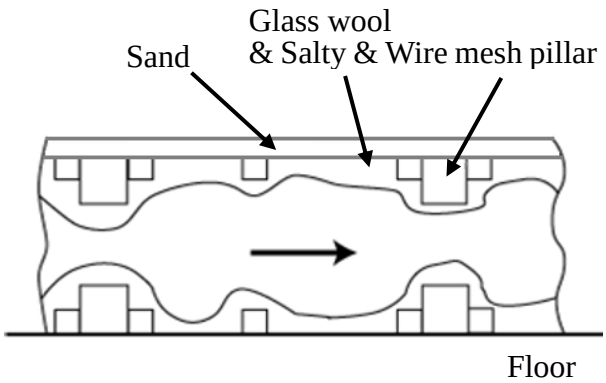

Figure 2.12 Cross section of silencing room

2.3 Test Cascade and Experimental Condition

A linear compressor cascade consisted of 7 double circular arc (DCA) blades was selected as the study object, as shown in Figure 2.13. The blades are numbered as blade -3 to +3 from upstream to downstream location. The central blade 0 can be oscillated in translational mode by a magnetic oscillator. The measurement was conducted on the oscillating blade (blade 0) and two stationary neighbour blades (blade +1 and -1) and based on influence coefficient method.

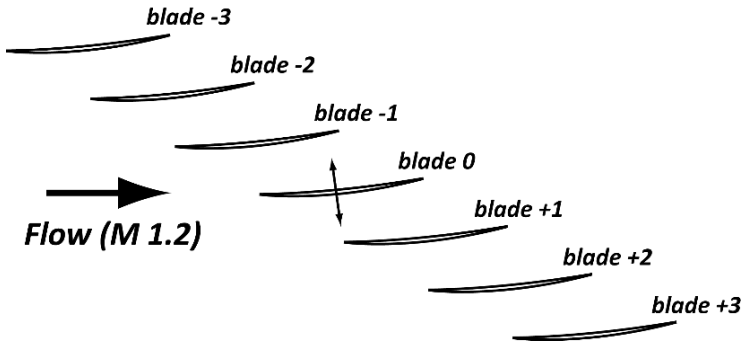

Figure 2.13 Test compressor cascade

2.3.1 Blade Profile

The configurations and main specifications of test DCA blade are shown in Figure 2.14 and Table 2.3. The DCA blade is lead edge-trailing edge symmetric and generally applied in the flow field from high subsonic to transonic. It is used to simulate the relative velocity condition of rotor blade.

The blade is design with chord length 45.15mm, pitch length 27.09mm, span length 49.5mm (with tip clearance 0.5mm) and blade thickness/chord ratio 0.04. The stagger angle of cascade is 55deg and the chamber angle is 10deg. In test section, the angle between blade chord and horizontal direction was set to be 5.5deg, and the angle of incidence in this condition was defined to be 0deg.

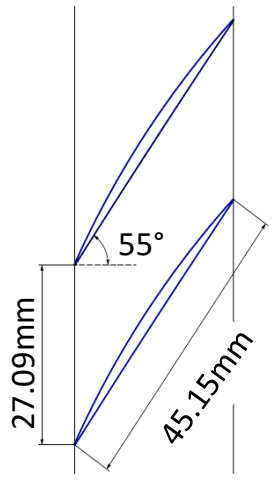

Figure 2.14 Configuration of blade

Table 2.3 Main specifications of blade

Airfoil	DCA	
Chord length	45.15	[mm]
Pitch length	27.09	[mm]
Span length	49.5	[mm]
Tip clearance	0.5	[mm]
Max thickness	1.807	[mm]
Thickness/chord ratio	0.04	
Solidity	1.67	
Stagger angle	55	[deg]
Chamber angle	10	[deg]

2.3.2 Oscillation Mechanism

The appearance of oscillating mechanism is shown in Figure 2.15. It can realize translational oscillation for the central blade 0 in the direction perpendicular to chordwise direction.

The oscillating mechanism uses an oscillator (C-5015, ASAHI SEISAKUSYO) with a power amplifier (APD-602, ASAHI SEISAKUSYO). The waveform is controlled by a function generator (WF1973, NF Corporation). The oscillating frequency can be adjusted in the range of DC~8000Hz. And the oscillating amplitude can be adjusted by adjusting output electric current value.

In the system, there is no movable part in the system except the linear motion guide to reduce the undesirable high order harmonics. A trunnion (1) is used to adjust the oscillating angle. A long screw (4) is used to connect the oscillator (2) and oscillating arm (5). The linear motion guide system (6) uses two slide blocks to eliminate the influence of single side force. The fixing plate (3) is designed to be symmetric for adding counterbalance. The fixing plate (3) is made with long hole for fine adjustment of relative position from the wind tunnel wall.

Besides, laser displacement meter (LK-G30, KEYENCE) fixed on the circular disk is used to measure the location of central oscillating blade and the oscillating amplitude and phase can be known.

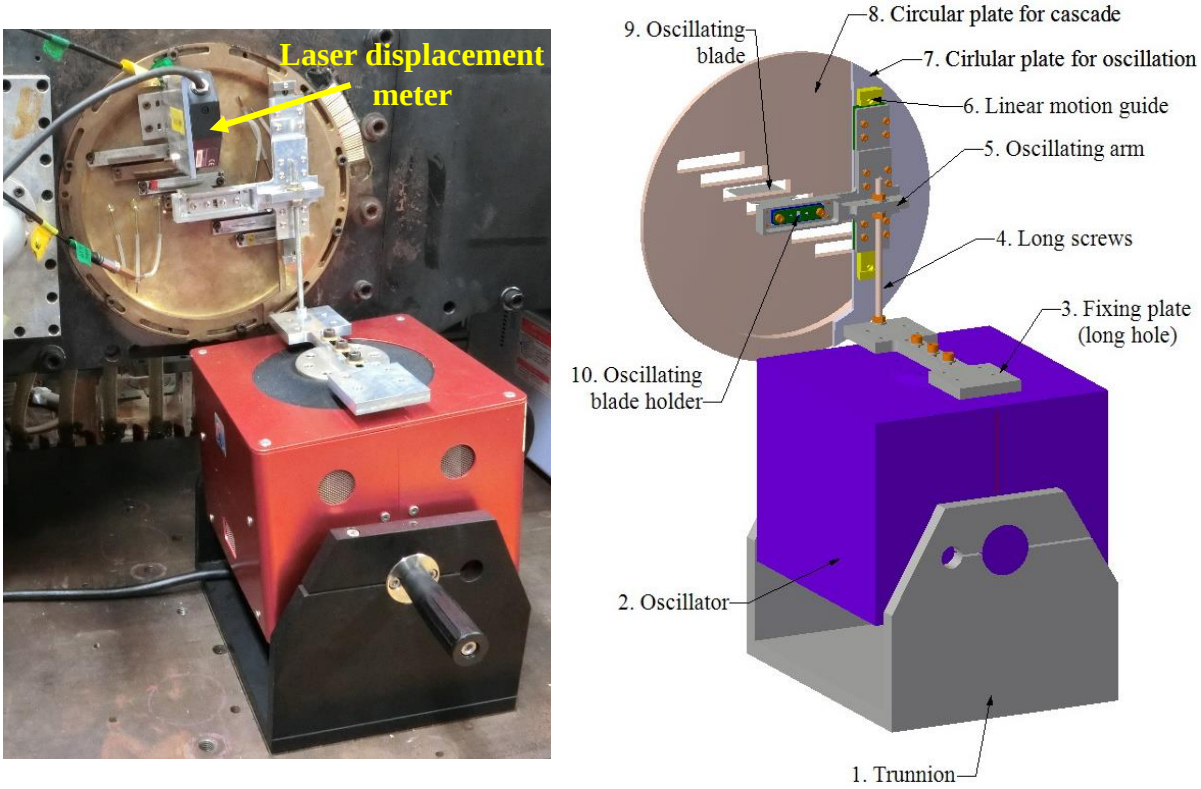

Figure 2.15 Oscillation mechanism

2.4 Experimental Condition

In this study, inlet Mach number and pressure ratio (P.R.) are used to define the flow condition. Inlet Mach number of the cascade is defined as the isentropic Mach number at 1.0 chord-length upstream from the middle chord of blade 0. Before starting the experiment, we adjust the inlet total pressure to make inlet Mach number of the cascade to be 1.2 and then the total pressure is fixed. Pressure ratio is defined as the ratio of the static pressure at 1.0 chord-length downstream to the static pressure at half chord-length upstream from the middle chord of blade 0, which can be changed by adjusting the downstream throttle valve. P.R. is generally used to evaluate the pressurization capability of the compressor cascade.

The experimental condition in this study is shown in Table 2.4. The inlet Mach number was adjusted to 1.2, and inlet turbulence intensity was about 1.2% of the main flow velocity. The incidence angle was set to 0 degree and the static pressure ratio of outlet pressure to inlet pressure of the cascade was adjusted in the range of 1.15~1.45. The oscillation frequency was set from 20Hz to 140Hz, and the corresponding reduced frequency was from 0.0078 to 0.0547.

Table 2.4 Experimental condition

Total pressure	160	[kPa]
Total temperature	293	[K]
Inlet Mach number	1.2	
Reynolds number	1.2×10^6	
Angle of incidence	0	[deg]
Static pressure ratio	1.15~1.45	
Oscillation mode	Translational mode	
Oscillating frequency	20~140	[Hz]
Reduced frequency	0.0078~0.0547	
Oscillating amplitude (P-P)	0.8, 0.6, 0.5	[mm]
	(20~100, 120, 140Hz)	

2.5 Flow Visualization Approaches

2.5.1 Oil Flow

Oil flow is a wall tracing method which can forms a flow pattern on painted surface which responds to the surface shear stress. It can indicate the boundary of a flow separation since the oil cannot penetrate separation boundary. The oil is a mixture made from liquid paraffin and titanium (IV) oxide. The mixing ratio of liquid paraffin and titanium (IV) oxide is $50cm^3$: 20g.

In this study, oil flow method is used to understand the appearance of shock patterns, tip leakage flow and corner separation under several different back pressure cases. The oil-painted blade is blown by the air flow for enough time period until the residual oil is stable. Then, the flow patterns are observed and recorded by camera.

2.5.2 Schlieren

The schlieren method is a visualization method based on the change of refractive index induced by air density change. The brightness change shows the first-order derivative of air density in doing schlieren visualization.

The schlieren visualization system using a round-trip optical path method is shown in Figure 2.16. One glass window and one mirror disk are used as side walls of test section. Blade 0 is set in cantilever state and blades are fixed by pins for both tip and hub sides. The light produced by a xenon light source (XDS-75-HV, KATO KOKEN) passes a pinhole, a half mirror and reflected by a mirror and incident into a concave mirror. The total optical distance between the light source and concave mirror is set to be 2m which is the focal distance of concave mirror. The light reflected by the concave mirror becomes parallel light and enter the test section. Then, the flow-passed light is reflected by the mirror disk in test section and goes back in a round-trip path. The flow-passed light will be reflected by the half mirror and is taken by the high speed camera (FASTCAM-APX RS, Photron). Schlieren video can be taken when the knife edge is placed in front of camera, while the shadow graph video can be taken without a knife edge.

This method can realize high-quality visualization in relative small space, because that the image taken at half mirror is small enough. Less mirrors and smaller space are needed to realize the visualization of whole scope of test section and the result is only restricted by the area of the glass window. The uniformity of the cascade can be observed in an intuitionistic way which can provide a reference of wind tunnel adjustment.

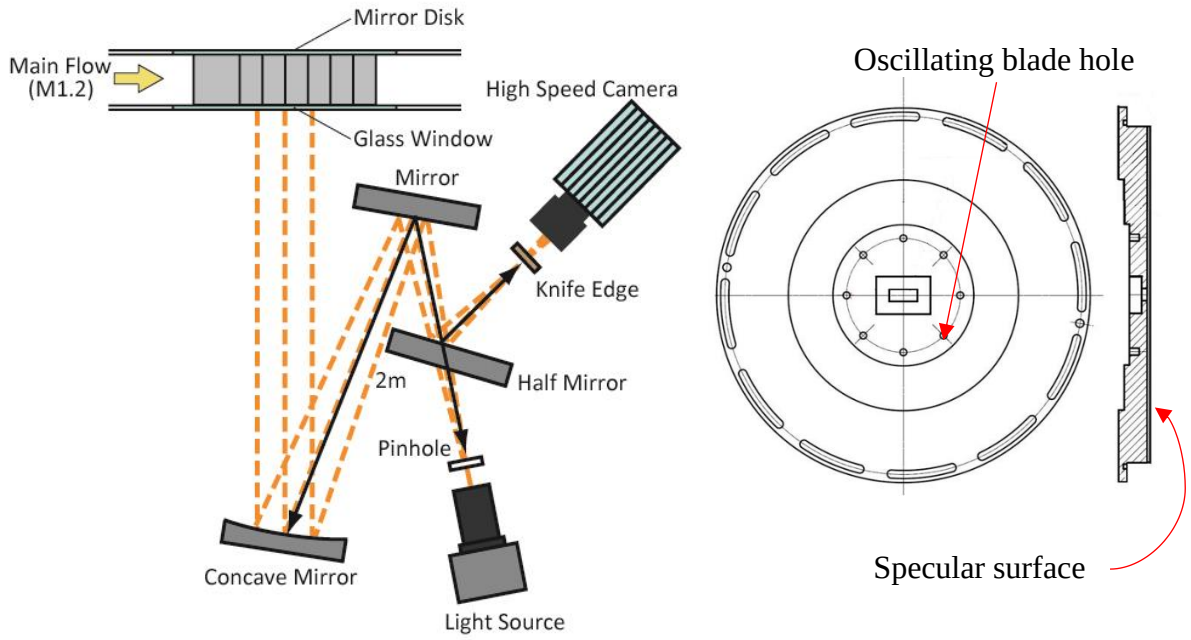

(a) Optical-path setting (b) Mirror disk

Figure 2.16 Schlieren visualization system using round-trip optical path method

2.6 Conventional Pressure and Aerodynamic Force Measurement Methods

2.6.1 Steady Pressure Measurement

In order to understand the uniformity characteristic of the cascade and accumulate the blade surface pressure data for calibrating PSP measurement results, the total pressure in settling chamber and static pressure measurement on test section wall and blade surface were measured by using steady pressure transducer.

Figure 2.17 shows the positions of 6 pressure taps at middle span of the blades (one for pressure side and one for suction side). The pressure taps are located at every 0.13 chord length from the beginning point at 0.18 chord length. Figure 2.18 shows the pressure taps distribution on the circular disk used as the hub wall. Every pressure tap is connected through thin metal tube (outer diameter: ϕ1.5, inner diameter: ϕ1.0) and silicone tube, and finally connected to the pressure transducer (PD64S-500K, JTEKT). The specification of pressure transducer is shown in Table 2.5. Then, output voltage of transducer is amplified by a DC amplifier (AA4500D, DEICY), and collected by DAQ (USB-6259, National Instruments). For steady measurement, the pressure is averaged by 0.5s data with sampling rate 1000Hz.

Table 2.5 Specification of pressure transducer

Model	JTEKT PD64S-500K	
Rated pressure	500	[kPa-G]
Rated power	≥ 100	mV
Sensitivity of output	≥ 20	mV/kgf/cm^2
Operating temperature	-30~80	
Repeatability precision	± 0.15%	
Force current (DC)	4	mA

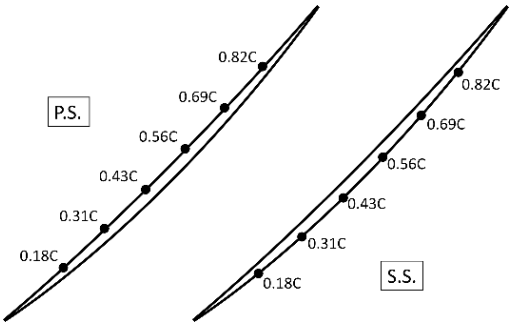

Figure 2.17 Pressure tap blade

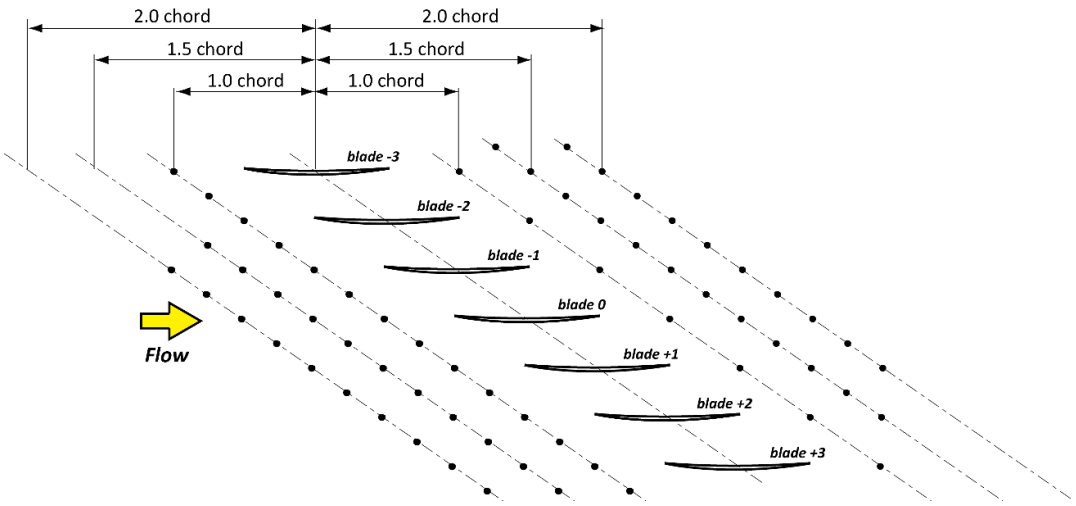

Figure 2.18 Static holes for static pressure measurement on wind tunnel wall

2.6.2 Strain Gauge

The steady and unsteady aerodynamic forces of the blades are measured by using strain gauge. When blade 0 is oscillated, the unsteady aerodynamic forces induced by blade oscillation acting on each blade can be measured individually. Then, the strain gauge results are used for validating the PSP measurement results.

Aerodynamic force measurement method for stationary blade (blade -1~blade +1) and oscillating blade (blade 0) are shown in Figure 2.19. Stain gauges are pasted at the roots of the blades, where is made shorter in chordwise direction.

The strain gauge (KFG-2-120-C1-23L1M2R, KYOWA) is connected through the bridge box (DB-120T-8, KYOWA), and then connected to the amplifier (MCD-8A, KYOWA). The low pass filter with cut-off frequency 300Hz is used and the correction is conducted based on the gain characteristic and phase characteristic of the equipment. Finally, the data is collected by DAQ and transmitted to PC. For oscillating blade measurement, both the wind-off and wind-on values are measured to subtract the inertia force so as to focus only on the aerodynamic force. The positive direction of aerodynamic force is defined as the direction of lift acting on the blade.

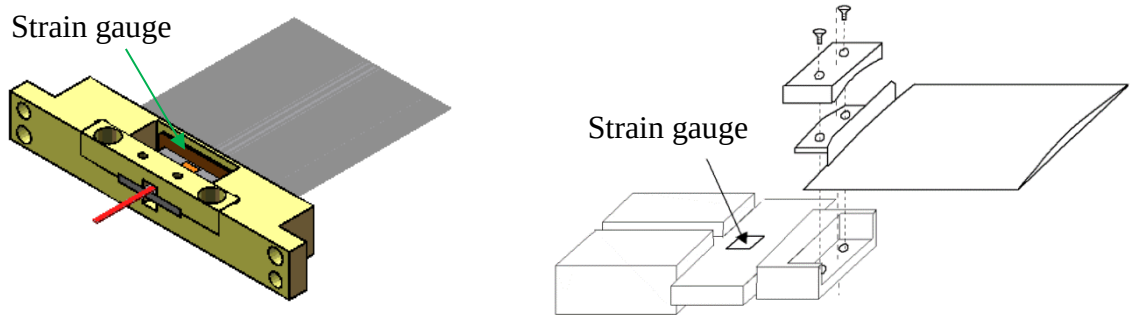

(a) Stationary blade with strain gauge (b) Oscillating blade with strain gauge

Figure 2.19 Strain gauge method

2.7 AA-PSP Technique

2.7.1 Theory of AA-PSP

AA-PSP has a nano-open structure and yields high mass diffusion. It consists of a molecular pressure probe of a luminophore and an anodized aluminum supporting matrix. As schematically shown in Figure 2.20, the luminophore on the anodized-aluminum surface is excited by an illumination source and gives off luminescence. This luminescence is related to gaseous oxygen in a test gas, by a process called oxygen quenching. Because the gaseous oxygen can be described as a partial pressure of oxygen as well as a static pressure, the luminescence from PSP can be described as a static pressure.

In this study, bathophen ruthenium ($[Ru(dpp)_3]^{2+}$) was used as luminophore of which the excitation wavelength is around 460nm and luminescence wavelength is around 615nm. And aluminum alloy (Al5052) was used as the blade material to make porous binder. The making

procedure for AA-PSP includes anodization treatment, dye absorption and hydrophobization. The fabricated anodized aluminum layer has a thickness around 10nm and a pore diameter around 20 nm. An example of made AA-PSP blade is shown in Figure 2.21.

The details of general chemical theory of PSP and the making procedure of AA-PSP are introduced in Appendix A.1.

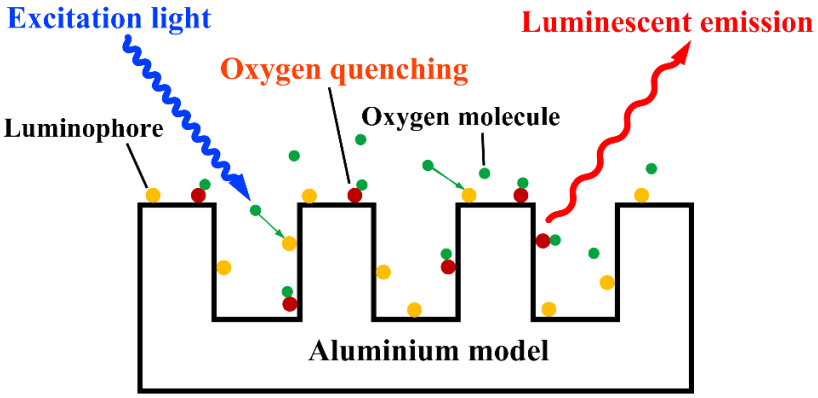

Figure 2.20 Mechanism of AA-PSP

Figure 2.21 AA-PSP blade

2.7.2 Evaluation of Temperature Dependency in Using AA-PSP

For evaluating the applicability and performance of AA-PSP in transonic flow, the impact of surface temperature variation must be taken into consideration. In transonic cascade, the static temperature before and after shock wave is different, and there is also temperature difference between middle span and hub or tip due to wall boundary layer effect.

The temperature were measured by K-type thermocouples on the pressure side of blade. The measuring positions are 10%, 50% and 90% span length at 30% and 70% chord length. Both global and local temperature variation were found in wind-on condition.

Wind-on temperature was lower than wind-off temperature and decreasing with time. To solve this problem, we measured the pressure on blade at certain time period after starting the wind tunnel and using in-situ calibration method to dismiss the impact of temperature difference between wind-off reference image and wind-on image. As to the local temperature distribution on blade surface, the maximum difference is about 2~3K. Due to the investigation on luminophore $[Ru(dpp)_3]^{2+}$ published by Kameda [26], I_{ref}/I will decrease 6% when pressure increases 10kPa and I/I_{ref} decreases 5% when temperature increase 10K. In current case, when the temperature difference is 3K, the error of I/I_{ref} will be 1%. So, the error of C_P was calculated about 0.015 compared to real value, which is about 2.5% compared to the range of C_P (-0.3~0.3) around the blade surface. This errors caused by local temperature difference were ignored in the measurement of this study. The detailed progress of temperature measurement on blade surface and error analysis are written in Appendix A.3.

2.7.3 AA-PSP Measurement System

The schematic diagram of PSP measurement system is shown in Figure 2.22. PSP excitation and image capture were realized by a metal-halide light source and a high speed camera (FASTCAM-APX RS, Photron), respectively. A band pass filter (460nm, half width 100nm) was placed in front of the light source to obtain the blue light for exciting the AA-PSP. A long pass filter (570nm) was placed in front of the high speed camera, and the AA-PSP is excited into orange colour as shown in Figure 2.23. The camera exposure time was set to the reciprocal of frame rate, compromising between image brightness and stability. The details of camera and lens setting is shown in Table 2.1.

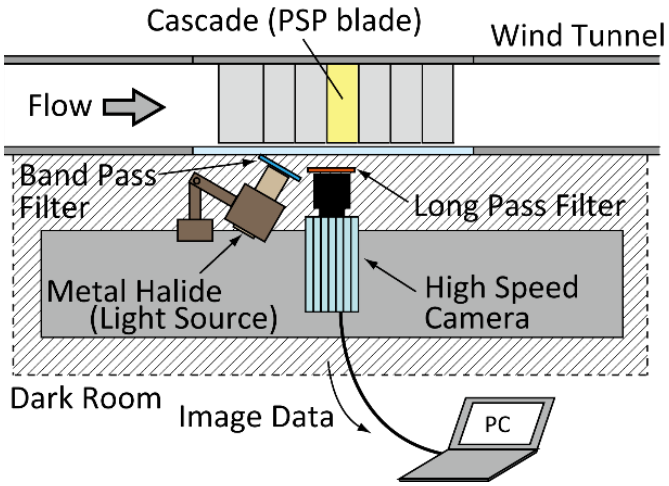

Figure 2.22 PSP measurement system

Figure 2.23 Excited AA-PSP blades

Table 2.1 High speed camera and lens setting for PSP measurement

Frame rate	1000	[fps]
Shutter speed	1/frame	[s]
Resolution	512×256	pixel^2
Lens	50mm F1.2S	
F-number	2.0	

Due to the theory of PSP, the surface pressure value can be calculated from the luminescent intensity. The relationship between luminescent intensity I and surface static pressure P is represented by Stern-Volmer relation equation as written in eqn.(2.8).

$$\frac{P}{P_{ref}} = \sum_n C_n \left(\frac{I_{ref}}{I}\right)^n = C_0 + C_1 \times \frac{I_{ref}}{I} + C_2 \times \left(\frac{I_{ref}}{I}\right)^2 + \cdots \tag{2.8}$$

In above equation, I_{ref} and P_{ref} are the reference luminescent intensity and reference pressure, respectively. In the present experiment, the wind-off image and atmosphere pressure

were used as the reference values. The parameters C_1 and C_0 were obtained by the in-situ calibration method of PSP. In-situ calibration uses pressure tap data to determine calibration coefficients and has the merit of reducing errors associated with global temperature variation with the main flow and other factors.

2.7.4 Image Processing Method

The procedures of image processing for PSP measurement is shown in Figure 2.24. At first, both wind-off and wind-on images were captured by the camera. Then, to realize pixel to pixel image registration, affine transformation was conducted to obtain rectangle images by adopting some auto positioning methods. Then, spatial cell averaging filter was applied on the images for noise reduction. After that, I_{ref}/I image was calculated and finally, the pressure distribution was obtained by in-situ method.

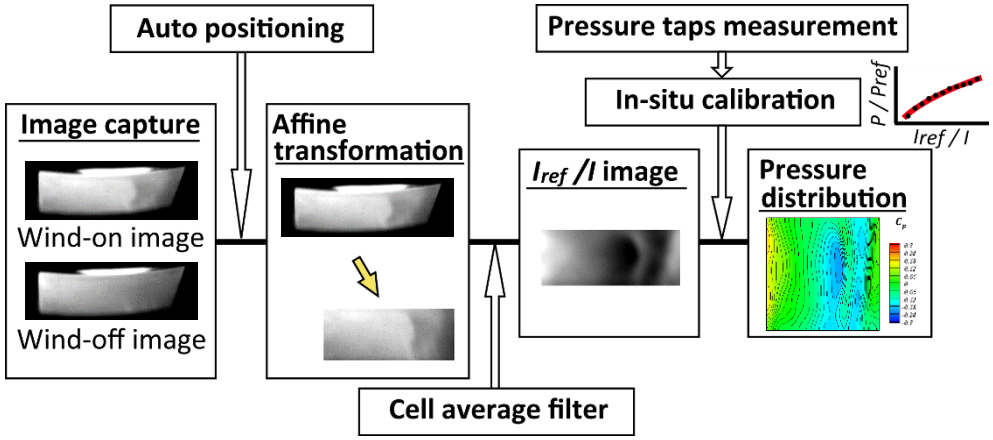

Figure 2.24 Image processing procedures

(1) Time Averaging Processing (for Steady Cases)

To reduce the influence of temporal intensity change of excitation light and noise of camera shot on PSP precision, the time averaging is carried out for obtain steady results.

(2) Auto Positioning by Hough Transformation Based Edge Detection

Because the output of PSP is expressed as I_{ref}/I in every pixel point, the pixel to pixel image registration is of great importance for wind-off and wind-on images. Besides, in current cascade condition, the camera sight was oblique and the blade zone deformed due to aerodynamic force and forced oscillation. Due to above reasons, the coordinate transformation should be carried out. The coordinate transformation coefficients should be calculated by positioning some auxiliary points.

An auto positioning method by Hough transformation based edge detection is proposed here and the details and verification of this method are illustrated in Appendix A.2. Hough transformation is a technique that can be adopted to isolate the features of a particular shape within an image. Current airfoil is double circular arc (DCA) of which the tip and hub edges are arcs and the leading and trailing edges are straight lines. Seen from the images, the leading

edge and trailing edge are bended by aerodynamic force into curves which can be searched by using quadratic fitting. So the Hough transformation is suitable for current situation. Figure 2.25(a) shows the edge curves detected by Hough transformation and Figure 2.25(b) shows auxiliary points obtained on the edge curves. Finally, the coordinates of auxiliary points are obtained for the next step.

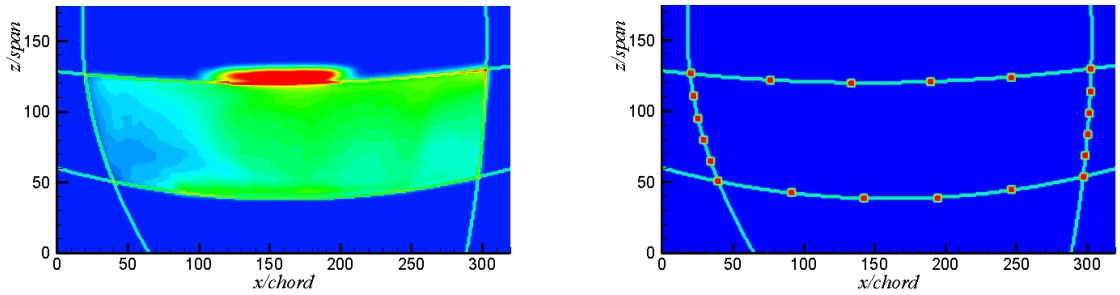

(a) Hough transformation for blade edge

(b) Corner intersection points and auxiliary edge points

Figure 2.25 Hough Transformation Based Edge Detection

(3) Affine Transformation

By knowing the real coordinates of searched auxiliary point in the images and the coordinates of these points when observed right ahead, affine transformation is conducted for both wind-off and wind-on images and the blade zone is transformed into a rectangle image. Affine transformation can eliminate the influence of blade deformation on image processing precision caused by the aerodynamic force and oscillating movement. Transformation of the coordinates can be expressed as eqn.(2.9).

$$\begin{aligned} x_i &= a_1 + a_2\tilde{x}_i + a_3\tilde{y}_i + a_4\tilde{x}_i^2 + a_5\tilde{x}_i\tilde{y}_i + a_6\tilde{y}_i^2 \\ y_i &= b_1 + b_2\tilde{x}_i + b_3\tilde{y}_i + b_4\tilde{x}_i^2 + b_5\tilde{x}_i\tilde{y}_i + b_6\tilde{y}_i^2 \end{aligned} \tag{2.9}$$

i: number of auxiliary point

j: number of coordinate transformation coefficient (1~6, 2nd precision)

(x_i, y_i): coordinates before affine transformation

$(\tilde{x}_i, \tilde{y}_i)$: coordinates after affine transformation

a_j, b_j: coordinate transformation coefficient for x and y

Based on the least square method, the coordinate coefficients a_j and b_j are calculated by making the RSS (residual sum of squares) of all auxiliary points to be minimum. The RSS is expressed in eqn.(2.10). Finally, a_j and b_j are obtained by making 1st order differential to be 0 which is expressed in eqn.(2.11). Through the coordinate transformation, assignment of the grey scale value to the new rectangle image is conducted according to the original image.

$$\begin{aligned} f(a_j) &= \sum_i (a_1 + a_2\tilde{x}_i + a_3\tilde{y}_i + a_4\tilde{x}_i^2 + a_5\tilde{x}_i\tilde{y}_i + a_6\tilde{y}_i^2 - x_i)^2 \\ g(b_j) &= \sum_i (b_1 + b_2\tilde{x}_i + b_3\tilde{y}_i + b_4\tilde{x}_i^2 + b_5\tilde{x}_i\tilde{y}_i + b_6\tilde{y}_i^2 - y_i)^2 \end{aligned} \tag{2.10}$$

$$\frac{\partial f(a_j)}{\partial a_j} = 0\,, \quad \frac{\partial g(b_j)}{\partial b_j} = 0 \tag{2.11}$$

(4) Spatial Smoothing Processing

After obtaining the rectangle images, spatial cell averaging filter is used to reduce spatial noise by averaging neighboring pixels. Figure 2.26 shows the schematic diagram of this method. The processing pixel and it surrounding 8 pixels are used to do cell averaging by using eqn.(2.12). For processing edge pixels, the boundary is treated as a mirror boundary.

The influence of filtering times on pressure distribution is shown in Figure 2.27. It shows the C_P counters obtained by setting the cell filter times to be 10, 100 and 200 times, and the comparison of mid-span distribution. The appropriate filtering times is important to reduce the spatial noise and keep the shape of pressure distribution. If the number of times is too few as shown in Figure 2.27 (a), the counter shows non-ignorable spatial noises. With the increasing of filtering times, the counters become smooth as shown in Figure 2.27 (b), (c). However, the drastic pressure change around 0.3~0.4 x/c is attenuated due to excessive filtering. So, 100 times was considered to be an appropriate selection for using cell averaging filter.

$$I_{i.j} = \frac{1}{2} I_{i.j} + \frac{1}{2} \times \frac{1}{1 + 4C_1 + 4C_2} \times \{I_{i.j} + C_1(I_{i-1.j} + I_{i+1,j} + I_{i,j-1} + I_{i,j+1}) + C_2(I_{i-1.j-1} + I_{i-1,j+1} + I_{i+1,j-1} + I_{i+1,j+1})\} \tag{2.12}$$

$$C_1 = \frac{1}{1 + \frac{1}{\sqrt{2}}}\,, \quad C_2 = \frac{C_1}{\sqrt{2}}\,, \quad I_{i,j} : \textit{the luminescence intenstiy at } (i,j)$$

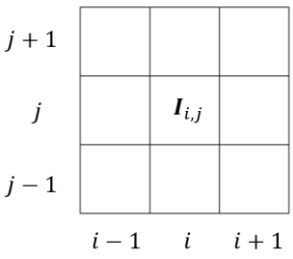

(a) Internal cells

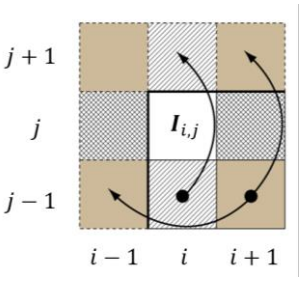

(b) Boundary cells

Figure 2.26 Diagram of cell averaging method

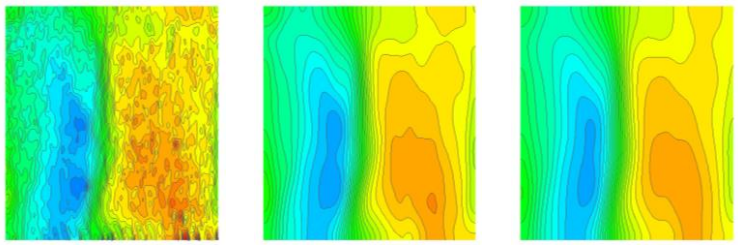

(a) 10 times (b) 100 times (c) 200times

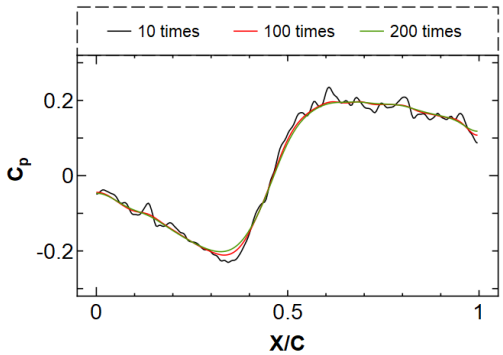

(d) Mid-span C_P

Figure 2.27 Influence of number of filtering times on pressure distribution

(5) Division Processing

After that, then luminescent intensity of wind-off image is divided by that of wind-on image in each pixel to get the I_{ref}/I distribution image.

(6) Pressure Calculation by Luminescent Intensity-Pressure Calibration

In the present study, in-situ calibration is used to transform the luminescent intensity ratio to pressure coefficient. The relational expression based on Stern-Volmer expression between pressure measured by pressure taps blade and luminescent intensity ratio at same points is solved by curve fitting, and the calibration coefficients are calculated.

Finally, transform luminescent intensity ratio to pressure coefficient with calibration coefficients.

2.8 Summary

The used equipment for the experiment is shown in Table 2.2.

Table 2.2 Experimental equipment

Experiment	Function	Maker	Model
Data collection	DAQ	National Instruments	USB-6259
Oscillation	Vibration generator	ASAHI SEISAKUSYO	C-5015
	Power amplifier	ASAHI SEISAKUSYO	APD-602
	Function generator	NF Corporation	WF1973
	Laser displacement meter	KEYENCE	LK-G30
Pressure measurement	Pressure transducer	JTEKT	PD64S-500K
	DC amplifier	DEICY	AA4500D
Aerodynamic force measurement	Strain gauge	KYOWA	KFG-2-120-C1-11
	DC amplifier	DEICY	AA6210
Schlieren visualization	High speed camera	Photron	FASTCAM-APX RS
	Camera lens	Nikkor	60mm
	Light source	KATO KOKEN	MODEL XDS-75-HV
PSP measurement	High speed camera	Photron	FASTCAM-APX RS
	Camera lens	Nikkor	50mm F1.2S
	PSP excitation light	Sumita Optical Glass	LS-M210
	Band pass filter	ASAHI SPECTRA	Pb0009
	Long pass filter	ASAHI SPECTRA	XF594

Chapter 3 Numerical Simulation Approaches

3.1 Overview of CFD Scheme

In present study, numerical simulation is based on the in-house RANS code "SHUS". For the unsteady calculation, moving-grid method which can deform the meshes is used to simulate blade oscillation. Then, influence coefficient method is used to solve the cascade flutter problem under one normal oscillation mode. Overview of the scheme is shown in Table 3.1.

Table 3.1 CFD scheme

Governing equation	RANS
Convection term	SHUS+3rd MUSCL
Diffusion term	2nd central difference
Turbulence model	k-ω (Wilcox 1988)
Time marching (steady)	Euler Implicit method (1st order precision) with TCPGS-RBGS
Time marching (unsteady)	3 point backward difference (2nd order precision) with TCPGS-RBGS

3.2 Governing Equations

3.2.1 Navier-Stokes Equations

In this study, the three dimensional compressible Navier-Stokes (N-S) equations were applied for evaluating the flow phenomena in the wind tunnel cascade and absolute coordinate system was appropriate. The N-S equations can be written into Cartesian coordinates as eqn.(3.1).

$$\frac{\partial \boldsymbol{Q}}{\partial t}+\frac{\partial(\boldsymbol{F}-\boldsymbol{F_v})}{\partial x}+\frac{\partial(\boldsymbol{G}-\boldsymbol{G_v})}{\partial y}+\frac{\partial(\boldsymbol{H}-\boldsymbol{H_v})}{\partial z}=\boldsymbol{0} \tag{3.1}$$

$$\boldsymbol{Q}=\begin{bmatrix}\rho\\ \rho u\\ \rho v\\ \rho w\\ e\end{bmatrix},\boldsymbol{F}=\begin{bmatrix}\rho u\\ \rho u^2+p\\ \rho uv\\ \rho uw\\ (e+p)u\end{bmatrix},\boldsymbol{G}=\begin{bmatrix}\rho v\\ \rho vu\\ \rho v^2+p\\ \rho vw\\ (e+p)v\end{bmatrix},\boldsymbol{H}=\begin{bmatrix}\rho w\\ \rho wu\\ \rho wv\\ \rho w^2+p\\ (e+p)w\end{bmatrix},$$

$$\boldsymbol{F}_v=\begin{bmatrix}0\\ \sigma_x\\ \tau_{yx}\\ \tau_{zx}\\ \beta_x\end{bmatrix},\boldsymbol{G}_v=\begin{bmatrix}0\\ \tau_{xy}\\ \sigma_y\\ \tau_{zy}\\ \beta_y\end{bmatrix},\boldsymbol{H}_v=\begin{bmatrix}0\\ \tau_{xz}\\ \tau_{yz}\\ \sigma_z\\ \beta_z\end{bmatrix}$$

$$\sigma_x=\frac{2}{3}\mu\left(2\frac{\partial u}{\partial x}-\frac{\partial v}{\partial y}-\frac{\partial w}{\partial z}\right),\sigma_y=\frac{2}{3}\mu\left(2\frac{\partial v}{\partial y}-\frac{\partial w}{\partial z}-\frac{\partial u}{\partial x}\right),\sigma_z=\frac{2}{3}\mu\left(2\frac{\partial w}{\partial z}-\frac{\partial v}{\partial y}-\frac{\partial u}{\partial x}\right)$$

$$\tau_{xy}=\tau_{yx}=\mu\left(\frac{\partial u}{\partial y}+\frac{\partial v}{\partial x}\right),\tau_{yz}=\tau_{zy}=\mu\left(\frac{\partial v}{\partial z}+\frac{\partial w}{\partial y}\right),\tau_{zx}=\tau_{xz}=\mu\left(\frac{\partial w}{\partial x}+\frac{\partial u}{\partial z}\right)$$

$$\beta_x=\sigma_x u+\tau_{xy}v+\tau_{xz}w+\kappa\frac{\partial T}{\partial x}\ ,\qquad \beta_y=\tau_{yx}u+\sigma_y v+\tau_{yz}w+\kappa\frac{\partial T}{\partial y}\ ,$$

$$\beta_z=\tau_{zx}u+\tau_{zy}v+\sigma_z w+\kappa\frac{\partial T}{\partial z}$$

Here, t is time; ρ is density; u, v, w are the velocity components at x, y, z direction; T, p are temperature and pressure; e is the total energy per unit volume; $\sigma_x, \sigma_y, \sigma_z$ are the normal stress components; $\tau_{xy}, \tau_{yz}, \tau_{zx}$ are the shearing stress components. The equations are written based on the conservation laws of mass, momentum and energy.

3.2.2 Coordinate Transformation into Generalized Coordinates

Eqn.(3.1) has expressed the equations in Cartesian coordinates $x = (x, y, z, t)$. However, the body-fitted grid is necessary in doing CFD calculation, so that the coordinate transformation into generalized coordinates $\chi = (\xi, \eta, \zeta, t)$ is required. The matrix used for transforming generalized coordinates into Cartesian coordinates for minute elements is written in eqn.(3.2). And the inverse matrix is written is eqn.(3.3).

$$\begin{bmatrix} dx \\ dy \\ dz \end{bmatrix} = \begin{bmatrix} x_\xi & x_\eta & x_\zeta \\ y_\xi & y_\eta & y_\zeta \\ z_\xi & z_\eta & z_\zeta \end{bmatrix} \begin{bmatrix} d\xi \\ d\eta \\ d\zeta \end{bmatrix} \tag{3.2}$$

$$\begin{bmatrix} d\xi \\ d\eta \\ d\zeta \end{bmatrix} = J \begin{bmatrix} y_\eta z_\zeta - y_\zeta z_\eta & z_\eta x_\zeta - z_\zeta x_\eta & x_\eta y_\zeta - x_\zeta y_\eta \\ y_\zeta z_\xi - y_\xi z_\zeta & z_\zeta x_\xi - z_\xi x_\zeta & x_\zeta y_\xi - x_\xi y_\zeta \\ y_\xi z_\eta - y_\eta z_\xi & z_\xi x_\eta - z_\eta x_\xi & x_\xi y_\eta - x_\eta y_\xi \end{bmatrix} \begin{bmatrix} dx \\ dy \\ dz \end{bmatrix} \tag{3.3}$$

$$\frac{1}{J} = x_\xi (y_\eta z_\xi - y_\zeta z_\eta) + x_\eta (y_\zeta z_\xi - y_\xi z_\zeta) + x_\zeta (y_\xi z_\eta - y_\eta z_\xi)$$

Here, J that is called Jacobian is the transformation coefficient. And the inverse matrix can also be written in eqn.(3.4) with 9 metrics.

$$\begin{bmatrix} d\xi \\ d\eta \\ d\zeta \end{bmatrix} = \begin{bmatrix} \xi_x & \xi_y & \xi_z \\ \eta_x & \eta_y & \eta_z \\ \zeta_x & \zeta_y & \zeta_z \end{bmatrix} \begin{bmatrix} dx \\ dy \\ dz \end{bmatrix} \tag{3.4}$$

$$\xi_x = J(y_\eta z_\zeta - y_\zeta z_\eta), \quad \xi_y = J(z_\eta y_\zeta - z_\zeta x_\eta), \quad \xi_z = J(x_\eta y_\zeta - x_\zeta y_\eta)$$
$$\eta_x = J(y_\zeta z_\xi - y_\xi z_\zeta), \quad \eta_y = J(z_\zeta x_\xi - z_\xi x_\zeta), \quad \eta_z = J(x_\zeta y_\xi - x_\xi y_\zeta)$$
$$\zeta_x = J(y_\xi z_\eta - y_\eta z_\xi), \quad \zeta_y = J(z_\xi x_\eta - z_\eta x_\xi), \quad \zeta_z = J(x_\xi y_\eta - x_\eta y_\xi)$$

The Jacobian is equivalent to the volume ratio of each hexahedron cell unit enclosed by the coordinate points.

$$J = \frac{\partial(\xi, \eta, \zeta)}{\partial(x, y, z)} = \frac{[cell\ volume\ of\ computational\ space]}{[cell\ volume\ of\ physical\ space]} \tag{3.5}$$

By using above relational expressions, N-S equations can be written into eqn.(3.6).

$$\frac{\partial \widehat{\boldsymbol{Q}}}{\partial t} + \frac{\partial(\widehat{\boldsymbol{F}} - \widehat{\boldsymbol{F}}_{\boldsymbol{v}})}{\partial \xi} + \frac{\partial(\widehat{\boldsymbol{G}} - \widehat{\boldsymbol{G}}_{\boldsymbol{v}})}{\partial \eta} + \frac{\partial(\widehat{\boldsymbol{H}} - \widehat{\boldsymbol{H}}_{\boldsymbol{v}})}{\partial \zeta} = \boldsymbol{0} \tag{3.6}$$

$$\widehat{\boldsymbol{Q}} = \frac{1}{J}\begin{bmatrix} \rho \\ \rho u \\ \rho v \\ \rho w \\ e \end{bmatrix}, \widehat{\boldsymbol{F}} = \frac{1}{J}\begin{bmatrix} \rho U \\ \rho u U + \xi_x p \\ \rho v U + \xi_y p \\ \rho w U + \xi_z p \\ (e + p)U - \xi_t p \end{bmatrix}, \widehat{\boldsymbol{G}} = \frac{1}{J}\begin{bmatrix} \rho V \\ \rho u V + \eta_x p \\ \rho v V + \eta_y p \\ \rho w V + \eta_z p \\ (e + p)V - \eta_t p \end{bmatrix}, \widehat{\boldsymbol{H}} = \frac{1}{J}\begin{bmatrix} \rho W \\ \rho u W + \zeta_x p \\ \rho v W + \zeta_y p \\ \rho w W + \zeta_z p \\ (e + p)W - \zeta_t p \end{bmatrix}$$

$$\widehat{\boldsymbol{F}}_{\boldsymbol{v}} = \frac{1}{J}\begin{bmatrix} 0 \\ \xi_x\tau_{xx} + \xi_y\tau_{xy} + \xi_z\tau_{xz} \\ \xi_x\tau_{yx} + \xi_y\tau_{yy} + \xi_z\tau_{yz} \\ \xi_x\tau_{zx} + \xi_y\tau_{zy} + \xi_z\tau_{zz} \\ \xi_x\beta_x + \xi_y\beta_y + \xi_z\beta_z \end{bmatrix}, \qquad \widehat{\boldsymbol{G}}_{\boldsymbol{v}} = \frac{1}{J}\begin{bmatrix} 0 \\ \eta_x\tau_{xx} + \eta_y\tau_{xy} + \eta_z\tau_{xz} \\ \eta_x\tau_{yx} + \eta_y\tau_{yy} + \eta_z\tau_{yz} \\ \eta_x\tau_{zx} + \eta_y\tau_{zy} + \eta_z\tau_{zz} \\ \eta_x\beta_x + \eta_y\beta_y + \eta_z\beta_z \end{bmatrix},$$

$$\widehat{\boldsymbol{H}}_{\boldsymbol{v}} = \frac{1}{J}\begin{bmatrix} 0 \\ \zeta_x\tau_{xx} + \zeta_y\tau_{xy} + \zeta_z\tau_{xz} \\ \zeta_x\tau_{yx} + \zeta_y\tau_{yy} + \zeta_z\tau_{yz} \\ \zeta_x\tau_{zx} + \zeta_y\tau_{zy} + \zeta_z\tau_{zz} \\ \zeta_x\beta_x + \zeta_y\beta_y + \zeta_z\beta_z \end{bmatrix}$$

Here, U, V, W are the transformed velocity components; ξ_t, η_t, ζ_t are the time marching of metrics which are used for moving grid method.

$$U = \xi_t + \xi_x u + \xi_y v + \xi_z w, \quad V = \eta_t + \eta_x u + \eta_y v + \eta_z w, \quad W = \zeta_t + \zeta_x u + \zeta_y v + \zeta_z w$$

3.2.3 Turbulence Model

Turbulence is any pattern of fluid motion characterized by chaotic changes in pressure and flow velocity. It is accompanied by vortices from large scale to small scale. When doing numerical simulation of turbulence by solving N-S equations directly, the mesh size has to be set extremely small to match the minimum vortex scale in order to reproduce the accurate turbulence phenomena.

The minimum dimension of common developed turbulence is Kolmogorov scale, and the minimum gird width must be smaller than it. Kolmogorov scale is defined in eqn.(3.7).

$$l_k = \left(\frac{\nu^3}{\varepsilon}\right)^{\frac{1}{4}} \tag{3.7}$$

Here, ε is turbulent energy dissipation; ν is kinematic viscosity coefficient. By supposing the representative speed of flow to be $\bar{U}$ and representative length to be L, ε is calculated as eqn.(3.8).

$$\varepsilon = \frac{\bar{U}^3}{L} \tag{3.8}$$

And eqn.(3.9) is established.

$$\frac{L}{l_k} = \left(\frac{\bar{U}L}{\nu}\right)^{\frac{3}{4}} = Re^{\frac{3}{4}} \tag{3.9}$$

Assuming the representative length as the maximum width, L/l_k is the necessary grid number for direct turbulence capture. In doing 3D computation for turbulence flow directly, the needed grid number will be more than the 9/4 power of Reynolds number. Under the transonic flow field ($Re \simeq 10^6$) in this study, the grid number should be on order of 10^{13} which is unrealistic under current computation capability. Therefore, the modelling of turbulence phenomena is considered an effective approach in which the grid with is not necessary to be smaller than Kolmogorov scale. In this study, the widely used Reynolds average model is

adopted and forms the Reynold-averaged Navier-Stokes equations (RANS).

(1) Reynold-Averaged Model

Reynold-averaged model divides the turbulence into large scale motion and micro perturbation by time averaging of N-S equations. The micro perturbation is replaced by turbulence model. In the 3D compressible N-S equations, equation of continuity and equation of motion are written in eqn.(3.10)(3.11).

$$\frac{\partial \rho}{\partial t} + \frac{\partial \rho u_i}{\partial x_i} = 0 \tag{3.10}$$

$$\frac{\partial \rho u_i}{\partial t} + \frac{\partial \rho u_i u_j}{\partial x_j} = -\frac{\partial p}{\partial x_i} + \frac{\partial \sigma_{ij}}{\partial x_j} \tag{3.11}$$

$$\sigma_{ij} = \mu\left(2S_{ij} - \frac{2}{3}S_{kk}\delta_{ij}\right) , \qquad S_{ij} = \frac{1}{2}\left(\frac{\partial u_i}{\partial x_j} + \frac{\partial u_j}{\partial x_i}\right) \tag{3.12}$$

Here, u, p, ρ, μ are velocity vector component, pressure, density and viscosity coefficient. The physical quantity f is divided into Reynolds average quantity $\bar{f}$ and turbulence quantity f'. Then, Favre average quantity $\tilde{f} = \overline{\rho f}/\bar{\rho}$ is introduced with the turbulence quantity f''.

$$f = \bar{f} + f' = \tilde{f} + f'' \tag{3.13}$$

By substituting the physical quantities in eqn.(3.10)(3.11) with eqn.(3.13), the following equations can be obtained.

$$\frac{\partial \bar{\rho}}{\partial t} + \frac{\partial \bar{\rho}\tilde{u}_i}{\partial x_i} = 0 \tag{3.14}$$

$$\frac{\partial \bar{\rho}\tilde{u}_i}{\partial t} + \frac{\partial \rho\tilde{u}_i\tilde{u}_j}{\partial x_j} = -\frac{\partial \bar{p}}{\partial x_i} + \frac{\partial \bar{\sigma}_{ij}}{\partial x_j} + \frac{\partial \tau_{ij}}{\partial x_j} \tag{3.15}$$

$$\bar{\sigma}_{ij} = 2\mu\overline{\left(S_{ij} - \frac{1}{3}S_{kk}\delta_{ij}\right)} \approx 2\bar{\mu}\left(\tilde{S}_{ij} - \frac{1}{3}\tilde{S}_{kk}\delta_{ij}\right) , \qquad \tau_{ij} = \bar{\rho}u_i''u_j'' \tag{3.16}$$

Here, τ_{ij} that is called Reynolds stress is a new term generated from Reynolds average processing.

To solve the Reynolds average equations, the Reynolds stress is approximated based on Boussinesq approximation. τ_{ij} can be written into eqn.(3.17) and k is turbulence energy. This model is called eddy viscosity model where μ_t is still an unknown.

$$\tau_{ij} = 2\mu_t\left(\tilde{S}_{ij} - \frac{1}{3}\tilde{S}_{kk}\delta_{ij}\right) - \frac{2}{3}\bar{\rho}k\delta_{ij} , \qquad k = \frac{[(u_1'')^2 + (u_2'')^2 + (u_3'')^2]}{2} \tag{3.17}$$

The turbulence models use some auxiliary equations to solve μ_t. And these models can be classified into 0, 1, 2 equation(s) model by the number of equation. In this study, one of the 2 equations model, $k-\omega$ model is adopted.

(2) $k-\omega$ Turbulence Model (Wilcox 1988)

$k-\omega$ turbulence model solves the transport equations regarding the turbulence kinetic energy k and the specific dissipation rate ω ($\omega=\varepsilon/k$), and calculates the turbulence viscosity coefficient μ_t. Here, ε is the viscous dissipation rate ($\varepsilon=\overline{\sigma_{ij}''u_{ij}''}/\bar{\rho}$).

When using the $k-\omega$ turbulence model developed by Wilcox, the calculation in near-wall zone is independent on velocity gradient and more robust than $k-\varepsilon$ model. The calculation is stabilized based on the characteristics that the attenuation function is not necessary in viscous sublayer and the boundary condition can be set as Dirichlet conditions.

The equations regarding turbulence kinetic energy k and the specific dissipation rate ω can be written as eqn.(3.18)(3.19).

$$\frac{\partial}{\partial t}(\bar{\rho}k)+\frac{\partial}{\partial x_j}\left(\bar{\rho}\tilde{u}_j k\right)=\tau_{ij}^{t}\frac{\partial\tilde{u}_i}{\partial x_j}-\beta^{*}\bar{\rho}\omega k+\frac{\partial}{\partial x_j}\left[(\bar{\mu}+\sigma^{*}\mu_t)\frac{\partial k}{\partial x_j}\right] \tag{3.18}$$

$$\frac{\partial}{\partial t}(\bar{\rho}\omega)+\frac{\partial}{\partial x_j}\left(\bar{\rho}\tilde{u}_j \omega\right)=\alpha\frac{\omega}{k}\tau_{ij}^{t}\frac{\partial\tilde{u}_i}{\partial x_j}-\beta\bar{\rho}\omega^{2}+\frac{\partial}{\partial x_j}\left[(\bar{\mu}+\sigma\mu_t)\frac{\partial \omega}{\partial x_j}\right] \tag{3.19}$$

Here, turbulence viscosity coefficient is calculated by using the solved k and ω; turbulence dissipation rate is calculated as $\varepsilon=\beta^{*}\omega k$; length scale is $l=k^{1/2}/\omega$; turbulence Reynolds number is $Re=k/\omega\nu$; turbulence viscosity coefficient is $\mu_t=\alpha^{*}\rho k/\omega$. Considering the effect of compressibility, the $k-\omega$ equations are modified by using eqn.(3.20).

$$\begin{gathered}\beta^{*}=\beta_0^{*}[1+\xi^{*}F(M_t)]\ ,\qquad \beta=\beta_0-\beta_0^{*}\xi^{*}F(M_t)\\ F(M_t)=|M_t^2-m_{t0}^2|H(M_t-M_{t0})\end{gathered} \tag{3.20}$$

H is the Heaviside step function and the constants are defined as follows.

$$\begin{gathered}\beta_0^{*}=\frac{9}{100}\ ,\qquad \alpha=\frac{5}{9}\ ,\qquad \beta_0=\frac{3}{40}\ ,\qquad \sigma=\sigma^{*}=\frac{1}{2},\\ \xi^{*}=\frac{3}{2}\ ,\qquad M_{t0}=\frac{1}{4}\ ,\qquad \alpha^{*}=1\end{gathered} \tag{3.21}$$

3.3 Numerical Simulation Methods

3.3.1 Finite Volume Method

The finite volume method (FVM) is a method that expresses evaluates the partial differential equation into algebraic equation form. “Finite volume” means the small volume surrounding each node point on a mesh. The values are calculated at discrete mesh cells. In FVM, by using the divergence theorem, volume integrals in a partial differential equation which contains a divergence term are converted into surface integrals. Then, the fluxes at the surfaces of every finite volume are evaluated by these surface integral terms. Because the flux entering a given volume is equivalent to the corresponding flux leaving the neighbouring volume, FVM is a conservative method.

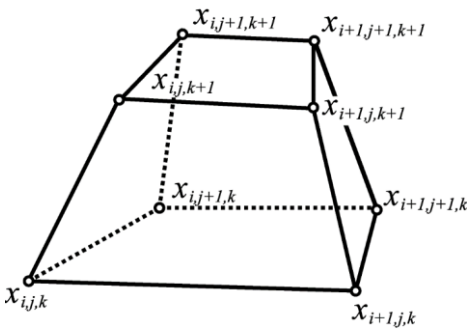

Figure 3.1 3D metrics

The cell is defined as the domain where $\Delta\xi = \Delta\eta = \Delta\zeta = 1$ in generalized coordinates. By integrating eqn.(3.6) with minute volume $d\xi d\eta d\zeta$, eqn.(3.22) is obtained.

$$\begin{aligned}\frac{\partial}{\partial t_\chi}\int \widehat{\boldsymbol{Q}} d\xi d\eta d\zeta = &-\int \left(\widehat{\boldsymbol{F}} - \widehat{\boldsymbol{F}}_v\right)_{\xi=i+\frac{1}{2}} d\eta d\zeta + \int \left(\widehat{\boldsymbol{F}} - \widehat{\boldsymbol{F}}_v\right)_{\xi=i-\frac{1}{2}} d\eta d\zeta \\ &-\int \left(\widehat{\boldsymbol{G}} - \widehat{\boldsymbol{G}}_v\right)_{\eta=j+\frac{1}{2}} d\zeta d\xi + \int \left(\widehat{\boldsymbol{G}} - \widehat{\boldsymbol{G}}_v\right)_{\eta=j-\frac{1}{2}} d\zeta d\xi \\ &-\int \left(\widehat{\boldsymbol{H}} - \widehat{\boldsymbol{H}}_v\right)_{\zeta=k+\frac{1}{2}} d\xi d\eta + \int \left(\widehat{\boldsymbol{H}} - \widehat{\boldsymbol{H}}_v\right)_{\zeta=k-\frac{1}{2}} d\xi d\eta\end{aligned} \tag{3.22}$$

The flux on cell boundary is evaluated by surface center value and surface area, which is written as eqn.(3.23). Then, the spatial discretization about the time marching of cell averaging value can be expressed as eqn.(3.24).

$$\begin{aligned}&\int \phi d\xi d\eta d\zeta = \phi_{i,j,k}\,, \qquad \int \phi_{\xi=i+\frac{1}{2}} d\eta d\zeta = \phi_{i+\frac{1}{2},j,k}\,, \\ &\int \phi_{\eta=i+\frac{1}{2}} d\xi d\zeta = \phi_{i,j+\frac{1}{2},k}\,, \int \phi_{\zeta=i+\frac{1}{2}} d\xi d\eta = \phi_{i,j,k+\frac{1}{2}}\end{aligned} \tag{3.23}$$

$$\begin{aligned}\frac{\partial}{\partial t_\chi}\widehat{\boldsymbol{Q}} = &-\int \left(\widehat{\boldsymbol{F}} - \widehat{\boldsymbol{F}}_v\right)_{i+\frac{1}{2},j,k} + \left(\widehat{\boldsymbol{F}} - \widehat{\boldsymbol{F}}_v\right)_{i-\frac{1}{2},j,k} \\ &-\int \left(\widehat{\boldsymbol{G}} - \widehat{\boldsymbol{G}}_v\right)_{i,j+\frac{1}{2},k} + \left(\widehat{\boldsymbol{G}} - \widehat{\boldsymbol{G}}_v\right)_{i,j-\frac{1}{2},k} \\ &-\int \left(\widehat{\boldsymbol{H}} - \widehat{\boldsymbol{H}}_v\right)_{i,j,k+\frac{1}{2}} + \left(\widehat{\boldsymbol{H}} - \widehat{\boldsymbol{H}}_v\right)_{i,j,k-\frac{1}{2}}\end{aligned} \tag{3.24}$$

3.3.2 Moving Grid Method

In doing oscillating cascade calculation, the moving grid method is applied to realize the grid deformation. From the view of numerical computation, the time marching terms ξ_t, η_t, ζ_t are introduced. An important point in using moving gird method is that the Geometric Conservation Law (GCL) must be satisfied in doing grid deformation. The essential expression of GCL is written in eqn.(3.25).

$$\frac{d}{dt}\int_R dV = \int_{\partial R} \boldsymbol{W}\cdot d\boldsymbol{S} \qquad (3.25)$$

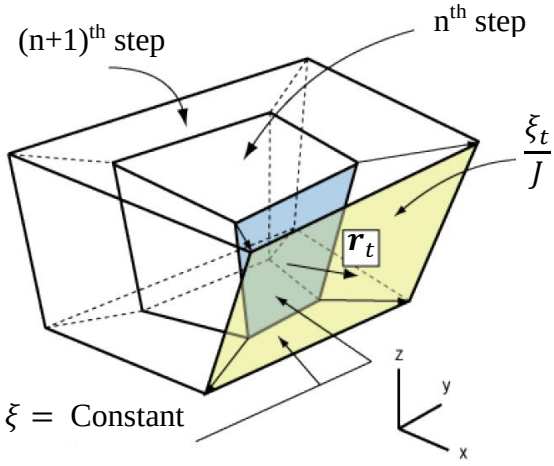

Figure 3.2 Time marching of metrics

Here, the left side means the time change rate of control volume, and it must equal the right side which means the change rate of sweeping volume formed by check surface ∂R with moving velocity $\boldsymbol{W}$. Eqn.(3.25) can be written into eqn.(3.26) by transforming into generalized coordinates.

$$\frac{\partial}{\partial t}\left(\frac{1}{J}\right)+\frac{\partial}{\partial \xi}\left(\frac{\xi_t}{J}\right)+\frac{\partial}{\partial \eta}\left(\frac{\eta_t}{J}\right)+\frac{\partial}{\partial \zeta}\left(\frac{\zeta_t}{J}\right)=0 \qquad (3.26)$$

As shown in Figure 3.2, by assuming that ξ is Constant, $\boldsymbol{r}_t$ is the moving velocity of the boundary surface and $\boldsymbol{S}^{\xi}$ is the area vector, eqn.(3.27). And so are the other components.

$$\frac{\xi_t}{J}=-(\boldsymbol{r}_t\cdot\boldsymbol{S}^{\xi}),\qquad \frac{\eta_t}{J}=-(\boldsymbol{r}_t\cdot\boldsymbol{S}^{\eta}),\qquad \frac{\zeta_t}{J}=-(\boldsymbol{r}_t\cdot\boldsymbol{S}^{\zeta}) \qquad (3.27)$$

After all, the metrics evaluation of time marching terms is connected with the evaluation of hexahedral cell sweeping towards (n+1)th step.

3.3.3 Evaluation of Convection Term (Including Pressure Term)

(1) Uni-Particle Upwind Scheme

Various schemes used for finite volume method are different in evaluating the numerical flux across the boundary. Many such schemes calculate the numerical flux by approximately solving Riemann problem at boundary surface, such as FDS (Flux different splitting) and FVS (Flux vector splitting).

Shima [47] improved FVS scheme by introducing a new concept, “Uni-particle upwind scheme”. FVS scheme determines the upwind difference of convection term according to the plus-minus of eigenvalue, while uni-particle upwind scheme corrects FVS by using one fluid particle to represent convection term. However, the separation formats of mass flux and pressure term are inherited.

As an example, the numerical flux $\hat{F}$ in ξ direction can be expressed as the following separation format written in eqn(3.28).

$$\widehat{\boldsymbol{F}} = \frac{1}{J}(m\boldsymbol{\Phi} + p\boldsymbol{N}) \,, \boldsymbol{\Phi} = \begin{bmatrix} 1 \\ u \\ v \\ w \\ h \end{bmatrix}, \boldsymbol{N} = \begin{bmatrix} 0 \\ \xi_x \\ \xi_y \\ \xi_z \\ \xi_t \end{bmatrix} \tag{3.28}$$

$$m = \rho U, U = \xi_x u + \xi_y v + \xi_z w, h = \frac{e+p}{\rho}$$

Here, m is mass flux; U is transformed velocity; h is total enthalpy per unit mass. Uni-particle upwind scheme uses FDS or FVS scheme to solve mass flux m, and calculates the flux vector $\widehat{\boldsymbol{F}}$ as written in eqn.(3.29) by resolving the upwind direction based on the sign of m. The symbol $\pm$ means the variable on the left (+) or right (-) surface of boundary. $\tilde{p}$ is the mixed pressure by using the left and right Mach number $Ma_{\pm}$.

$$\widehat{\boldsymbol{F}} = \frac{m+|m|}{2}\boldsymbol{\Phi}_+ + \frac{m-|m|}{2}\boldsymbol{\Phi}_- + \tilde{p}\boldsymbol{N} \tag{3.29}$$

$$\tilde{p} = \beta_+ p_+ + \beta_- p_-$$

$$\begin{cases} \beta_{\pm} = \frac{1}{4}(2 \mp Ma_{\pm})(Ma_{\pm} \pm 1)^2 & ,if \ |Ma_{\pm}| \leq 1 \\ \beta_+ = 1, \beta_- = 0 & ,if \ Ma_{\pm} > 1 \\ \beta_+ = 0, \beta_- = 1 & ,if \ Ma_{\pm} < -1 \end{cases}$$

(2) <u>SHUS (Simple High Resolution Upwind Scheme)</u>

In formulating uni-particle upwind scheme, SHUS (Simple High-resolution Upwind Scheme) is used which has the merits in computation time, robustness and precision. As written in eqn.(3.30), the mass flux m is expressed by left and right averaging, convection velocity based upwind difference, and pressure contribution.

$$\begin{aligned} m_i = \frac{1}{2}\Bigg\{ & (\rho U_i)_+ + (\rho U_i)_- - |\overline{U}_i|\Delta\rho - \frac{|\overline{Ma}_i + 1| - |\overline{Ma}_i - 1|}{2}\bar{\rho}\Delta U_i \\ & - \frac{(|\overline{Ma}_i + 1| - |\overline{Ma}_i - 1| - 2|\overline{Ma}_i|)}{2}\frac{\Delta p}{\bar{c}} \Bigg\} \end{aligned} \tag{3.30}$$

$$\overline{Ma}_i = \frac{\overline{U}_i}{\bar{c}} \,, \qquad \overline{U}_i = \frac{\overline{U}_{i+} + \overline{U}_{i-}}{2} \,, \qquad \bar{\rho} = \frac{\rho_+ + \rho_-}{2}$$

Here, Δ is the difference of left and right of cell boundary ($\Delta q = q_- - q_+$) and $\bar{c}$ is averaged sound velocity. Because this scheme is insensitive in averaged sound velocity, the averaged sound velocity is written as follows.

$$\bar{c} = \sqrt{\gamma \frac{p_+ + p_-}{\rho_+ + \rho_-}}$$

$\beta_{\pm}$ can be expressed by using $\bar{c}$ as following equation.

$$\beta_{\pm} = \frac{1}{4}\left(2 \mp \frac{U_{i\pm}}{\bar{c}}\right)\left(\frac{U_{i\pm}}{\bar{c}} \pm 1\right)^2$$

In conclusion, SHUS can accurately capture the contact discontinuity phenomena and is also of good robustness in processing shock wave or symmetrical expansion.

(3) High Order Precision Scheme (MUSCL)

In finite volume method, only the cell averaged physical quantities are reserved in doing computation and the spatial distribution information disappear. In such situation, the spatial precision is promoted by assigning the cell boundary value based on distribution function assumption inside the cell.

When using upwind difference with 1st order precision, to satisfy the TVD (total variation diminishing) property, MUSCL scheme is applied to calculate the numerical flux by interpolating cell boundary values (u_L, u_R) from surroundings physical quantities. In the process of interpolation, difference method with simple high order precision can be achieved without using flux limiting function. Furthermore, the TVD property can be satisfied by introducing flux limiting function into interpolation process. In doing computation, MUSCL interpolation with 3rd order precision is carried out to realize high order precision of the scheme.

The distribution of physical quantity inside the cell is generally defined as $u(x)$, the true value of variable u, and expanded around cell center u_j by 2nd order Taylor's formula until which is written in eqn.(3.31).

$$\begin{gathered} u(x) = u_j + \frac{1}{\Delta x}(x - x_j)\delta_j u + \frac{3\kappa}{2(\Delta x)^2}\left[(x - x_j)^2 - \frac{(\Delta x)^2}{12}\right]\delta_j^2 u \\ \left(x_{j-\frac{1}{2}} \le x \le x_{j+\frac{1}{2}}\right) \\ u_j = \frac{1}{\Delta x}\int_{j-\frac{1}{2}}^{j+\frac{1}{2}} u(x)dx \end{gathered} \tag{3.31}$$

When $\kappa = 1/3$, eqn.(3.31) becomes quadratic curve distribution and gets 3rd order precision. By given that

$$\delta_j u = \frac{1}{2}(u_{j+1} - u_{j-1}), \qquad \delta_j^2 u = u_{j+1} - 2u_j + u_{j-1}$$

and $u_j - u_{j-1} = \Delta_-, u_{j+1} - u_j = \Delta_+$, the physical quantity on cell boundary is written into eqn.(3.32)(3.33). L and R mean the left side and right side of cell boundary.

$$\begin{aligned} (u_L)_{j+\frac{1}{2}} &= u_j + \frac{1}{2}\delta_j u + \frac{\kappa}{4}\delta_j^2 u \\ &= u_j + \frac{1}{4}(1-\kappa)(u_j - u_{j-1}) + \frac{1}{4}(1+\kappa)(u_{j+1} - u_j) \\ &= u_j + \frac{1}{4}[(1-\kappa)\Delta_- + (1+\kappa)\Delta_+]_j \end{aligned} \tag{3.32}$$

$$\begin{aligned} (u_R)_{j+\frac{1}{2}} &= u_{j+1} - \frac{1}{2}\delta_{j+1} u + \frac{\kappa}{4}\delta_{j+1}^2 u \\ &= u_{j+1} - \frac{1}{4}(1+\kappa)(u_{j+1} - u_j) - \frac{1}{4}(1-\kappa)(u_{j+2} - u_{j+1}) \\ &= u_{j+1} - \frac{1}{4}[(1-\kappa)\Delta_+ + (1+\kappa)\Delta_-]_{j+1} \end{aligned} \tag{3.33}$$

(4) Flux Limiting Function

To satisfy TVD property, Minmod limiter and Van Albada's limiting function are applied as flux limiting function. The values on cell boundary by using Van Albada's limiting function are expressed as following equations.

$$(u_L)_{j+\frac{1}{2}} = u_j + \left[\frac{s}{4}\{(1-s\kappa)\Delta_- + (1+s\kappa)\Delta_+\}\right]_j \tag{3.34}$$

$$(u_R)_{j+\frac{1}{2}} = u_{j+1} - \left[\frac{s}{4}\{(1+s\kappa)\Delta_- + (1-s\kappa)\Delta_+\}\right]_{j+1} \tag{3.35}$$

$$s = \frac{2\Delta_+\Delta_- + \varepsilon_j}{{\Delta_+}^2 + {\Delta_-}^2 + \varepsilon_j}\,, \qquad \varepsilon_j = 10^{-15} \tag{3.36}$$

3.3.4 Evaluation of Diffusion Term (Viscous Term & Thermal Conduction Term)

The viscous term is evaluated as the flux by solving the viscous stress, impulse and work acting on the cell surfaces. In using FVM, the physical quantities are merely represented by the cell center values. So values of the physical quantities on cell surfaces should be estimated by some methods.

When solving the stress tensor on cell surface, the spatial gradient of velocity is necessary. As an example, the velocity gradient in ξ direction on $i+\frac{1}{2}$ cell surface is written as eqn.(3.37) and it can be expressed with the velocity differential in generalized coordinates and metrics by using the chain rule.

$$\left(\frac{\partial \boldsymbol{u}}{\partial x}\right)_{i+\frac{1}{2},j,k} = \left(\frac{\partial \boldsymbol{u}}{\partial \xi}\right)_{i+\frac{1}{2},j,k} \left(\frac{\partial \xi}{\partial x}\right)_{i+\frac{1}{2},j,k} \tag{3.37}$$

At first, the velocity differentials in 3 directions in generalized coordinates are evaluated by using 2nd order central difference with the width of 1, as written in eqn.(3.38)(3.39)(3.40).

$$\left(\frac{\partial \boldsymbol{u}}{\partial \xi}\right)_{i+\frac{1}{2},j,k} \simeq \frac{\boldsymbol{u}_{i+1,j,k} - \boldsymbol{u}_{i,j,k}}{\Delta\xi} \tag{3.38}$$

$$\left(\frac{\partial \boldsymbol{u}}{\partial \eta}\right)_{i+\frac{1}{2},j,k} \simeq \frac{\boldsymbol{u}_{i+\frac{1}{2},j+\frac{1}{2},k} - \boldsymbol{u}_{i+\frac{1}{2},j-\frac{1}{2},k}}{\Delta\eta} \tag{3.39}$$

$$\left(\frac{\partial \boldsymbol{u}}{\partial \zeta}\right)_{i+\frac{1}{2},j,k} \simeq \frac{\boldsymbol{u}_{i+\frac{1}{2},j,k+\frac{1}{2}} - \boldsymbol{u}_{i+\frac{1}{2},j,k-\frac{1}{2}}}{\Delta\zeta} \tag{3.40}$$

However, when the defined point is not at the difference point, the value should be calculated by interpolating surrounding values. That is to say, the physical quantities at points of $i \pm \frac{1}{2}$, $j \pm \frac{1}{2}$ and $k \pm \frac{1}{2}$ should be calculated as the following equations, as examples.

$$\boldsymbol{u}_{i+\frac{1}{2},j+\frac{1}{2},k} \simeq \frac{\boldsymbol{u}_{i+1,j+\frac{1}{2},k} + \boldsymbol{u}_{i,j+\frac{1}{2},k}}{2} \simeq \frac{\boldsymbol{u}_{i+1,j+1,k} + \boldsymbol{u}_{i+1,j,k} + \boldsymbol{u}_{i,j+1,k} + \boldsymbol{u}_{i,j,k}}{4} \tag{3.41}$$

$$\boldsymbol{u}_{i+\frac{1}{2},j,k+\frac{1}{2}} \simeq \frac{\boldsymbol{u}_{i+1,j,k+\frac{1}{2}} + \boldsymbol{u}_{i,j,k+\frac{1}{2}}}{2} \simeq \frac{\boldsymbol{u}_{i+1,j,k+1} + \boldsymbol{u}_{i+1,j,k} + \boldsymbol{u}_{i,j,k+1} + \boldsymbol{u}_{i,j,k}}{4} \tag{3.42}$$

By using such 2nd order interpolation and difference method, the 2nd order precision is realized in evaluating the viscous stress tensor, viscous work on cell surfaces. Besides, the same method is adopted in processing heat fluxes for solving temperature gradient on cell surfaces.

3.3.5 Variable Conversion (Pre-Processing Matrix)

To explain the pre-processing method, we define the convection term as $\boldsymbol{F}_i$ and viscous term as $\boldsymbol{F}_{vi}$. The compressible N-S equations in generalized coordinates can be expressed as eqn.(3.43). Here, $\boldsymbol{Q}$ includes conservation quantities as written in eqn.(3.44).

$$\frac{\partial \boldsymbol{Q}}{\partial t} + \frac{\partial \boldsymbol{F}_i}{\partial \xi_i} + \frac{\partial \boldsymbol{F}_{vi}}{\partial \xi_i} = 0 \tag{3.43}$$

$$\boldsymbol{Q} = \frac{1}{J}[\rho, \rho u, \rho v, \rho w, e]^T \tag{3.44}$$

In this calculation, the computation code uses basic physical quantities as the variables, so that the variable conversion from conservation quantities to basic physical quantities is pre-requisite. The pre-processing matrix is introduced in doing variable conversion. Pre-processing method and pre-processing matrix is explained as follows.

No matter viscous or non-viscous calculation, it is common to let the calculation of time marching to proceed based on characteristic velocity calculated from the state quantities at each grid point. This method is useful for large range of Reynolds number. However, if the compressible code is used for extremely slow flow compared to characteristic velocity, the velocity difference will cause the non-convergence and nonphysical numerical oscillation problem. One solution for this problem is the pre-processing method. Pre-processing method manipulates the eigenvalues of basic equations by introducing pseudo sound velocity, and makes the characteristic velocity and convection velocity to be same comparable level.

Pre-processing method converts the independent variables from conservation quantities in $\boldsymbol{Q}$ into basic physical quantities in $\widetilde{\boldsymbol{Q}}$.

$$\widetilde{\boldsymbol{Q}} = \frac{1}{J}[p, u, v, w, T]^T \tag{3.45}$$

Eqn.(3.43) can be deformed as eqn.(3.46).

$$\frac{\partial \boldsymbol{Q}}{\partial \widetilde{\boldsymbol{Q}}}\frac{\partial \widetilde{\boldsymbol{Q}}}{\partial t} + \frac{\partial \boldsymbol{F}_i}{\partial \xi_i} + \frac{\partial \boldsymbol{F}_{vi}}{\partial \xi_i} = 0 \tag{3.46}$$

$\partial \boldsymbol{Q}/\partial \widetilde{\boldsymbol{Q}}$ in eqn.(3.46) is the variable conversion matrix. We define $\boldsymbol{\Gamma} = \partial \boldsymbol{Q}/\partial \widetilde{\boldsymbol{Q}}$ here and $\boldsymbol{\Gamma}$ is expressed as eqn.(3.48).

$$\boldsymbol{\Gamma}\frac{\partial \widetilde{\boldsymbol{Q}}}{\partial t} + \frac{\partial \boldsymbol{F_i}}{\partial \xi_i} + \frac{\partial \boldsymbol{F_{vi}}}{\partial \xi_i} = 0 \tag{3.47}$$

$$\boldsymbol{\Gamma} = \begin{bmatrix} \rho_p & 0 & 0 & 0 & \rho_T \\ \rho_p u & \rho & 0 & 0 & \rho_T u \\ \rho_p v & 0 & \rho & 0 & \rho_T v \\ \rho_p w & 0 & 0 & \rho & \rho_T w \\ \rho_p h - (1 - \rho h_p) & \rho u & \rho v & \rho w & \rho_T h + \rho h_T \end{bmatrix} \tag{3.48}$$

The conversion between basic physical quantities and conservation quantities which is expressed as eqn.(3.49) is established for infinitesimals. Also, $\boldsymbol{\Gamma}^{-1}$ can be written as eqn.(3.50).

$$\boldsymbol{\Gamma} = \frac{\partial \boldsymbol{Q}}{\partial \widetilde{\boldsymbol{Q}}} \;\Leftrightarrow\; \partial \widetilde{\boldsymbol{Q}} = \boldsymbol{\Gamma}^{-1} \partial \boldsymbol{Q} \tag{3.49}$$

$$\boldsymbol{\Gamma}^{-1} = \begin{bmatrix} \big(\rho h_T + \rho_T(h-2\phi)\big)/d & \rho_T u/d & \rho_T v/d & \rho_T w/d & -\rho_T/d \\ -u/\rho & 1/\rho & 0 & 0 & \rho_T u \\ -v/\rho & 0 & 1/\rho & 0 & \rho_T v \\ -w/\rho & 0 & 0 & 1/\rho & \rho_T w \\ \big[\big(1-\rho h_p\big) - \rho_p(h-2\phi)\big]/d & -\rho_p u/d & -\rho_p v/d & -\rho_p w/d & \rho_p/d \end{bmatrix} \tag{3.50}$$

$$\phi = \frac{1}{2}(u^2 + v^2 + w^2) \tag{3.51}$$

$$d = \rho_T + \rho\big(\rho_p h_T - \theta \rho_T h_p\big) \tag{3.52}$$

When using pre-processing method, ρ_p in $\boldsymbol{\Gamma}, \boldsymbol{\Gamma}^{-1}$ is replaced by pre-processing parameter θ. When the value of U_r included in θ equals sound velocity, θ equals ρ_p, then eqn.(3.47) is strictly equivalent to eqn. (3.43). By changing the value of U_r and introducing pseudo sound velocity, the variable matrix becomes the pre-processing matrix and the pre-processing method is applied. Under such condition, even though eqn.(3.47) is different from eqn.(3.43), the converged solution obtained by eqn.(3.47) where the time differential term can be ignored is the same with the converged solution obtained by eqn.(3.43).

The pre-processing parameter θ and pre-processing matrix $\boldsymbol{\Gamma}_{pre}, \boldsymbol{\Gamma}_{pre}^{-1}$ can be written as follows.

$$\theta = \frac{1}{U_r^2} - \frac{\rho_T\big(1-\rho h_p\big)}{\rho h_T} \tag{3.53}$$

$$\boldsymbol{\Gamma}_{pre} = \begin{bmatrix} \theta & 0 & 0 & 0 & \rho_T \\ \theta u & \rho & 0 & 0 & \rho_T u \\ \theta v & 0 & \rho & 0 & \rho_T v \\ \theta w & 0 & 0 & \rho & \rho_T w \\ \theta h - \big(1-\rho h_p\big) & \rho u & \rho v & \rho w & \rho_T h + \rho h_T \end{bmatrix} \tag{3.54}$$

$$\boldsymbol{\Gamma}_{pre}^{-1} = \begin{bmatrix} \big(\rho h_T + \rho_T(h-2\phi)\big)/d & \rho_T u/d & \rho_T v/d & \rho_T w/d & -\rho_T/d \\ -u/\rho & 1/\rho & 0 & 0 & \rho_T u \\ -v/\rho & 0 & 1/\rho & 0 & \rho_T v \\ -w/\rho & 0 & 0 & 1/\rho & \rho_T w \\ \big[\big(1-\rho h_p\big) - \theta(h-2\phi)\big]/d & -\theta u/d & -\theta v/d & -\theta w/d & \theta/d \end{bmatrix} \tag{3.55}$$

$$d = \rho_T + \rho\big(\theta h_T - \rho_T h_p\big) \tag{3.56}$$

In this calculation, the pseudo sound velocity was not adopted and the pre-processing method wasn't applied, while only the variable conversion between basic physical quantities and conservation quantities was conducted by using the above pre-processing matrix.

3.3.6 Time Marching Method

(1) Implicit Method

Time integral can be classified into explicit methods and implicit methods. Explicit methods calculate the state of a system at a later time (*n+1 step*) from the state of the system at the current time (*n step*), while implicit methods find a solution by solving an equation involving both the current state of the system and the later one. Even though discretized equations by explicit methods are simple and easy to solve, the computation cost is inclined to be high due to short time step length caused by the requirement of CFL condition. Therefore, the implicit method with mild CFL condition limit is used in this study.

For simple demonstration, Euler equations is used and it can be discretized into eqn.(3.57).

$$\frac{\widehat{\boldsymbol{Q}}^{n+1}-\widehat{\boldsymbol{Q}}^{n}}{\Delta t}+\left\{\lambda\left(\frac{\partial\widehat{\boldsymbol{F}}}{\partial\xi}\right)^{n+1}+(1-\lambda)\left(\frac{\partial\widehat{\boldsymbol{F}}}{\partial\xi}\right)^{n}+\lambda\left(\frac{\partial\widehat{\boldsymbol{G}}}{\partial\eta}\right)^{n+1}+(1-\lambda)\left(\frac{\partial\widehat{\boldsymbol{G}}}{\partial\eta}\right)^{n}+\lambda\left(\frac{\partial\widehat{\boldsymbol{H}}}{\partial\zeta}\right)^{n+1}+(1-\lambda)\left(\frac{\partial\widehat{\boldsymbol{H}}}{\partial\zeta}\right)^{n}\right\}=0 \tag{3.57}$$

Here, λ is Crank-Nicolson coefficient, and the detail of time marching schemes with different λ is shown as follows.

$\lambda=1$	:	Euler implicit method	1st order precision
$\lambda=1/2$	:	Crank-Nicolson implicit method	2nd order precision

The unknowns in next time step are required to solve the numerical fluxes $\widehat{\boldsymbol{F}}^{n+1},\widehat{\boldsymbol{G}}^{n+1},\widehat{\boldsymbol{H}}^{n+1}$ in each direction. Here, as an example, the numerical flux in ξ direction can be linearized as eqn.(3.58).

$$\widehat{\boldsymbol{F}}^{n+1}=\widehat{\boldsymbol{F}}^{n}+\left(\frac{\partial\widehat{\boldsymbol{F}}}{\partial\widehat{\boldsymbol{Q}}}\right)^{n}\left(\widehat{\boldsymbol{Q}}^{n+1}-\widehat{\boldsymbol{Q}}^{n}\right)=\widehat{\boldsymbol{F}}^{n}+\widehat{\boldsymbol{A}}^{n}\Delta\widehat{\boldsymbol{Q}} \tag{3.58}$$

$\widehat{\boldsymbol{A}}$ is the flux Jacobian matrix in ξ direction. Similarly, $\widehat{\boldsymbol{B}},\widehat{\boldsymbol{C}}$ are defined as flux Jacobian matrices in η,ζ direction. Therefore, eqn.(3.57) can be rewritten into eqn.(3.59). The right side of eqn.(3.59) is abbreviated as $\left[\widehat{\boldsymbol{RHS}}\right]$ in the later expressions.

$$\left[\boldsymbol{I}+\lambda\Delta t\frac{\partial}{\partial\xi}\widehat{\boldsymbol{A}}^{n}+\lambda\Delta t\frac{\partial}{\partial\eta}\widehat{\boldsymbol{B}}^{n}+\lambda\Delta t\frac{\partial}{\partial\zeta}\widehat{\boldsymbol{C}}^{n}\right]\Delta\widehat{\boldsymbol{Q}}=-\Delta t\left[\left(\frac{\partial\widehat{\boldsymbol{F}}}{\partial\xi}\right)^{n}+\left(\frac{\partial\widehat{\boldsymbol{G}}}{\partial\eta}\right)^{n}+\left(\frac{\partial\widehat{\boldsymbol{H}}}{\partial\zeta}\right)^{n}\right] \tag{3.59}$$

To solve $\Delta\widehat{\boldsymbol{Q}}$, it is easily considering to multiply the inverse matrix of left side coefficient matrix by $\left[\widehat{\boldsymbol{RHS}}\right]$. However, it is not realistic to solve the inverse matrix directly due to the large amount of elements. Therefore, when doing matrix inversion, some approximation methods are applied which are explained as follows.

(2) TCPGS Method with RBGS

TCPGS method [48] proposed by Shima is extended from the MFGS (Matrix-free Gauss-Seidel) method. The original TCPGS uses the variables p,v,s (s: entropy), while variables

p, v, T are formulated in this study. The Red-Black Gauss-Seidel iteration method is used in the internal iteration of linear equations. This method can obtain simpler than LU-SGS scheme and the convergence performance can be promoted remarkably.

At first, by converting the variables into basic physical quantities, the fundamental equation containing discretized time term can be written as eqn.(3.60).

$$\Delta\widetilde{\boldsymbol{Q}} + \Delta t \boldsymbol{B}_i \frac{\partial \Delta\widetilde{\boldsymbol{Q}}}{\partial \xi_i} = \left[\widehat{\boldsymbol{RHS}}\right], \qquad \left[\widehat{\boldsymbol{RHS}}\right] = \boldsymbol{\Gamma}^{-1}\left[\widehat{\boldsymbol{RHS}}\right] \tag{3.60}$$

Similar to LU-SGS method in doing upwind difference for flux Jacobian matrix, even in this form, approximate upwind difference can be realized with maintaining superior diagonality by adding numerical viscosity to $\boldsymbol{B}_i$. For simplifying, assuming the numerical viscosity is given as a diagonal matrix and seeing a general compressibility scheme as the object, the numerical dissipation $\boldsymbol{D}_i$ is expressed as eqn.(3.61). And it is given by the maximum spectral radius in the compressive flux.

$$\boldsymbol{D}_i = diag\left[d_p, d_v, d_v, d_v, d_T\right], \qquad d_p = d_v = d_T = |V_i| + c\sqrt{\xi_{i,k}\xi_{i,k}} \tag{3.61}$$

The flux Jacobian matrix with added numerical dissipation is written as eqn.(3.62) same as LU-SGS method.

$$\boldsymbol{B}_i = \boldsymbol{B}_i^+ + \boldsymbol{B}_i^-, \qquad \boldsymbol{B}_i^{\pm} = \frac{\boldsymbol{B}_i \pm \boldsymbol{D}_i}{2} \tag{3.62}$$

$+/-$ component is backward/forward difference. Also, to ensure the stability of viscous term, the correction of diagonal term is conducted same as LU-SGS method. When evaluating the matrix in using implicit method, in order to simplify the calculation, the coefficient matrix for updating (i, j, k) cell is based on the values of (i, j, k) cell. The final discretization is written as eqn.(3.63).

$$\begin{aligned}\left[\boldsymbol{I} + \Delta t(\boldsymbol{D}_1 + \boldsymbol{D}_2 + \boldsymbol{D}_3)\Delta\widetilde{\boldsymbol{Q}}_{i,j,k} - \Delta t\left(\boldsymbol{B}_1^+\Delta\widetilde{\boldsymbol{Q}}_{i-1,j,k} + \boldsymbol{B}_2^+\Delta_{i,j-1,k} + \boldsymbol{B}_3^+\Delta_{i,j,k-1}\right)\right. \\ \left. + \Delta t\left(\boldsymbol{B}_1^-\Delta\widetilde{\boldsymbol{Q}}_{i+1,j,k} + \boldsymbol{B}_2^-\Delta\widetilde{\boldsymbol{Q}}_{i,j+1,k} + \boldsymbol{B}_3^-\Delta\widetilde{\boldsymbol{Q}}_{i,j,k+1}\right)\right] = \left[\widehat{\boldsymbol{RHS}}\right]_{i,j,k}\end{aligned} \tag{3.63}$$

Without using the approximate LDU decomposition here, the above equation is directly solved by linear iteration based on Red-Black-Gauss-Seidel method. Gauss-Seidel method updates the variable as eqn.(3.64), by uses the upper triangle component of the discretized term, lower triangle component of the discretized term, and the newest $\Delta\widetilde{\boldsymbol{Q}}$.

$$\Delta\widetilde{\boldsymbol{Q}}_{i,j,k}^{new} = \boldsymbol{D}^{-1}\left(\left[\widehat{\boldsymbol{RHS}}\right]_{i,j,k} - \boldsymbol{L}\Delta\widetilde{\boldsymbol{Q}} - \boldsymbol{U}\Delta\widetilde{\boldsymbol{Q}}\right) \tag{3.64}$$

At that time, the order dependence is eliminated by the parallelization method described as follows.

✧ Group 1 : $j + k = (odd)$ .and. $i = (even)$, $j + k = (even)$ .and. $i = (odd)$ (“Red” cells)

✧ Group 2 : $j + k = (odd)$ .and. $i = (odd)$, $j + k = (even)$ .and. $i = (even)$ (“Black” cells)

Based on the above determine statements, the structured grid is divided into two groups arraying with a 3D staggered pattern. The visualization of the groups can be seen in Figure 3.3 with red and black colors. By doing such group division, the data in group 1 and group2 has no order dependence, so the parallelization can be realized. The parallelization is conducted by the variable $j \times k$ which merges the loops in j direction and k direction.

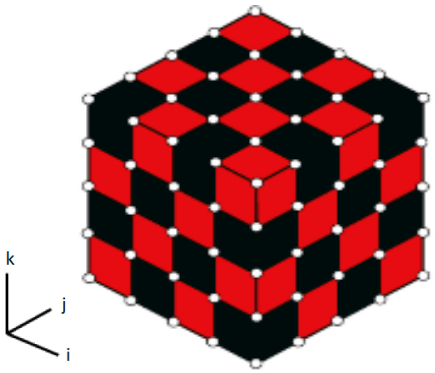

Figure 3.3 Cell grouping for Red-Black Gauss-Seidel relaxation

(3) Local Time Stepping Method

For the steady calculation, the final convergence solution is achieved when the fluxes in all the cells are converged and is not relevant to the time step length. Due to the large grid width range of grid cells, the global CFL condition is determined by the smallest cell which causes large time consumption.

In this study, the local time step length method is adopted. The time step length Δt is set locally at every grid point. The larger Δt will make the total convergence speed faster. Δt has an upper limit locally which is determined by the CFL condition. Here, Δt_{limit} is calculated with given CFL_{limit} as written in eqn.(3.65). U, V, W are the contravariant velocity components. CFL_{limit} for steady computations in this study is set to 1.0.

$$\Delta t_{limit} = \min\left(\frac{CFL_{limit}}{|U| + c\sqrt{\xi_{1,i}\xi_{1,i}}}, \quad \frac{CFL_{limit}}{|V| + c\sqrt{\xi_{2,i}\xi_{2,i}}}, \quad \frac{CFL_{limit}}{|W| + c\sqrt{\xi_{3,i}\xi_{3,i}}}\right) \tag{3.65}$$

(4) Newton-Raphson Method

Time precision for unsteady cascade flutter calculation of high importance, while when using implicit method, the approximations in matrix inversion deteriorates the time precision. To solve this problem, 3 points backward difference with 2nd order precision are used for the time term and furthermore, Newton-Raphson method is applied to ensure the time precision.

The 1D Euler equation is written in eqn.(3.66) as an example to illustrate the Newton-Raphson method in unsteady calculation. The time term uses 3 points backward difference.

$$\frac{3\widehat{\boldsymbol{Q}}^{n+1} - 4\widehat{\boldsymbol{Q}}^{n} + \widehat{\boldsymbol{Q}}^{n-1}}{2\Delta t} + \left\{\lambda\left(\frac{\partial \widehat{\boldsymbol{F}}}{\partial \xi}\right)^{n+1} + (1-\lambda)\left(\frac{\partial \widehat{\boldsymbol{F}}}{\partial \xi}\right)^{n}\right\} = 0 \tag{3.66}$$

As written in eqn.(3.67), the m[th] value $\widehat{\boldsymbol{Q}}_{(m)}^{n+1}$ has the error $\Delta\widehat{\boldsymbol{Q}}_{(m)}$, and the linearization can be conducted by eqn.(3.58) , as same as the condition of implicit time integral.

$$\widehat{\boldsymbol{Q}}^{n+1} = \widehat{\boldsymbol{Q}}_{(m)}^{n+1} + \Delta\widehat{\boldsymbol{Q}}_{(m)} \tag{3.67}$$

$$\widehat{\boldsymbol{F}}^{n+1} = \widehat{\boldsymbol{F}}_{(m)}^{n+1} + \widehat{\boldsymbol{A}}_{(m)}^{n+1}\Delta\widehat{\boldsymbol{Q}}_{(m)} \tag{3.68}$$

By substituting the above equations, eqn.(3.69) can be obtained.

$$\left[\frac{3}{2}\boldsymbol{I}+\lambda\Delta t\frac{\partial}{\partial\xi}\widehat{\boldsymbol{A}}_{(m)}^{n+1}\right]\Delta\widehat{\boldsymbol{Q}}_{(m)} = -\Delta t\left\{\lambda\left(\frac{\partial\widehat{\boldsymbol{F}}}{\partial\xi}\right)_{(m)}^{n+1}+(1-\lambda)\left(\frac{\partial\widehat{\boldsymbol{F}}}{\partial\xi}\right)^{n}\right\}-\frac{3\widehat{\boldsymbol{Q}}^{n+1}-4\widehat{\boldsymbol{Q}}^{n}+\widehat{\boldsymbol{Q}}^{n-1}}{2} \tag{3.69}$$

Then, eqn.(3.69) is iteratively calculated with updating the equation by $\widehat{\boldsymbol{Q}}_{(m+1)}^{n+1}=\widehat{\boldsymbol{Q}}_{(m)}^{n+1}+\Delta\widehat{\boldsymbol{Q}}_{(m)}$. Theoretically, $\Delta\widehat{\boldsymbol{Q}}_{(m)}$ converges towards 0 and eqn.(3.70) is established. The time precision is independent on the approximation methods acting on the left matrix, such as diagonalization and factorization.

$$\widehat{\boldsymbol{Q}}_{(m)}^{n+1}=\frac{2}{3}\left[4\widehat{\boldsymbol{Q}}^{n}-\widehat{\boldsymbol{Q}}^{n-1}-\Delta t\left\{\lambda\left(\frac{\partial\widehat{\boldsymbol{F}}}{\partial\xi}\right)_{(m)}^{n+1}+(1-\lambda)\left(\frac{\partial\widehat{\boldsymbol{F}}}{\partial\xi}\right)^{n}\right\}\right] \tag{3.70}$$

However, the time cost for the iterative computation will increase with the number of times increasing. So, the convergence limit exits and the number of iteration times should be selected appropriately.

3.3.7 Physical Property Values

(1) Molecular Viscosity Coefficient

In continuum mechanics, a Newtonian fluid is a fluid in which the viscous stresses at every point are linearly proportional to the velocity gradient (local strain rate). And this proportionality constant is called molecular viscosity coefficient. In the condition without molecular dissociation, molecular viscosity coefficient is verified to be merely dependent on temperature and independent on pressure in large range. Sutherland's law is written in eqn.(3.71). The application scope of Sutherland's law is 120~1500K.

$$\mu=\mu_{ref}\left(\frac{T_{ref}+S}{T+S}\right)\left(\frac{T}{T_{ref}}\right)^{\frac{3}{2}} \tag{3.71}$$

Reference temperature: $T_{ref}=288.15[K]$

Sutherland temperature: $S=110.40[K]$

Viscosity at the reference temperature: $\mu_{ref}=1.82\times10^{-5}[Pa\cdot sec]$

(2) Molecular Heat Transfer Coefficient and Turbulence Heat Transfer Coefficient

In the condition without molecular dissociation, molecular heat transfer coefficient is merely dependent on temperature has close relationship with molecular viscosity coefficient μ through Prandtl number Pr.

$$\kappa=\frac{\mu C_p}{Pr} \tag{3.72}$$

Similarly, turbulence heat transfer coefficient can be calculated by using turbulence viscosity coefficient μ_t through turbulence Prandtl number Pr_t

$$\kappa_t=\frac{\mu_t C_p}{Pr_t} \tag{3.73}$$

3.3.8 Boundary Condition

In this calculation, the values of u, v, w, T, p, k, ω at the boundary surfaces are given as boundary conditions by the code. The boundary conditions are divided into 4 types, including steady inlet & outlet boundary condition, unsteady inlet & outlet boundary condition, inter-block boundary condition & periodic boundary condition and wall boundary condition as shown in Figure 3.4. Here, the quasi 1D non-reflection boundary condition is used in unsteady calculation to suppress non-physical reflection at inlet & outlet boundaries.

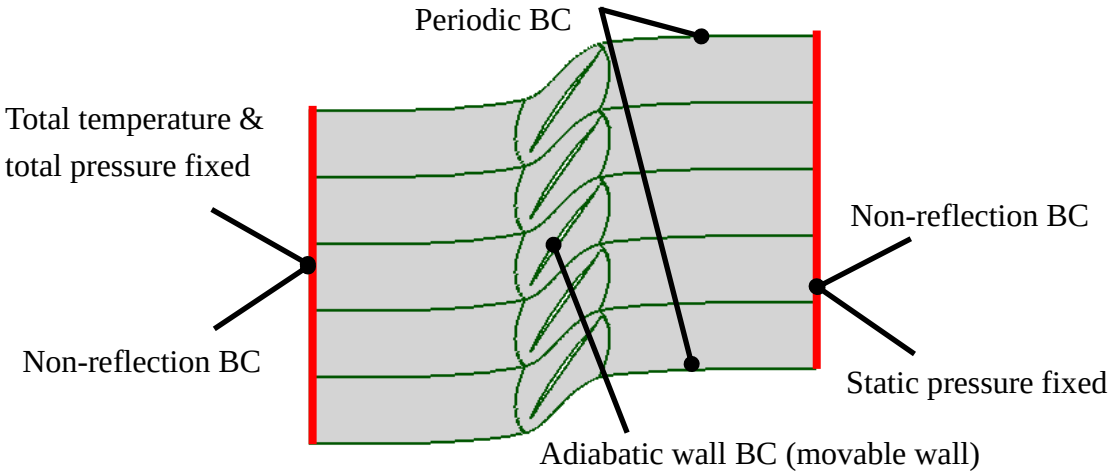

Figure 3.4 Boundary condition classification of 3D cascade

(1) <u>Inlet & Outlet Boundary Condition</u>

✧ Inlet boundary condition

The boundary conditions on inlet boundary is given based on the characteristic quantity-Riemann invariants, which means the characteristic propagation velocities of isentropic wave and pressure wave. Therefore, Riemann invariants include 3 type characteristic propagation velocities of waves as written in eqn.(3.74).

$$R_1 = c, \qquad R_3 = u + \frac{2c}{\gamma - 1}, \qquad R_3 = u - \frac{2c}{\gamma - 1} \tag{3.74}$$

On inlet boundary, velocity is given by extrapolating Riemann invariant R_3 which is along the backward wave. The inlet velocity calculation is conducted as eqn.(3.75).

$$V_{inlet} = \frac{(\gamma - 1)R_3 + \sqrt{4\gamma(\gamma + 1)C_p T_t - 2(\gamma - 1)R_3^2}}{\gamma + 1} \tag{3.75}$$

In this calculation, total pressure, total temperature and inlet flow angle on inlet boundary are set as constant. As to the 3D inlet boundary condition, $u_{inlet}, v_{inlet}, w_{inlet}$ are the 3 components of velocity vector and calculated based on inlet flow angle; static temperature $T_{s\,inlet}$ is solved by the relational formula with total temperature and Mach number; static pressure $p_{s\,inlet}$ is calculated by the relational formula with total pressure and Mach number. The inlet boundary condition vector is written in eqn.(3.76).

$$[u \quad v \quad w \quad T \quad p]^T = [u_{inlet} \quad v_{inlet} \quad w_{inlet} \quad T_{s\,inlet} \quad p_{s\,inlet}]^T \tag{3.76}$$

For comparing the CFD results with experimental results, the inlet boundary layer is set by giving the inlet spanwise velocity distribution calculated by Prandtl's $(1/7)^{th}$ power law of velocity profile.

$$\frac{\bar{u}}{U_0} = \left(\frac{y}{\delta}\right)^{\frac{1}{7}} \tag{3.77}$$

✧ Outlet boundary condition

On outlet boundary, the static pressure is set as constant according to experimental data and other variables are extrapolated from the neighbored cells. The outlet boundary condition is given as eqn.(3.78).

$$[u \quad v \quad w \quad T \quad p]^T = [u_{extrap} \quad v_{extrap} \quad w_{extrap} \quad T_{extrap} \quad p_{ref}]^T \tag{3.78}$$

(2) <u>Quasi 1D Non-Reflection Boundary Condition (NRBC)</u>

When doing CFD simulation for cascade flow, the nonphysical reflection phenomena caused by the pressure wave, shock wave or expansion wave were observed at the boundaries. The non-reflection boundary condition was developed to solve this problem. In this study, Giles's method [49] was adopted.

The theory of NRBC is simply introduced here. Eqn.(3.79) shows the 2D governing equation.

$$\frac{\partial \boldsymbol{q}}{\partial t} + \boldsymbol{A}\frac{\partial \boldsymbol{q}}{\partial x} + \boldsymbol{B}\frac{\partial \boldsymbol{q}}{\partial y} = 0 \tag{3.79}$$

$$\boldsymbol{q} = \begin{bmatrix} \rho \\ u \\ v \\ p \end{bmatrix}, \quad \boldsymbol{A} = \begin{bmatrix} u & \rho & 0 & 0 \\ 0 & u & 0 & 1/\rho \\ 0 & 0 & u & 0 \\ 0 & \gamma p & 0 & u \end{bmatrix}, \quad \boldsymbol{B} = \begin{bmatrix} v & 0 & \rho & 0 \\ 0 & v & 0 & 0 \\ 0 & 0 & v & 1/\rho \\ 0 & 0 & \gamma p & v \end{bmatrix}$$

To grasp the steady and unsteady components of $\boldsymbol{q}$, the linearization is done by $\boldsymbol{q} = \bar{\boldsymbol{q}} + \tilde{\boldsymbol{q}}$. Then eqn.(3.79) can be written into eqn.(3.80). The coefficient matrices $\bar{\boldsymbol{A}}, \bar{\boldsymbol{B}}$ are of the same values locally.

$$\frac{\partial \tilde{\boldsymbol{q}}}{\partial t} + \bar{\boldsymbol{A}}\frac{\partial \tilde{\boldsymbol{q}}}{\partial x} + \bar{\boldsymbol{B}}\frac{\partial \tilde{\boldsymbol{q}}}{\partial y} = 0 \tag{3.80}$$

$$\tilde{\boldsymbol{q}} = \begin{bmatrix} \tilde{\rho} \\ \tilde{u} \\ \tilde{v} \\ \tilde{p} \end{bmatrix}, \quad \bar{\boldsymbol{A}} = \begin{bmatrix} \bar{u} & \bar{\rho} & 0 & 0 \\ 0 & \bar{u} & 0 & 1/\bar{\rho} \\ 0 & 0 & \bar{u} & 0 \\ 0 & \gamma\bar{p} & 0 & \bar{u} \end{bmatrix}, \quad \bar{\boldsymbol{B}} = \begin{bmatrix} \bar{v} & 0 & \rho & 0 \\ 0 & \bar{v} & 0 & 0 \\ 0 & 0 & \bar{v} & 1/\bar{\rho} \\ 0 & 0 & \gamma\bar{p} & \bar{v} \end{bmatrix}$$

The disturbance is considered sufficiently small compared to the steady component. That is a utilization restriction of NRBC. Giles introduced the quasi 1D characteristic equation here. The eigenvalues of eqn. (3.69) is solved and written in eqn.(3.81).

$$\begin{bmatrix} c_1 \\ c_2 \\ c_3 \\ c_4 \end{bmatrix} = \begin{bmatrix} -\bar{c}^2 & 0 & 0 & 1 \\ 0 & 0 & \overline{\rho c} & 0 \\ 0 & \overline{\rho c} & 0 & 1 \\ 0 & -\overline{\rho c} & 0 & 1 \end{bmatrix} \begin{bmatrix} \tilde{\rho} \\ \tilde{u} \\ \tilde{v} \\ \tilde{p} \end{bmatrix} \tag{3.81}$$

$$\begin{bmatrix} \tilde{\rho} \\ \tilde{u} \\ \tilde{v} \\ \tilde{p} \end{bmatrix} = \begin{bmatrix} -1/\bar{c}^2 & 0 & 1/2\bar{c}^2 & -1/2\bar{c}^2 \\ 0 & 0 & 1/2\overline{\rho c} & -1/2\overline{\rho c} \\ 0 & 1/\overline{\rho c} & 0 & 1 \\ 0 & 0 & 1/2 & 1/2 \end{bmatrix} \begin{bmatrix} c_1 \\ c_2 \\ c_3 \\ c_4 \end{bmatrix} \tag{3.82}$$

c_1 : entropy wave c_2 : vorticity wave

c_3, c_4 : pressure wave propagating toward upstream or downstream

NRBC can be implemented as following steps.

✧ Solve the physical quantity $\bar{\boldsymbol{q}}$ on inlet and outlet boundary.

✧ Solve the fluctuation quantity by $\tilde{\boldsymbol{q}} = \boldsymbol{q}_{inter} - \bar{\boldsymbol{q}}$, where $\boldsymbol{q}_{inter}$ is the boundary inside quantity.

✧ Substitute into eqn.(3.81) where the coefficient matrix uses $\bar{\boldsymbol{q}}$.

✧ Set c_1, c_2, c_3 on inlet boundary and c_4 on outlet boundary to be 0. And use the extrapolation values as eigenvalues.

✧ Substitute $c_1 \sim c_4$ into eqn.(3.82) to solve the fluctuation quantity $\tilde{\boldsymbol{q}}$. Finally, the boundary values are updated by $\boldsymbol{q} = \bar{\boldsymbol{q}} + \tilde{\boldsymbol{q}}$.

(3) <u>Wall Boundary Condition</u>

The wall boundary conditions can be divided into steady/unsteady and viscous/nonviscous conditions. The non-slip condition is appropriate for viscous calculation, while the slip condition is used for nonviscous calculation. In this study, all the walls are set as non-slip condition for 3D cascade calculation, while the slip condition is used in the spanwise boundaries for 2D wind tunnel calculation.

✧ Non-slip adiabatic & static wall

In the static cascade calculation, the wall velocity is set to 0 which is the Dirichlet boundary condition; temperature and pressure are extrapolated from neighbored cells.

$$\boldsymbol{V}_{wall} = \begin{bmatrix} u_{wall} \\ v_{wall} \\ w_{wall} \end{bmatrix} = \begin{bmatrix} 0 \\ 0 \\ 0 \end{bmatrix} \tag{3.83}$$

$$[u \quad v \quad w \quad T \quad p]^T = [u_{wall} \quad v_{wall} \quad w_{wall} \quad T_{extrap} \quad p_{extrap}]^T \tag{3.84}$$

✧ Non-slip adiabatic & moving wall

For the oscillating blade cases, the moving velocity of blade wall is calculated as eqn.(3.85).

$$\boldsymbol{V}_{wall} = \begin{bmatrix} u_{wall} \\ v_{wall} \\ w_{wall} \end{bmatrix} = \begin{bmatrix} \xi_x & \xi_y & \xi_z \\ \eta_x & \eta_y & \eta_z \\ \zeta_x & \zeta_y & \zeta_z \end{bmatrix}^{-1} \begin{bmatrix} -\xi_t \\ -\eta_t \\ -\zeta_t \end{bmatrix} \tag{3.85}$$

✧ Slip wall

On the slip wall, the vertical component of velocity is 0. By defining normal vector of the wall $\boldsymbol{n}$, the velocity y slip wall boundary can be calculated as eqn.(3.86). $\boldsymbol{V}_{wall}$ is the same as

eqn.(3.83) or eqn.(3.85). The boundary condition is given by eqn.(3.87).

$$\boldsymbol{V_{slip}} = \boldsymbol{V_{extrap}} - \{(\boldsymbol{V_{extrap}} - \boldsymbol{V_{wall}}) \cdot \boldsymbol{n}\}\boldsymbol{n} \tag{3.86}$$

$$[\boldsymbol{u} \quad \boldsymbol{v} \quad \boldsymbol{w} \quad \boldsymbol{T} \quad \boldsymbol{p}]^{\boldsymbol{T}} = [\boldsymbol{u_{slip}} \quad \boldsymbol{v_{slip}} \quad \boldsymbol{w_{slip}} \quad \boldsymbol{T_{extrap}} \quad \boldsymbol{p_{extrap}}]^{\boldsymbol{T}} \tag{3.87}$$

(4) Inter-block Boundary Condition and Periodic Boundary Condition

The structured grid with good orthogonality is made for only one blade flow passage with multi-block structure (H-O-H topology). The inter-block boundary surfaces of 2 adjacent blocks are with same grid points and connected with each other. Also, in pitchwise direction, the upper boundary and lower boundary are with same grid distribution at a distance of one pitch length. The periodic boundary condition is applied on pitchwise boundaries to realize infinite periodic cascade.

The inter-block boundary condition or periodic boundary condition is calculated by averaging the physical quantities in the corresponding cells.

3.4 Computational Grid

The 3D grid with tip clearance is used for CFD computation which is shown in Figure 3.5. The main flow region uses an H-O-H type gird, and the tip clearance region is divided into 3 parts. Total grid number is about 1.6 million for one blade passage. The detailed grid number distribution is written in Table 3.2. When doing unsteady computation for oscillating, periodic 11 blade passages were adopted based on influence coefficient method.

Table 3.2 Computational grid number distribution

Zone	I	J	K	Total number
1	25	58	99	143550
2	281	40	69	775560
3	25	58	99	143550
4	281	40	31	348440
5	281	11	31	95821
6	113	29	31	101587
Sum				1608508

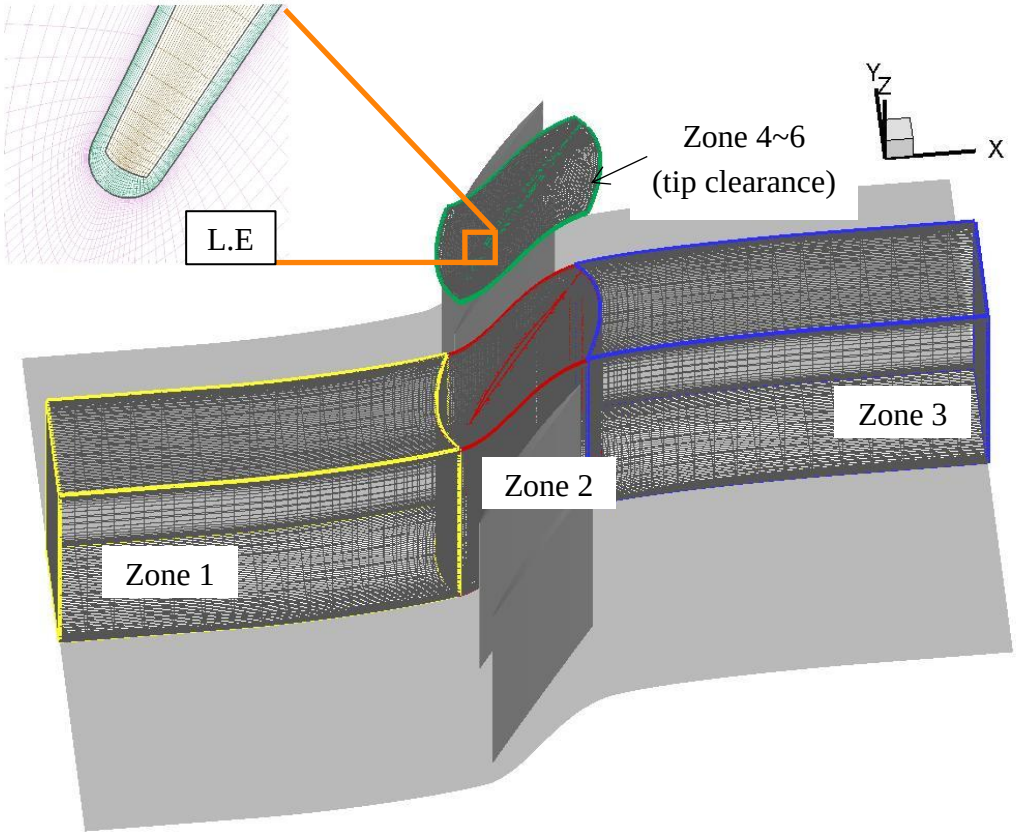

Figure 3.5 Computational grid

Chapter 4 Results and Discussions of Steady Flow Field

4.1 Overview

This chapter is aimed at illustrating the steady flow field inside the transonic compressor cascade with different shock pattern, which is considered the premise of unsteady phenomena analysis on the oscillating cascade. Both experimental measurements and CFD calculations were conducted. Schlieren and oil flow methods were applied to visualize the flow field of the test cascade, while pressure taps and strain gauges were used to collect the data of surface pressure at blade mid-span and aerodynamic force. The spatial pressure distribution on blade surface was obtained by PSP measurement. Furthermore, CFD works were conducted to help understanding more flow details.

4.2 Experimental Condition and Wind Tunnel Characteristics

4.2.1 Experimental Condition

The experimental condition is shown in Table 4.1. For investigating the steady flow field under different working condition, the pressure ratio was adjusted in the range of 1.15~1.45 (also including detached shock case) by adjusting static pressure ratio, while the inlet Mach number kept the same except detached shock case.

Table 4.1 Experimental condition

Total pressure	160	[kPa]
Total temperature	293	[K]
Inlet Mach number	1.2	
Reynolds number	1.2×10^6	
Angle of incidence	0	[deg]
Static pressure ratio	1.15~1.45	

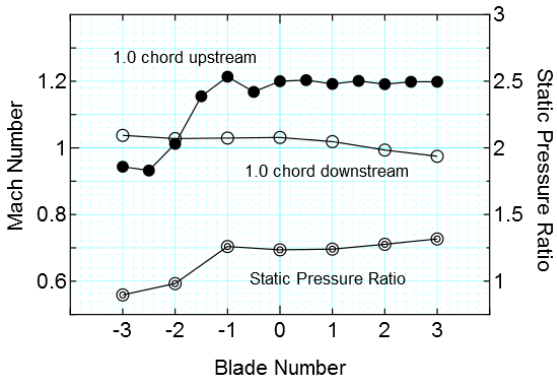

Figure 4.1 Mach number and pressure ratio distribution

4.2.2 Uniformity of Test Cascade

Uniformity of test cascade was investigated by inlet and outlet isentropic Mach number distribution, as shown in Figure 4.1. The uniformity of central 3 blades are considered to be satisfactory with similar inlet and outlet flow field. Besides, the visualization by schlieren and oil flow methods also helped understanding the uniformity of cascade which is explained in Section 4.3.

However, a subsonic zone was found in the upstream of upper blades which can be seen more clearly in Figure 4.2. The reason was desired to be clarified for future wind tunnel improvement and the detailed analysis by experimental approaches and 2D RANS simulation for whole wind

tunnel structure based on overset grid method is introduced in Appendix B.

In a brief summary, an all-span normal shock wave exists in the rear of the nozzle with Mach number around 1.4. The flow after the shock wave becomes subsonic and then is reaccelerated by the expansion wave generated from the suction side of blade -3 which helps forming the downstream periodic inlet flow. The total pressure loss occurs due to the nozzle shock wave and is evaluated by the following formula of total pressure ratio. The corrected Mach number at measuring point of test cascade is about 1.17.

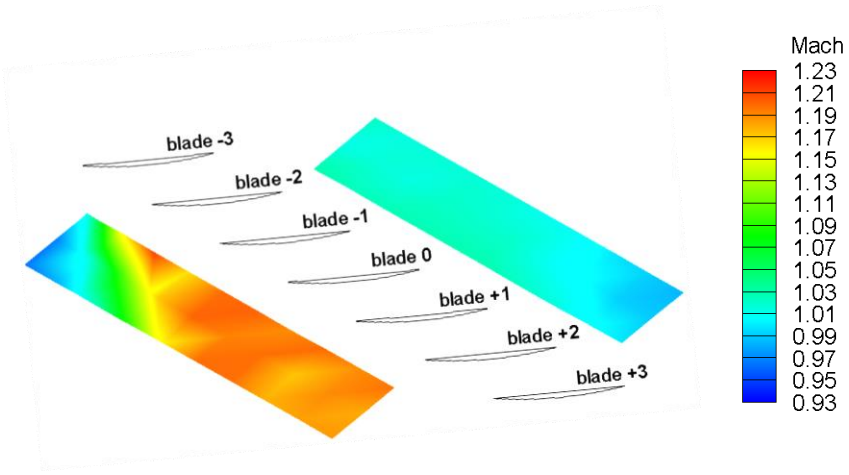

Figure 4.2 Isentropic Mach number distribution at test section

$$\delta = \frac{P_2^*}{P_1^*} = \frac{\left[\frac{(\gamma+1)\times Ma_1^2}{2+(\gamma-1)\times Ma_1^2}\right]^{\frac{\gamma}{\gamma-1}}}{\left[\frac{2\gamma}{\gamma+1}\times Ma_1^2 - \frac{\gamma-1}{\gamma+1}\right]^{\frac{1}{\gamma-1}}} \approx 0.9582 \tag{4.1}$$

4.3 Visualization of Transonic Flow Field with Shock Waves

4.3.1 Shock Pattern

Schlieren visualization method is effective for detecting the flow field with shock waves in transonic cascade [50][51]. In using this method, different flow information can be extracted by adjusting the relative angle of the knife edge. In current experiment, as shown in Figure 4.3(a), by putting the knife edge in horizontal direction, the density gradient in flow direction can be seen more clearly, such as inlet flow, wake and blade surface separation. The inlet boundary layer thickness of bottom wall can be obtained by identifying the black zone of inlet flow and white zone of boundary layer. As shown in Figure 4.3(b), when putting knife edge in vertical direction, the vertical information can be seen more clearly, such as shock waves and expansion waves. In current research, by considering that the shock waves are the focused flow phenomena, the photos were mainly taken by putting the knight edge into vertical direction.

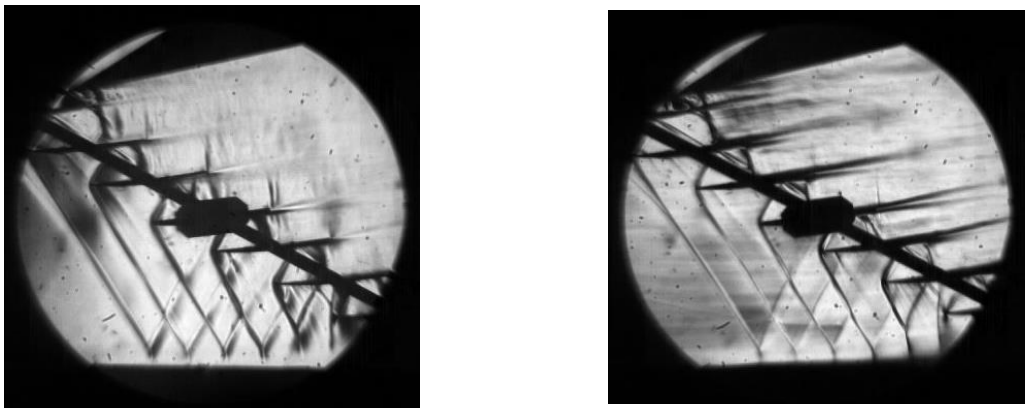

(a) Vertical knife edge (b) Horizontal knife edge

Figure 4.3 Schlieren photos with different knife edge direction (P.R.=1.25)

Figure 4.4 shows the shock patterns visualized by schlieren photos, density gradient counters and Mach number counters at mid-span obtained by CFD. Both results have good accordance with each other and tell the flow pattern in mid-span of the cascade.

In lower pressure ratio range (P.R.=1.15~1.35), there are two shock waves can be seen in the inter blade passage, where one is the incidence oblique from blade leading edge in the upstream, and the other is a normal passage shock in the downstream. The oblique shock wave also has an external branch towards downstream blades which helps forming the periodic inflow. With the increasing of given pressure ratio, the passage shock wave moves upstream and the oblique shock wave keeps in same angle and location before detached. The oblique shock wave is reflected by the suction side of upstream blade and the reflected wave will touch blade pressure side when the interval between the two shock waves is enough. As to the passage shock, its feet on both suction side and pressure side are in a λ shape which is more obvious under lower P.R..

In higher pressure ratio range (1.35~detach), the oblique shock foot and passage shock foot on suction side of the upstream blade merge with each other gradually. This phenomenon continues until reaching the peak pressure ratio which is around 1.44. When the back pressure continues to be increased, the inlet Mach number decreases drastically and oblique shock wave detaches from blade leading edge. The shock angle becomes larger and finally evolves into a detached normal shock which is almost perpendicular to the chordwise direction. In detached shock conditions, the P.R. cannot be used to evaluate the cases due to the change of inlet static pressure.

Besides, in low P.R. range (P.R.=1.15~1.25), an expansion wave can be observed which is generated form blade trailing edge towards upstream blade outlet. The expansion wave becomes short and finally disappears with P.R. increasing.

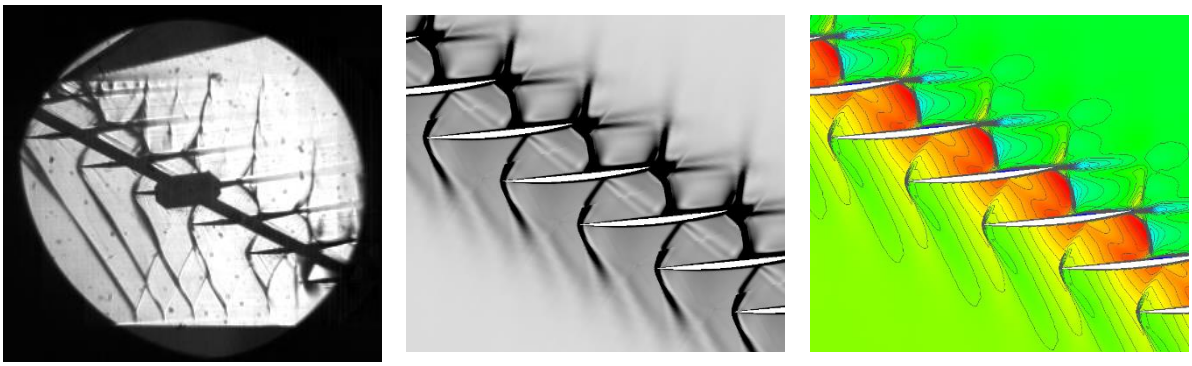

(a) P.R.=1.15

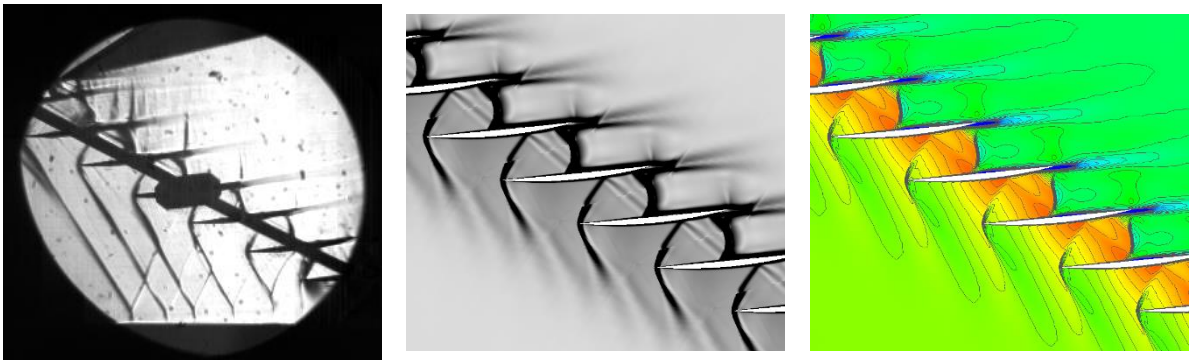

(b) P.R.=1.25

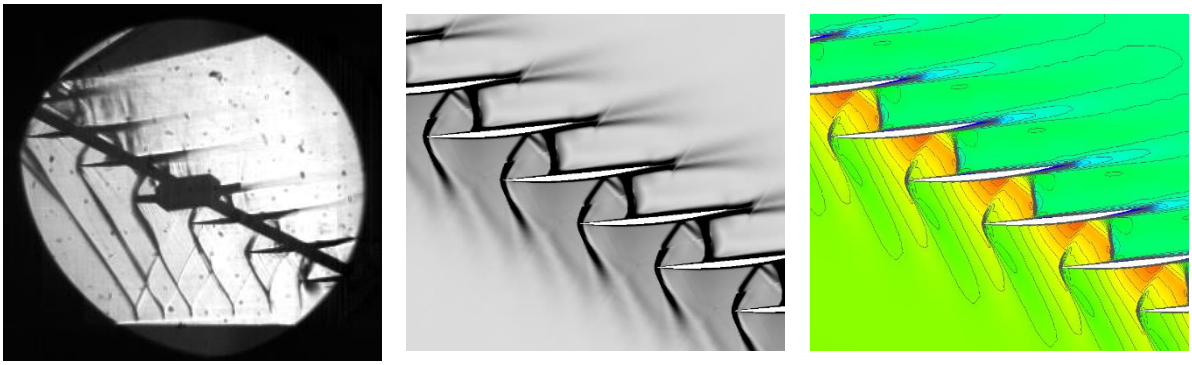

(c) P.R.=1.35

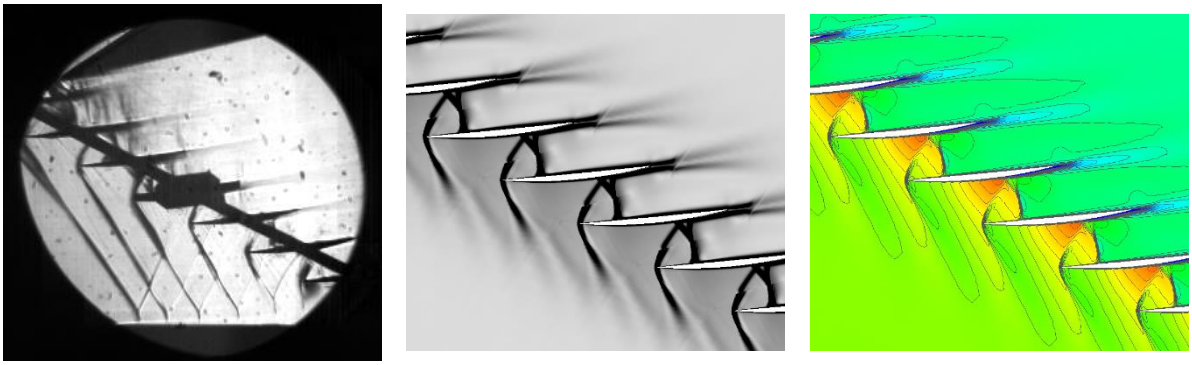

(d) P.R.=1.40

(e) Detached shock

From left: Schlieren photo, density gradient counter (CFD), Mach number counter (CFD)

Figure 4.4 Shock pattern visualization

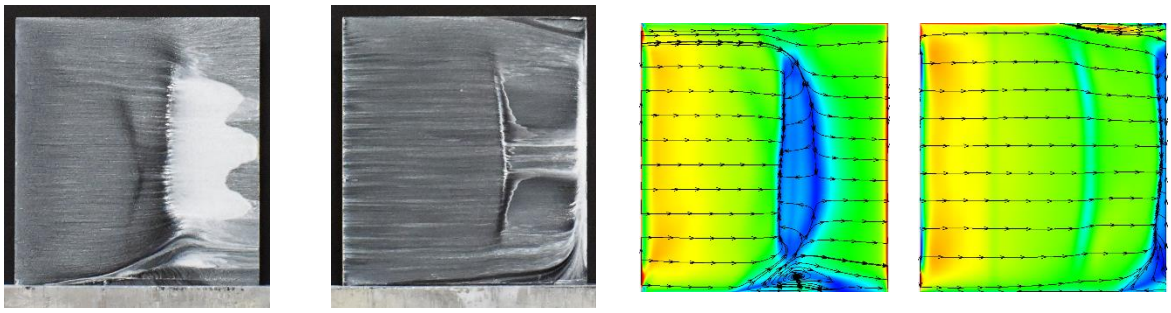

(a) P.R.=1.15

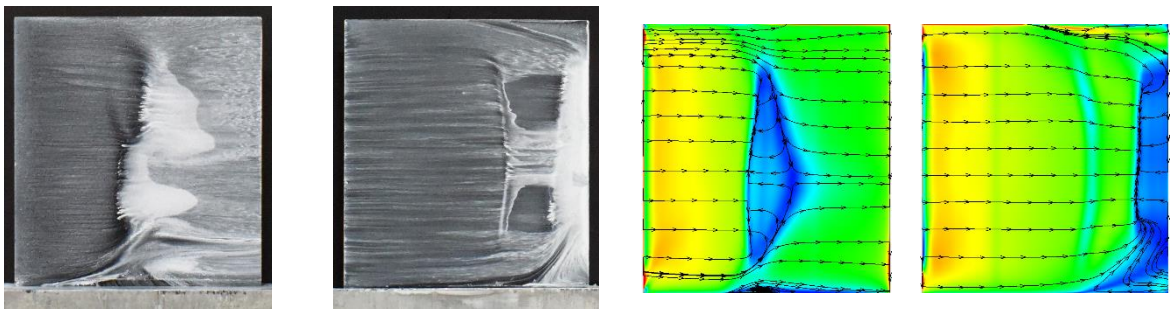

(b) P.R.=1.25

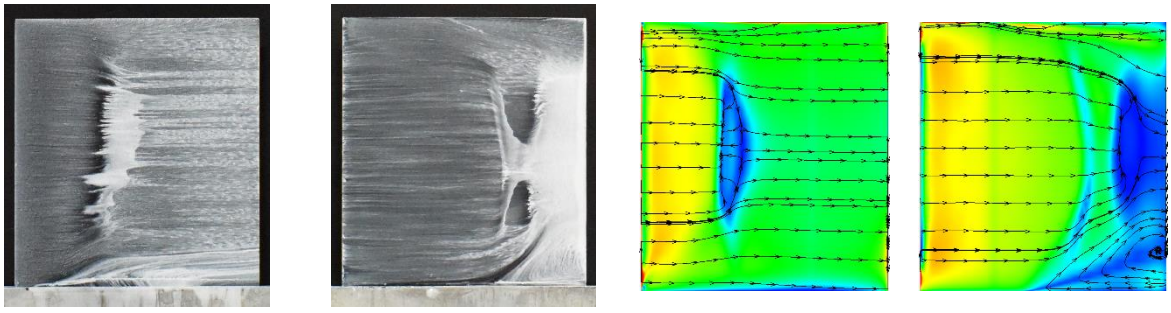

(c) P.R.=1.35

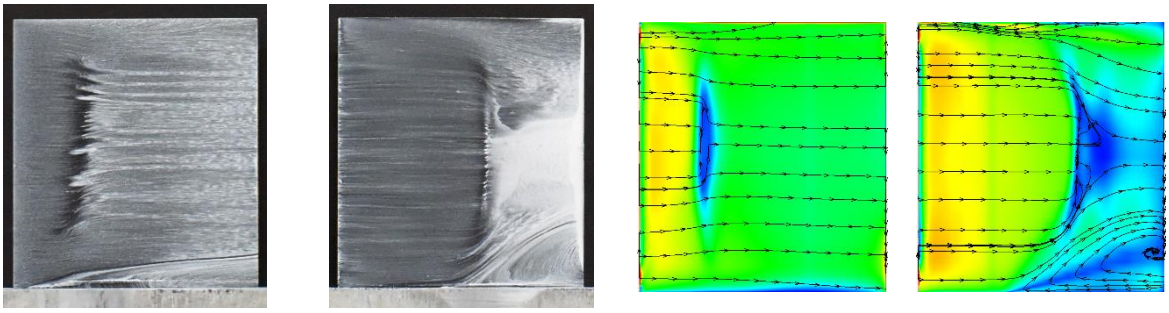

(d) P.R.=1.40

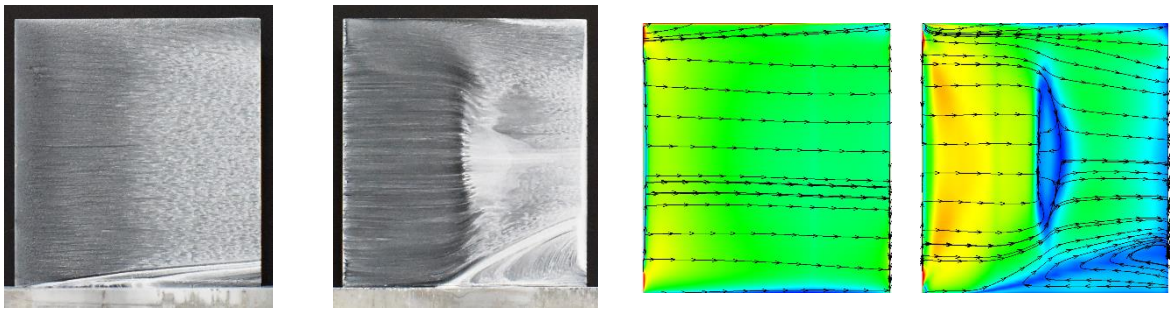

(e) Detached shock

From left: P.S./S.S. Oil flow photos, P.S./S.S. velocity counters with streamlines (CFD)

Figure 4.5 Blade surface limiting streamlines

(a) -1 P.S. (b) 0 P.S. (c) +1 P.S.

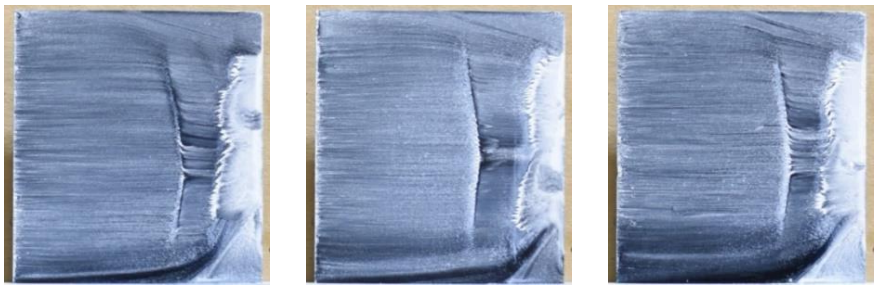

(d) -1 S.S. (e) 0 S.S. (f) +1 S.S.

Figure 4.6 Oil flow photos of 3 central blade (P.R.=1.25)

4.3.2 Flow Pattern on Blade Surface

As the flow structure at blade middle span was already known, the shock feet and flow separation pattern can be observed on blade surface by oil flow method. Figure 4.5 shows oil flow photos and also the velocity counter with surface streamlines obtained by CFD. The results have good correlation with above explained shock patterns.

For verifying cascade periodicity, oil flow experiment was also conducted on the neighbor blades under P.R.=1.25. As shown in Figure 4.6, the results show a similar flow pattern on each blade. Corresponding CFD results in Figure 4.5 also show the same trend. As shown in the surface velocity counters with limiting streamlines, the areas with more oil residual are also with lower velocity.

(1) Oblique Shock Foot on S.S. & Reflected Wave Foot on P.S.

The oblique shock foot can only be seen on the suction side in lower pressure ratio range (P.R.=1.15~1.35), with a shape of thin and curved separation line. The separation line located at 60~70% in chordwise direction and 20~80% in spanwise direction. The reason for shock wave curving is considered the influence of wall boundary layer development in flow direction. Also, the reflected wave foot can be seen on pressure side under P.R.=1.15 with similar shape and length as the oblique shock foot, while this foot is with no oil residual and high velocity. At P.R.=.1.25, only the upper part of the reflected wave foot can be seen.

(2) Passage Shock Feet on P.S. and S.S.

The passage shock feet can be observed on suction side in all P.R. range and also be observed on pressure side except detached shock case. The large separation area appears from the passage shock foot to the trailing edge on suction side, while the flow reattaches to the blade surface after separation area on pressure side. Under detached shock condition, the shock foot on pressure side disappears.

With P.R. increasing, the passage shock wave moves upstream and interacts with the oblique shock wave. Passage shock foot merges with oblique shock foot on suction side at middle span firstly, and finally in all span range. This merged shock foot is straight in spanwise direction which is considered as a stronger normal shock wave. It has a corresponding total developed separation zone until trailing edge on suction side.

On pressure side, the separation area following the passage shock foot is quite larger at lower P.R. range than higher P.R. This phenomenon is clarified by seeing the counters of Mach number and pressure at middle span as shown in Figure 4.7. Under low pressure ratio, the Mach number is larger and cause a larger flow separation near blade surface. The interaction between shock wave and separation makes the shock foot to form a λ shape. Under high pressure ratio, shock wave becomes weak and separation is suppressed with the shock foot becoming straight and narrower. Furthermore, the corresponding pressure counters shows wider pressurization area at lower pressure ratio. So, these oil residuals can be understood as the separation induced by shock wave with λ shape foot.

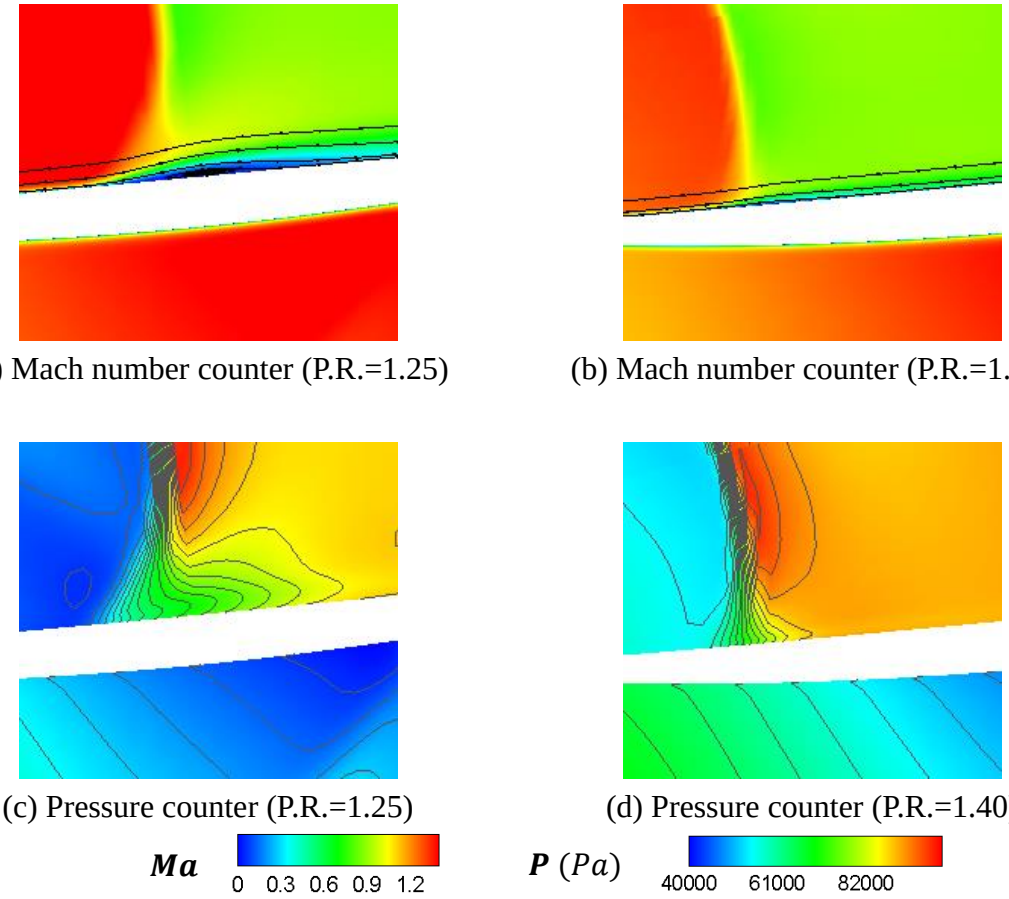

(a) Mach number counter (P.R.=1.25) (b) Mach number counter (P.R.=1.40)

(c) Pressure counter (P.R.=1.25) (d) Pressure counter (P.R.=1.40)

Figure 4.7 Mach number and pressure counters at middle span

(3) 3D Effects on Flow Pattern

Furthermore, the 3D effects can also be found which is caused by the side walls. The hub side corner separation and tip leakage flow shorten the spanwise length of passage shock foot on blade surface. With the increase of pressure ratio, the corner separation has a tendency to become larger towards upstream direction on suction side, while pressure side hub separation becomes weaker. The start point of tip side flow leakage moves towards upstream direction and the influence area becomes larger with P.R. increase.

In a brief summary, the three dimensional shock wave shape can be understood. The oblique shock wave is with a curved surface in spanwise direction and followed by a reflected wave. Passage shock wave is a normal shock wave with λ shape feet near blade surface. In spanwise direction, the shock waves are shorten by the development of boundary layer, corner separation and tip leakage flow.

4.4 Steady Aerodynamic Force and Surface Pressure Acting on Blade

4.4.1 Steady Aerodynamic Force

To grasp the steady aerodynamic force acting on blade and validate the performance of steady pressure measurement by PSP, the aerodynamic force was measured by both strain gauge and PSP. Figure 4.8 shows the comparisons of the results. The force obtained by PSP was the integrating value of the pressure on the blade surface. The forces were normalized into aerodynamic force coefficient C_F. All results agree well each other. Figure 4.9 shows C_F variation with pressure ratio change. Both experimental and numerical results show almost linear increasing of aerodynamic force coefficient with P.R..

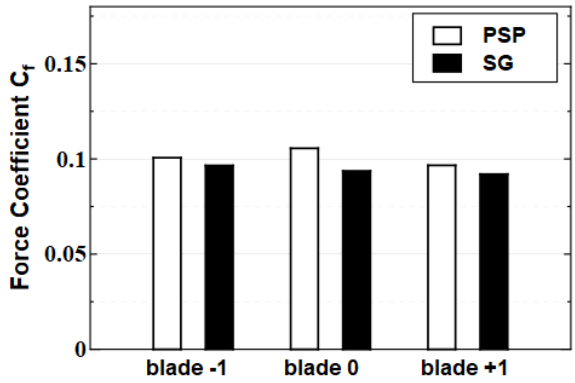

Figure 4.8 Aerodynamic force coefficient comparison of different blades (P.R.=1.25)

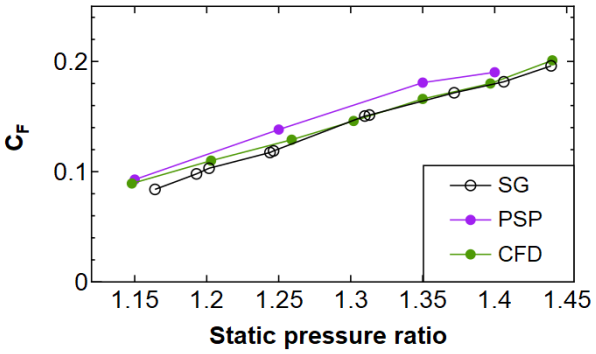

Figure 4.9 Aerodynamic force coefficient variation with pressure ratio

4.4.2 Steady Surface Pressure Distribution

Based on the understanding of the flow structure inside blade passage, the steady pressure acted on blade surface by the flow is analyzed here. The pressure coefficient (C_P) distribution at blade mid-span was measured by pressure transducers. Then, the 2D spatial C_P distributions were also captured by PSP and CFD. As shown in Figure 4.10 and Figure 4.11, the results obtained by pressure taps, PSP and CFD have good agreements with each other.

On P.S., under not-detached condition, the pressure decreasing which is almost linear can be seen in chordwise direction from leading edge to the passage shock wave area. Then, the large pressure rising occurs at the passage shock wave area.

In lower P.R. range (P.R.=1.15~1.25), the large λ foot of passage shock wave expand the pressurization area in chordwise direction, so that the pressure increases in two stages, a steep stage and a gradual stage. After the pressurization area, pressure decreases gradually from maximum value until the trailing edge which is caused by the expansion wave at blade trailing edge.

In higher P.R. range (P.R.=1.35~1.40), the pressurization area becomes narrower and only one steep stage can be seen. After the shock wave, it keeps an almost constant high pressure until the trailing edge.

As to under detached shock condition, the shock wave detaches from the leading edge and shock foot only touches blade suction side, the pressure side keeps high pressure in chordwise direction with no large pressure change.

On S.S., the pressure decreases linearly chordwise direction from leading edge to the first shock wave area. In lower P.R. range (P.R.=1.15~1.25), there are two low pressure areas with downstream pressure increase induced by oblique shock wave and passage shock wave. The pressure decreases at the interval between the two shock waves. In this range, the first low pressure area keeps almost the same, while the second low pressure area is narrowed by movement of passage shock and shortened by enlargement of corner separation and tip clearance flow with P.R. increase.

With P.R. increase, the second low pressure area becomes smaller and finally disappears. Then, two shock waves merge with each other and the merged shock wave moves towards upstream direction with the first low pressure area becoming smaller.

Even though the current blade is with a 2D profile, the pressure distribution still have spanwise discrepancy owing to the development of side wall boundary layer, corner separation and tip clearance flow. With the increasing of pressure ratio, the corner separation and tip clearance flow become larger towards upstream direction and influence on the upstream low pressure areas. On suction side, corner separation shortens and weakens the second low pressure area firstly, and afterwards the first low pressure area. As to the tip side, the impact of tip clearance flow on pressure distribution is weaker than hub side in pushing the low pressure area towards upstream direction.

From the above results on aerodynamic force and surface pressure distribution, the current PSP technique was considered effective and reliable for the quantitative measurement of steady flow field.

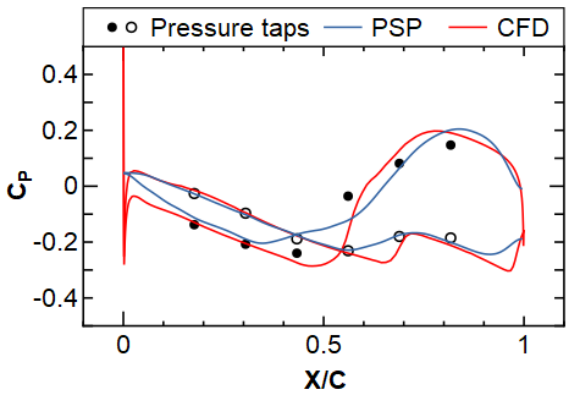

(a) P.R.=1.15

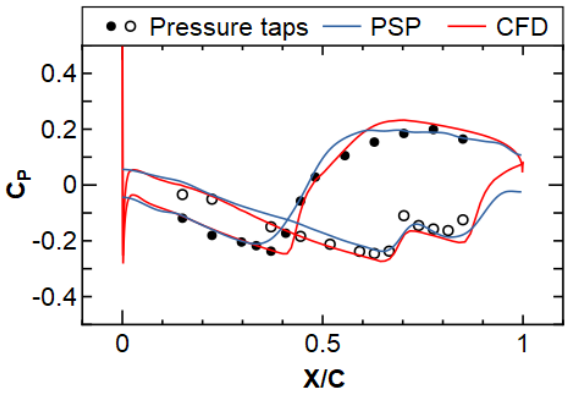

(b) P.R.=1.25

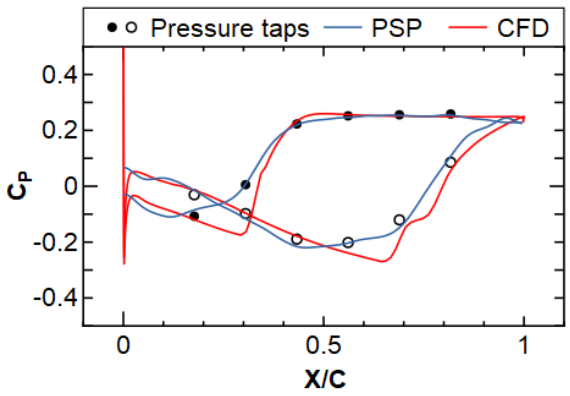

(c) P.R.=1.35

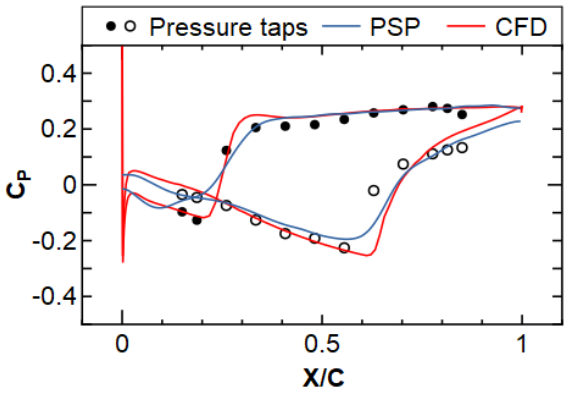

(d) P.R.=1.40

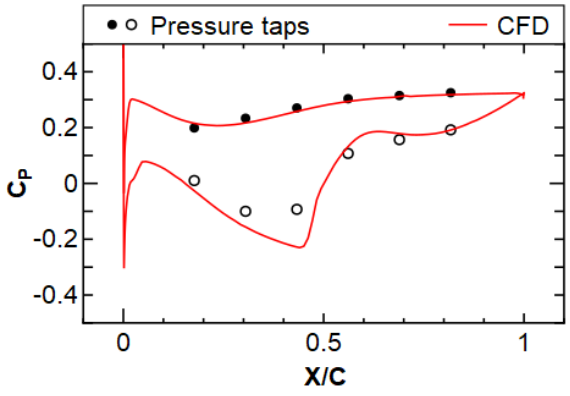

(e) Detached shock

Figure 4.10 Mid-span pressure coefficient distribution

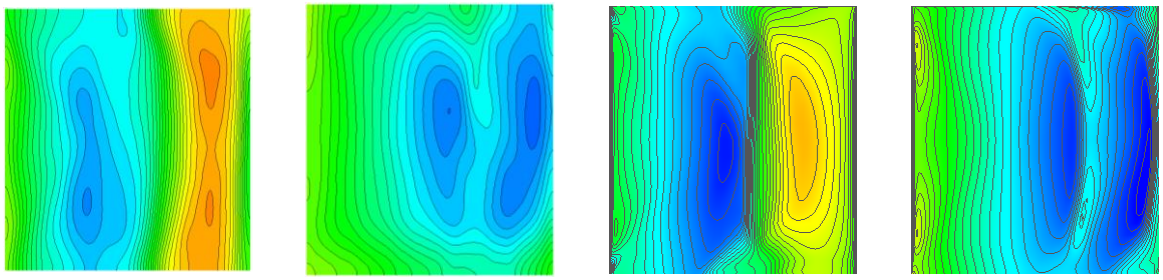

(a) P.R.=1.15

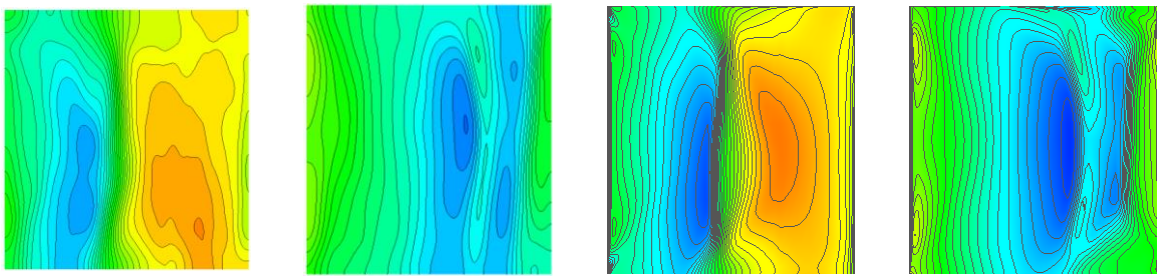

(b) P.R.=1.25

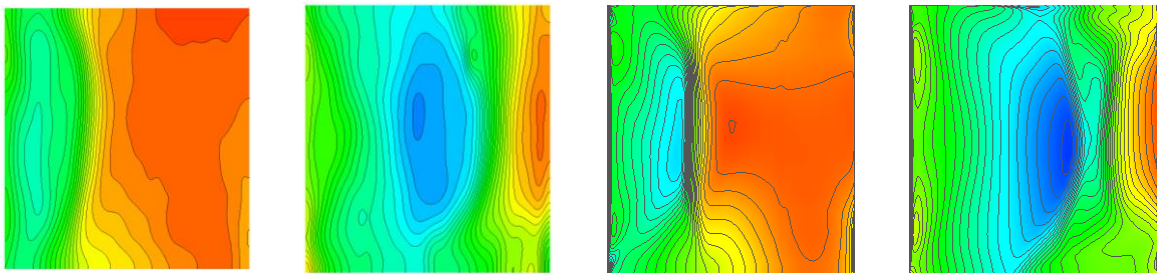

(c) P.R.=1.35

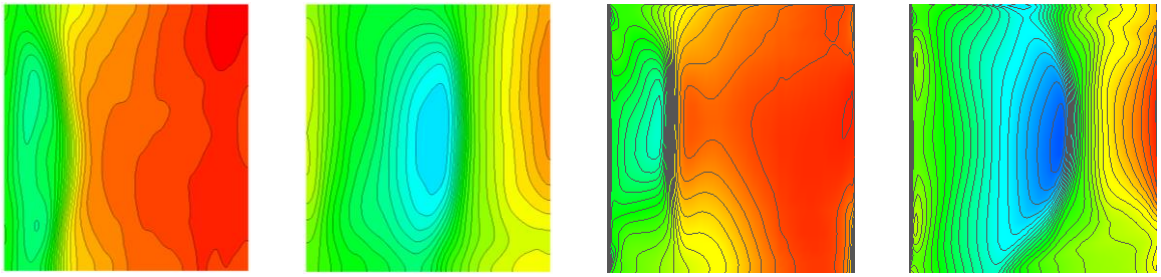

(d) P.R.=1.40

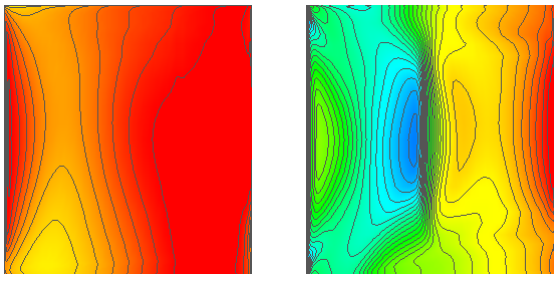

(e) Detached shock

From left: P.S./S.S. C_P (PSP), P.S./S.S. pressure coefficient C_P (CFD)

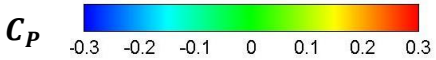

Figure 4.11 Blade surface limiting streamlines

4.5 Flow Characteristics and Shock Pattern Classification

4.5.1 Flow Characteristic Curve

Based on the above results, the current CFD technique was considered to be effective in evaluating the steady flow field and surface pressure under various flow conditions. Experimental measurement is relatively costly and limiting than CFD computation. So, more interval operation points were calculated by CFD method.

Current cascade with DCA profile was used to simulate flow field of rotor blade in relative velocity condition. So, even though the experimental object is a static linear compressor cascade, the graph like a compressor characteristic curve is used to illustrate the relationship between static pressure ratio and mass flowrate, as shown in Figure 4.12. The horizontal axis indicates the axial mass flowrate in one blade passage and the vertical axis indicates the static pressure ratio for evaluating the pressurization capability of the linear compressor cascade.

With P.R. decrease under non-detached condition, the axial mass flowrate increases rapidly at first until pressure ratio 1.35. Then it decreases slowly and finally converges to be stable at the choked mass flowrate. If the back pressure continues to be increased from the maximum pressure ratio condition, the inlet Mach number will decrease corresponding to the detaching of oblique shock wave from blade leading edge. In such condition, the parameter P.R. cannot be used to evaluate the flow condition and the ratio of back pressure and inlet total pressure P_{out}/P_{in}^{*} was used.

4.5.2 Inlet and Outlet Flow Condition

For the supersonic and high subsonic flow, the flow angle is difficult to be measured experimentally. Therefore, based on the verified CFD method, the inlet and outlet flow angle were analyzed. Figure 4.13 shows pitchwise Mach number distribution at middle span of the 1.0c upstream and 1.0c downstream. Figure 4.14 shows the corresponding incidence angle at 1.0c upstream and deviation angle at 1.0c downstream.

As the results show, except the detached shock case, the inlet Mach number distribution keeps the same with a peak value around normalized pitchwise position ζ=0.6. The corresponding incidence angle also shows an accordance which is considered as “unique incidence” zone. When the shock detaches, the Mach number decreases at ζ=0.55~1.0 with the incidence increasing. As to the outlet, generally speaking, the Mach number decreases with the pressure ratio increasing. In the choked flow range, a supersonic area appears around ζ=0.7. In the double shock waves range, the deviation angle decreases with the pressure ratio increasing, while the tendency reverses in the merged shock waves range. Finally, the deviation angle converges to about 3.5 degree.

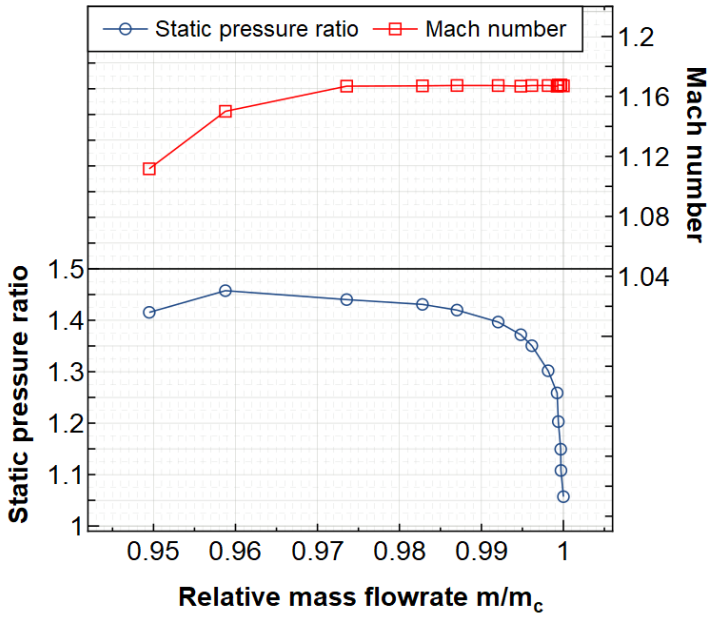

Figure 4.12 Characteristic curve of compressor cascade

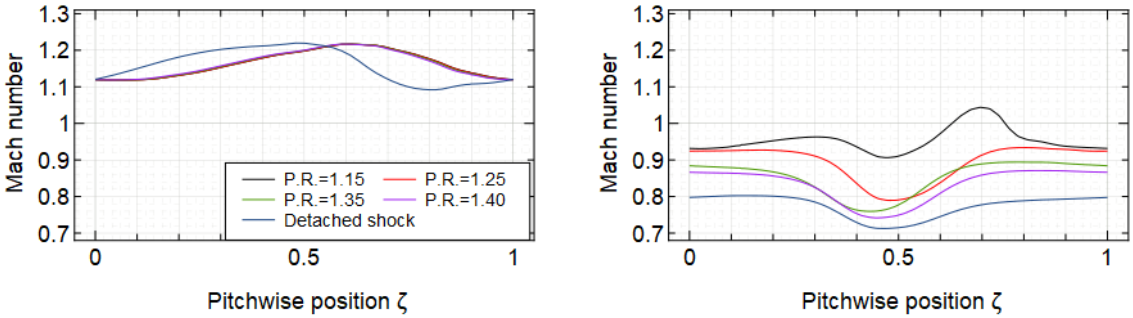

(a) 1.0 *c* upstream (b) 1.0 *c* downstream

Figure 4.13 Pitchwise Mach number distribution at mid-span

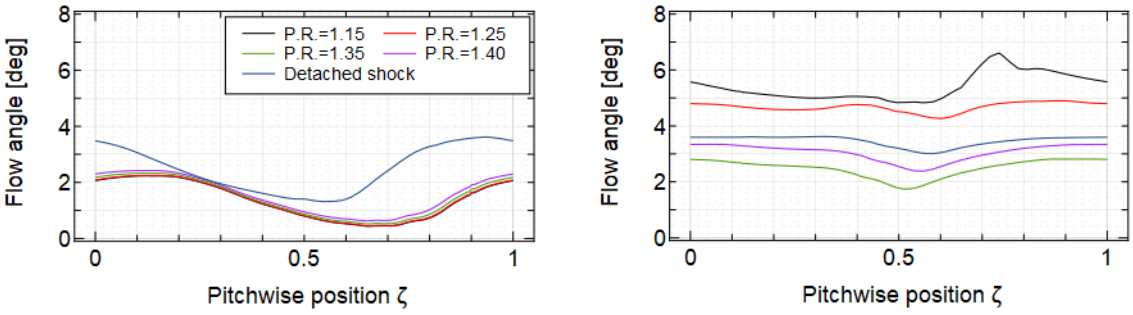

(a) Incidence angle at 1.0 *c* upstream (b) Deviation angle at 1.0 *c* downstream

Figure 4.14 Pitchwise flow angle distribution at mid-span

4.5.3 Shock Pattern Classification

Transonic compressor cascades are under continuous research to satisfy the demands of axial compressor with higher efficiency and stage pressure ratio. In compressor operation, the transonic cascade stage undergoes various operating conditions which are corresponded with different shock pattern. The shock system is the dominant flow phenomenon in transonic cascade by considering that it is of great importance on performance of both energy loss and pressurization capability [52]. The major losses are shock losses with related viscous losses from shock-boundary layer interaction and most of the static pressure rise are achieved by the shock system. Therefore, for understanding the cascade stability and flutter phenomena, the shock wave configuration under different pressure ratio should be interpreted in advance.

Based on above results, the evolution of shock pattern with P.R. change in current transonic compressor cascade can be summarized here. Figure 4.15 shows the shock waves configurations under more operating points, which are illustrated by mid-span density gradient. The range of pressure ratio can be divided into several parts and the shock pattern in each part has different characteristic. The shock pattern evolution with the pressure ratio increasing and corresponding pressure ratio range are shown in Figure 4.16 and Table 4.2. The classification is expressed as choked flow pattern, double shocks pattern, merged shocks pattern and detached shock pattern. And the details are described here.

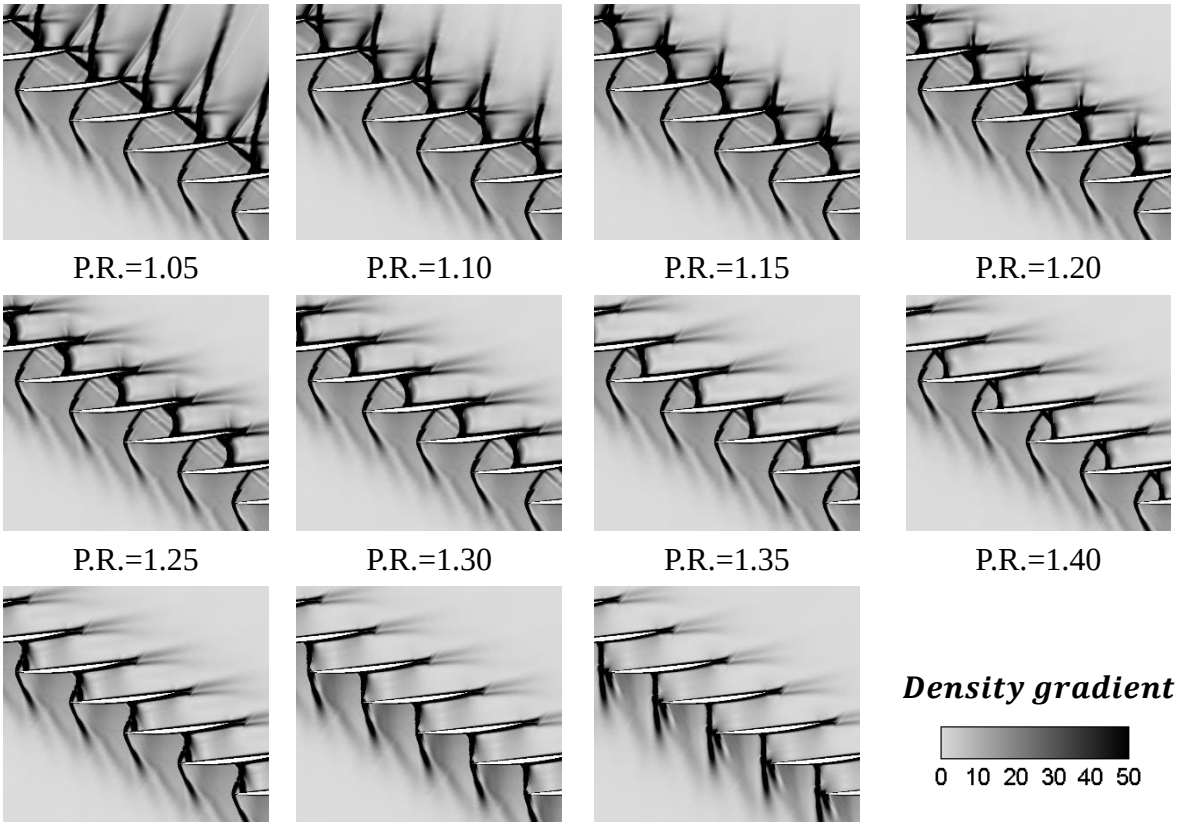

Figure 4.15 Density gradient counter under different operating condition

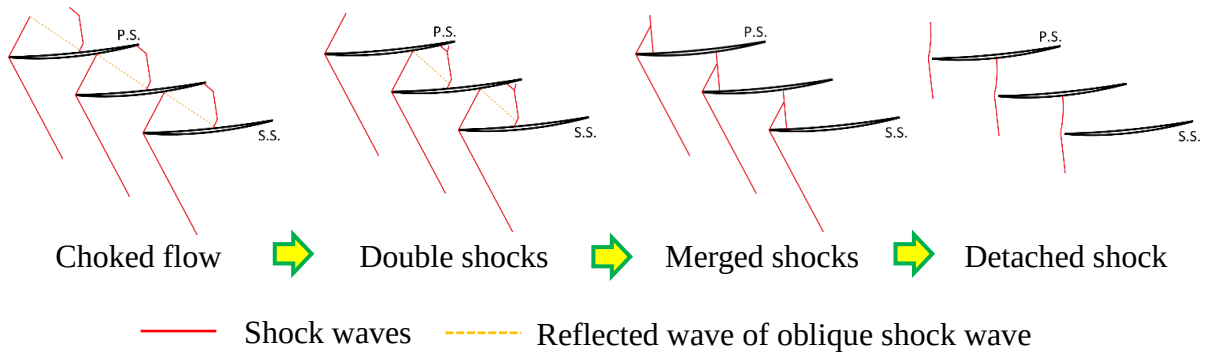

Figure 4.16 Shock pattern classification

Table 4.2 Pressure ratio range of different shock pattern

Shock pattern	**Pressure ratio range**
Choked flow pattern	< 1.15
Double shocks pattern	1.15 ~ 1.40
Merged shocks pattern	1.40 ~ 1.45
Detach shock pattern	Mach number decrease

(1) Choked Flow Pattern & (2) Double Shocks Pattern

The detail of double shocks pattern or choked flow pattern is shown in Figure 4.17. In unique incidence condition, the double shock waves configuration is a common structure in which one oblique shock is located at blade leading edge and one passage shock is located near the trailing edge. The oblique shock wave is reflected by blade suction side. The reflected shock wave intersects with the pressure side of the downstream neighbor blade or the passage wave shock of downstream blade passage. The two feet of passage shock wave on both suction side and pressure side are with a λ shape. At blade trailing edge, an expansion wave appears from pressure side to the wake area in order to balance the static pressure between downstream area of passage shock wave with high pressure and cascade outlet with relatively low back pressure.

With the pressure ratio increasing from the choked flow condition, the inlet Mach number keeps the same and the inlet oblique shock keeps same angle, while the passage shock wave moves upstream and both λ type shock feet become narrower.

(3) Merged Shocks Pattern

Then, with larger P.R., the oblique shock wave and passage shock wave gradually merge with each near the shock foot on suction side, and the trailing edge expansion wave disappears. The detail of merged shocks pattern is shown in Figure 4.18. In the merging process, at first, the angle of oblique shock wave keeps unchanged, while the end of oblique shock wave disappears. It is still under unique incidence condition with the same inlet Mach number. Then, when the degree of mergence is deepened, the passage shock shortens the oblique shock greatly and makes the angle of oblique shock larger with Mach number at inlet measuring point decreasing.

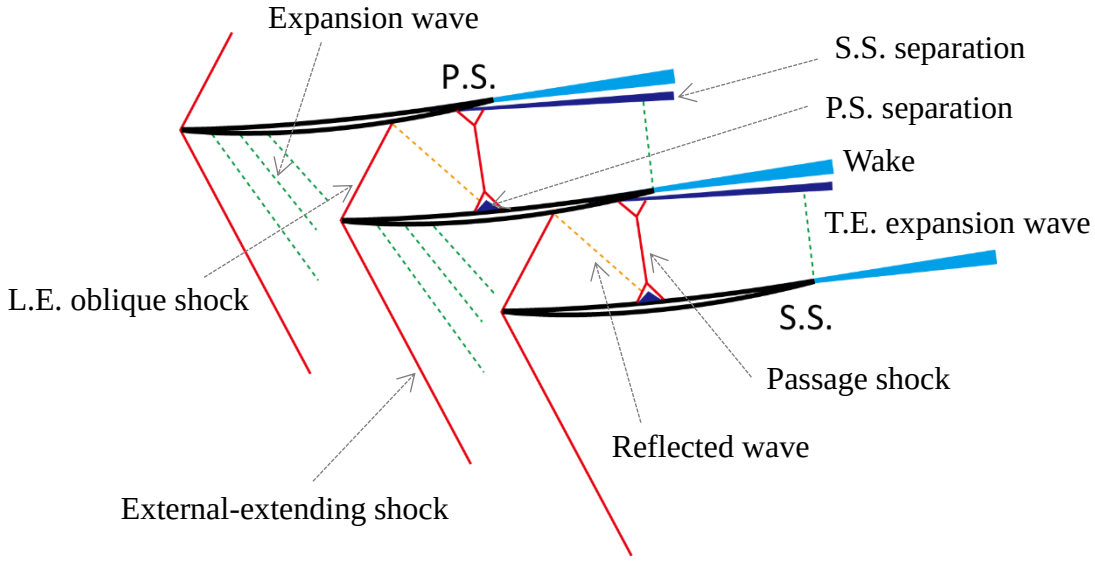

Figure 4.17 Double shocks pattern

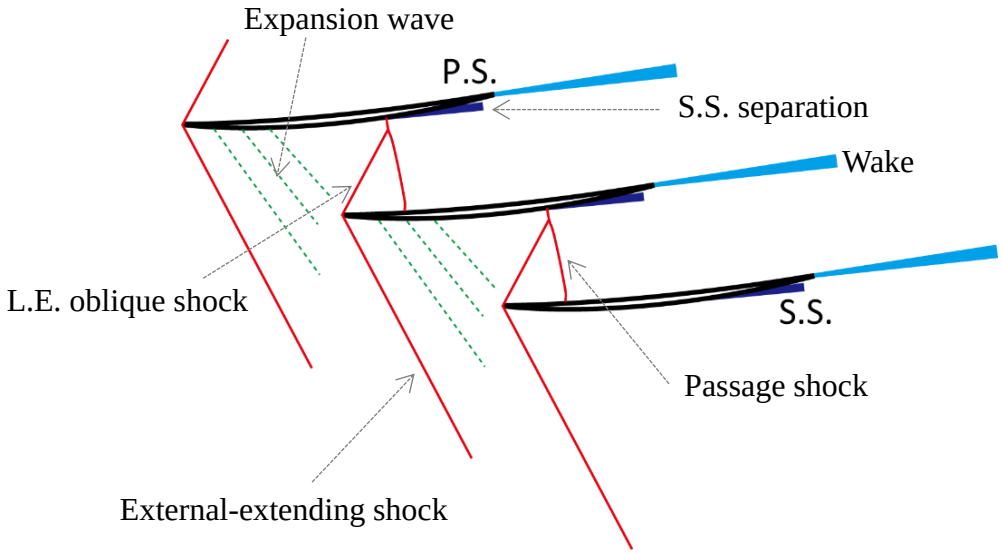

Figure 4.18 Merged shocks pattern

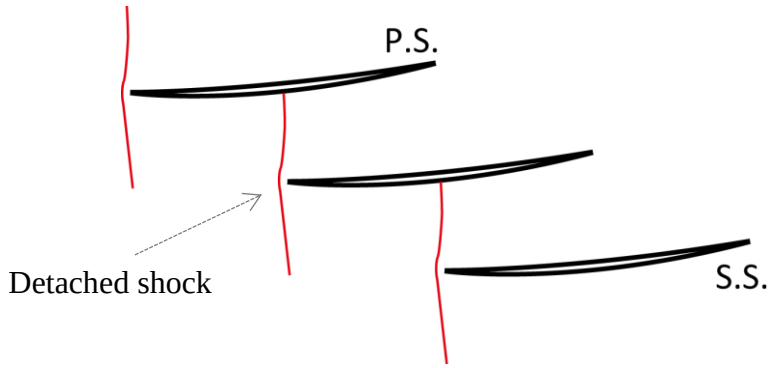

Figure 4.19 Detached shock pattern

(4) Detached Shock Pattern

When the back pressure continues to increase, the shock waves will merge completely into one shock wave and the shock wave detaches from the blade with changing of shock angle. It causes inlet Mach number decreasing. Figure 4.19 shows the detached shock pattern in current cascade. Detached shock wave (also called bow shock or normal shock) is a curved and stationary shock wave forming when supersonic flow past a finite body. The shock detaches from the body when the needed rotation of the fluid exceeds the maximum achievable rotation angle for an oblique attached shock. The downstream of detached shock wave is subsonic and the detached shock wave significantly increases the drag and the flow across the detached shock is non-isentropic.

4.5.4 Shock Wave Evolution Mechanism

(1) Passage Shock Wave

Under double shock pattern, large pressure difference exists between the downstream of passage shock and outlet induces expansion wave near T.E. under lower P.R. range. With increasing of back pressure, more uniform downstream pressure field suppresses the expansion wave, reduces the pressure after passage shock wave, and "push" the shock wave towards upstream direction

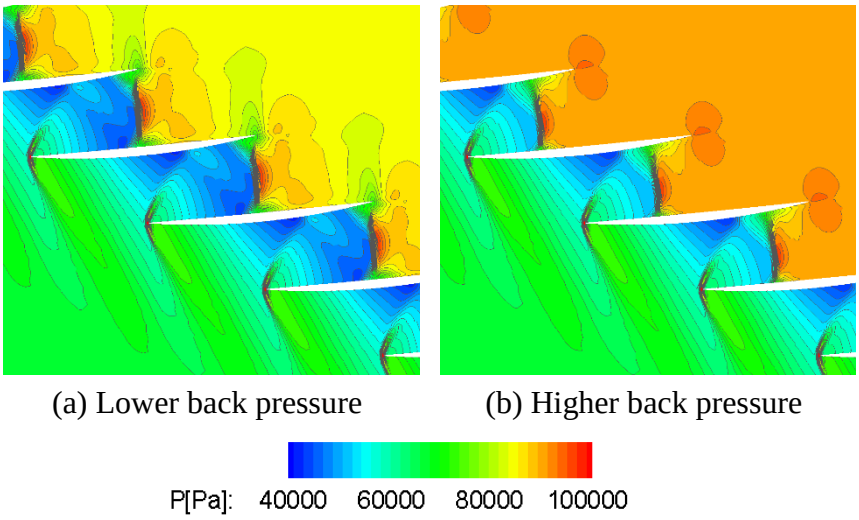

(a) Lower back pressure (b) Higher back pressure

Figure 4.20 Pressure counters with different passage shock wave location

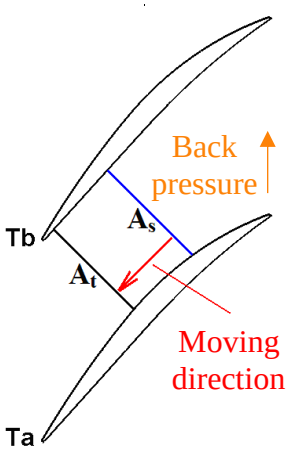

Figure 4.21 Passage shock wave movement

(2) L.E. Oblique Shock Wave

In condition that the L.E. oblique shock wave is merged with downstream passage shock wave and the part near L.E. remains an oblique shape, the downstream of the shock wave is entirely subsonic and back pressure can propagate up to the area just behind oblique shock. Then, the increasing of back pressure induces the increase of pressure difference before and

after the shock wave. Such pressure difference make the shock wave be stronger with shock angle increasing until the shock become normal shock completely and detaches from L.E..

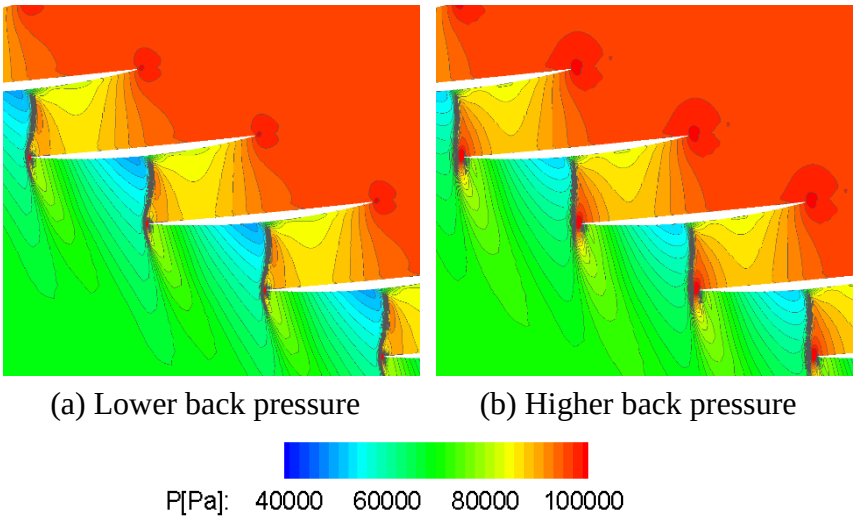

Figure 4.22 Pressure counters with different oblique shock wave location

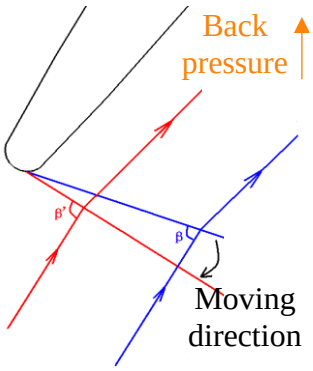

Figure 4.23 Oblique shock wave movement

4.6 Discussions of Steady Flow Field Details

4.6.1 Corner Separation and Tip Leakage Flow

The tip leakage flow and hub corner separation flow is the reason of spanwise asymmetry and the source of total pressure loss near wall. The evolution of tip leakage and corner separation with pressure ratio change is clarified here. Figure 4.24 shows the turbulence kinetic energy distribution on the chordwise cross sections and the 3D streamlines near tip side and hub side.

Under choked flow condition, the tip flow leaks from pressure side to suction side at 0.8~0.9 x/c and the flow is almost along chordwise direction. With the increasing of pressure ratio, the location of flow leakage moves upstream and it enhances the pitchwise component of the flow. The turbulence kinetic energy also shows a pitchwise propagation and contributes to the downstream tip leakage. The pitchwise flow component is considered to be the reason for the expansion of energy and enhance the propagation of pressure fluctuation.

As to the hub side corner separation, it shows larger turbulence kinetic energy level than tip side and is not easy to propagate so as to affect the downstream flow passage. Under choked flow condition, two separation zones can be observed. One appears at 0.5 x/c in pressure side which is caused by the strong passage shock near pressure side. The other appears near the trailing edge in suction side. With pressure ratio increasing, the P.S. separation becomes weaker and the S.S. separation becomes strong.

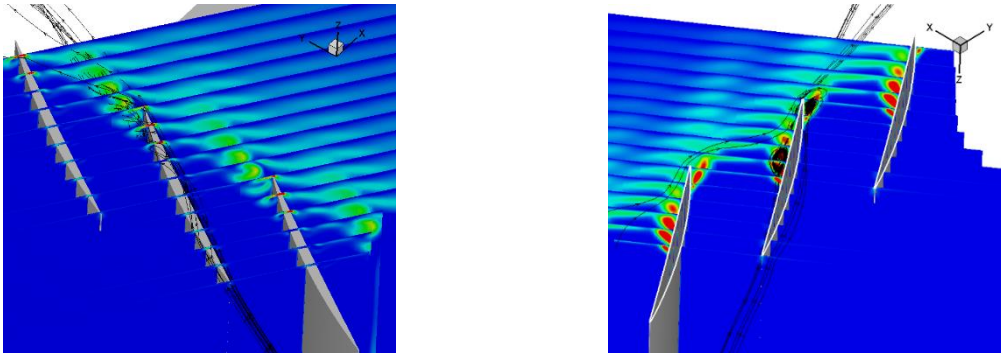

(a) P.R.=1.15 (choked flow)

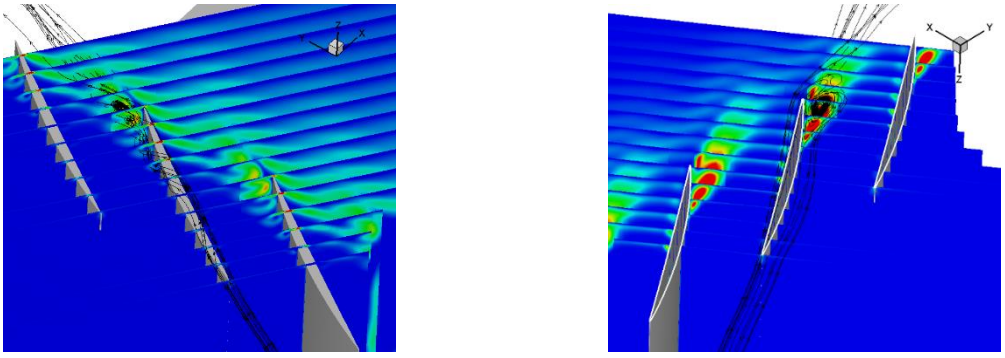

(b) P.R.=1.25 (double shocks)

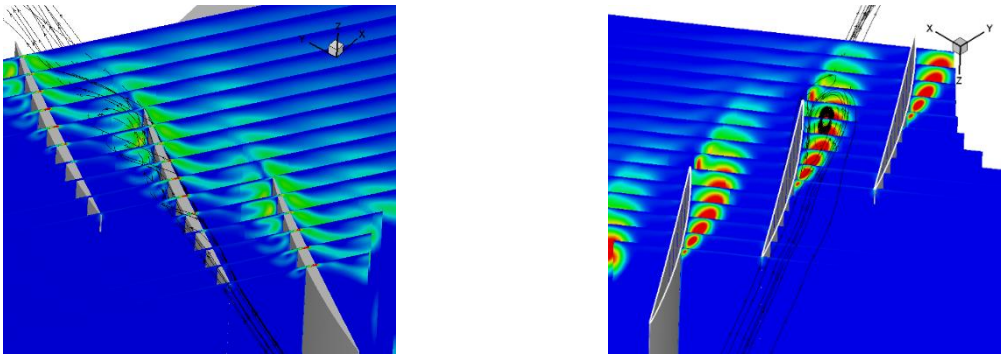

(c) P.R.=1.40 (merged shocks)

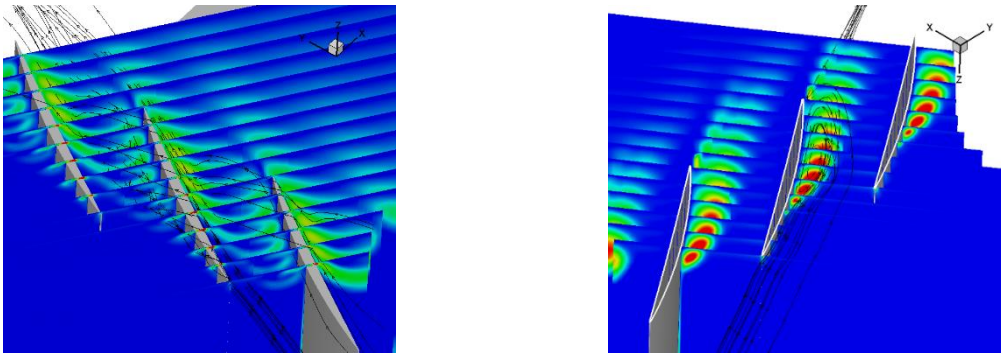

(d) P_{out}/P_{in}^{*}=0.64 (Detached shock)

(Left: tip side; right: hub side)

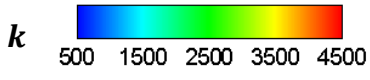

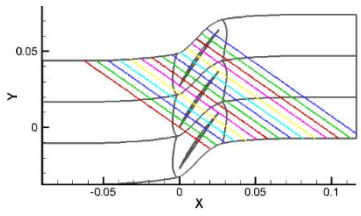

Figure 4.24 Turbulence kinetic energy distribution at near wall zones

4.6.2 Total Pressure Loss

Total pressure loss coefficient $\bar{\omega}$ which is directly related with cascade efficiency is used to evaluate the aerodynamic performance. It is calculated as eqn.(4.2).

$$\bar{\omega} = \frac{P_{in}^* - P^*}{P_{in}^* - P_{in}} \tag{4.2}$$

Figure 4.25 shows the pitchwise $\bar{\omega}$ distribution in middle span at 1.0 chord downstream. P.R.1.25 has the maximum weak loss, while P.R.1.15 has maximum averaged loss. With the shock wave moving upstream, the middle span total pressure loss decrease.

Figure 4.26 shows the counters of $\bar{\omega}$ in 1.0c downstream cross section. At middle span, the high loss zone is related to the shock wave-boundary layer separation and the wave. In lower P.R. range, the mass flowrate is larger with higher supersonic flow velocity. The Mach number before the passage shock wave is quite larger and causes drastic separation and loss near blade surface. Total pressure loss decreases with the pressure ratio increasing, which is caused by the smaller blade surface separation with the shock wave moving towards upstream.

The loss near tip side is strongest under choked flow condition, while the loss is weakened at higher pressure ratio with influence area becoming larger. In detached shock condition, tip side loss occupies almost 1/4 of the cross section which is the largest loss source. As to the hub side, it shows similar phenomena as the tip side, while in detached shock condition, the hub side loss doesn't change a lot compared to the merged shock pattern.

Generally speaking, even though the middle span total pressure loss decreases with the pressure ratio increasing, the influence of tip/hub loss becomes larger. The total pressure loss in mid-span is mainly caused by the wake and blade surface separation. And the total pressure loss near tip and hub side is considered to be related with the tip clearance flow and blade surface-hub wall separation.

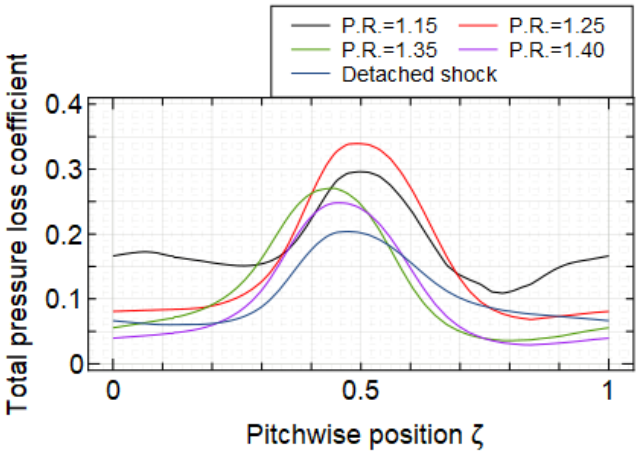

Figure 4.25 Pitchwise distribution of total pressure loss at mid-span (1.0 c downstream)

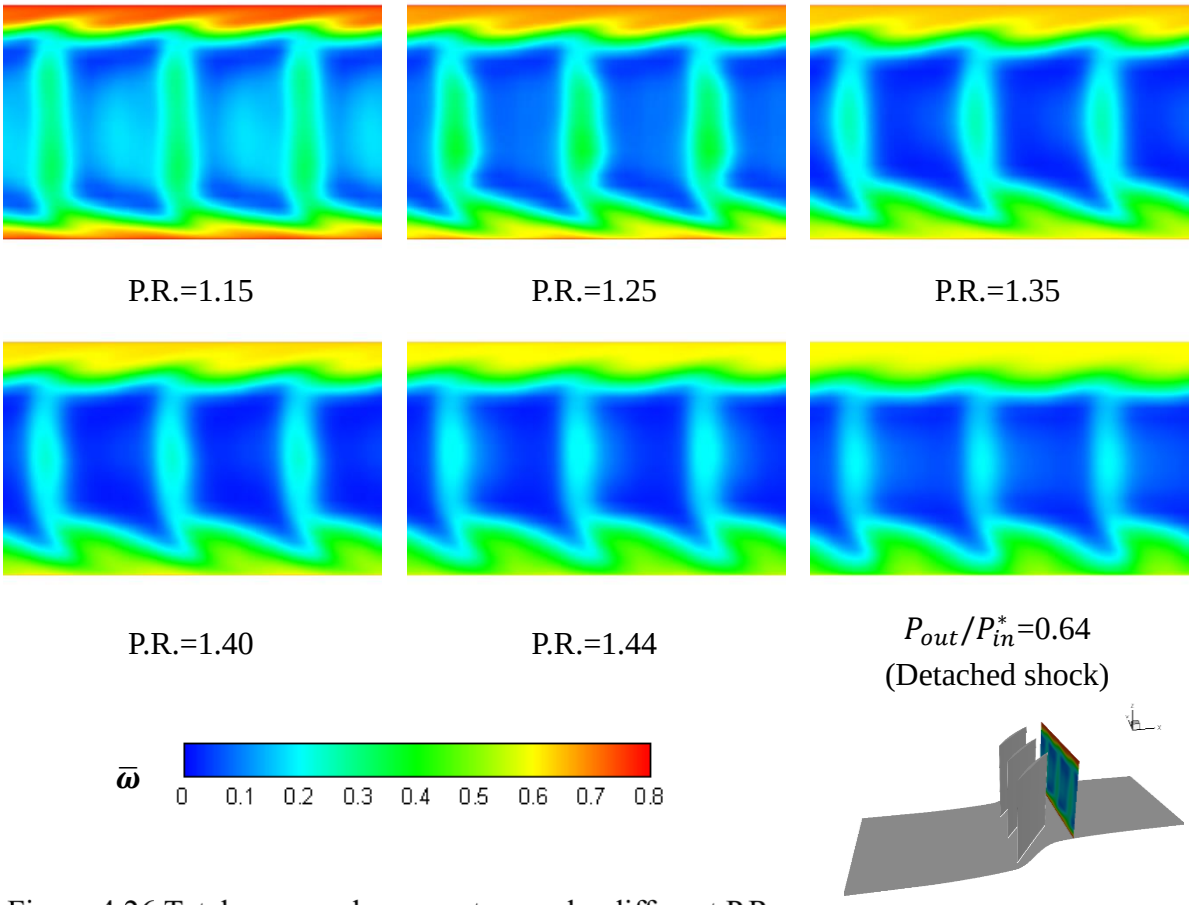

Figure 4.26 Total pressure loss counters under different P.R.

4.6.3 Extreme Operating Conditions

The extreme working conditions including choked flow condition and detached shock condition were analyzed in details to find the evolution laws.

(1) Choked Flow Condition

Figure 4.27 and Figure 4.28 show the Mach number and pressure coefficient distributions in choked flow range with the change of static pressure ratio.

In choked flow range, with the decrease of pressure ratio, the oblique shock keeps the same shape and the passage shock with λ feet changes gradually. The passage shock foot on pressure side moves downstream with P.R. decreasing. And distance between the two branches of λ foot becomes longer with enhanced expansion wave from trailing edge. The flow velocity reaches maximum in such condition and the flowrate won't increase any more. As shown in Figure 4.28, the low pressure zone on P.S. moves downstream and becomes larger while the pressure on S.S. keeps almost the same with only slight change in the corner zones.

(2) Detached Shock Wave Condition

Figure 4.29 and Figure 4.30 show the Mach number and pressure coefficient distributions in detached shock range with the change of back pressure.

In detached shock wave range, with the increasing of back pressure, leading edge shock

changes from oblique shock to normal shock with the Mach number in the supersonic zone before the shock wave becoming small. The flow after the shock becomes completely subsonic.

As shown in Figure 4.30, the pressure on P.S. keeps high value in all chordwise direction. Pressure on S.S. shows the violent influence from the tip side flow. The low-pressure area before the shock foot is pressed by the tip sider flow and moves toward the hub side. Figure 4.31 also shows the same phenomenon where the tip side flow is enhanced and causes large corner separation in tip-trailing edge corner. Conversely, the hub side corner separation becomes smaller. Generally speaking, in complete detached flow, the tip leakage flow and tip side corner separation are considered to be the dominant factors for the cascade aerodynamic performance.

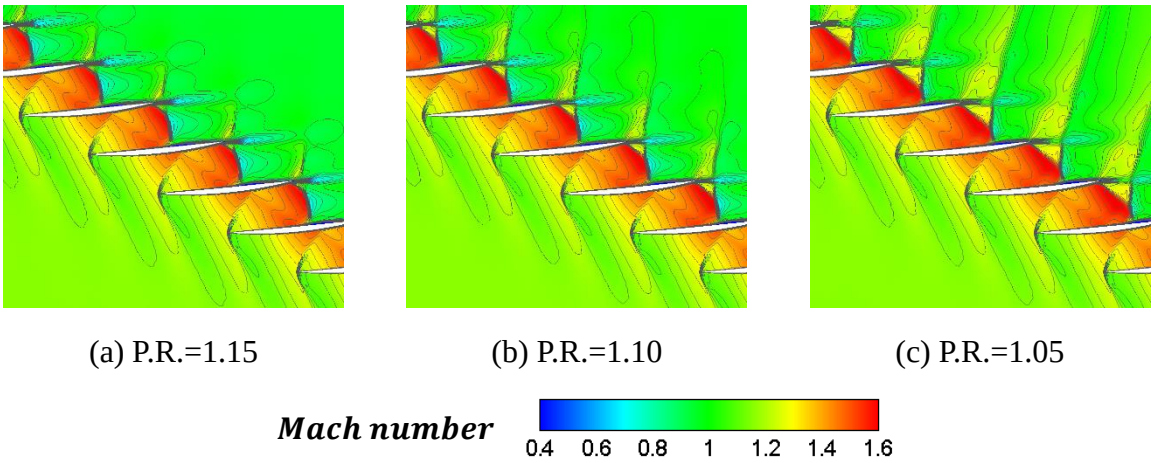

(a) P.R.=1.15 (b) P.R.=1.10 (c) P.R.=1.05

Figure 4.27 Mach number counters in choked flow range

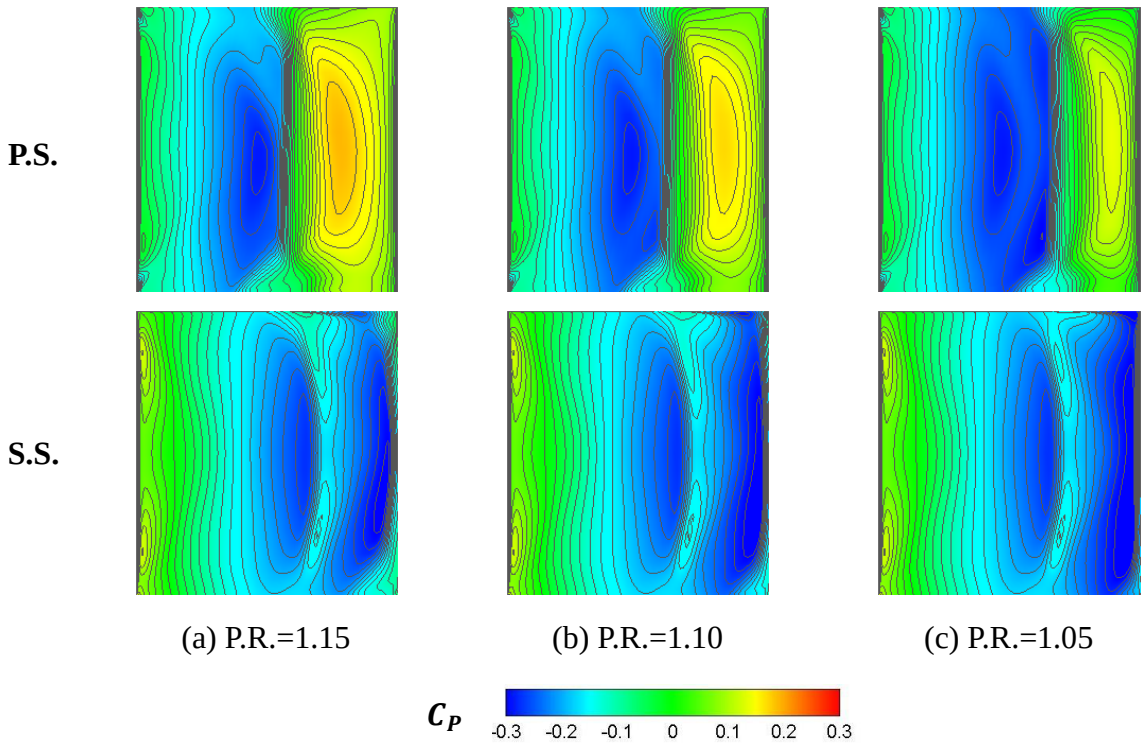

(a) P.R.=1.15 (b) P.R.=1.10 (c) P.R.=1.05

Figure 4.28 Pressure coefficient counter on blade surface in choked flow range

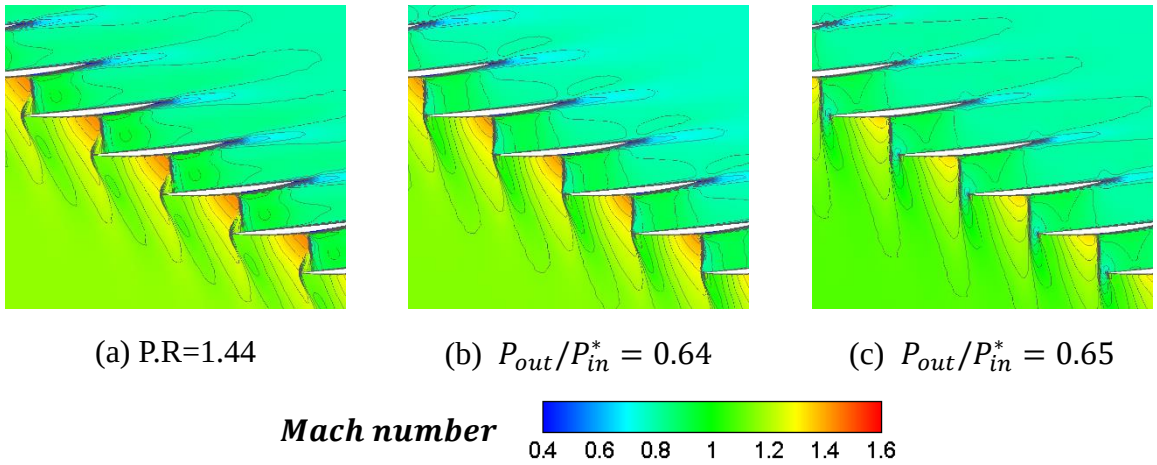

(a) P.R=1.44 (b) $P_{out}/P_{in}^{*} = 0.64$ (c) $P_{out}/P_{in}^{*} = 0.65$

Figure 4.29 Mach number counters in detached shock range

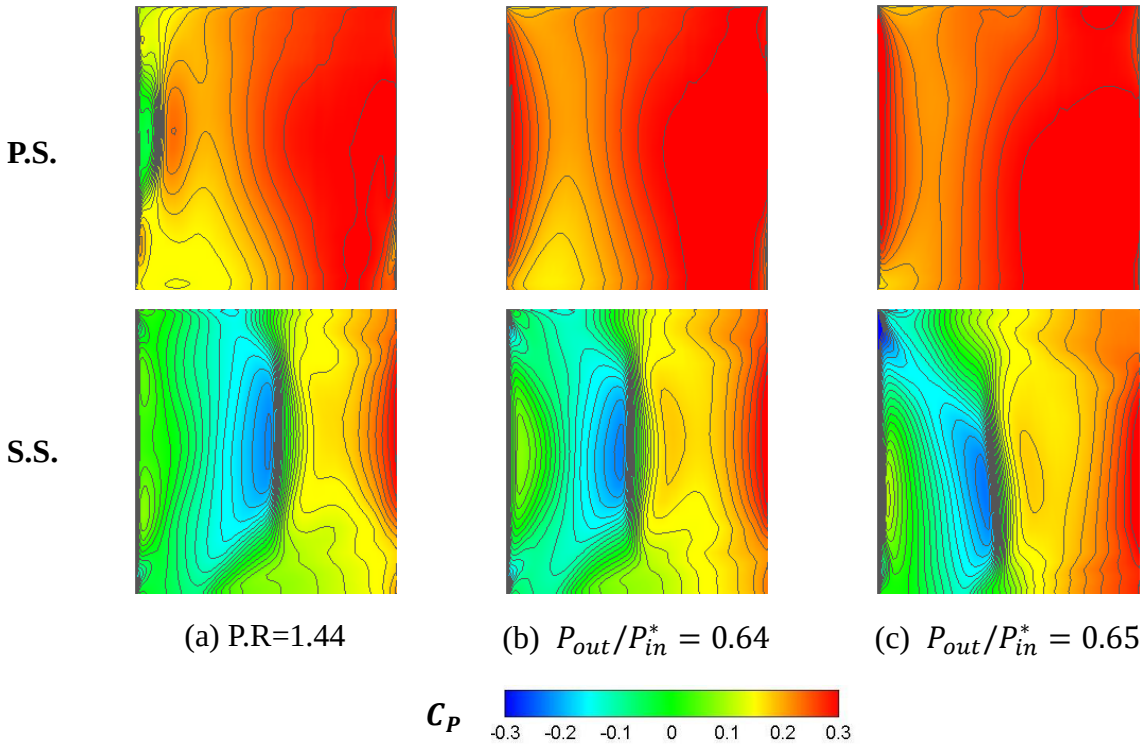

(a) P.R=1.44 (b) $P_{out}/P_{in}^{*} = 0.64$ (c) $P_{out}/P_{in}^{*} = 0.65$

Figure 4.30 Pressure coefficient counter on blade surface in detached shock range

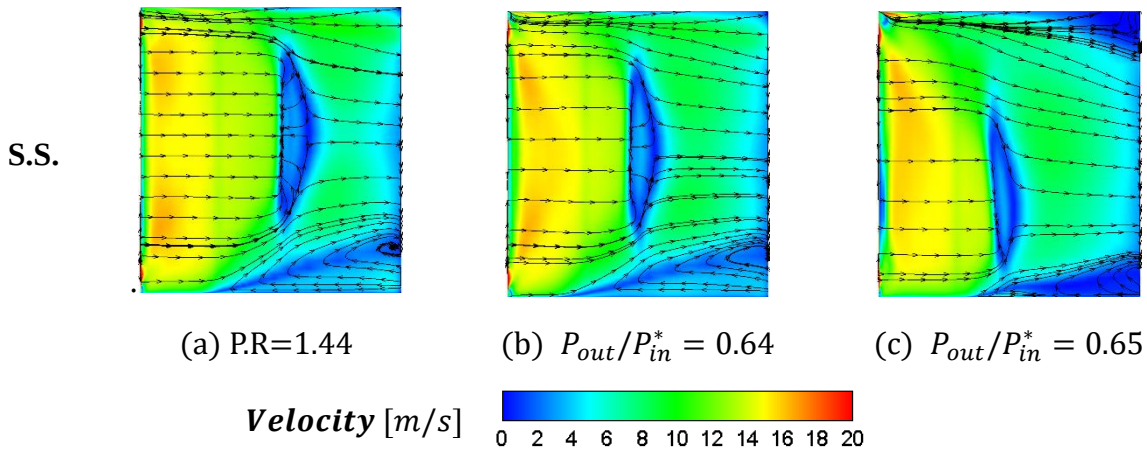

Figure 4.31 Limiting streamlines and velocity distribution on blade surface

4.7 Summary

In this chapter, the experimental and numerical approaches were applied to clarify the steady flow field with different shock pattern. Experimental results visualized the flow field and were used for CFD validation. More details of the flow field of the cascade has been obtained by CFD computation. The following conclusions can be obtained.

(1) PSP is effective for steady pressure measurement under various flow conditions in transonic flow. The formation reasons of spatial pressure distribution related to shock waves and flow separation were illustrated.

(2) The shock configurations in current transonic compressor cascade are classified in to 4 types, including choked flow pattern, double shocks pattern, merged shocks pattern and detached shock pattern. In choked flow pattern range, with the pressure ratio decreasing, the pressure on P.S. continues to change, while pressure on S.S. keeps almost the same; in double shocks pattern range, the cascade has relative weak pressurization capability and the inside mass flowrate is near the choked mass flowrate with small variation.; in merged shocks pattern range, the cascade has relative strong pressurization capability and the inside mass flowrate decreases rapidly with the increasing of pressure ratio; In detached shock pattern range, the leading edge shock wave changes from oblique shock to normal shock and detaches.

Chapter 5 Unsteady Aerodynamic Characteristics of Oscillating Cascade

5.1 Overview

Based on the results and analysis of steady flow field, the unsteady pressure measurements were conducted by using PSP technique. CFD calculations were also carried out where the converged steady CFD results were used as the initial flow field data for unsteady calculation of the cascade including 11 blade passages with the central blade oscillating in translational mode. Then, the obtained surface pressure distributions obtained by PSP were used to validate the CFD method. The unsteady pressure analysis were conducted based on both PSP and CFD results. Furthermore, the aerodynamic stability of oscillating cascade was illustrated by using influence coefficient method.

5.2 Oscillation Mode and Study Cases

5.2.1 Oscillation Mode

In this study, the blade was assumed to be oscillated at pure translational mode which should be confirmed by the real measurement. The inertial force of oscillating blade 0 measured by strain gauge in a wide frequency range is shown in Figure 5.1. It can be seen that the peak of inertial force appears at oscillating frequency of 220Hz with the phase change from 0 degree to -180 degree. Therefore, the natural frequency of test blade was considered to be around 220Hz. As confirmed by the video of blade oscillation (wind-off) taken by high speed camera, at low oscillating frequency range from 20Hz to 140Hz, the blade is in the rigid translational vibration mode with all location in same trajectory. At oscillating frequency 240Hz which is above natural frequency, the vibration mode changes to non-rigid. In such condition, the displacement amplitude of tip side is quite larger than hub side and the spanwise location also has phase discrepancy.

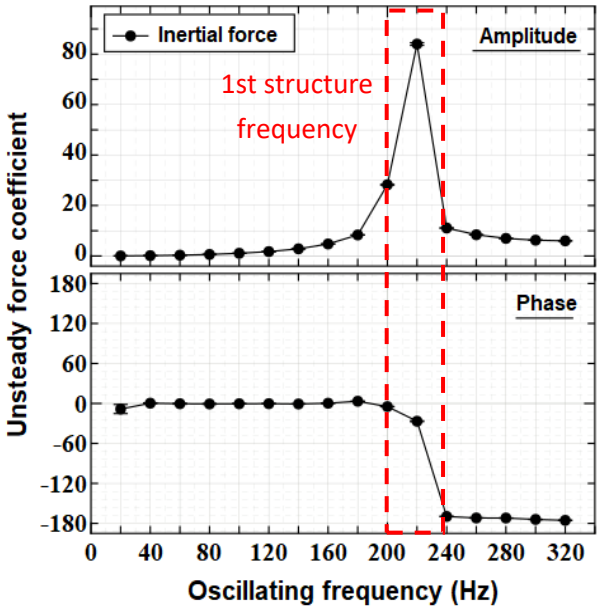

Figure 5.1 Inertial force variation with oscillating frequency (wind-off condition)

In present study, we were focusing on the rigid vibration zone. In doing aerodynamic force measurement for oscillating blade by using strain gauge, the solution was obtained by subtracting inertial force (wind-off value) from resultant force (wind-on value) in complex plane. For evaluating the degree of unsteadiness of flutter problem, the parameter reduced frequency k is adopted by normalizing frequency by chord length c and inflow velocity U_∞ as the following formula.

$$k = fc/U_\infty \tag{5.1}$$

5.2.2 Application of PSP Technique in Current Cascade

Among the shock patterns (shown in Figure 5.2), the double shocks pattern and merged shocks pattern are representative patterns with quite distinct steady flow filed. And these patterns occupy the main operating ranges of compressor cascade. With the existence of shock wave feet on blade surface, the static pressure fluctuation induced by blade oscillation is obvious in shock wave areas where the PSP technique is applicable for unsteady pressure measurement. Otherwise, in doing the unsteady PSP measurement, some cases are difficult to be measured. In choked flow case, the relatively small steady aerodynamic force and pressure fluctuation which increase the difficulties of PSP measurement. In detached shock case, the periodicity of cascade flow field is deteriorated due to the detached shock wave, which is hard to understand the interactive relationship of the unsteady pressure on each blade.

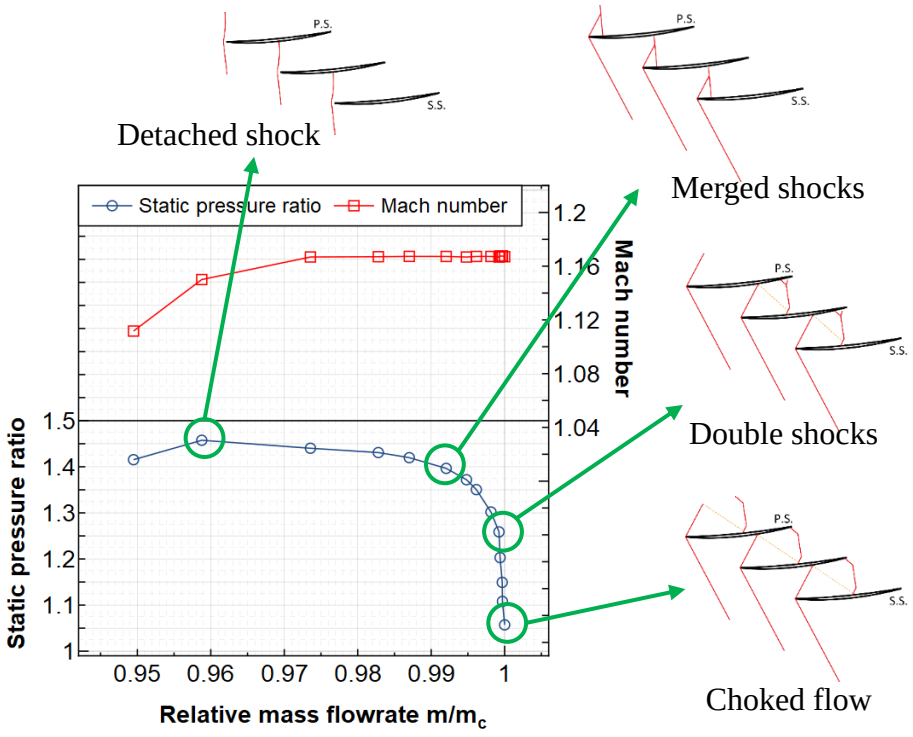

Figure 5.2 Relationship between shock pattern and flowrate characteristic

5.2.3 Selection of Study Cases

Due to the above reasons, the double shocks pattern and merged shocks pattern were selected for unsteady pressure measurement by PSP technique. The experimental condition is shown in Table 5.1. For the investigation of unsteady flow field, 2 kinds of shock patterns were set by adjusting static pressure ratio to 1.25 and 1.40. The reduced frequency range were set to be 0.0078~0.0547.

Besides, other cases including choked flow pattern and detached shock pattern were investigated by CFD calculation results.

Table 5.1 Experimental condition of oscillating cascade

Static pressure ratio	1.25, 1.40	
Oscillation mode	Translational mode	
Oscillating frequency	20~140	[Hz]
Reduced frequency	0.0078~0.0547	
Oscillating amplitude (P-P)	0.8, 0.6, 0.5	mm
	(20~100, 120, 140Hz)	

5.3 Unsteady Pressure Measurement under Different Pressure Ratio

5.3.1 Unsteady Aerodynamic Forces Acting on Blades

The unsteady aerodynamic forces acting on 3 central blades (-1, 0, +1) were investigated. Figure 5.3 show the force change with reduced frequency obtained by strain gauge, PSP and CFD under P.R.=1.25. The amplitude and the phase shift of unsteady aerodynamic force were calculated through discrete Fourier transformation. Generally speaking, the results have good agreements with each other.

For blade -1, the amplitude of unsteady aerodynamic force is relatively small compared to blade 0 and +1. Under P.R.=1.25, the phase shift is around 0° and have no obvious variation with reduced frequency. For blade 0, the increase of amplitude can be observed. The phase shifit tends to keep unchanged with frequency increasing and has a large deviation from 0°. Because the PSP measurement for oscillating blade for lower P.R. has relatively low signal-noise ratio, the integrated aerodynamic force on blade 0 calculated by PSP was difficult to compare with other results. For blade +1, it also shows increasing tendency of amplitude and delaying tendency of phase from 180°.

The phase shift variations of blade 0 and +1 with P.R. change were investigated at 40Hz (reduced frequency 0.0156) which is shown in Figure 5.4. The results obtained by strain gauge and CFD show a similar trend. It can be observed that the amplitude has a tendency of accelerated growth in P.R. range 1.15~1.40, especially when the pressure ratio is greater than 1.30. That is to say the pressure fluctuation on blade surface becomes much more drastic when the pressure ratio become larger. About blade 0, the phase shift from 0° becomes larger with P.R. decreasing at first and becomes smaller conversely under P.R.=1.15. As to the blade +1,

with the decrease of pressure ratio, the phase delays slightly which is slower than blade 0, which indicates that the pressure propagation towards downstream blade under larger P.R. is faster.

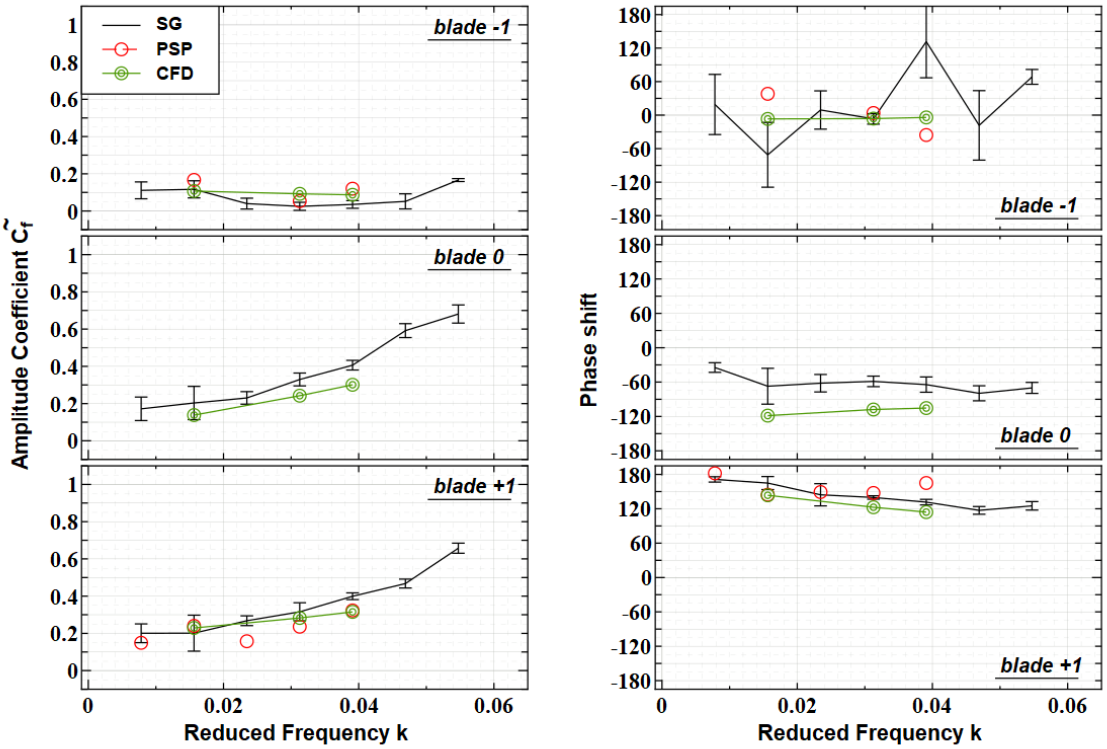

Figure 5.3 Unsteady aerodynamic forces change with reduced frequency (P.R.=1.25)

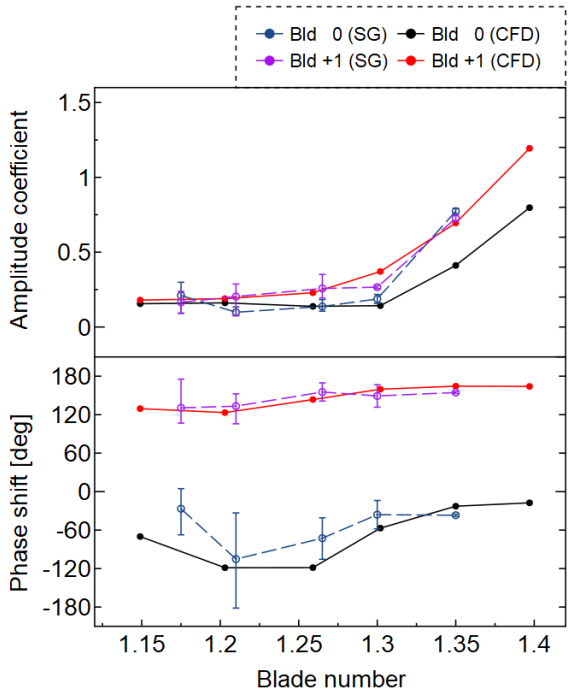

Figure 5.4 Unsteady aerodynamic force variation with pressure ratio (40Hz)

5.3.2 Unsteady Pressure Distribution on Blade surface

Based on the understanding of performance of total unsteady aerodynamic forces, this section discusses the details of unsteady pressure acting on blade surface under different P.R. at 40Hz. The unsteady PSP measurement were conducted on the central 3 blades. The phase angle is defined as 0 degree when the oscillating blade was at the central position and the blade velocity is towards its suction side. The surface pressure was measured every time step and post-processed by Fourier transformation at oscillation frequency in order to extract the unsteady component. The process can be express as the following equation.

$$C_p(t) = \tilde{C}_p e^{i\omega t} = \left\{\tilde{C}_p(Re) + \tilde{C}_p(Im)\right\} e^{i\omega t} \tag{5.2}$$

The figures in this section shows the unsteady pressure distribution which includes real part $\tilde{C}_p(Re)$ and imaginary part $\tilde{C}_p(Im)$. The real part is understood as displacement synchronizing component, and the imaginary part as velocity synchronizing component.

(1) <u>Double Shocks pattern (P.R.=1.25, 40Hz)</u>

Figure 5.5~Figure 5.6Figure 5.7 show unsteady pressure distributions under P.R.=1.25 on each blade surface in one passage captured by PSP and CFD. Total speaking, both results have a qualitative agreement. In large pressure fluctuation areas induced by shock waves, quantitative accordance was also obtained. Besides, the unsteady pressure results of oscillating blade measured by PSP have relative low signal-noise ratio than the stationary blades.

On -1 S.S., the pressure fluctuations induced by oblique shock wave and passage shock can be seen in $\tilde{C}_P(Re)$ counters with negative values, which indicate that pressure change is in reverse phase compared with blade motion. Both the two shock waves have the same moving direction at this case. $\tilde{C}_P(Re)$ at the interval between shock waves shows a positive value which is caused by the steady pressure drop between shock waves.

The unsteady pressure with negative $\tilde{C}_P(Re)$ caused by passage shock on 0 P.S. shows good correlation with -1 S.S, which indicate the passage shock feet are with same moving direction. The area from blade L.E. to shock wave foot shows a positive $\tilde{C}_P(Re)$ which is caused by the steady pressure decrease at P.S. supersonic area.

As seen in the counters of $\tilde{C}_P(Im)$, no obvious fluctuations can be seen in shock wave areas. Under current low reduced frequency (0.0156) condition, the blade is quasi-steady in each location comparing to the inflow velocity, and the shock wave movement has good following behavior with the blade motion.

As to the downstream flow passage of oscillating blade, the shock wave movement is converse to the upstream flow passage. The real part $\tilde{C}_P(Re)$ of unsteady pressure at shock wave areas is with positive value which is synchronous to the blade motion.

On 0 S.S., a different phenomenon with -1 S.S. was found that an area with negative $\tilde{C}_P(Re)$ and positive $\tilde{C}_P(Im)$ exists at 0.8x/c of tip side following oblique shock wave. This unsteady pressure is considered to be induced by tip leakage flow and propagates towards the downstream blades. It also shows phase different from the blade motion and shock wave motion.

On +1 P.S., two continuous peaks at mid-span were captured by both PSP and CFD, which is considered to be the two λ feet of passage shock wave. The absolute value of $\tilde{C}_P(Im)$ in passage shock wave area is larger than that of 0 P.S. which is considered to be related with the propagation of shock wave-boundary layer separation.

For the farther blade surfaces, it shows quite different results. The upstream blade -1 P.S. has ignorable unsteady pressure values, while downstream blade +1SS has obvious fluctuation in the areas of passage shock wave and tip leakage flow. That is to say that the pressure fluctuation caused by blade oscillation is easier to propagate towards downstream blade passages and the main phenomenon is passage shock oscillation with the impact of tip leakage flow.

(2) Merged Shocks pattern (P.R.=1.40, 40Hz)

Similarly, Figure 5.8 shows the results of 0 S.S./+1 P.S. passage under pressure ratio 1.40 at 40Hz. The shock wave area shows negative $\tilde{C}_P(Re)$ and positive $\tilde{C}_P(Im)$ values and $\tilde{C}_P(Re)$ is dominant component of the unsteady pressure. This phenomenon tells that the moving direction of the passage shock is reverse to blade motion in 0 S.S./+1 P.S. blade passage.

Compared to the double shocks pattern, the shock wave motion is in reverse direction with quite larger unsteady pressure amplitude and wider influence area.

In this case, the mass flowrate is very sensitive to the pressure ratio or shock wave location. The blade movement causes the inter-blade flow area variation so as to change the flowrate. The shock wave is considered to respond to both the blade location and flowrate change.

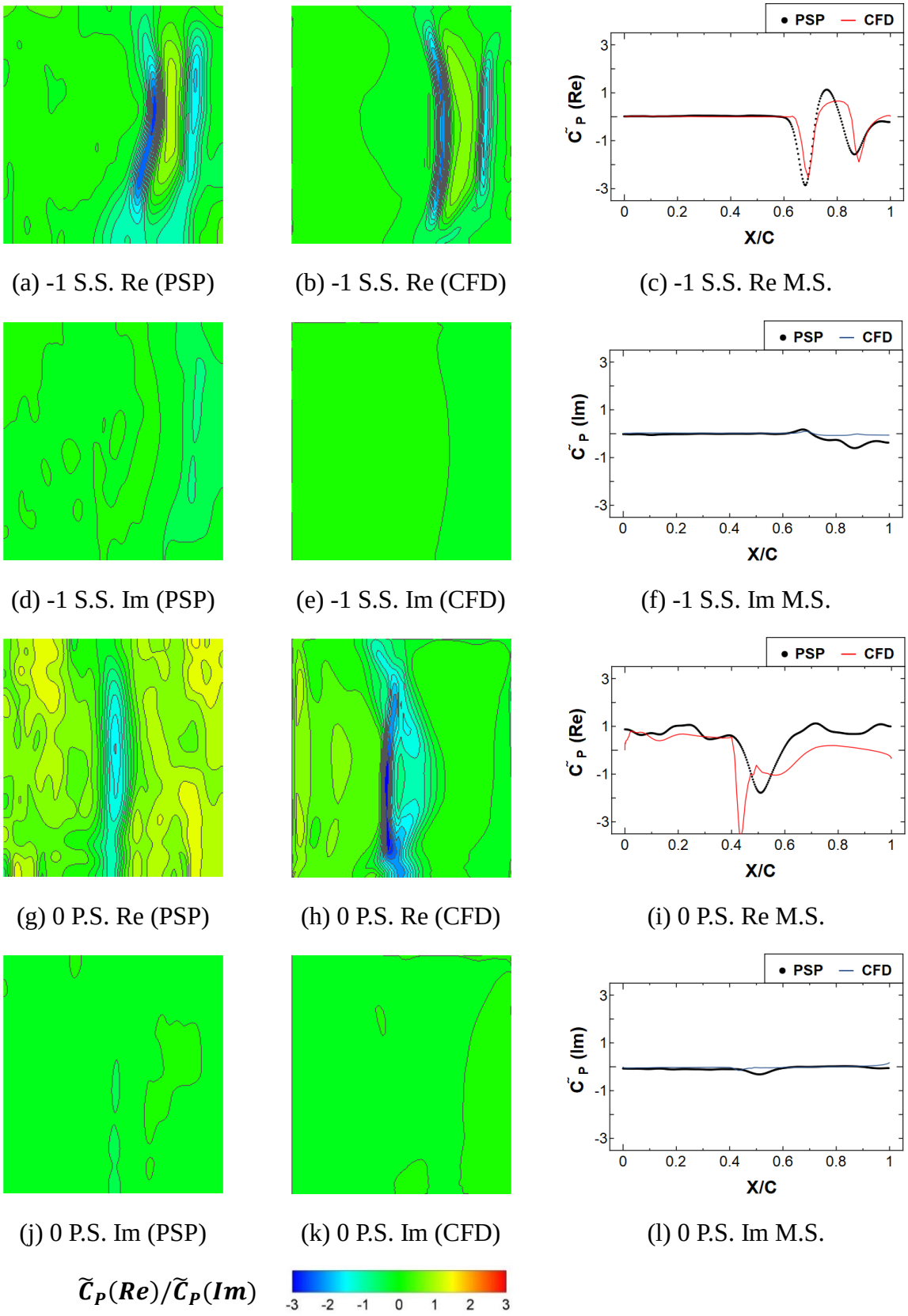

(a) -1 S.S. Re (PSP) (b) -1 S.S. Re (CFD) (c) -1 S.S. Re M.S.

(d) -1 S.S. Im (PSP) (e) -1 S.S. Im (CFD) (f) -1 S.S. Im M.S.

(g) 0 P.S. Re (PSP) (h) 0 P.S. Re (CFD) (i) 0 P.S. Re M.S.

(j) 0 P.S. Im (PSP) (k) 0 P.S. Im (CFD) (l) 0 P.S. Im M.S.

Figure 5.5 Unsteady pressure distribution on –1 S.S./ 0 P.S. (P.R.=1.25)

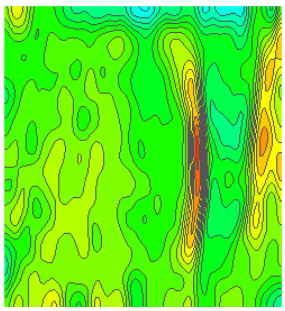

(a) 0 S.S. Re (PSP)

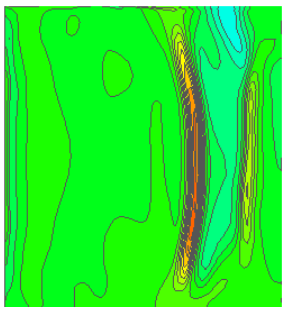

(b) 0 S.S. Re (CFD)

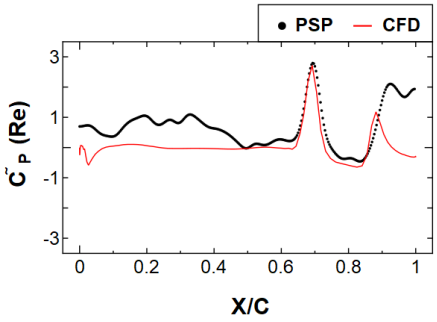

(c) 0 S.S. Re M.S.

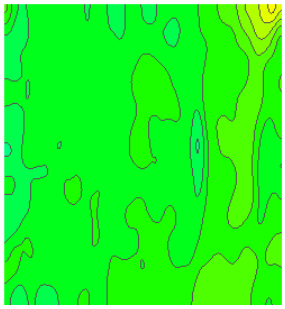

(d) 0 S.S. Im (PSP)

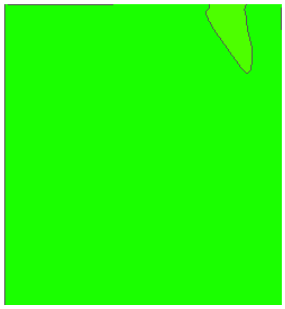

(e) 0 S.S. Im (CFD)

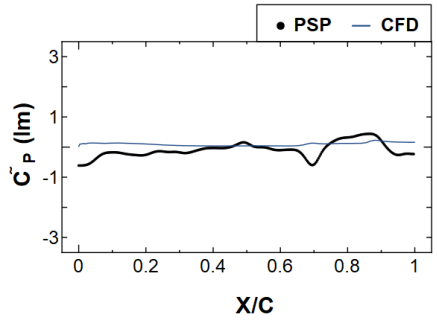

(f) 0 S.S. Im M.S.

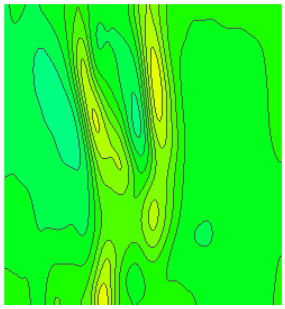

(g) +1 P.S. Re (PSP)

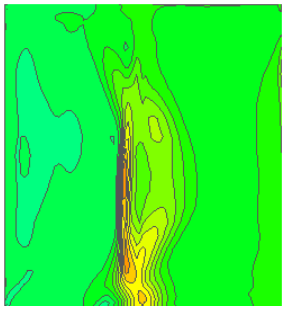

(h) +1 P.S. Re (CFD)

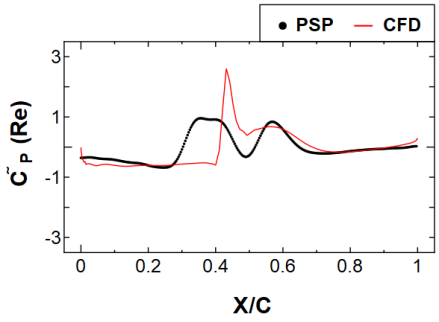

(i) +1 P.S. Re M.S.

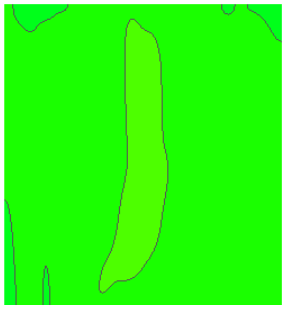

(j) +1 P.S. Im (PSP)

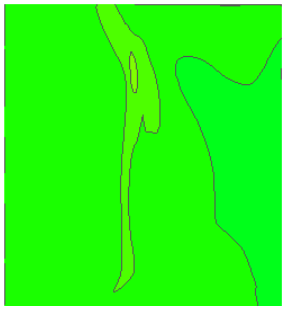

(k) +1 P.S. Im (CFD)

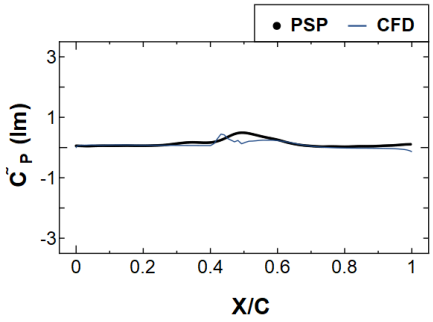

(l) +1 P.S. Im M.S.

$\widetilde{C}_P(Re)/\widetilde{C}_P(Im)$

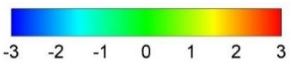

Figure 5.6 Unsteady pressure distribution on 0 S.S./ +1 P.S. (P.R.=1.25)

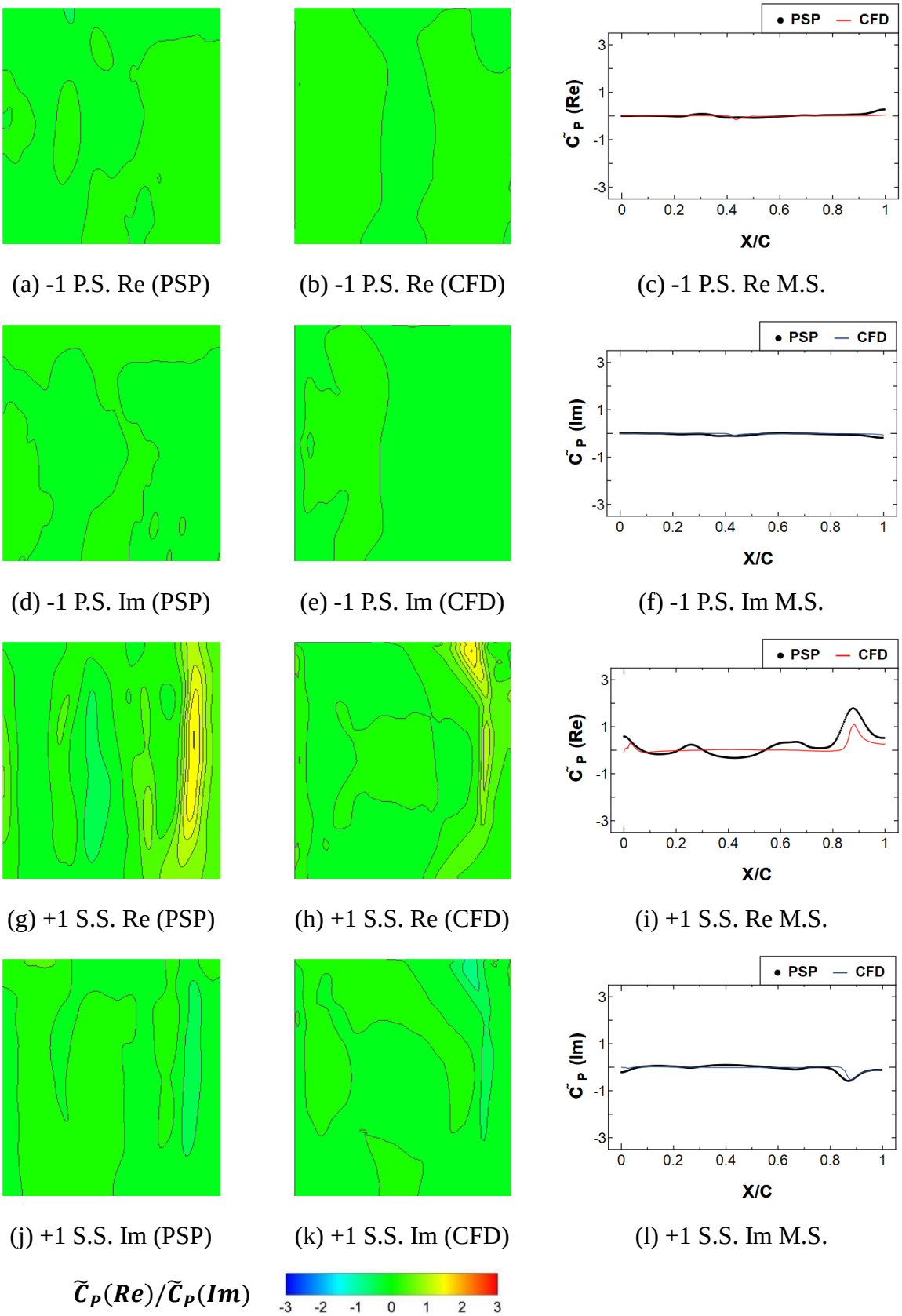

(a) -1 P.S. Re (PSP) (b) -1 P.S. Re (CFD) (c) -1 P.S. Re M.S.

(d) -1 P.S. Im (PSP) (e) -1 P.S. Im (CFD) (f) -1 P.S. Im M.S.

(g) +1 S.S. Re (PSP) (h) +1 S.S. Re (CFD) (i) +1 S.S. Re M.S.

(j) +1 S.S. Im (PSP) (k) +1 S.S. Im (CFD) (l) +1 S.S. Im M.S.

Figure 5.7 Unsteady pressure distribution on –1 P.S. & +1 S.S. (P.R.=1.25)

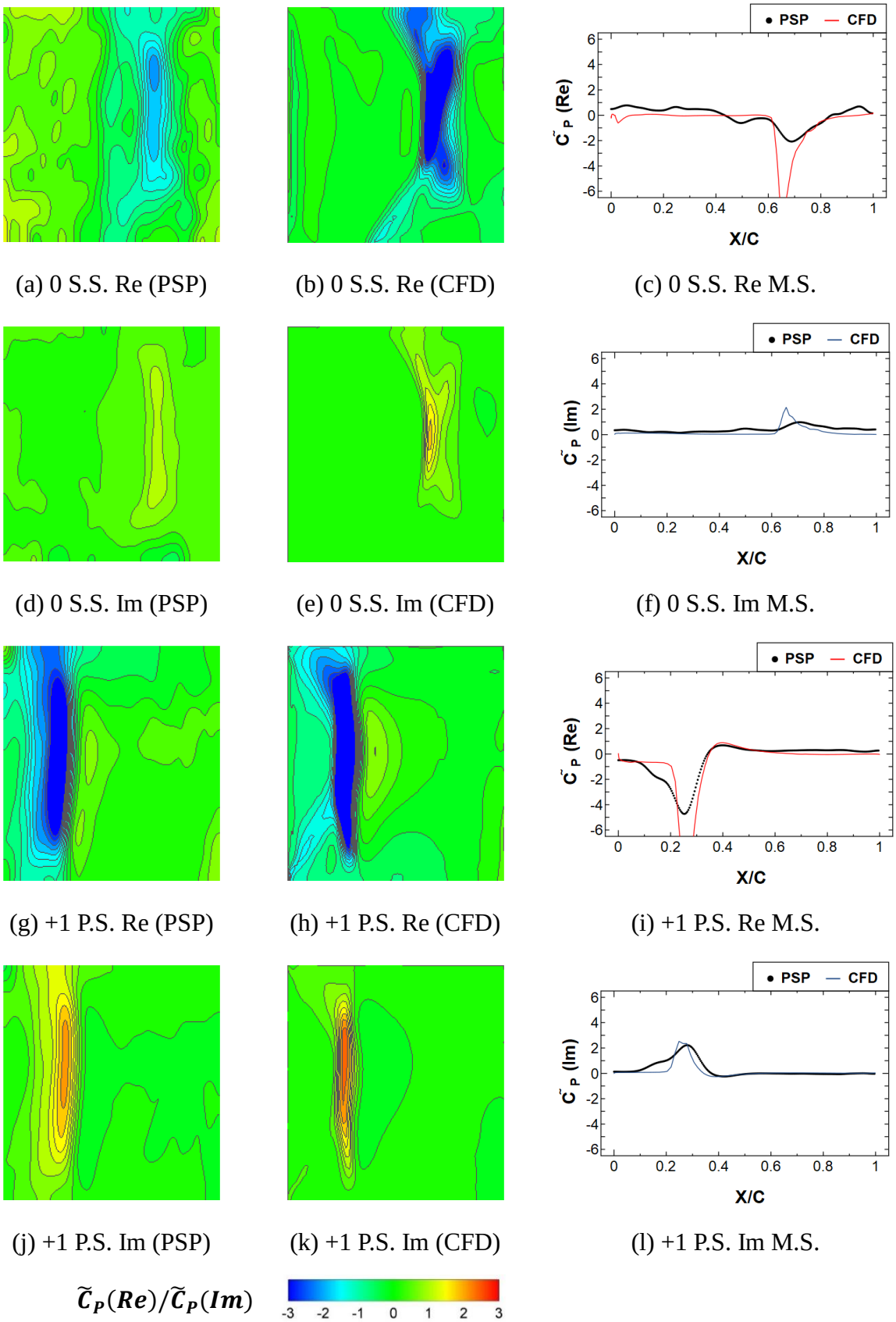

(a) 0 S.S. Re (PSP) (b) 0 S.S. Re (CFD) (c) 0 S.S. Re M.S.

(d) 0 S.S. Im (PSP) (e) 0 S.S. Im (CFD) (f) 0 S.S. Im M.S.

(g) +1 P.S. Re (PSP) (h) +1 P.S. Re (CFD) (i) +1 P.S. Re M.S.

(j) +1 P.S. Im (PSP) (k) +1 P.S. Im (CFD) (l) +1 P.S. Im M.S.

Figure 5.8 Unsteady pressure distribution on 0 S.S./ +1 P.S. (P.R.=1.40)

5.4 Unsteady Pressure Propagation Mechanisms

5.4.1 Shock Wave Movement Analysis

Based on above analysis of unsteady pressure on blade surface, the shock wave movement with blade oscillation can be summarized as Figure 5.9.

Under merged shock waves condition, the mass flowrate is sensitive to P.R. change and passage shock wave movement. When the blade moves down, the 0 S.S./ +1 P.S. passage becomes narrow and the flow tend to accelerate with longer distance under supersonic condition in order to compensate area loss. So, the passage shock wave moves towards downstream direction to increase the accelerating length on blade surface. It causes pressure decrease on blade surface. The -1 S.S./ 0 P.S. passage is in reverse condition.

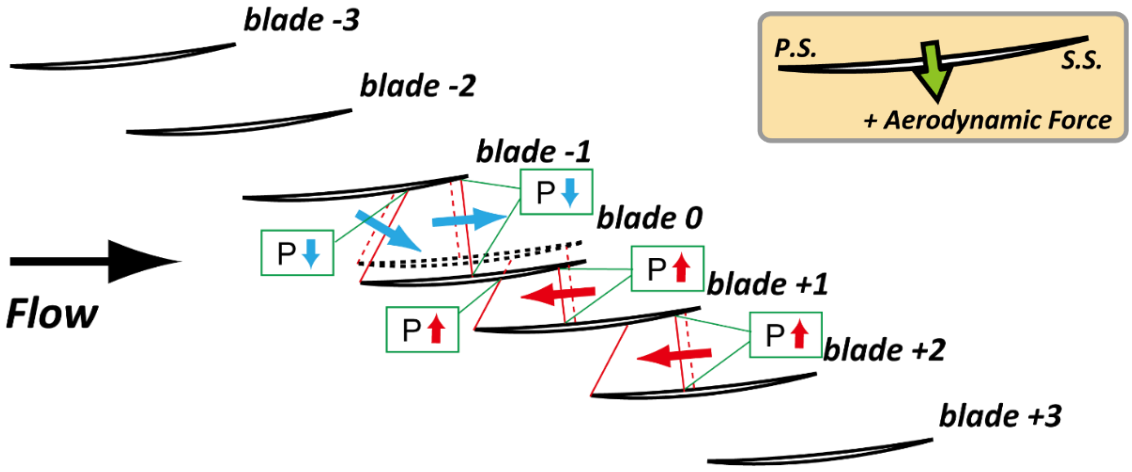

(a) Double shocks pattern

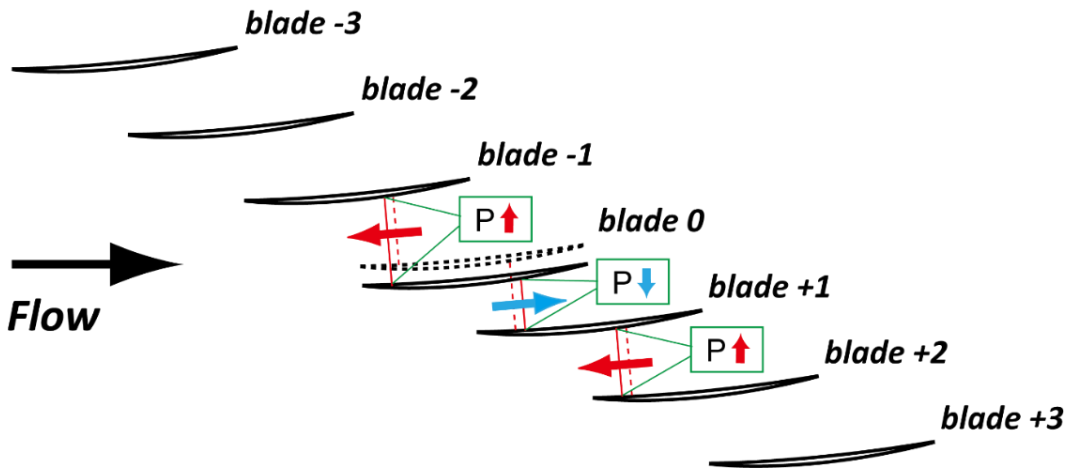

(b) Merged shocks pattern

Figure 5.9 Shock wave movement direction corresponding to blade oscillation

Under double shock waves condition, the mass flowrate which is near to choke mass flowrate is insensitive to P.R. change and shock wave movement. The oblique shock wave movement is directly influenced by blade motion. In 0 S.S./ +1P.S. passage, the oblique shock wave of blade +1 keeps its angle and the intersection point of shock and 0 S.S. goes upstream in chordwise direction with shock length shortened when blade moving down. As to the passage shock wave, the interval between oblique shock and passage shock tends to keep constant to balance the outlet pressure.

5.4.2 Shock Wave Intensity and Displacement

The unsteady pressure phenomena caused by shock waves and the moving directions of shock waves under different shock pattern were clarified in above section. The amplitude of unsteady pressure caused by shock wave under merged shocks pattern is quite larger value than that of double shocks pattern. Whether stronger shock wave intensity or longer shock foot displacement can be the possible reasons for this phenomenon. To clarify this question, the mid-span pressure gradient was extracted to indicate the shock wave intensity. Figure 5.10 (a) (b) shows the pressure gradient at different time points of one cycle in 0 S.S. / +1 P.S. blade passage. Under double shocks pattern, the passage shock wave is stronger than the oblique shock wave, while it shows quite smaller position variation comparing to oblique shock wave. Under merged shocks pattern, the merged shocks foot on S.S. and passage shock foot on P.S. cause large pressure gradients which is with comparable intensity and quite larger displacement, comparing to the passage shock wave under double shocks pattern.

Then, the displacement of shock foot was calculated by time history of mid-span C_P distribution, as shown in Figure 5.10 (c). The displacement is normalized by chord length and expressed as %chord. As a reference, the amplitude of blade displacement is 1.8%chord (0.8mm peak to peak). The waveforms of shock foot movement have good correspondence on 0 S.S. and +1 P.S.. Under double shocks pattern, two shock waves show same phase shift and oblique shock wave has a quite larger displacement amplitude of 1.7%chord than passage shock wave. The displacement amplitude of passage shock foot on +1 P.S. is 0.6%chord while it on 0 S.S. is smaller. As to the merged shocks pattern, the displacement amplitude was calculated to be 3%chord. As described in section 4.3.2, under double shocks pattern, the passage shock foot on P.S. is followed by a large separation area, and the reason of smaller displacement of passage shock foot is considered that the shock foot movement is damped by this separation area. Totally speaking, shock foot displacement has more effect on unsteady pressure amplitude than the difference in shock wave intensity.

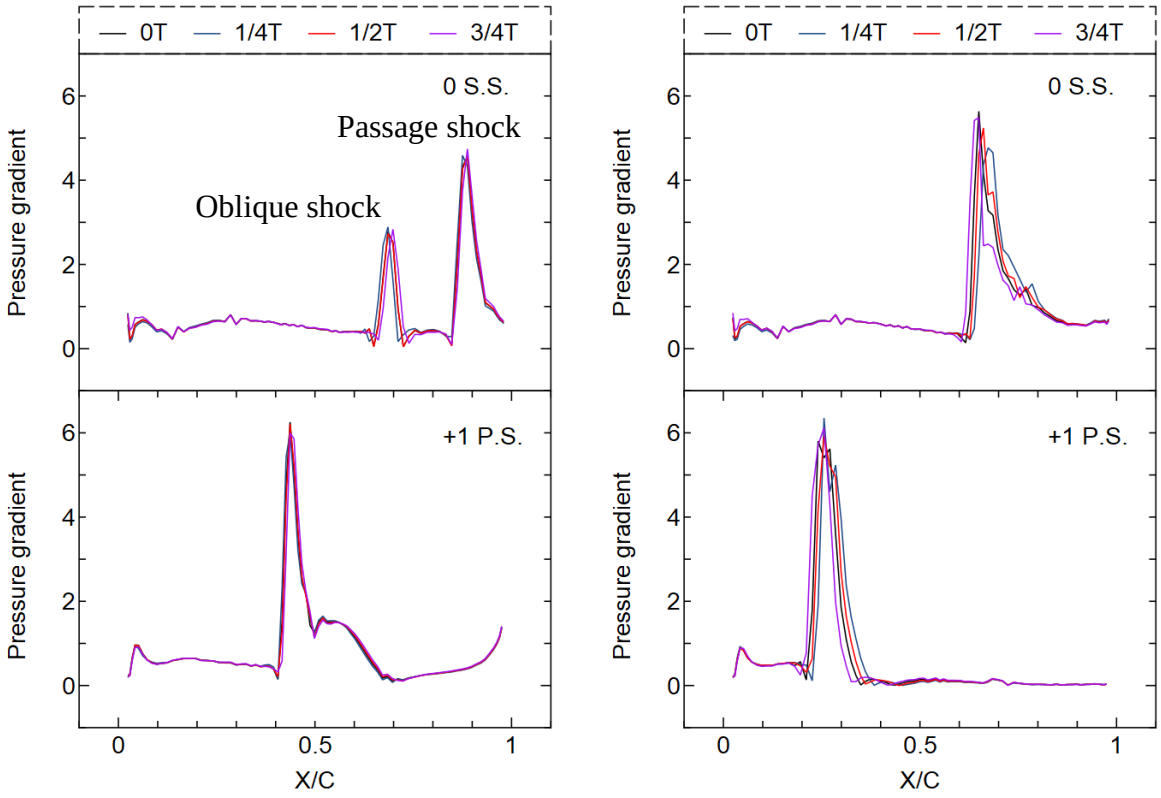

(a) Double shocks pattern

(b) Merged shocks pattern

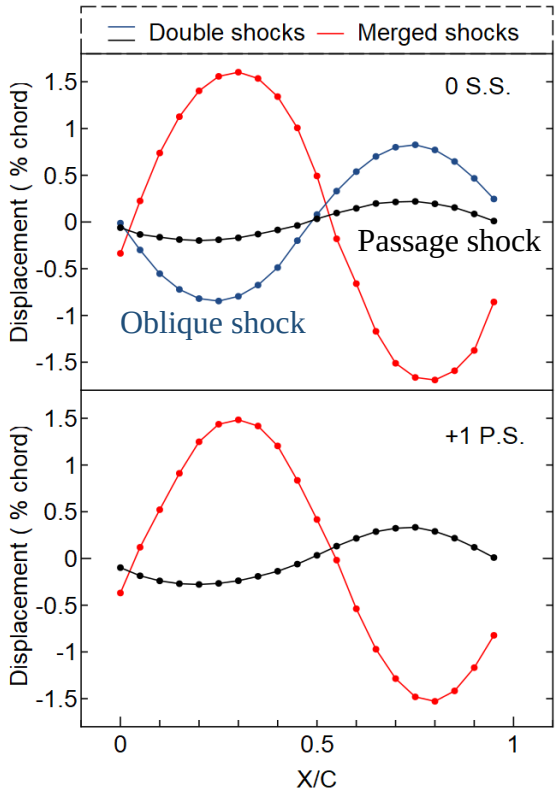

(c) Displacements of shock waves

Figure 5.10 Intensity and displacement of shock waves under different shock pattern

5.4.3 Inter-Blade Unsteady Pressure Propagation

Then, the unsteady pressure propagation mechanisms are analyzed here. Figure 5.11, Figure 5.12 and Figure 5.13 show the unsteady pressure counters of two shock patterns at different spanwise cross sections. The figures show the amplitude and phase counters of unsteady pressure coefficient on different spanwise cross sections. To extract the main unsteady pressure areas, the value blanking by amplitude was conducted on the phase counters.

At blade middle span as shown in Figure 5.11, the obvious pressure fluctuations induced by oblique shock wave are only seen at the shock zone of blade 0 and blade +1 which cannot propagate toward upstream supersonic area. The unsteady pressure caused by passage shock wave is propagating in subsonic area, while the pressure fluctuation in downstream blade passages is larger than upstream ones. With the distance increase from the central blade, the unsteady pressure becomes weak.

In tip side as shown in Figure 5.12, there are two main directions of pressure propagation, one is the inter-blade direction and one is tip leakage flow direction. The leakage flow is oscillated by the blade and enhances the pressure fluctuation of blade +1. The pressure propagates only towards downstream blade passages for both cases. Under double shocks pattern, obvious unsteady pressure amplitude can be seen in 0 S.S./ +1 P.S. and +1 S.S./ +2 P.S. flow passages. Under merged shocks pattern, it propagates farer and has larger values.

In hub side as shown in Figure 5.13, there is no large pressure fluctuations compared to middle span and tip side. The pressure propagation in hub zone is weak due to low flow velocity and solid structure consisted of blade wall and hub wall.

Also, the phase relationship of the unsteady flow phenomena was illustrated.

Under merged shocks pattern, unsteady pressure over all span height in each passage shows the same phase. So, these unsteady phenomena are all synchronous in one blade passage. In pitchwise direction, the unsteady pressure propagates with increasing phase delay from alternating 0° and 180°. At tip side, the unsteady pressure has peak value near blade suction side in one blade passage, where is the location of tip leakage flow. The most influence blades include blade 0, +1, +2, and has no obvious unsteady pressure propagation towards upstream blade passages due to the direction of tip clearance flow. At hub side cross section, the corner separation area near blade suction side has no large amplitude value except the separation boundaries including forepart boundary and rear boundary. So, the pressure inside corner separation area on blade surface has a relatively stable value with blade oscillation. The influenced areas are limited to the two neighbour blade passages of oscillating blade, which can’t propagate to farther blade passages through the solid blade walls.

As to double shocks pattern, the phase shows a spanwise discrepancy. At middle span as shown in Figure 5.11 (a), the double shock waves have the same phases as blade displacement in downstream blade passage of oscillating blade and reverse phases in upstream blade passage. The L.E. supersonic area near P.S. and the interval area between two shock waves near S.S. have reverse phase from the shock waves. At tip clearance cross section as shown in Figure 5.12 (a), in 0S.S./+1P.S. blade passage, the phase of tip leakage flow is different from the middle

span shock waves, and the reason is considered that the pressure fluctuation in tip clearance is directly dominated by blade motion, and not by the shock waves. At hub side as shown in Figure 5.13 (a), the unsteady pressure areas mainly defined as two types. One is the shock wave influenced areas with same phase as mid-span shock waves. The other one is located at leading edge area and the rear of corner separation vortex, which has reverse phase value compared with blade motion and isn't necessary consistent with the shock waves.

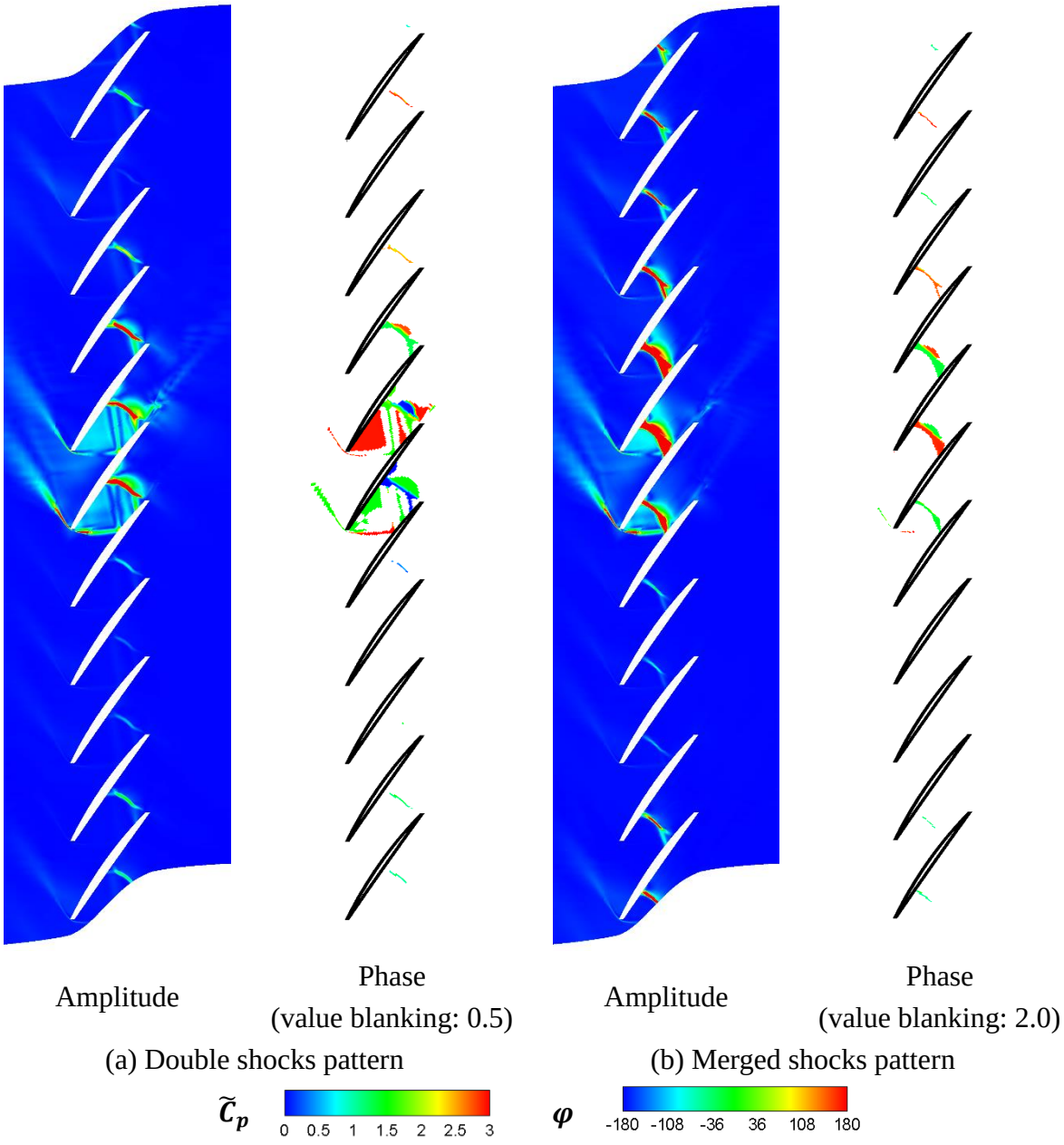

Figure 5.11 Unsteady Pressure Propagation at middle span (50% span length)

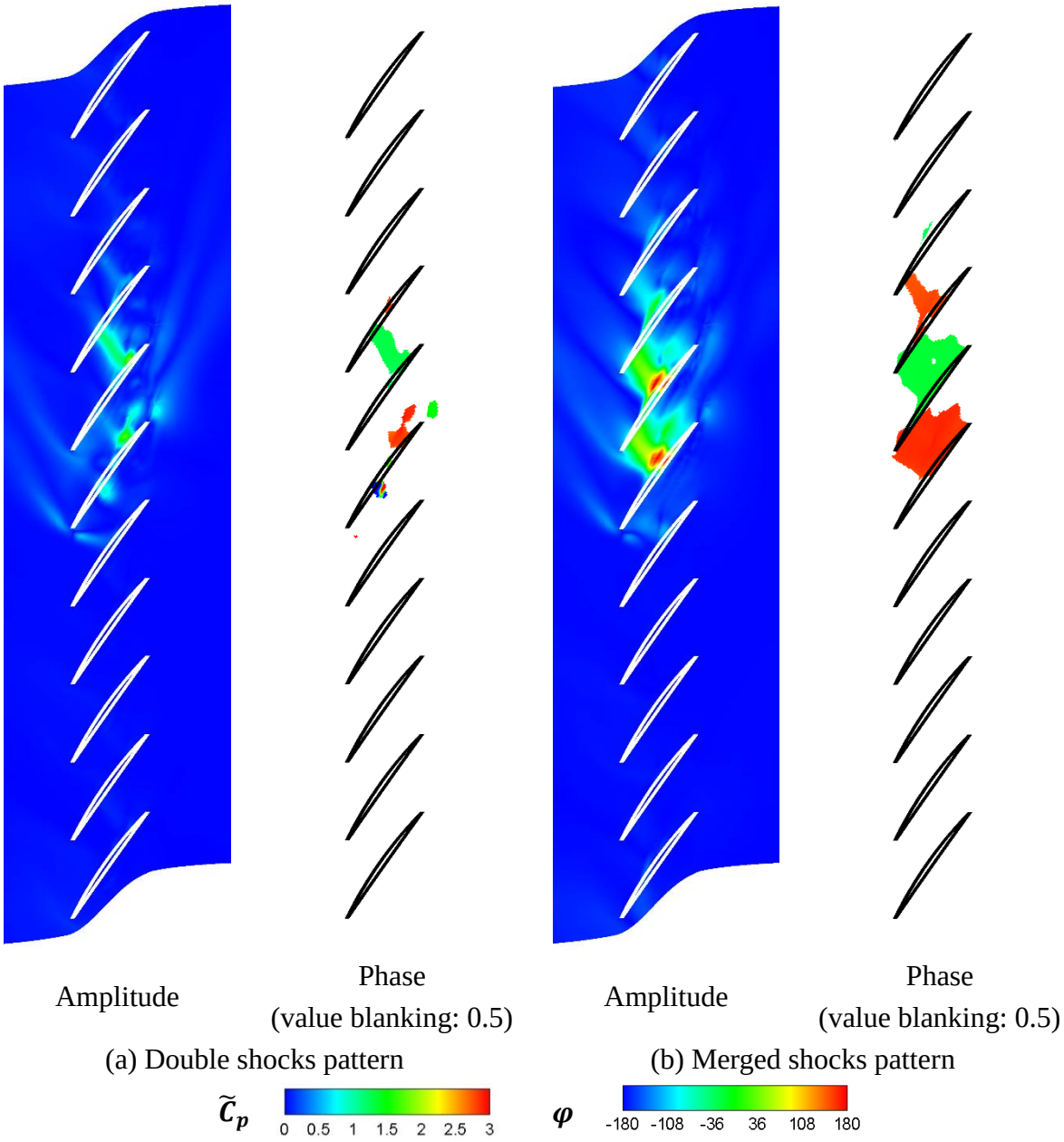

Figure 5.12 Unsteady Pressure Propagation at tip side (100.5% span length)

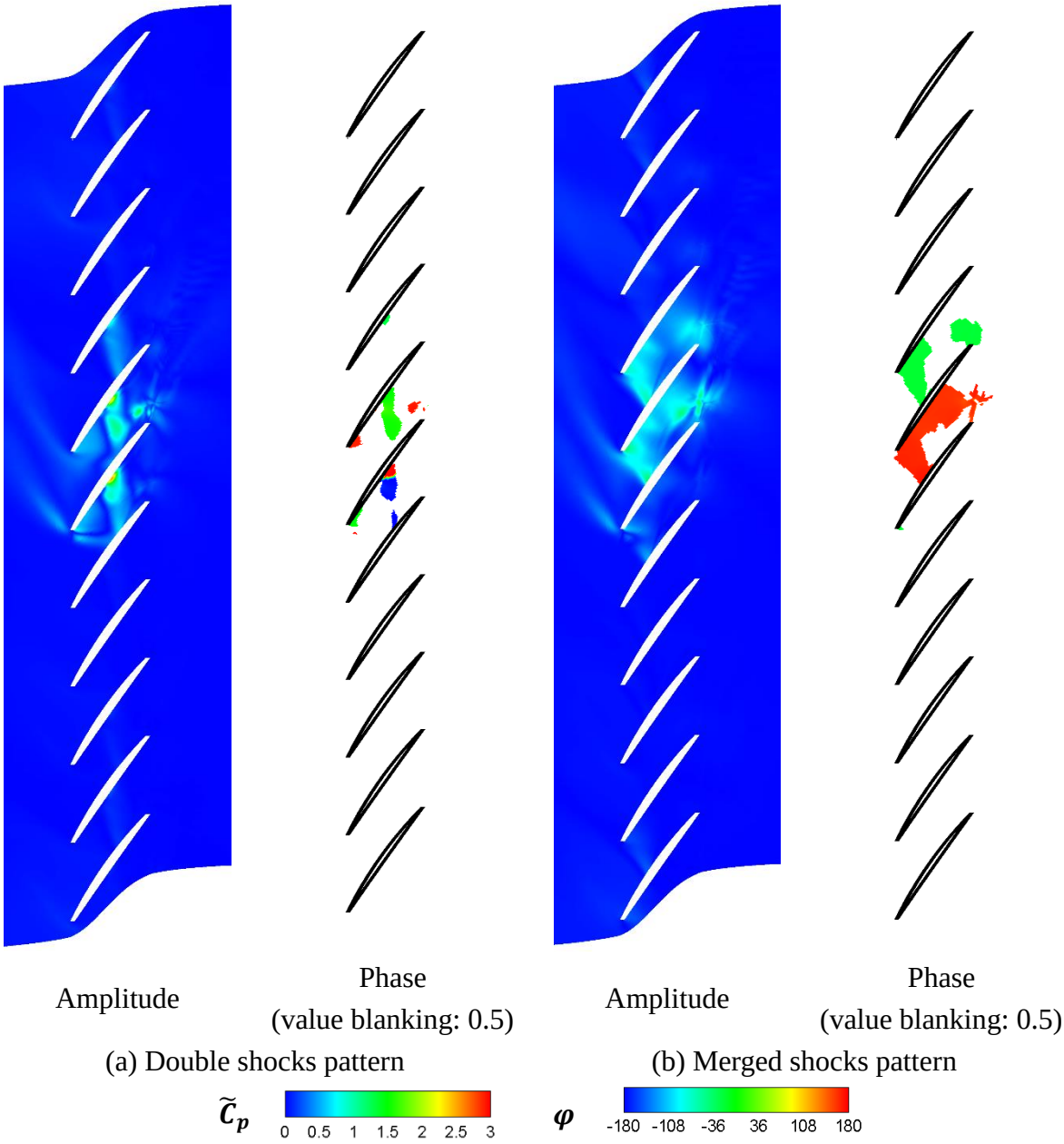

Figure 5.13 Unsteady Pressure Propagation at hub side (0.5% span length)

5.4.4 Transition of Shock Wave Movement

Due to above analysis, the two shock patterns have quite different performance in responding the blade oscillation. Therefore, the transition process between the 2 patterns is desired to clarify.

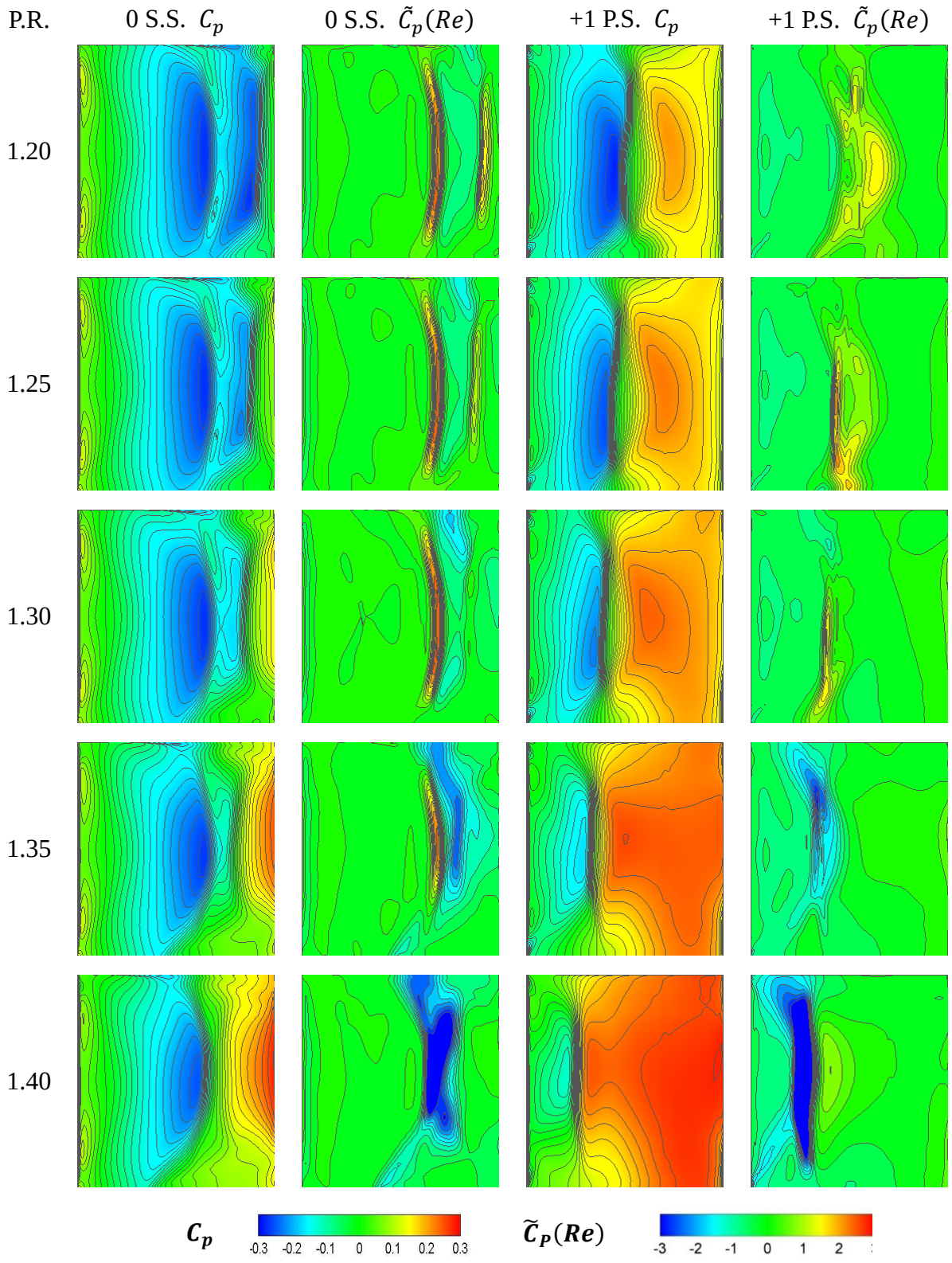

Figure 5.14 Steady and unsteady pressure distribution on 0 S.S./ +1 P.S. (40Hz)

Figure 5.14 shows the steady and unsteady pressure distribution on 0 S.S./ +1 P.S. at 40Hz under P.R.=1.20~1.40. Only the real part is shown because it is dominant in this low frequency case. It can be known that when the interval distance between the two shock waves is long enough, the oblique shock wave keeps same movement and induces same unsteady pressure distribution under P.R.=1.20~1.30. The corresponding reflected wave also has impact on +1 P.S which can be observed under P.R.=1.20~1.25. The movement of passage shock wave under P.R.=1.20~1.25 is in same direction with oblique shock and it induces smaller unsteady pressure. And the interval area between two shock waves has negative unsteady pressure value which is opposite to the areas of shock waves.

With the increase of P.R. and decrease of interval distance between shock waves, the pressure fluctuation caused by passage shock wave becomes smaller and finally changes the sign of value under P.R.=1.35, while unsteady pressure induced by tip clearance flow become larger with negative value. When the passage shock wave touches the oblique shock wave, the oblique shock foot on S.S. is influenced in shape and finally disappears under P.R.=1.40. Then the merged shock wave which has a characteristic of passage shock wave becomes the dominant factor of the unsteady pressure with quite large negative value.

5.5 Aerodynamic Stability Variation with Pressure Ratio

PSP has helped understanding the shock wave movement in oscillating cascade and validating CFD methods in unsteady pressure evaluation. For the analysis of aerodynamic stability based on system aerodynamic work, PSP measurement has limitation in the measuring range of blades which is only central 3 blade. In using influence coefficient method, the used blade number for calculation is directly related to the result accuracy. So, the unsteady aerodynamic work W calculation and stability analysis were conducted based on unsteady CFD results with periodic 11 blades.

5.5.1 Double Shocks Pattern (P.R.=1.25, 40Hz)

The unsteady aerodynamic work results under double shocks pattern are explained here.

As shown in Figure 5.15, by using the amplitude and phase of the unsteady aerodynamic forces on each blade, the total unsteady aerodynamic work of the cascade can be calculated as a curve with 5 order harmonics and changes with IBPA. At current low reduced frequency k=0.0156, there exists an IBPA range where W is greater than 0 and the cascade is aerodynamically unstable.

The point with maximum positive value of W is located at IBPA=114deg at 40Hz and the details of this point is shown in Figure 5.16 (a) and the integrated value of W done by each blade is shown in Figure 5.16 (b). Under the most unstable IBPA, the main positive W is sourced from blade +2, +1, and -1, while the main negative W is sourced from blade 0. The detailed location of positive and negative W influxes on blades surfaces can be found as follows.

- Positive work influxes
  - -1 S.S. : oblique shock wave and passage shock wave areas with the impact of hub side separation
  - +1 P.S. : L.E. supersonic area
  - +1 S.S. & +2 P.S. : passage shock wave area and the impact of tip clearance flow and hub side separation
  - 2 S.S. : passage shock wave area and impact of tip leakage flow

- Negative work influxes
  - -1 S.S. : interval area between double shocks
  - 0 S.S. : passage shock wave area with impact of tip leakage flow
  - +1 P.S. : passage shock wave area with impact of hub side separation

Then, W distribution acting on all blades was summarized into one blade by using influence coefficient method, as shown in Figure 5.16 (c). Two shock waves, tip clearance flow and P.S. supersonic area were considered the dominant factors of aerodynamic stability. By considering the 3D characteristics of current cascade, in the most unstable state, the influence of tip clearance flow on aerodynamic stability is overwhelmingly larger than hub side flow.

5.5.2 Merged Shocks Pattern (P.R.=1.40, 40Hz)

Similar analysis was done for merged shocks pattern based on the results shown in Figure 5.17 and Figure 5.18. The point with maximum positive value of W is located at IBPA=117deg at 40Hz and the main positive W is sourced from blade +1 and +2, while the main negative W is sourced from blade 0 and -1. The main unstable areas include the follows.

- Positive work influxes
  - +1~+2 P.S. : passage shock wave areas with impact of tip clearance flow
  - +1~+2 S.S.: merged shock wave areas with impact of tip leakage flow

- Negative work influxes
  - -1~ 0 S.S. : merged shock wave area

By summarizing the results into one blade, the dominant factors of aerodynamic stability were considered to be work done by passage shock wave on pressure side and also the influence of tip clearance flow.

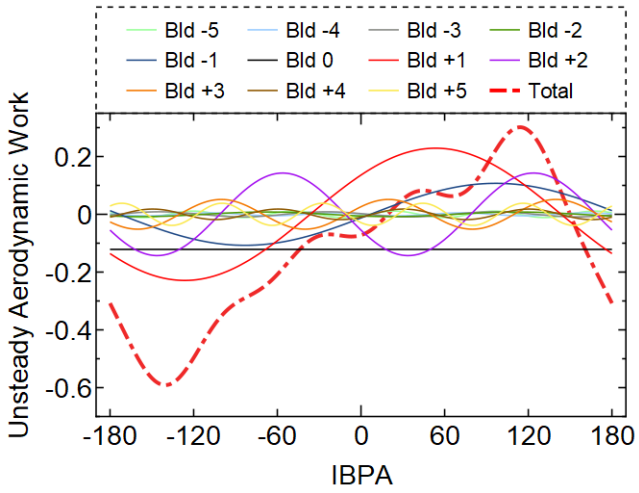

Figure 5.15 Unsteady aerodynamic work variation with IBPA (P.R.=1.25, 40Hz)

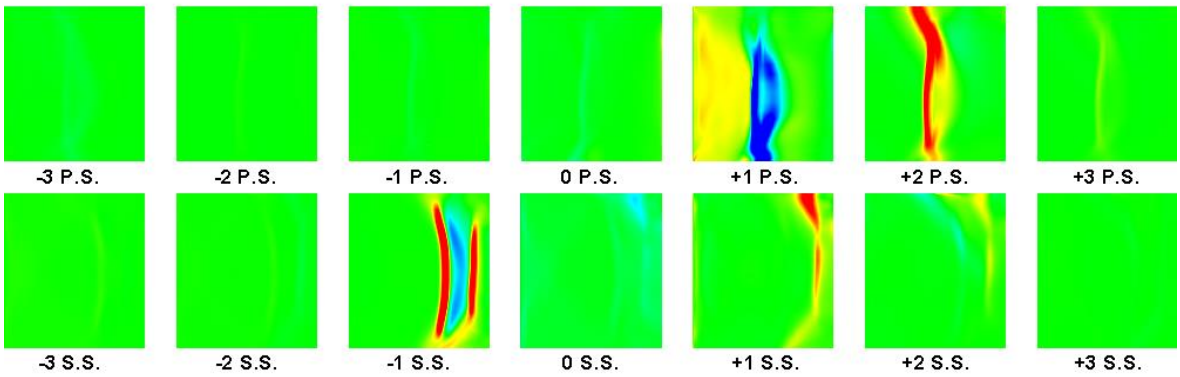

(a) Unsteady aerodynamic work distribution on each blade

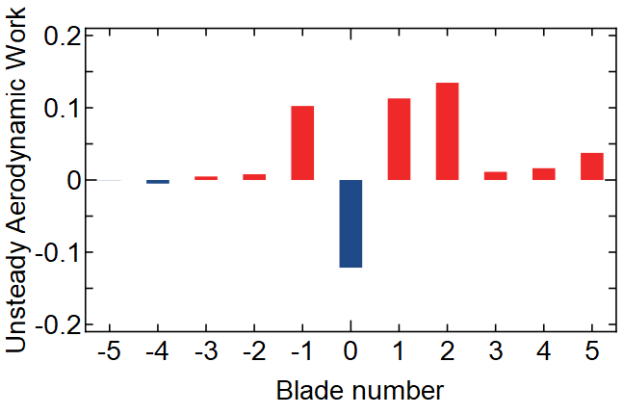

(b) Total work done by each blade

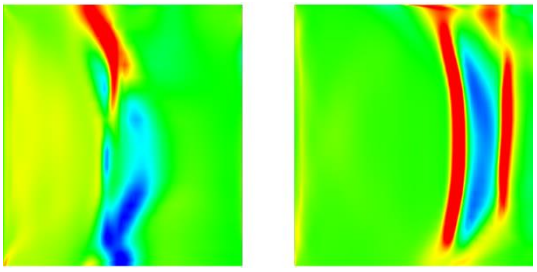

(c) Unsteady aerodynamic work distribution summrized into one blade

Figure 5.16 Unsteady aerodynamic work distribution on blade surface (P.R.=1.25, 40Hz)

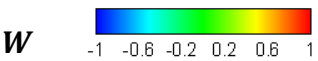

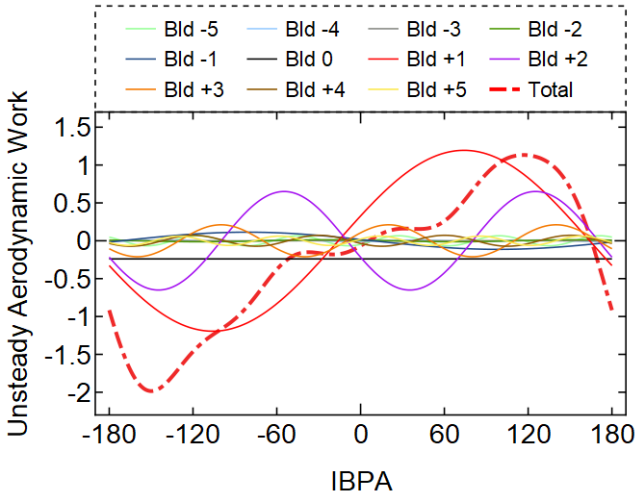

Figure 5.17 Unsteady aerodynamic work variation with IBPA (P.R.=1.40, 40Hz)

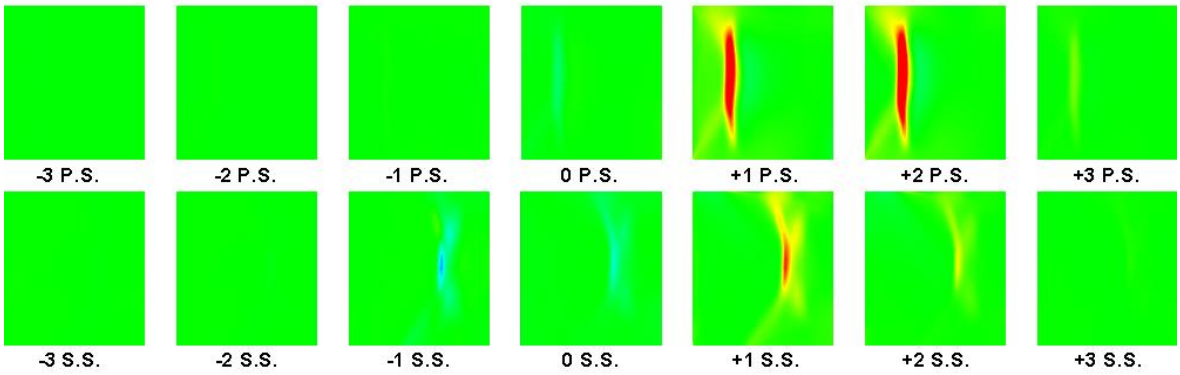

(a) Unsteady aerodynamic work distribution on each blade

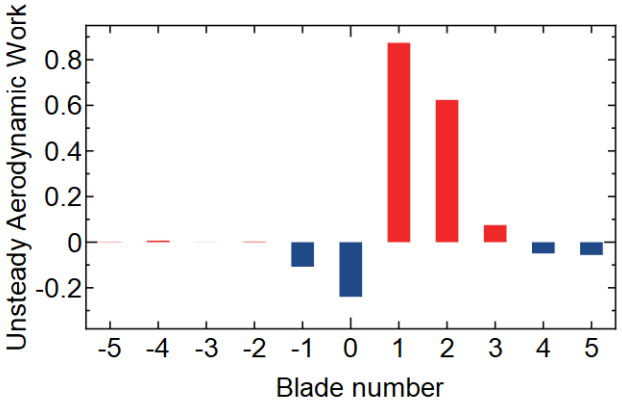

(b) Total work done by each blade

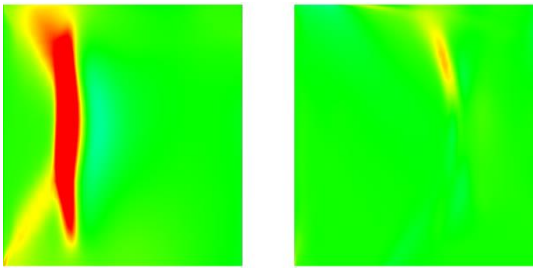

(c) Unsteady aerodynamic work distribution summrized into one blade

Figure 5.18 Unsteady aerodynamic work distribution on blade surface (P.R.=1.40, 40Hz)

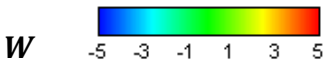

5.5.3 Unsteady Aerodynamic Work Change with Pressure Ratio

Then, the unsteady aerodynamic work variation with pressure ratio change was discussed based on the results of wider P.R. range at 40Hz.

Figure 5.19 shows the unsteady aerodynamic force distribution with blade number. With the increasing of pressure ratio, the amplitude of aerodynamic force shows an accelerated growth tendency, while the phase of downstream blades keep a similar shape with the values around alternative 0 or 180 degree. The most influenced blade by oscillating blade is blade +1 for all P.R. range. In higher P.R. range (1.35~detach), unsteady aerodynamic forces on blade 0 and blade +2 are also obviously affected by blade oscillation.

Figure 5.20 shows the total W change with IBPA. It shows that the maximum positive W increases drastically with P.R. increase and the corresponding IBPA value also has a tendency to increase with P.R.. The composition of maximum positive W on each blade is shown in Figure 5.21. Under higher P.R., W has a larger components on farer blades. Under P.R.=1.25, the positive W is mainly done by blade +1~+2; under P.R.=1.44, the positive W component on blade +1~+4 becomes dominant.

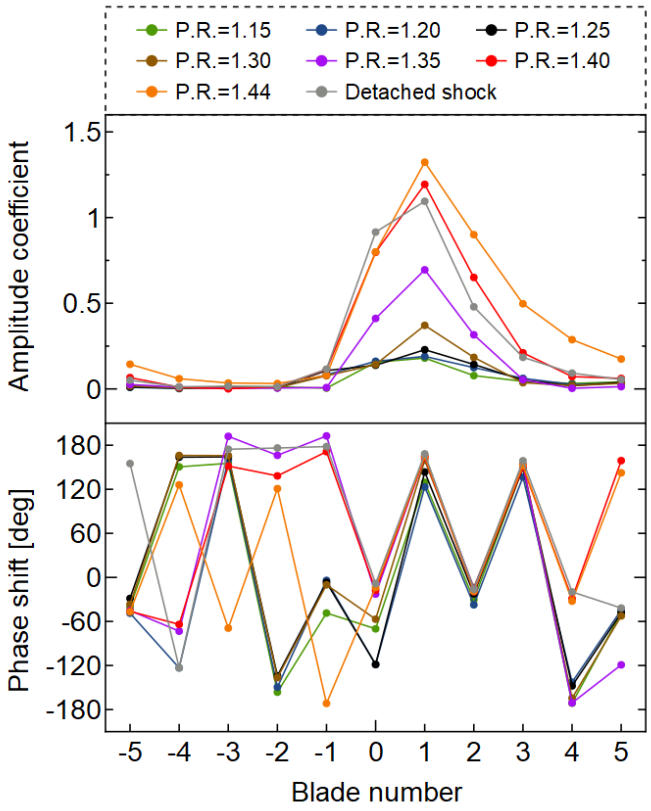

Figure 5.19 Unsteady aerodynamic force distribution with blade number (40Hz)

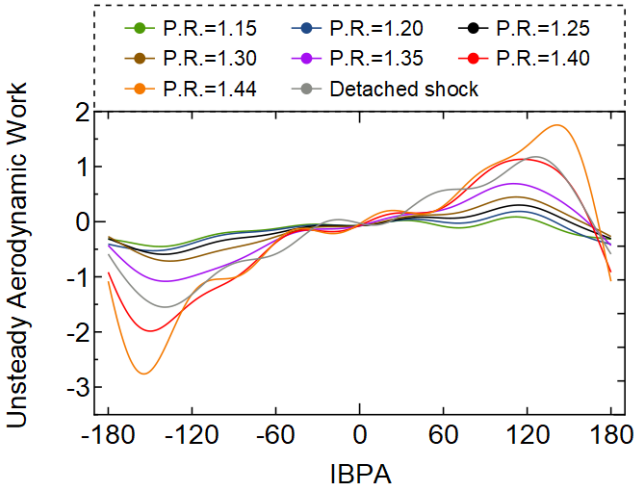

Figure 5.20 Unsteady aerodynamic work variation with P.R. (40Hz)

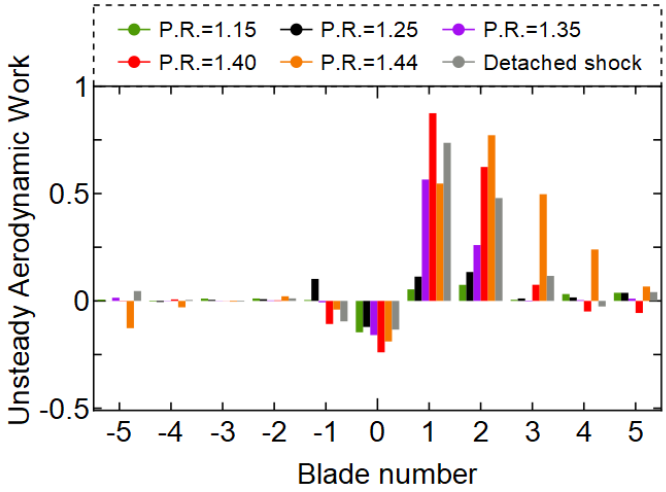

Figure 5.21 Unsteady aerodynamic work distribution with blade number (40Hz)

Figure 5.22 shows the W distribution at maximum W point summarized into one blade under different P.R. at 40Hz. Shock waves with impacts of wall effects considered as the dominant factors of aerodynamic instability. In lower pressure ratio range (choked flow/ double shocks pattern), the total W is of relatively small value and sourced from shock waves, P.S. supersonic area and tip clearance flow. In higher pressure ratio range (merged shocks pattern), the total W is of relatively large value and caused by passage shock wave and tip clearance flow. In detached shock case, P.S. is in subsonic condition and the leading edge has server positive W influx.

By considering the 3D characteristics of current cascade, the influence of tip clearance flow on aerodynamic stability is overwhelmingly larger than hub side flow. By synthetically analysing all the working conditions of DCA cascade, the leading edge area (0~0.3x/c) is most vulnerable to be affected by large unsteady aerodynamic work influxes, which is also a thin and weak part of the airfoil in view of structural mechanics.

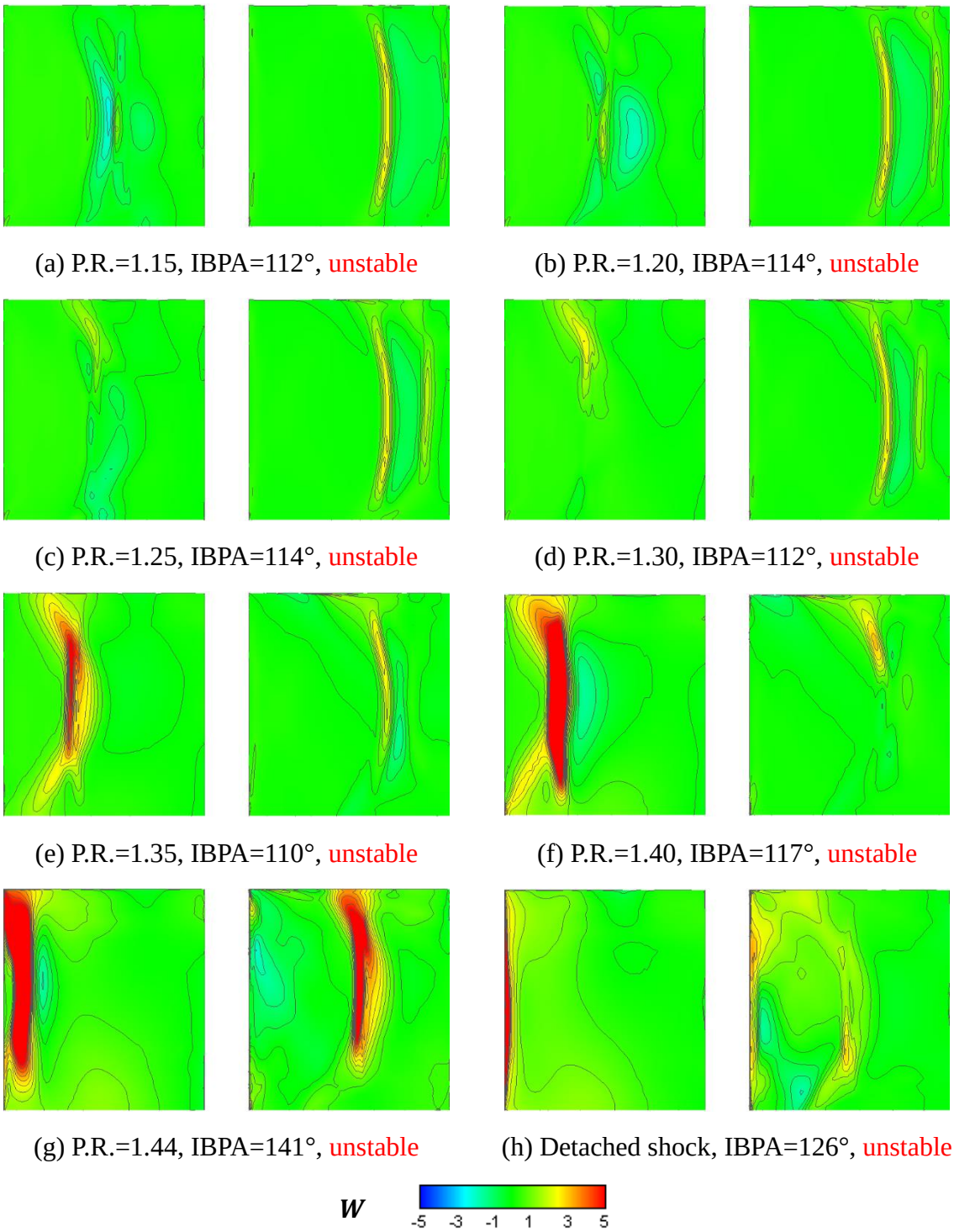

(a) P.R.=1.15, IBPA=112°, unstable

(b) P.R.=1.20, IBPA=114°, unstable

(c) P.R.=1.25, IBPA=114°, unstable

(d) P.R.=1.30, IBPA=112°, unstable

(e) P.R.=1.35, IBPA=110°, unstable

(f) P.R.=1.40, IBPA=117°, unstable

(g) P.R.=1.44, IBPA=141°, unstable

(h) Detached shock, IBPA=126°, unstable

Figure 5.22 Unsteady aerodynamic work distribution on blade surface (40Hz)

Finally, the excitation energy influx (unsteady aerodynamic work) into the oscillating cascade in one oscillation cycle was summarized into a counter as shown in Figure 5.23. The red line shows the demarcation line of stable and unstable areas. The horizontal axis is the static pressure ratio which indicates the evolution of shock pattern and also the load of the blade. The vertical axis is IBPA which indicates the vibration state of the cascade blades.

From this graph, it can be known that unstable states exist over all P.R. range at 40Hz. Under lower P.R. (1.15~1.20) there exist 2 unstable IBPA ranges which are around 30° and 110°. Under higher P.R. (≥1.25), the two ranges combines to one continuous range. The unstable IBPA range has tendency to expand with P.R. and the IBPA at peak energy influx point has an increasing tendency with P.R.. Besides, both the maximum and minimum of energy influx have increasing absolute values with P.R. increasing. The most dangerous states of the oscillating cascade is under high P.R. (1.35~1.44) with the IBPA range 80°~160°.

Generally speaking, the state of high pressure load on blade surface with merged shocks pattern is most dangerous to be aerodynamically unstable. And the unstable phenomenon is possible to occur when each oscillating blade has a phase shift of 80°~160° from upstream neighbour blade.

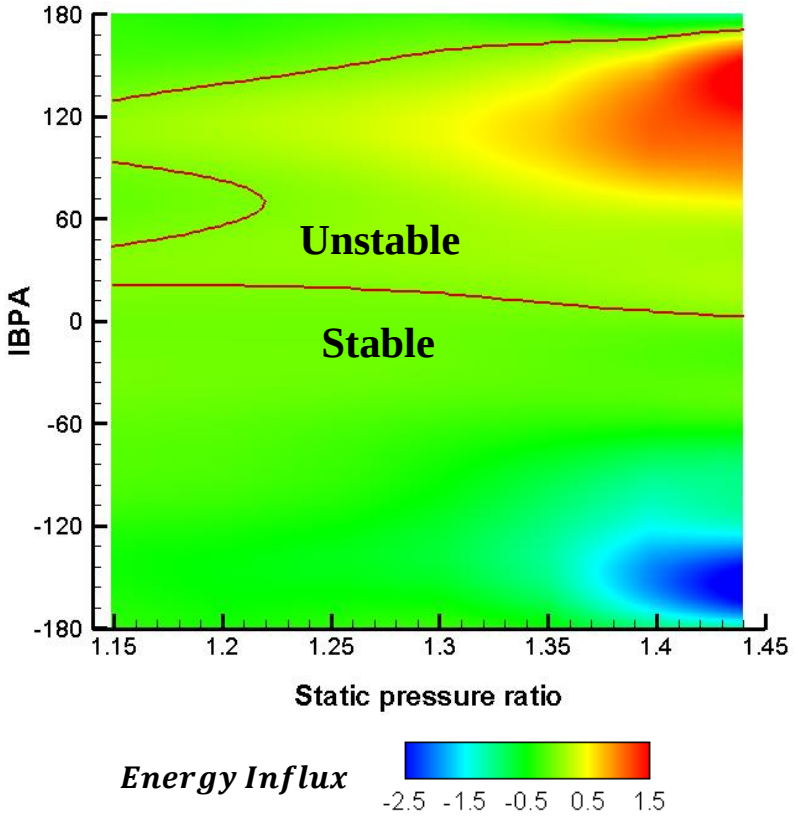

Figure 5.23 Excitation Energy Map of oscillating cascade (40Hz)

5.6 Aerodynamic Stability Variation with Oscillating Frequency

5.6.1 Double Shocks Pattern (P.R.=1.25)

Figure 5.24 shows the unsteady aerodynamic force distribution with blade number at different oscillating frequency. It shows that blade +1, 0, +2 are most influenced by central blade oscillation at lower frequency range. When the oscillating frequency is over 200Hz, the order of most influenced blades changes to blade 0, +1, +2. Phase shift of downstream blades +1~+3 has obvious tendency to delay with the increase of oscillating frequency. However, the phase shift of blade 0 keep almost constant which is not related to the oscillating frequency. So, it is considered that the unsteady phenomena acting on blade 0 is directly dominated by blade movement with quite faster response compared to the oscillating frequency.

Then, aerodynamic stability at more oscillating frequencies was analyzed and the results of maximum W which is confirmed by Figure 5.25 are shown in Figure 5.26. In low frequency range, the oscillating cascade is possible to be aerodynamically unstable. With the increasing of frequency, the maximum unsteady aerodynamic work decreases and the corresponding IBPA also decreases. In high frequency range, the cascade is stable in all IBPA range, while there are still some obvious positive work influx located in passage shock wave area. In lower frequency range, it shows spanwise contrary sign in tip and hub side. This is caused by the phase difference between shock wave and tip clearance flow.

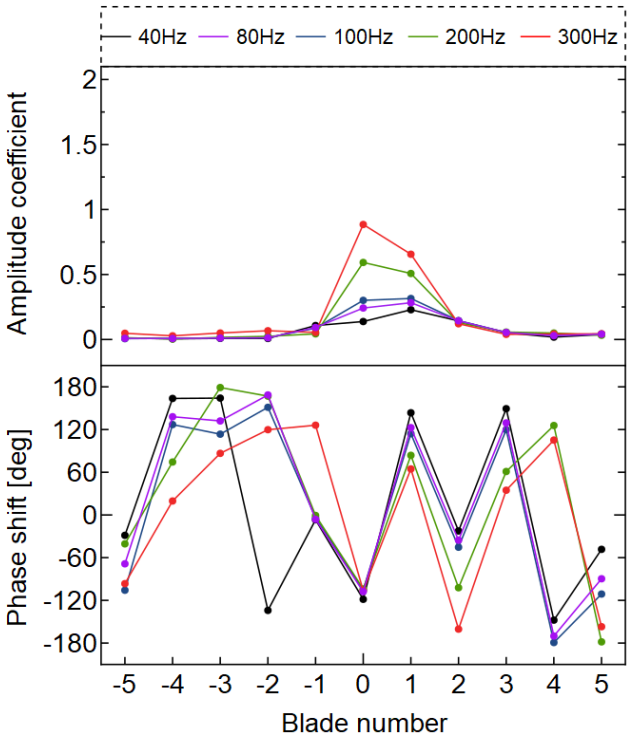

Figure 5.24 Unsteady aerodynamic forces distribution with blade number (P.R.=1.25)

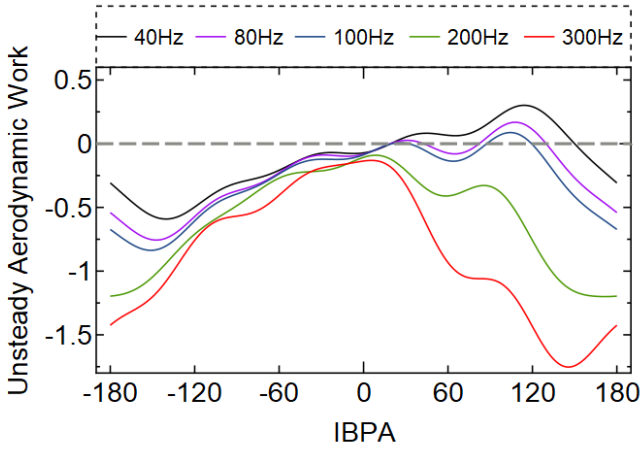

Figure 5.25 Unsteady aerodynamic work variation with oscillating frequency (P.R.=1.25)

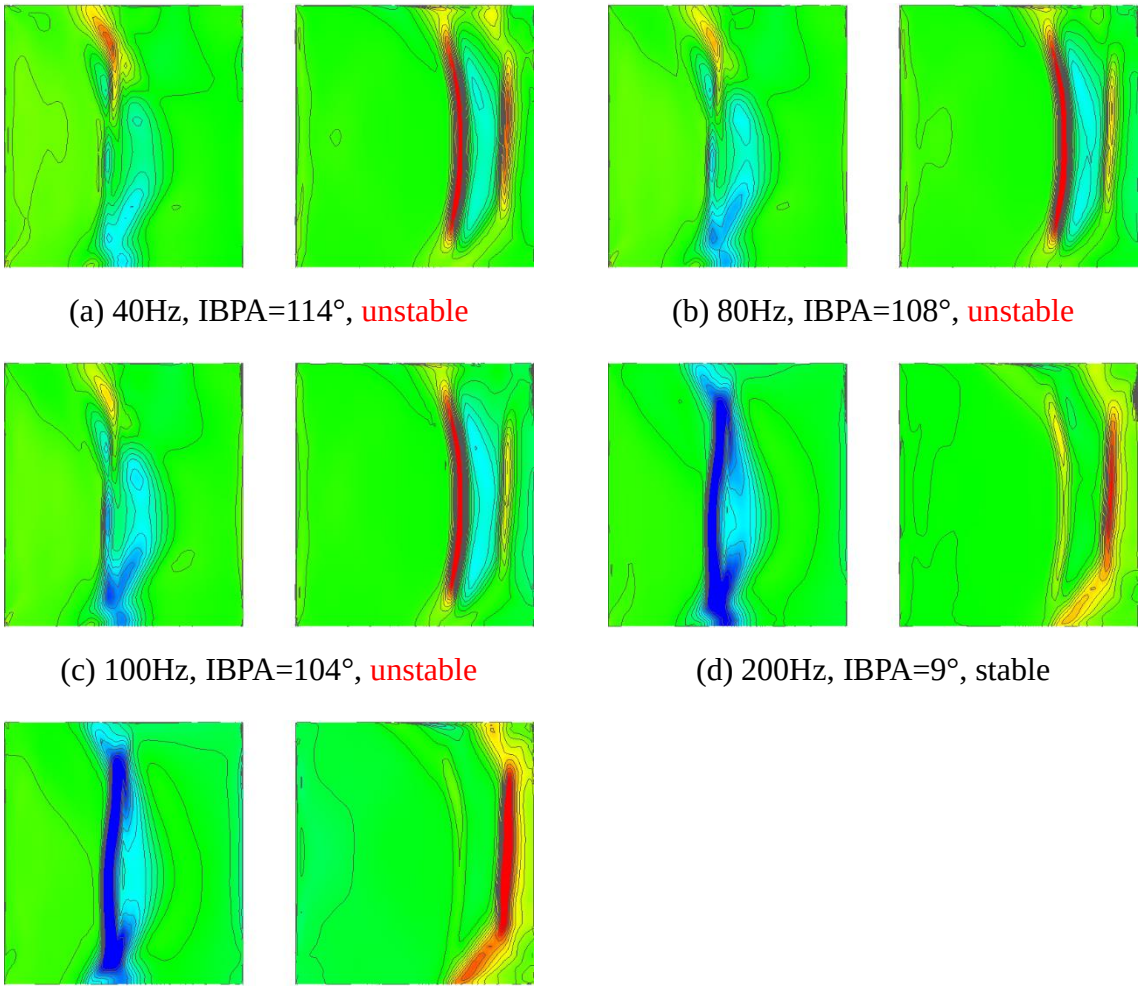

(a) 40Hz, IBPA=114°, unstable

(b) 80Hz, IBPA=108°, unstable

(c) 100Hz, IBPA=104°, unstable

(d) 200Hz, IBPA=9°, stable

(e) 300Hz, IBPA=6°, stable

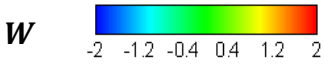

Figure 5.26 Unsteady aerodynamic work distribution on blade surface at different oscillating frequency (P.R.=1.25)

5.6.2 Merged Shocks Pattern (P.R.=1.40)

Also, the analysis was done for the merged shocks pattern, as shown in Figure 5.27~ Figure 5.29. It has a similar variation tendency with frequency. For both two cases, it can be found that with the increasing of oscillating frequency, the maximum aerodynamic force blade changes from blade +1 to blade 0 gradually. When the frequency is larger than 300Hz, the aerodynamic force of blade 0 is dominant in the cascade. The phase of blade 0 also delays with oscillating frequency increasing, which is different from double shocks pattern.

The stability characteristic of current case changes between 200Hz and 300Hz to be stable at all IBPA range. The frequency range of possible aerodynamic instability under merged shocks pattern is wider than the double shock pattern which becomes all IBPA stable at 200Hz. Both the total value and local values of unsteady aerodynamic work is also with quite larger value in this case. At high frequency range, the blade still has positive work influx in shock wave area.

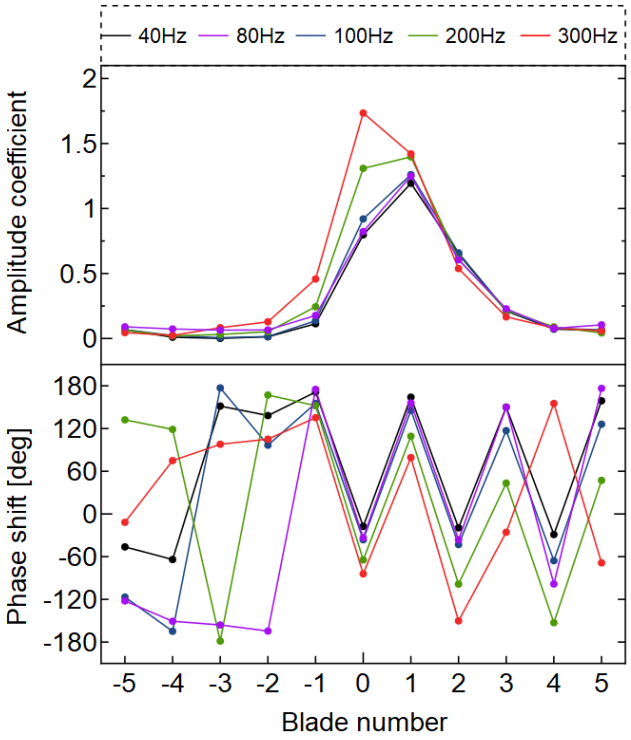

Figure 5.27 Unsteady aerodynamic forces distribution with blade number (P.R.=1.40)

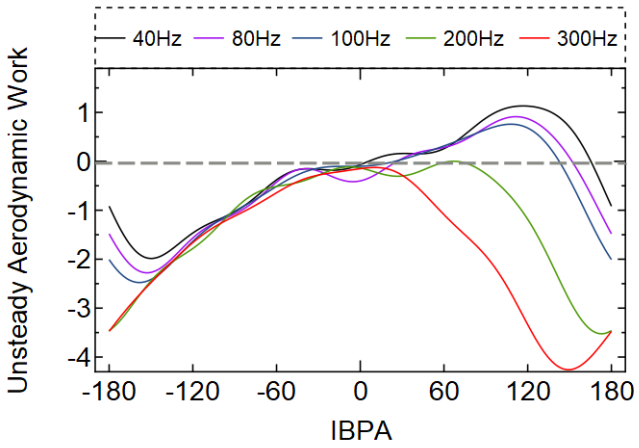

Figure 5.28 Unsteady aerodynamic work variation with oscillating frequency (P.R.=1.40)

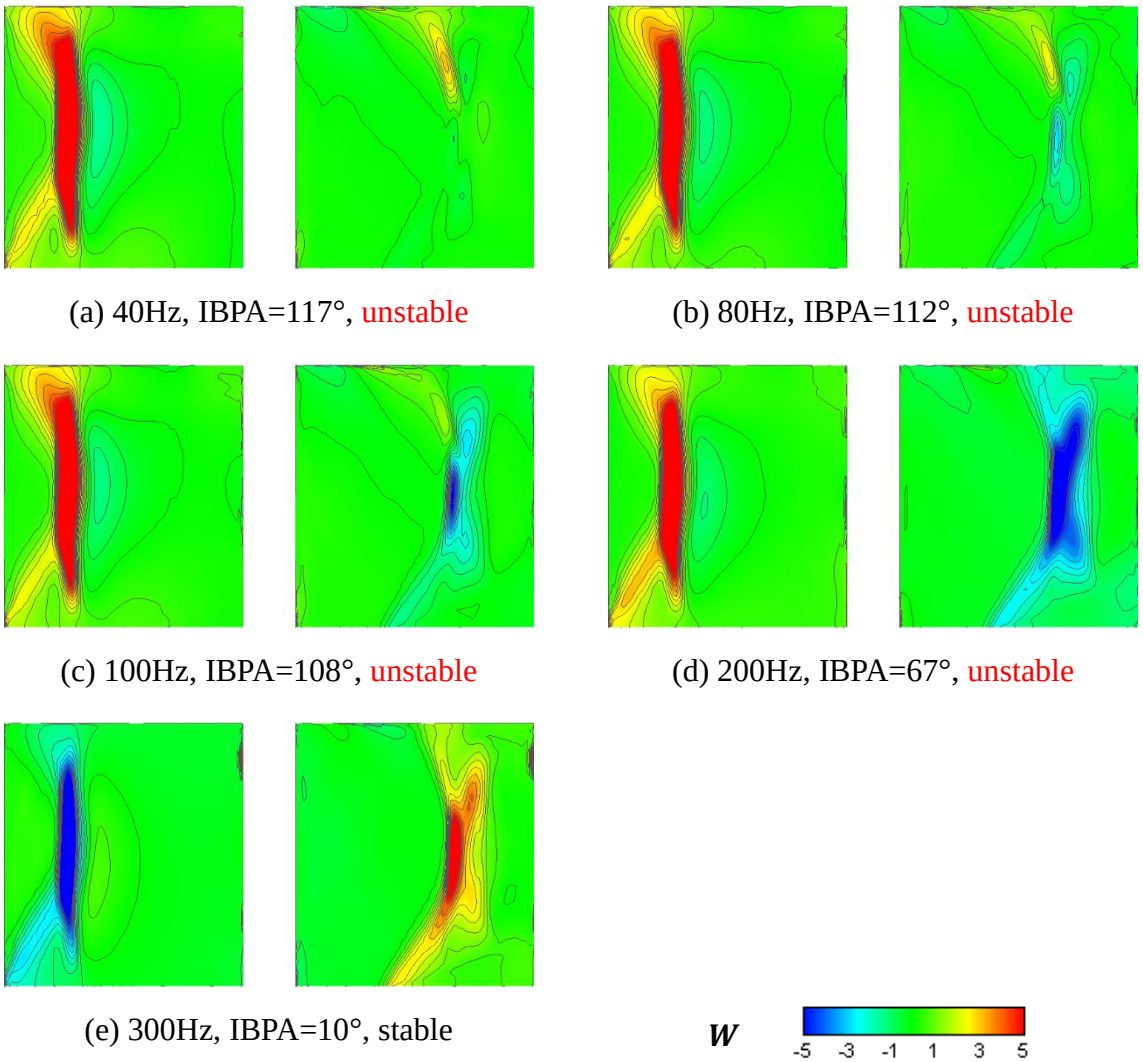

(a) 40Hz, IBPA=117°, unstable

(b) 80Hz, IBPA=112°, unstable

(c) 100Hz, IBPA=108°, unstable

(d) 200Hz, IBPA=67°, unstable

(e) 300Hz, IBPA=10°, stable

Figure 5.29 Unsteady aerodynamic work distribution on blade surface at different oscillating frequency (P.R.=1.40)

The reason of stable condition at all IBPA range is illustrated here. Figure 5.30 shows the unsteady work done by each blade at maximum W point under different P.R. and oscillating frequency. At 40Hz, W done by blade 0 is too small to determine the stability of the system. In some IBPA range, downstream blade can do the overwhelming positive unsteady aerodynamic works to destabilize the cascade. On the contrary, with the increase of oscillating frequency, the aerodynamic response of blade 0 increases faster than other stationary blades. So, there exists a point where the blade 0 becomes the dominant factor of the aerodynamic stability. For example, at 300Hz, the negative W done by blade 0 can counteract all the positive works done by other blades, so the system become all IBPA range stable.

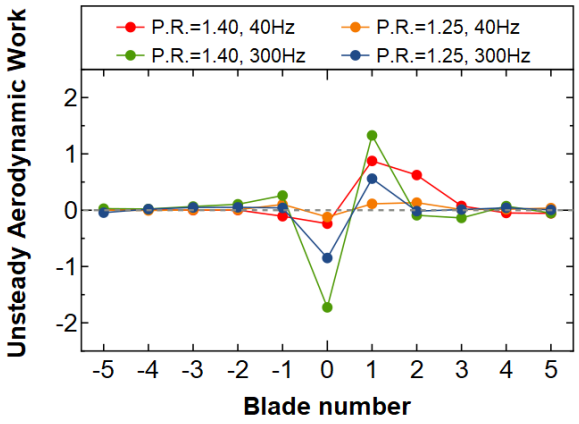

Figure 5.30 Comparison of unsteady aerodynamic works done by oscillating blade

5.7 Summary

In this chapter, unsteady aerodynamic characteristics and aerodynamic stability of oscillating cascade were analyzed based on experimental and numerical results.

(1) Unsteady surface pressure distribution on blade surface were measured with PSP technique, which helped understanding unsteady behavior of shock waves. Unsteady pressure obtained by CFD showed qualitative agreements with PSP, while the results in shock wave areas also showed quantitative accordance.

(2) The shock wave moving direction of double shocks pattern and merged shocks pattern is different due to different mass flowrate characteristics. The displacement of passage shock foot under merged shock pattern is quite larger than double shocks pattern.

(3) The amplitude of unsteady dynamic forces has a tendency of accelerated growth with pressure ratio increase. Oscillating blade has wider influence range on the cascade blades under higher pressure ratio and mainly influences on the downstream blade passage.

(4) Aerodynamic stability of transonic oscillating compressor cascade was analyzed by using influence coefficient method. Shock waves with the influence of wall effects were considered as the dominant factors of aerodynamic instability. In low reduced frequency range, the oscillating cascade is possible to be aerodynamically unstable. In low pressure ratio range, the total work is of relatively small value and sourced from shock waves, P.S. supersonic area and wall effects; in high pressure ratio range, the total work is of relatively large value and caused by the work done by passage shock on pressure side.

Chapter 6 Conclusions and Prospects of Future Research

6.1 General Conclusions

(1) The 2D spatial unsteady behavior of shock waves acting on blade surface were successfully observed and quantitatively measured with AA-PSP technique, which is newly in the research field of cascade flutter.

- ✓ "Automatic blade positioning" technique was proposed for image processing of PSP images taken by high speed camera.
- ✓ PSP was applied in steady and unsteady pressure measurement on oscillating compressor cascade in a transonic flow and validated by conventional methods.
- ✓ The movement of shock waves was observed under different working condition, which is very meaningful and essential for understanding cascade flutter phenomena and verifying the CFD methods.

(2) Steady flow fields with different shock pattern were illustrated based on experimental and numerical approaches.

- ✓ Steady flow field under different pressure ratio was visualized by schlieren and oil flow methods. The dominant factors in the flow field were discussed in details.
- ✓ Pressure results obtained by PSP and CFD have good accordance with conventional methods. Detailed pressure distribution caused by shock waves and wall effects were clarified.
- ✓ Shock wave structure in current transonic compressor cascade was classified into 4 types: choked flow/ double shocks/ merged shocks/ detached shock patterns.
- ✓ The characteristics of mass flowrate, flow angle and total pressure loss of each pattern were analyzed for comprehensively understanding the flow phenomena.

(3) Unsteady pressure distribution and propagation characteristics in oscillating cascade under different working condition were obtained and analyzed.

- ✓ PSP results showed qualitative agreements with CFD results, while the results in large pressure fluctuation areas (around shock wave feet areas) also showed quantitative accordance.
- ✓ The shock wave movement with blade oscillation was observed by PSP technique. The moving direction of double shocks pattern and merged shocks pattern is almost in reverse direction due to different mass flowrate characteristics. The displacement of passage shock feet under merged shock pattern is quite larger than double shocks pattern.
- ✓ Unsteady pressure distribution and its propagation mechanisms were discussed. The oscillation of shock waves is the dominant sources of unsteady pressure. Unsteady pressure amplitude has a tendency of accelerated growth with pressure ratio increase. Tip clearance flow enhances the pressure propagation towards downstream blade. The impact range of oscillating blade under merged shocks pattern is wider than double shocks pattern.

(4) Aerodynamic stability of transonic oscillating compressor cascade was analyzed by using influence coefficient method.

- ✓ Movement of shock waves and the influence of wall effects were considered as the dominant factors of aerodynamic instability.
- ✓ In low reduced frequency range, there exits an IBPA range where the oscillating cascade is aerodynamically unstable. The maximum positive unsteady aerodynamic work has a tendency of increasing with pressure ratio. The unsteady aerodynamic work distribution on blade surface was analyzed only at maximum work point. In low pressure ratio range (choked flow/ double shocks), the total work is of relatively small value and sourced from shock waves, tip clearance flow and P.S. supersonic area; in high pressure ratio range, the total work is of relatively large value and is dominated by the work done by passage shock on pressure side and tip clearance flow. In detached shock case, P.S. is in subsonic condition and the leading edge also has server positive work influx.
- ✓ In low reduced frequency range, by considering all the working conditions of current cascade, the leading edge area (0-0.3x/c) is vulnerable which is possible to be affected by large unsteady aerodynamic work influx, which is also thinnest part of the airfoil.
- ✓ In high reduced frequency range, the cascade is stable in all IBPA range, while there are still some obvious positive work influx located in passage shock foot area.

6.2 Future Prospects

In this study, the unsteady pressure measurement conducted by PSP was mainly focused on low reduced frequency range ($k < 0.06$), which is limited by the vibration characteristics of the blade made of aluminum alloy. Due to the time response capability of AA-PSP, it can capture high frequency pressure fluctuation more than 1 kHz. Also, current magnetic oscillator can produce oscillation on order of 1 kHz.

Furthermore, the flutter phenomena at high reduced frequency range are more complicated and essential for comprehensive understanding of their mechanisms. The 2D spatial unsteady pressure distribution for high reduced frequency cases is strongly expected for the improvement of flutter study and CFD verification.

According to these points and the conclusion of current study, the unsteady pressure measurement by PSP is desired to conduct at higher oscillating frequency range. Either selecting another solid blade profile or increasing the natural frequency of DCA blade is considered for experimental preparation.

References

[1] https://www.geaviation.com/commercial/engines/ge90-engine

[2] Srivastava, R., Panovsky, J., Kielb, R., Virgin, L. and Ekici, K., “Non-Linear Flutter in Fan Stator Vanes with Time Dependent Fixity”, ASME paper, GT2010-22555, 2010

[3] Kielb, R. E. and Imregun, M., “NASA Aeroelasticity Handbook Volume 2: Design Guides Part 2, Chapter: Aeroelasticity in Axial Flow Turbomachines”, NASA TP 2006-212490 Vol2/Part2, 2006

[4] Kielb, R. E., Barter, J. W., Thomas, J. P., and Hall, K. C., “Blade Excitation by Aerodynamic Instabilities- a Compressor Blade Study”, ASME Paper, GT-2003-38634, 2003

[5] McGee III, O.G., Fang, C., and El-Aini, Y., “A Reduced-Order Meshless Energy Model for the Vibrations of Mistuned Bladed Disks-Part I: Theoretical Basis”, Journal of Turbomachinery, Vol.135, 061001-1, 2013

[6] Sisto, F., “AGARD Manual on Aeroelasticity in Axial-flow Turbomachines Volume 1 Unsteady Turbomachinery Aerodynamics”, AGARD-AG-298, pp.1-2, 1987

[7] Carta, F. O., “Coupled blade-disk-shroud flutter instabilities in turbojet engine rotors”, ASME Journal of Engineering for Power, 89(3), 419-426, 1967

[8] Bendiksen, O. O., “Aeroelastic problems in turbomachines”, AIAA-90-1157, 1990

[9] Lane, F., “System mode shapes in the flutter of compressor blade rows”, Journal of the Aeronautical Sciences, 23(1): 54-66, 1956

[10] Hanamura, Y., Tanaka, H. and Yamaguchi, K., “A simplified Method to Measure Unsteady Forces Acting on the Vibrating Blades in Cascade”, Bulletin of JSME, Vol. 23, No.180, pp. 880-887, 1980

[11] 渡辺紀徳,“ガスタービンの空力弾性問題における CFD 解析”,日本ガスタービン学会誌, Vol.32, No.4, 2004, pp278-284

[12] Szechenyi, E., Cafarelli, I., Notin, C., Girault, J.P., “A straight cascade wind-tunnel study of fan blade flutter in started supersonic flow”, proceeding of the Third International Symposium: Unsteady Aerodynamics of Turbomachines and Propellers, Cambridge Univ., pp.447-458, 1984

[13] 小林紘, 生沼秀司, “曲げ振動する遷音速圧縮機環状翼列に作用する非定常空気力の測定 (第 2 報)”, ガスタービン学会誌, vol.19, No.75, 1991

[14] Watanabe, T. and Kaji, S., “Experimental Study on Unsteady Aerodynamic Characteristics of an Oscillating Cascade with Tip clearance”, JSME International Journal, Series II, Vol.31, No.4, 1988

[15] Watanabe, T. and Kaji, S., “Theoretical Study on Unsteady Aerodynamic Characteristics of an Oscillating Cascade with Tip clearance (In the Case of a Nonloaded Cascade)”,

JSME International Journal, Series II, Vol.32, No.3, 1989

[16] Watanabe, T. and Kaji, S., “Theoretical Study on Unsteady Aerodynamic Characteristics of an Oscillating Cascade with Tip clearance (In the Case of Loaded Cascade)”, JSME International Journal, Series II, Vol.35, No.1, 1992

[17] 柴田貴範, “遷音速翼列フラッターに関する研究”, 東京大学博士論文, 1996

[18] 青塚瑞穂, “高亜音速/遷音速流中で剥離を伴う振動翼列の空力特性に関する研究”, 東京大学博士論文, 2002

[19] Yang, H. and He, L., “Experimental Study on Linear Compressor Cascade with Three-Dimensional Blade Oscillation”, Journal of Propulsion and Power, Vol. 20, No. 1, pp. 180-188, 2004

[20] Bell, D.L. and He, L., “Three-Dimensional Unsteady Flow for an Oscillating Turbine Blade and the Influenceof Tip Leakage”, Journal of Turbomachinery, Vol.122, (2000), pp93-101

[21] Vogt, D., “Experimental Investigation of Three-Dimensional Mechanisms in Low-Pressure Turbine Flutter”, Ph.D. Thesis, Royal Institute of Technology KTH, Stockholm, Sweden, 2005

[22] Liu, T. and Sullivan, J.P., “Pressure and Temperature Sensitive Paint”, Springer, New York, 2005

[23] Gregory, J. W., Sakaue, H., Liu, T., and Sullivan, J.P., 2014, “Fast Pressure-Sensitive Paint for Flow and Acoustic Diagnostics”, Annu. Rev. Fluid Mech., 46(1), pp. 303-330

[24] Sakaue, H. and Sullivan, J.P., “Fast Response Time Characteristics of Anodized Aluminum Pressure Sensitive Paint”, 38th Aerospace Sciences Meeting and Exhibit, Reno, NV, AIAA 2000-0506, 2000

[25] Sakaue, H., “Anodized Aluminum Pressure Sensitive Paint for Unsteady Aerodynamic Applications” Ph.D. Thesis, Purdue University, USA, 2003

[26] Kameda, M., Tabei, T., Nakakita, K., Sakaue, H. and Asai, K., 2005, “Image measurements of unsteady pressure fluctuation by a pressure-sensitive coating on porous anodized aluminium”, Measurement Science and Technology, 16(2005), 2517-2524

[27] Engler, R., Mérienne, M.C., Klein, C. and Sant, Y., “Application of PSP in low speed flows”, Aerospace Science and Technology 6 (2002) 313-322, 2002

[28] Klein, C., Henne, U., Sachs, W. E., Egami, Y. and Mai, H., “Application of Pressure-Sensitive Paint for Determination of Dynamic Surface Pressures on an Oscillating 2D profile in Transonic Flow”, 46th AIAA Aerospace Sciences Meeting and Exhibit7 - 10 January 2008, Reno, Nevada, AIAA 2008-278, 2008

[29] Zare-Behtash, H., Gongora-Orozco, N. and Kontis, K., “PSP Visualization Studies on a Convergent Nozzle with an Ejector System”, Journal of Visualization, Vol. 11, No. 1 (2008)1-7, 2008

[30] Morita, K., Suzuki, K., Imamura, O. and Sakaue, H., “Temperature-Cancelled Anodized-Aluminum Pressure Sensitive Paint for Hypersonic Wind Tunnel Application”, 41st AIAA Fluid Dynamics Conference and Exhibit, Honolulu, Hawaii, AIAA 2011-3724, 2011

[31] Gregory, J.W., “Porous Pressure-Sensitive Paint for Measurement of Unsteady Pressures in Turbomachinery”, AIAA paper 2004-0294, 2004

[32] Kitamura, T., Kameda, M., Watanabe, W. and Horimoto, K., “Measurement of Unsteady Pressure Field in a Turbocharger Compressor Using Pressure-Sensitive Paint”, ASME paper, GT2018-76267, 2018

[33] Liu, T., Torgerson, S., Sullivan, J., Johnston, R. and Fleeter, S., “Transonic Rotor Blade Pressure Measurement Using Fluorescent Paints”, Journal of Propulsion and Power, Vol. 18, No.2 (2002), pp.491-493

[34] Fonov, S.D., Engler, R.H., Klein, Chr., Mihailov, S.V., Mosharov, V.E., Kulesh, V.P., Radchenko, V.N. and Schairer, E., “Pressure Sensitive Paint for Oscillating Pressure Fields Measurements”, IEEE, 1999

[35] Okabe, T., Miyazaki, T., Saitoh, K. and Sakaue, H., “Unsteady Pressure Distribution on a Fluttering Airfoil using Motion-Capturing PSP System”, 44th AIAA Thermophysics Conference, AIAA 2013-3014, 2013

[36] Watanabe, T., Azuma, T., Uzawa, S., Himeno, T. and Inoue, C., “Unsteady Pressure Measurement on Oscillating Blade in Transonic Flow Using Fast-Response Pressure-Sensitive Paint”, Journal of Turbomachinery, Vol. 140, 061003-1, 2018

[37] Hall, K. C., Thomas, J. P., and Clark, W. S., “Computation of unsteady nonlinear flows in cascades using a harmonic balance technique”, AIAA Journal, 40(5), 2002

[38] Hall, K., and Ekici, K., “Multistage coupling for unsteady flows in turbomachinery”, AIAA Journal, 43(3), 624–632, 2005

[39] Ekici, K., and Hall, K., “Nonlinear frequency-domain analysis of unsteady flows in turbomachinery with multiple excitation frequencies”, AIAA Journal, 46(8), 1912–1920, 2008

[40] Isomura, K., and Giles, M., “A Numerical Study of flutter in a Transonic Fan”, Journal of turbomachinery, Vol. 120, No. 3, pp. 500-507, 1998

[41] Srivastava, R., Bakhle, M., Keith Jr, T., and Stefko, G., “Flutter Analysis of a Transonic Fan”, NASA/TM 2002-211818, 2002

[42] Vahdati, M., Simpson, G., Imregun, M., “Mechanisms for Wide-Chord Fan Blade Flutter”, ASME Paper, GT2009-60098, 2009

[43] Aotsuka, M. and Murooka, T., “Numerical Analysis of Fan Transonic Stall Flutter”, ASME paper, GT2014-26703, 2014

[44] Funatogawa, O., “Research and Technology Development in Japanese Environmentally Compatible Engine for Small Aircraft Project”, ISABE-2005-1010, 2005.

[45] 立石敦, “流体構造連成とモード同定による多自由度翼列フラッター解析の研究”, 東京大学博士論文, 2015

[46] Duquesne, P., Rendu, Q., Ferrand, P. and Aubert, S., “Local Contribution of Blades Vibration on the Choke Flutter Stability in Transonic UHBR Fan”, 53rd 3AF International Conference on Applied Aerodynamics, France, 2018

[47] 嶋英志, 城之内忠正, “設計における数値解析の活用ついて(その 12) ~一粒子的風

上法とその検証~", 航空宇宙技術研究所特別資料 27 号, 第 12 回航空機計算空気力学シンポジウム論文集, pp.255-260, 1994

[48] 嶋英志, "圧縮性 CFD による低マッハ数流れ計算のための新しい陰的時間積分法", 第 25 回数値流体力学シンポジウム, 2011

[49] Giles, M. B., "Nonreflecting Boundary Conditions for Euler Equation Calculations", AIAA Journal, Vol.28, No.12, 1990

[50] Weber, A., Schreiber, H., Fuchs, R. and Steinert, W., "3-D Transonic Flow in a Compressor Cascade With Shock-Induced Corner Stall", Journal of Turbomachinery, Vol.124, pp.358-366, 2002

[51] Flaszynski, P., Doerffer, P., Szwaba, R., Kaczynski, P. and Piotrowicz, M., "Shock Wave Boundary Layer Interaction on Suction Side of Compressor Profile in Single Passage Test Section", Journal of Thermal Science, Vol.24, No.6(2015), pp.510-515, 2015

[52] Liu, B., Shi, H. and Yu, X., "A new method for rapid shock loss evaluation and reduction for the optimization design of a supersonic compressor cascade", Journal of Aerospace Engineering, Vol. 232(13), pp.2458-2476, 2018

[53] Chan W. M., Kim N., and Pandya S. A., "Advances in domain connectivity for overset grids using the X-rays approach", ICCFD7-1201, 2012

[54] Tateishi, A., Watanabe, T., etc., "Numerical method for an assessment of steady and motion-excited flowfields in a transonic cascade wind tunnel", Journal of the Global Power and Propulsion Society, 1:171-183, 2017

Appendix A: AA-PSP Technique

A.1 AA-PSP Theory and Making Procedure

A.1.1 Chemical Theory of AA-PSP

The essential mechanism of PSP can be described as a process which the luminophore molecules are excited to an elevated energy state, when illuminated by a light source with effective wavelength range. It can be described by the Jablonski energy-level diagram shown in Figure A.1. The lowest horizontal line represents the ground-state energy of the molecule, which is normally a singlet state denoted by S_0. The upper lines are energy levels for the vibrational states of excited electronic states. The successive excited singlet and triplet states are denoted by S_1 and S_2, and T_1, respectively. As is normally the case, the energy of the first excited triplet state T_1 is lower than the energy of the corresponding singlet state S_1.

The excited luminophores return to the ground state through a combined process of luminescence and radiationless decay. Luminescence arises when the photon emission occurs between states of the same spin state (e.g. $S_1 \rightarrow S_0$). Radiationless decay (or phosphorescence) which causes energy loss occurs when the spin state of the initial energy level is different from the final one (e.g. from $T_1 \rightarrow S_0$). The radiationless decay includes oxygen quenching and energy transfer. Oxygen quenching is the major photophysical mechanism of PSP, where the excited energy of the sensor molecules is transferred to the surrounding oxygen molecules. As a result, the luminescent intensity is reduced when the oxygen concentration increases.

The lifetime of a PSP formulation is the mean time required for the luminescent molecules to return to their ground state after being excited to a higher energy level, and can be described by the given reciprocal of the rate constant of the corresponding process. The response of the luminescent emission, after being excited by an excitation source, can be described as a first order system,

$$I(t) = Ae^{-\frac{t}{\tau}} \tag{A.1}$$

where τ is the luminescent lifetime of the paint, I is the luminescent intensity, t is the elapsed time, and A is a constant. The lifetime constant, τ, can be calculated by statistically fitting the luminescent intensity values as an exponential curve. An alternate way of obtaining the lifetime constant is to take the inverse of the slope of the linear relationship between the natural log of I and t. From eqn.(A.1), we get

$$ln(I) = -\frac{1}{\tau}t + ln(A) \tag{A.2}$$

The lifetime of luminescent molecules is an important property to consider before conducting an experiment using PSP methods because camera exposures are dependent on this parameter. If the lifetime of the paint is of the same order as the oscillation period of the pressure gradient

over the test model, significant blurring will be observed in the PSP data. This blurring is due to insufficient frequency response to the unsteady pressure changes since a luminescent molecule will not react to pressure changes until the molecule has relaxed back to its ground state. Therefore, the lifetime of the luminophore should be at least two orders of magnitude faster than the pressure oscillation frequency of interest.

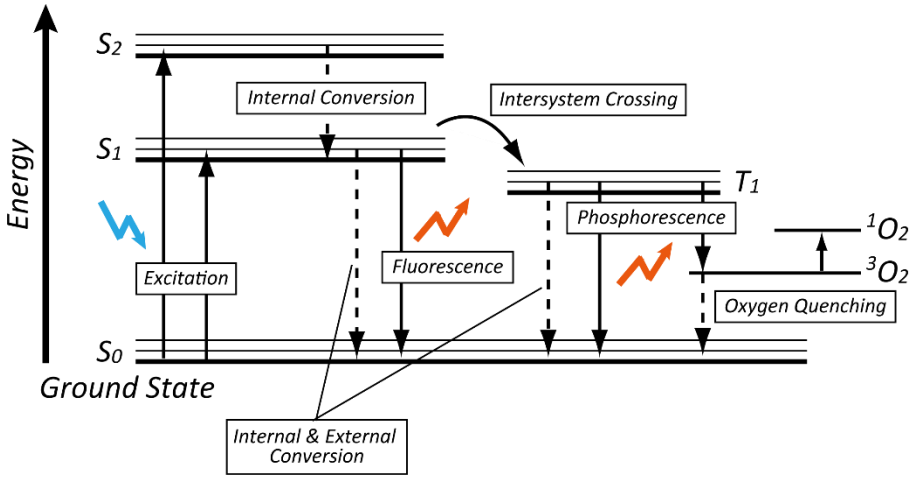

Figure A.1 Jablonski energy-level diagram

A.1.2 Structure of AA-PSP

AA-PSP is a porous PSP using an anodized aluminum layer as a porous supporting matrix for the luminophore. It provides an ordered pore structure as schematically shown in Figure A.2. The pore diameter is around 20~100nm. In aerodynamic measurement, AA-PSP is smooth enough because the pore diameter is much smaller than the mean free path of most aerodynamic test conditions. The layer is directly coated on an aluminum model anodization process which belongs to electrochemical processing. This process can be coated on a complex shape by making the layer thickness to be several microns. In this study, bathophen ruthenium is applied as the luminophore to give off luminenscence. Ruthenium complex consists of a ruthenium ion coordinated by organic ligands. The excitation and emission (luminescence) spectra of the luminophore and its structure is shown in Figure A.3. Ruthenium group can be excited in visible region. Ruthenium complexes have relatively high photo-stability and ignorable temperature dependency.

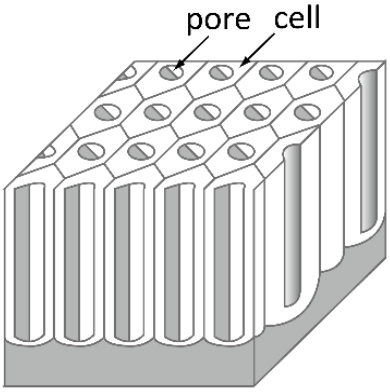

Figure A.2 Schematic of porous aluminum layer

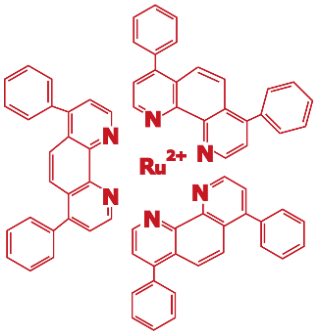

(a) Molecular structure

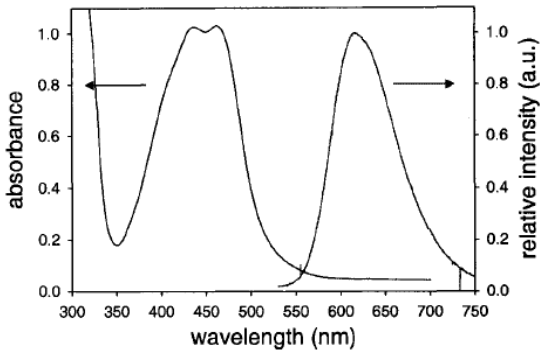

(b) Absorption and luminenscence spectra of Ruthenium complex based AA-PSP [25]

Figure A.3 Molecular structure and light characteristics of Ruthenium complex

A.1.3 Making Procedure of AA-PSP

Anodized-Aluminum Pressure-Sensitive Paint (AA-PSP) is used in our wind tunnel experiment with oscillating cascade. According to Sakaue et al [24], AA-PSP has the fastest response time, which is reported 34.8 μs. PSP blade is made from aluminum alloy, Al5052. Porous aluminum layer on the blade surface is produced by anodization treatment. In order to create uniformly distributed micro pores, it is necessary to conduct careful pre- and post-treatments. The procedure is shown in Figure A.4 and described as follows.

(1) Wiping

At first, degreasing of an aluminum surface is done with ethanol.

(2) Pre-treatment

Then the model is soaked for 5 min in dilute sodium hydroxide solution (2%wt), wash with distilled water and dry in a desiccator at least 15 min.

(3) Anodization

The model is anodized at constant current density of 12.5 mA/cm^2 in dilute sulfuric acid (1mol/L), which is kept at a constant temperature of about 17°C. Then the model is treated as an anode and the cathode is made from the same material as that the model. The applied voltage is about 20 V, which depends on the solution temperature. Continuous stirring is needed to keep uniform concentration and temperature of solution during anodization. After anodization, the model is washed with distilled water and soaked in dis-tilled water for 5 min. Then, the model is washed with dis-tilled water again and dried in a desiccator more than 30 min.

(4) Post-treatment

In order to remove hydrates or oxidation layer from the anodized surface, the model is soaked in a phosphoric acid (3%wt) for 20 min at a constant temperature (30°C). Then, the model is washed with distilled water and is again soaked in distilled water for 5 min. This process is

repeated two times. Finally, the model is washed with distilled water and is dried in a desiccator for more than 3 days.

(5) Dye absorption

The anodized model is then dipped into the dye solution to apply the luminophore. $[Ru(dpp)_3]^{2+}$ is used as a dye solution and CH_2Cl_2 is used as solvent. The concentration of the dye is 0.3×10^{-3} [mol/L]. The model is dipped for 1 min in the dye solution at 298 [K]. Then, the model is washed with CH_2Cl_2 and soaked in CH_2Cl_2 for 5 min. Finally, the model is washed with CH_2Cl_2 and dried in a desiccator for more than 1 day.

(6) Hydrophobization

The dye-adsorbed model is dipped in the stearic acid solution, in which the stearic acid is dissolved in hexane (C_6H_{14}) having concentration of 5×10^{-3} [mol/L]. The model is kept in the stearic solution for 24 hours at a temperature of 298 [K]. After dipping, the dye-adsorbed model is washed with C_6H_{14} and dried in a desiccator for at least 1 day.

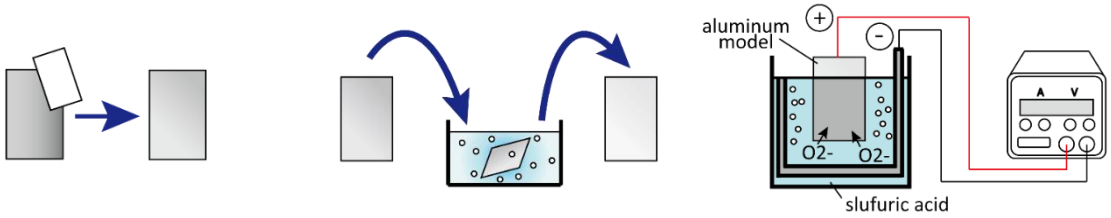

Step 1: wiping with ethanol Step 2: Rinse in *NaOH* 2%wt Step 3: Anodization

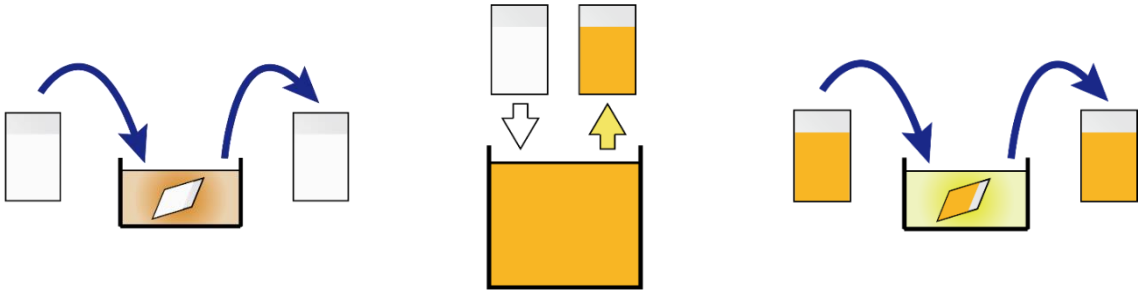

Step 4: Rinse in H_3PO_4 3%wt Step 5: Dye adsorption Step 6: Hydrophobization

Figure A.4 AA-PSP making procedure

A.2 Hough Transformation Based Auto-Positioning Method

A.2.1 Current Image Processing Method

Current image processing is based on the searching of marks made on auxiliary blade (Figure A.5 (a)) or directly on PSP blade (Figure A.5 (b)). The auxiliary blade method can give the accurate blade location information in steady cases or unsteady cases of stationary blade. But sometimes it fails to give good results for oscillating blade when the aerodynamic force is small and blade vibration in natural frequency is strong. Marked PSP blade method is able to obtain the location information of PSP blade in every time step for more accurate processing for oscillating blade. But it induces the faultiness of pressure information and the post processing is quite difficult owing to weak light source and blurring. In using these two methods, 36 points are marked on an auxiliary blade, while it is very difficult to find all the 36 points if they are marked on the PSP blade due to relative low contrast ratio.

Due to the limitations in using the above methods, Hough transformation based edge detection method is introduced here which can realize more robust automatic blade positioning.

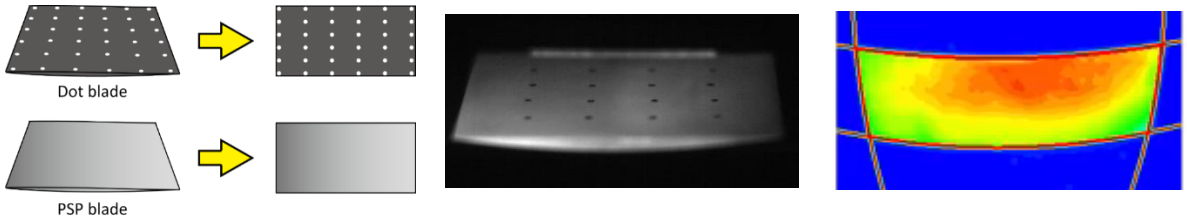

(a) Auxiliary dot blade (b) Marked PSP blade (c) Hough transformation

Figure A.5 Methods for blade positioning

A.2.2 Image Processing Method Based on Hough Transformation

Due to the knowledge that only the edge point coordinates can be sufficient for realizing accurate affine transformation, the blade edge detection is considered to be an alternative way to realize affine transformation. The method of the edge detection for current test object is proposed as follows which includes grey scale correction, gamma correction, binarization, edge detection, inner cleaning, Hough transformation, edge point coordinates calculation and affine transformation.

(1) <u>Gamma Correction (Figure A.6 (a))</u>

Gamma correction is a nonlinear operation used to adjust the brightness of an image. It can promote the image contrast by finding the deep color part and light color part in the image signal and making the ratio of the two larger. In the simplest case, it can be defined by the power-law expression as $V_{out} = A \times V_{in}^{\gamma}$.

The input value V_{in} is raised to the power γ and multiplied by the constant A, to get the output value V_{out}. In the common case of A = 1, inputs and outputs are typically in the range 0–1. When $\gamma > 1$, the bright part becomes dark and when $\gamma < 1$, the dark part becomes bright.

By selecting appropriate gamma value, the edge will be seen more clearly to realize more accurate edge detection. Before doing gamma correction, the grey scale correction should be done to set the intensity range of the image to be from 0~255.

(2) Binarization (Bernsen Method) (Figure A.6 (b))

This step is aimed to distinguish the blade surface zone from the surrounding. Binarization is the process of converting a pixel image to a binary image by setting a threshold value. If the pixels are trusted to be on the blade, the values will be set to 255, while others are set to 0. In current study, the luminance distribution on blade surface is non-uniform so that a global threshold is ineffective. An alternative method is Bernsen binarization method in which both local thresholds and global threshold to have better resolution for searching the zones of small grey scale difference.

(3) Edge Detection (Canny Edge Detector) (Figure A.6 (c))

The Canny edge detector is used to locate the outline of blade surface. In past attempts, the Canny edge detector was applied to the raw image without binarization, but the effect is not satisfactory in doing unsteady image processing due to the blurring near the edges. Binarization can give a clear edge so the edge detection becomes easier. This Canny method includes 5 steps:

1. Smooth the image to remove noises by Gaussian filter;
2. Calculate the intensity gradients of the image;
3. Apply non-maximum suppression to remove spurious response to edge detection;
4. Apply double threshold to determine possible edges;
5. Track edge by hysteresis to finish edge detection.

(4) Inner Cleaning (Figure A.6 (d))

In order to reduce errors and consumed time in doing Hough transformation, the known error sources are cleaned by using the edge information of last time step.

(5) Hough Transformation (Figure A.6 (e))

The objective of this step is to get the analytic expressions of the edge coordinates. Hough transformation is a technique that can be adopted to isolate the features of a particular shape within an image. Due to the requirement of feature description in parametric forms, Hough transformation is commonly used to detect regular curves such as lines, circles, ellipses, etc. The primary merits of the Hough transformation is its tolerance of gaps in feature boundary descriptions and relative insensitivity of image noise. Current airfoil is double circular arc (DCA) of which the tip and hub edges are arcs and the leading and trailing edges are straight lines. Seen from the images, the leading edge and trailing edge are bended by aerodynamic force into curves which can be searched by using quadratic fitting.

(6) Edge Point Coordinates Calculation (Figure A.6 (f))

Based on the analytic expressions of four curves, the coordinates of intersection points can be solved. Then, some auxiliary points on the edge curves are made for the application of affine transformation.

(7) Affine Transformation (Figure A.6 (g))

By using the coordinates of corner points and auxiliary edge points, the rectangle image can be obtained by the 6 parameters affine transformation using least square method which can realize translation, scaling, rotation and shear.

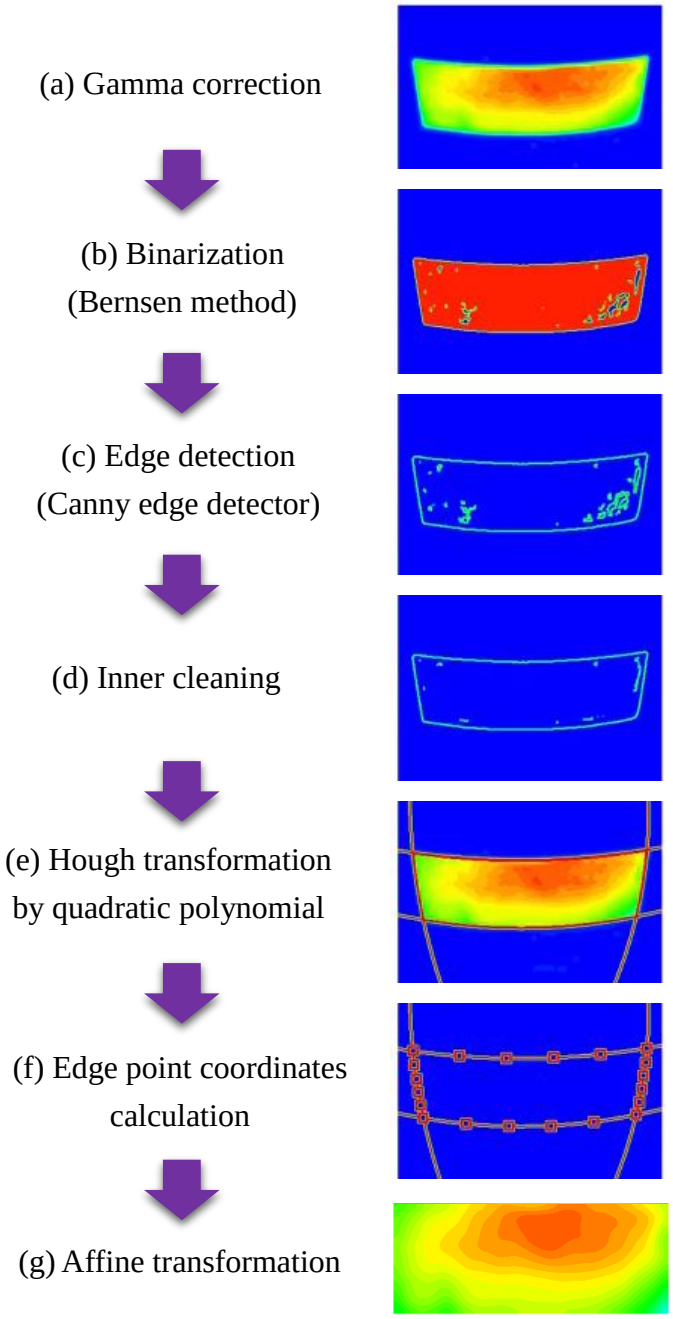

Figure A.6 Image processing method based on edge detection

A.2.3 Verification of Hough Transformation Method

Based on Hough transformation method, the time history of searched corner point is shown as Figure A.7. In wind-off condition, it is almost pure sine wave, while in wind-on condition, the influence of turbulence can also been observed.

Then, the accuracy of image processing method was verified by using the video (Figure A.8)

generated from CFD results where the pressure values were already known. The edge curves were found by Hough transformation as shown in Figure A.9. Averaged and unsteady pressure results were successfully obtained as shown in Figure A.10 for quantitative comparison. The results show good accordance with true value, except the phase in small amplitude zone. So, current image processing method is thought to be effective for processing blade deformation and oscillation with satisfactory accuracy.

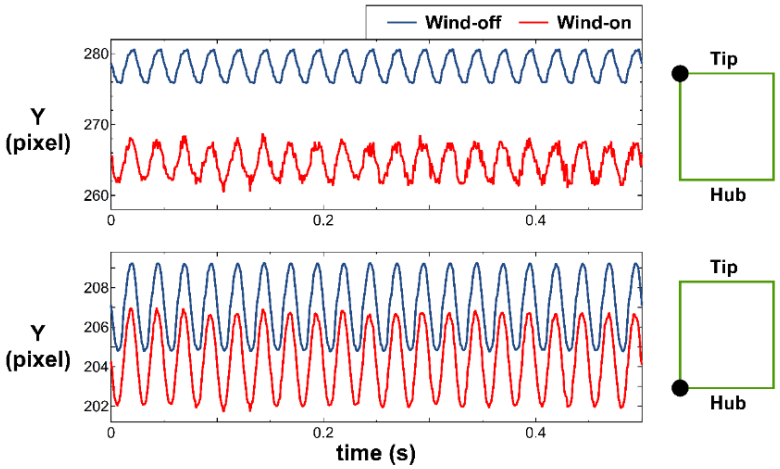

Figure A.7 Time history of corner points coordinates

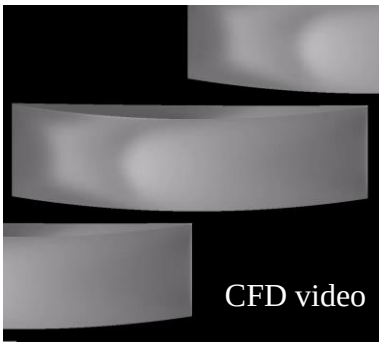

Figure A.8 CFD video

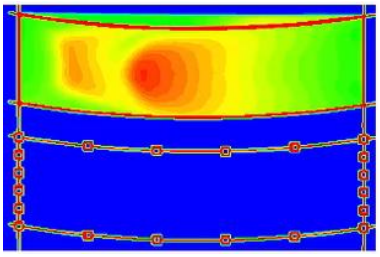

Figure A.9 Edge curves

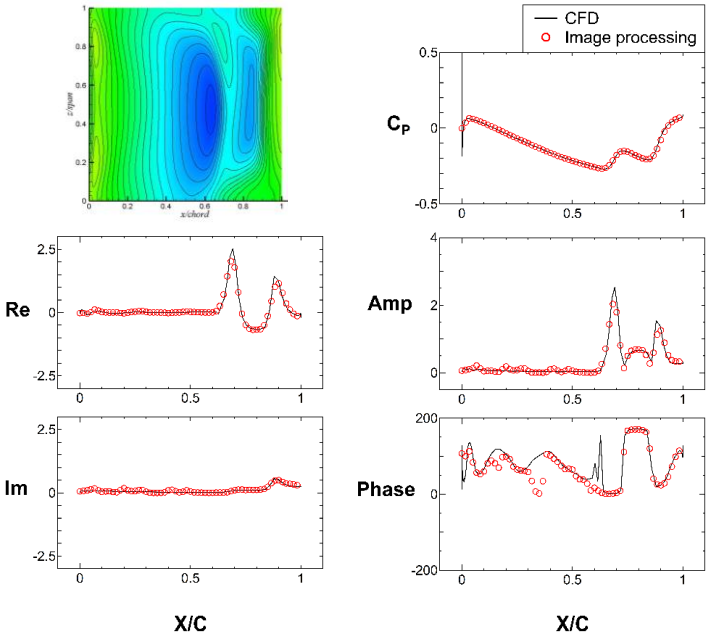

Figure A.10 Unsteady results obtained by image processing

A.3 Uncertainty Analysis of AA-PSP Measurement

Unsteady analysis of PSP is desirable for evaluating the precision of the results, which is very complex due to many influence factors [22]. These factors mainly include pressure resolution limiting, model deformation, temperature effect, calibration error, temporal variations in luminescence & illumination, spectral variability & filter leaking, pressure mapping error, etc. In this study, the transonic flow field is focused on where the pressure variation is obvious. The dominant error sources are considered temperature dependency, pressure resolution limiting, blade deformation and calibration error which are analyzed as follows.

A.3.1 Temperature Dependency

For evaluating current AA-PSP performance in transonic flow, the impact of surface temperature should be taken into consideration. In transonic cascade, the static temperature before and after shock wave is quite different, and there is also temperature difference between middle span and hub or tip due to wall boundary layer effect. So, to evaluate the influence of shock wave and wall, six ϕ 0.4 holes with 0.2mm K-type thermocouples are made in the pressure side of blade, and the positions are 10%, 50% and 90% span height at 30% and 70% chord length (named as TC1~TC6 shown in Figure A.11). The results including time history and spatial distribution of temperature are shown in Figure A.12.

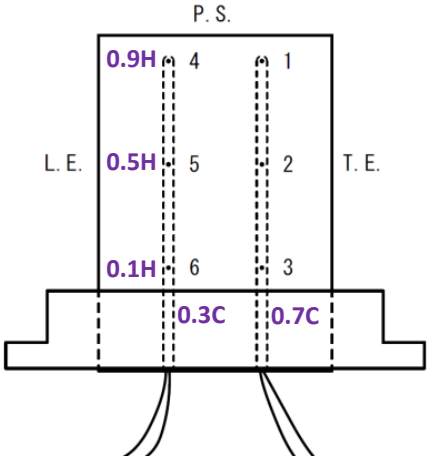

Figure A.11 Thermocouple blade

Generally speaking, the temperature on blade surface decreases continuously when the wind blows down, as shown in Figure A.12 (a). For conducting the experiment, the measuring time is after the total pressure becomes stable, as shown in Figure A.12 (b). This component of temperature difference is a global phenomenon and has repeatability. For dismiss this error source, the start time of measurement at each time is fixed after starting the wind tunnel, and the measuring time period is 3 seconds for PSP. The C_P distribution at middle span was also measured at relative same time point from wind tunnel starting with PSP. Then, the in-situ calibration method was used to calibrate the luminescent intensity ratio into pressure value. By using such process, the temperature change caused by wind tunnel can be compensated.

Besides, the local temperature can be seen in Figure A.12 (c). This component of temperature difference has influence on pressure measurement results. Due to previous tests [26], when $[Ru(dpp)_3]^{2+}$ is used as luminophore, I_{ref}/I decreases 6% as pressure increases 10kPa and I/I_{ref} decreases 5% as temperature increase 10K. In this study, when the temperature difference is 2K, the error of I/I_{ref} will be 1%. Then, the error of static pressure will be calculated about 1.5kPa and corresponding error of C_P is about 0.015, which is ignorable by considering the variation range of C_P (-0.3~0.3) around the blade surface.

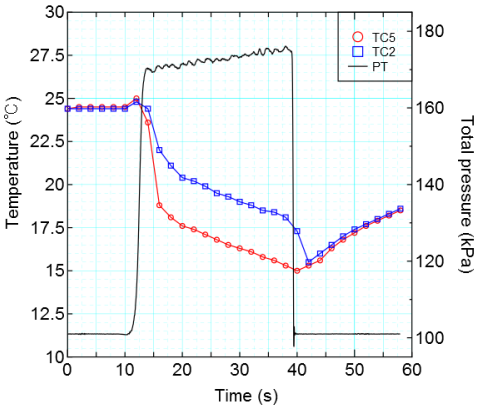

(a) Temperature change with time

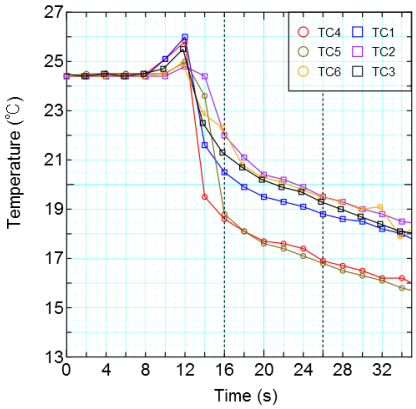

(b) Measuring time period

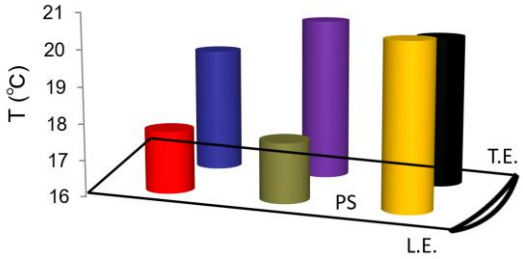

(c) Temperature distribution on blade pressure side

Figure A.12 Results of thermocouple measurement

A.3.2 Pressure Resolution

PSP measurement for small pressure change is difficult due to the pressure resolution limiting of the measurement system. The pressure resolution is a measure of pressure sensitivity of PSP. Higher pressure sensitivity indicates a larger luminescent intensity variation caused by the same pressure gradient. This characteristic is important to evaluate the pressure measuring capability of PSP. Eqn.(A.3) is applied for calibrating the luminescent intensity ratio in the experiment, and the resolution of C_P and P can be calculated as eqn.(A.4) through eqn.(A.5). Here, P_{dyn} is the inlet dynamic pressure calculated by $P_{dyn} = P_{in}^{*} - P_{in}$.

$$C_P = C_0 + C_1 \times \frac{I_{ref}}{I} \tag{A.3}$$

$$\Delta C_P = C_1 \times \Delta\left(\frac{I_{ref}}{I}\right) \tag{A.4}$$

$$Res(C_P) = \left|\frac{\Delta C_P}{\Delta I}\right| = \frac{C_1 \times I_{ref}}{I^2 + I \times \Delta I}\ , \qquad Res(P) = Res(C_P) \times P_{dyn} \tag{A.5}$$

In this study, the pressure resolution is estimated about 0.6~0.8kPa (static pressure) and 0.006~0.008 (C_P) by using the calibration coefficient C_1 and averaged values of I_{ref} and I.

A.3.3 Model Deformation

In this study, the deformation of blade area on the image was caused by aerodynamic loads and forced oscillation. The uncertainties are related to the non-uniform luminescent intensity distribution in wind-off condition and spatial difference of paint performance. So, image registration was carried out to eliminate these errors. So, the uncertainty of image registration method is evaluated by the standard deviations of least-squares estimation.

However, a kind of error can't be corrected which is caused by change in illumination intensity generated by light source on blade surface after blade movement. This error can be alleviate by improving the spatial uniformity of light illumination on blade surface zone.

A.3.4 Calibration Error

The uncertainty in Stern-Volmer coefficients C_0 and C_1 is the calibration error. In using in-situ calibration method, the data from pressure taps on blade surface was utilized in wind-on condition to determine the Stern-Volmer coefficients. It can considerably reduce some bias errors and naturally achieve good fit to pressure tap data. On the other hand, since the model is not isothermal, the spatial variation in surface temperature may complicate the in-situ calibration and produce the position-dependent calibration results. Generally, the uncertainty in paint calibration is characterized by the standard deviation in fitting calibration data.

Appendix B: Characteristics of Transonic Wind Tunnel

B.1 Overview

Wind tunnel test is a reliable and effective approach for flutter research, while the internal flow field of wind tunnel should be fully understood at first to evaluate the influence of wind tunnel structure on the flow field and make sure the effectiveness of the results of test section. In order to get such knowledge, the experimental and steady 2D RANS simulation results of flow field inside wind tunnel are obtained and analyzed in this chapter.

B.2 Experiment Description and CFD method

B.2.1 Experiment Description

The blow-down type transonic wind tunnel (details in section 2.1.3) is used to conduct the experiment. It contains inlet nozzle, test section and outlet zone. There are 13 static pressure taps on the lower wall of nozzle which are shown as the red short lines in Figure B.1. Suction is conducted through the side walls in the rear of nozzle and lower wall of test section to reduce the boundary layer thickness. Outlet zone includes two movable tailboards and one throttle valve. The location and angle of both the upper and lower tailboards can be adjusted. The fore-end of the pressure box is hollow with porous wall. The throttle valve is used to adjust the pressure ratio and the shock pattern. The distribution of main air flowrate and bypass air flowrate is controlled by the location of upper tailboard and lower tailboard. The experimental condition is same as Chapter 4 and the pressure ratio is set to 1.25.

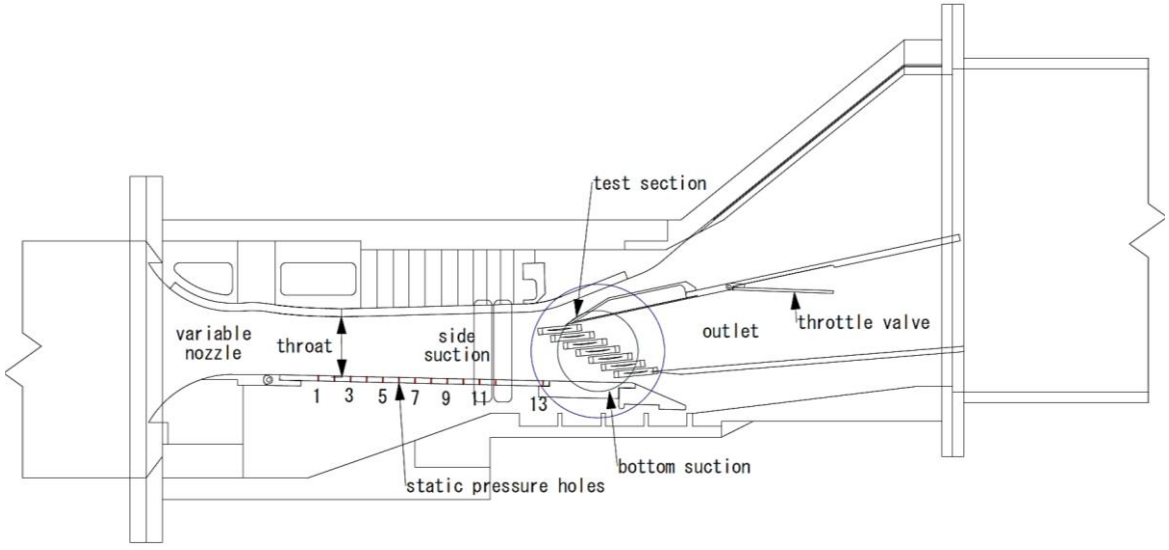

Figure B.1 Pressure measuring points on lower wall of nozzle

B.2.2 Computational Grid Generation by Overset Grid Method

In handling with complex structure with lots of separated walls and movable parts, it is difficult to generate structured grid with conventional junction method. In this study, the overall flow field in the wind tunnel is expected to be clarified for better understanding of the experimental condition which is realized by an overset gird method. In using this method, O-mesh or H-mesh are made around or along the surfaces of every wind tunnel component without considering the direct junction with the neighboring meshes. The data transmission is realized by trilinear interpolation.

The algorithm [53][54] combining distance-based blanking and iterative adjustment of fringe cells is used to realize the data connectivity in neighboring meshes. At first, the mesh cells are blanked according to the distance between the adjacent components. Next, the fringes of the activated cells are marked as receptor cells, and their corresponding cells (also called donor cells) in the adjacent meshes are searched for pairing. In this step, the cells which haven't found donor cells are named as orphan cells. Then, the blank cells adjacent to orphan cells are activated and the donor cell searching is conducted once more. By doing such iterations, the data set is finally established when the orphan cells are completely eliminated. In this computation, the receptor cell can't be donor cell, and all orphan cells are eliminated to suppress the numerical error. Figure B.2 shows an example of mesh assembly for the wind tunnel parts.

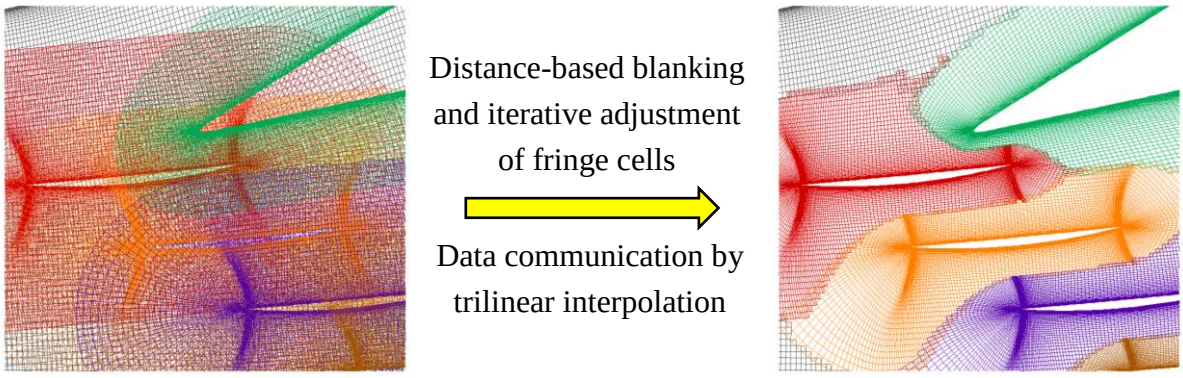

Figure B.2 Overset grid method

The steady 2D RANS numerical computation is conducted for getting more details of the flow field inside wind tunnel.

The 2D CFD works has been done using overset mesh approach. Firstly, O-mesh or H-mesh are made around or along the wall. Then, distance-based blanking and iterative adjustment of fringe cells are carried out to connect the different zones. Data transfer is realized by trilinear interpolation. Total cell number of one layer is about 0.7 million which includes 58 zones. The boundary condition of each zone are set to be non-slip wall or junction. Details of the grid are shown in Figure B.3.

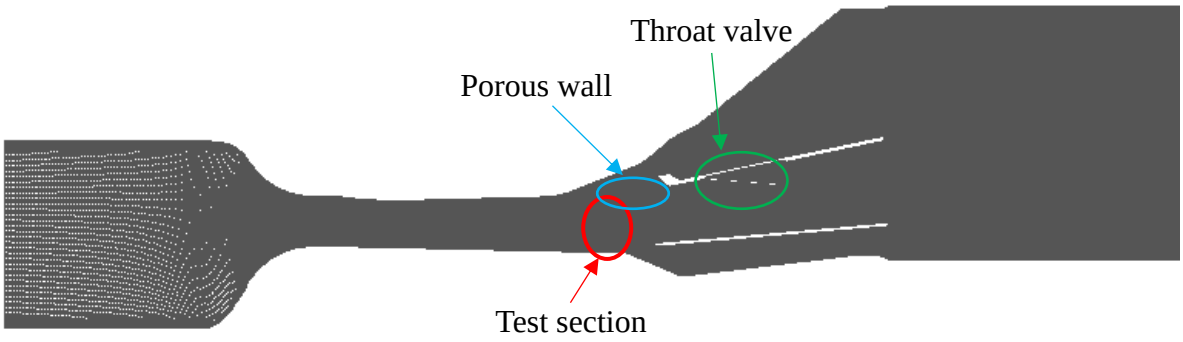

(a) Overall view

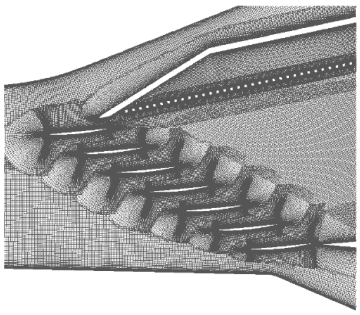

(b) Test section

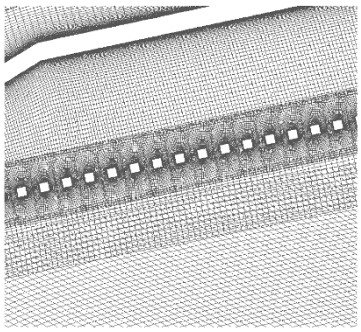

(c) Porous wall

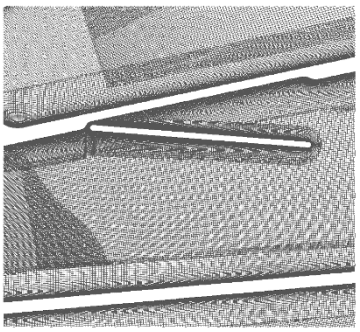

(d) Throat valve

Figure B.3 Details of computational grid by overset mesh approach

B.3 Flow Field inside Wind Tunnel

B.3.1 Global Visualization

Oil flow experiment was conducted for the visualization of limiting streamlines on the walls of wind tunnel components. The oil is applied on the upper, lower wall and side wall (blade hub side) of the nozzle rear. When the air flows, the applied oil will scatter with the flow and adhere to other low speed walls.

Figure B.4 shows the oil flow photos of the whole wind tunnel and the Mach number counter calculated by CFD is shown in Figure B.5. The general flow field near walls, separation in upper/lower bypass and tip leakage flow are observed in Figure B.4. As shown in Figure B.5, by calculating the same wind tunnel configuration with the experiment, CFD tells the existence of a shock wave in the rear of the nozzle or just before test section. The Mach number decreases from 1.4 to subsonic. The shock wave near the lower wall is almost normal. In current situation, more evidence should be found to prove this phenomenon and the reason should be clarified by detailed analysis of the flow field.

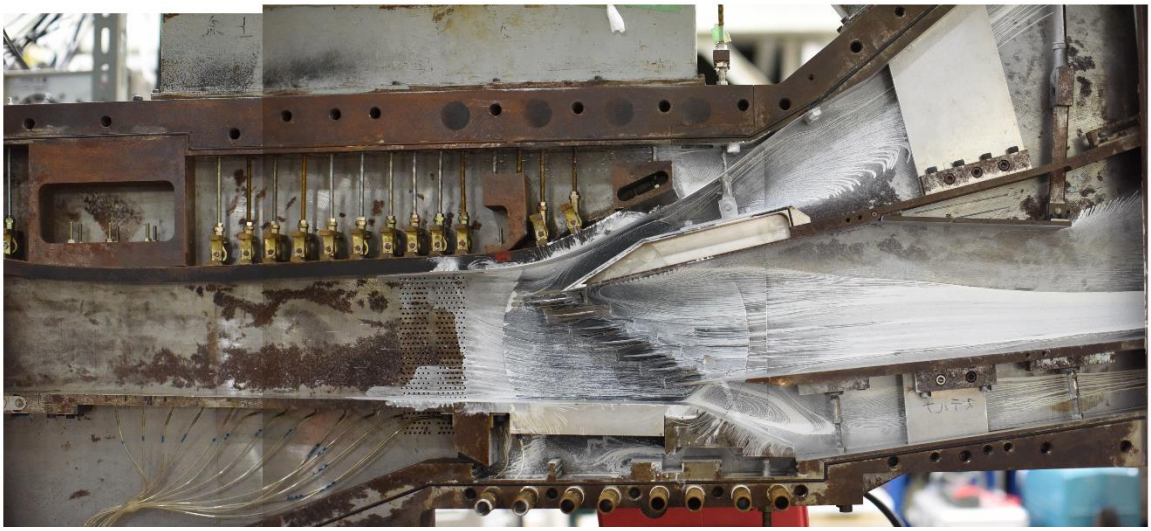

(a) Hub side

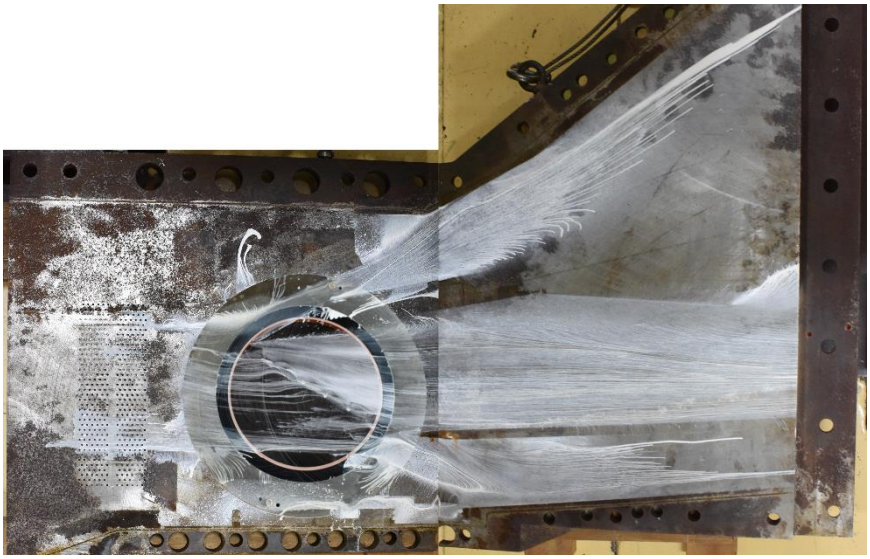

(b) Tip side

Figure B.4 Oil flow photos of wind tunnel walls

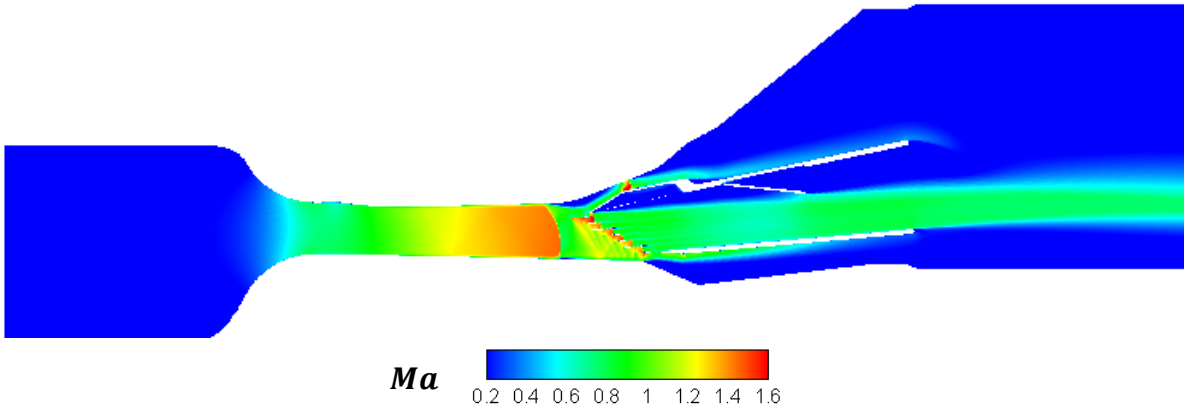

Figure B.5 Mach number distribution of whole wind tunnel (CFD)

B.3.2 Nozzle

Figure B.6 shows the isentropic Mach number distribution in the upstream nozzle calculated by the static pressure of the measuring points on nozzle wall. The experimental result with side wall suction has good agreement and a shock wave appears between static pressure point 12 and point 13. The result without suction shows an upstream and weaker shock which is induced by thicker boundary layer. The oil flow results shown in Figure B.7 also tell the same story. On the upper wall of nozzle, shock foot and double vortexes caused by the shock wave can be seen. Also, on the lower wall, a separation line appears just after the side suction zone between point 12 and point 13. The colors of residual oil before and after the upper wall separation line is obviously different, and the downstream oil is thicker than upstream oil. It is caused by the velocity decreasing caused by shock wave.

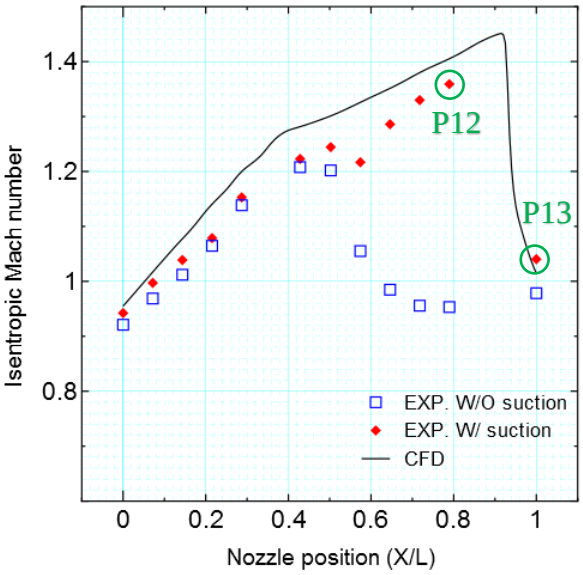

Figure B.6 Axial isentropic Mach number distribution along nozzle

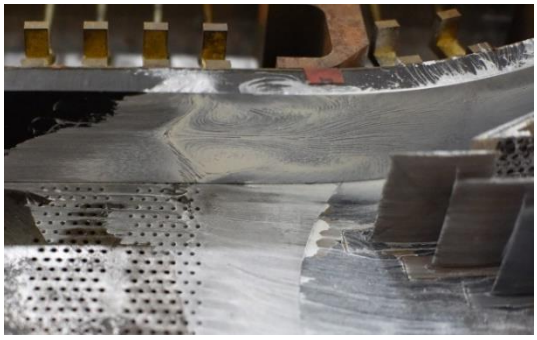

(a) Shock wave foot on upper wall

(b) Shock wave foot on lower wall

Figure B.7 Details of oil flow results

B.3.3 Test Section

The isentropic Mach number counters of test section are shown in Figure B.8. For inlet flow, both experimental and CFD results shows Mach number transition from subsonic before blade -3 to supersonic. The inlet flow is subsonic, then it becomes supersonic when it touches with blade -3 and is accelerated by an expansion wave. Due to the existence of the expansion wave, the lower blades -2 ~ +3 are in supersonic inlet condition and have satisfactory uniformity. This phenomenon can also been proved by schlieren photo shown in Figure B.9 where there are only six leading edge oblique shock waves in the test section. The schlieren result also shows that the angles of oblique shock waves and the locations of the passage shock are similar which also

indicates a good uniformity.

For quantitative comparison, the distribution isentropic Mach number at 1.0 chord upstream is used as shown in Figure B.10. The CFD results have good consistency with experimental results even though the CFD results have larger fluctuation than experiment. By increase the air suction velocity of lower wall numerically, the Mach numbers of lower blades increase and become smooth.

Figure B.12 shows residual oil on blade surfaces. For the pressure side, the passage shock foots can be seen in all the blade except blade -3. The shock foots on blade -1 ~ blade +2 are at similar location. As to suction side, the similar double shocks pattern can be observed on blade -2 ~ blade +1. Figure B.11 shows the residual oil on glass window which indicates the tip clearance flow. The tip leakage flow can be identified from the photo and the middle blades shows a good periodicity.

Finally, the uniformity of the test cascade is confirmed experimentally. The isentropic Mach number distribution in 1.0 chord upstream and 1.0 chord downstream, and the static pressure ratio distribution are measured. Figure B.13 shows the measured results. Based on the above results and analysis, the uniformity of blade -1, blade 0 and blade +1 can be confirmed to be satisfactory.

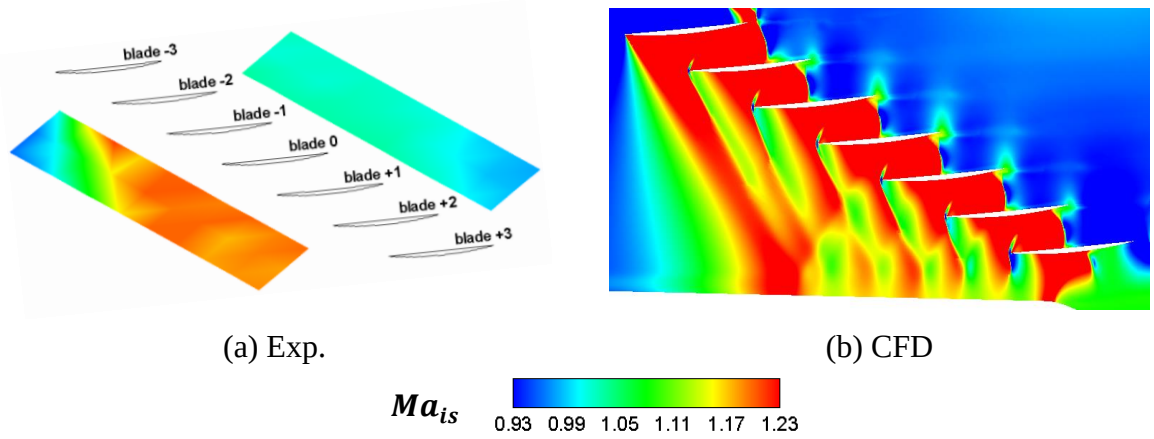

(a) Exp. (b) CFD

Figure B.8 Isentropic Mach number distribution in test section

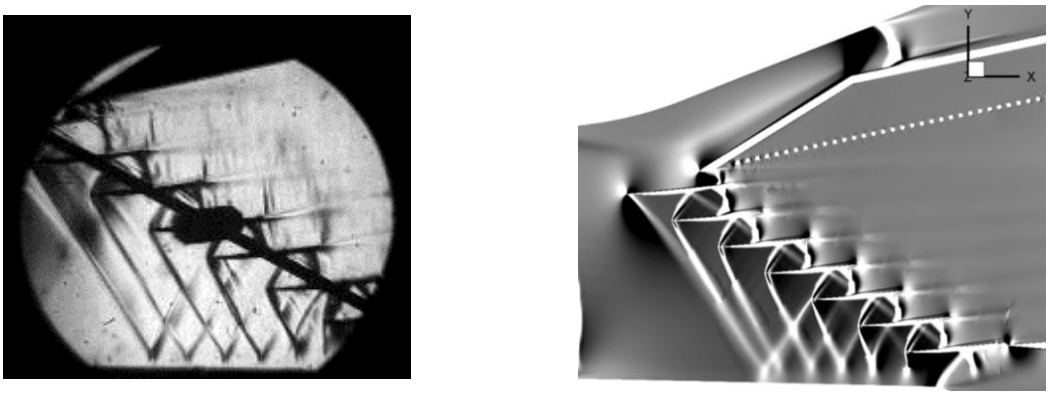

(a) Schlieren (b) CFD

Figure B.9 Comparison of density gradient

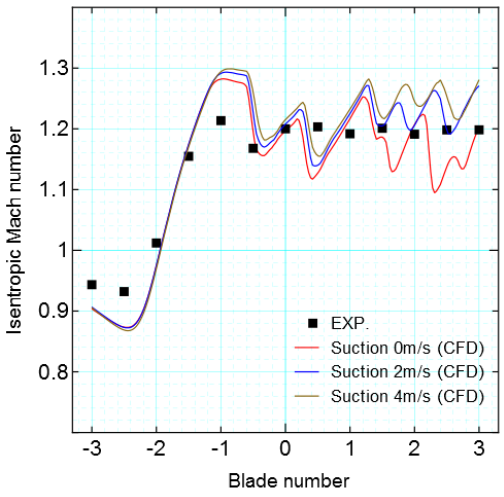

Figure B.10 Mach number distribution at 1.0 chord upstream

Figure B.11 Tip clearance flow (oil flow)

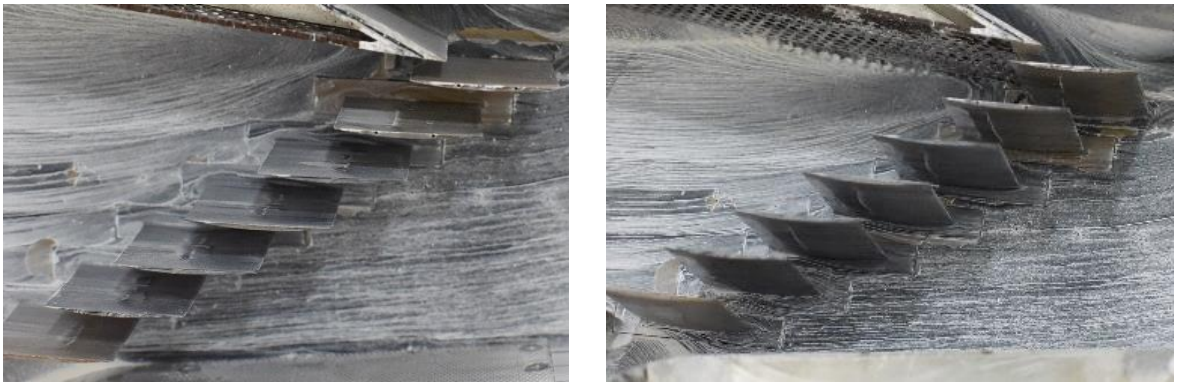

(a) Pressure side (b) Suction side

Figure B.12 Shock pattern on blade surface (oil flow)

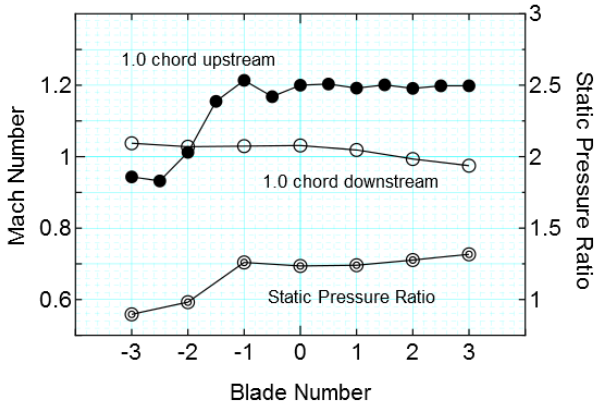

(a) Isentropic Mach number and pressure ratio

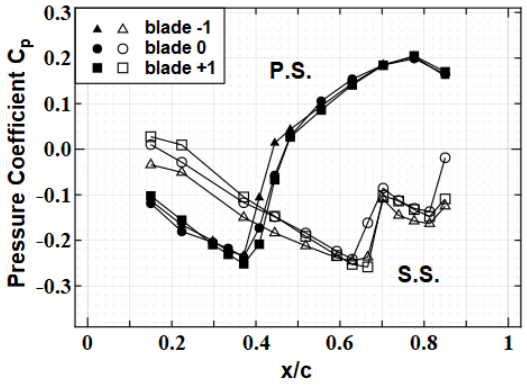

(b) C_P distribution in Mid-span

Figure B.13 Uniformity of test section

B.3.4 Bypass Flows

In the wind tunnel, the global flow structure is influenced by both the shape of upstream nozzle and the location of the downstream moving parts. Current setting of wind tunnel makes the upper and lower bypasses narrow and the supersonic air mass flow stagnates in the upstream of cascade and a shock wave forms. Figure B.14 shows the result of bypass separation. Both the upper bypass and lower bypass are blocked by large separation vortices, and the effective flow area becomes small. So the balance of upstream flowrate and effective bypass area is of great importance for flow structure adjustment. As shown in Figure B.15, the normal shock in nozzle disappears by increasing the effective flow area of upper bypass.

(a) Upper bypass

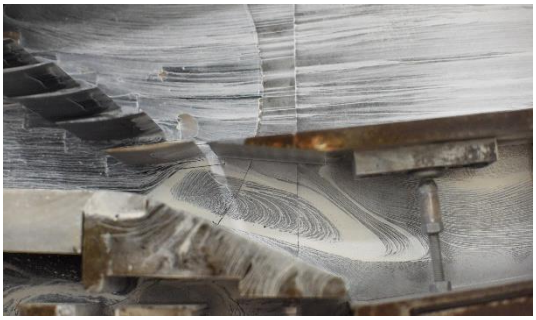

(b) Lower bypass

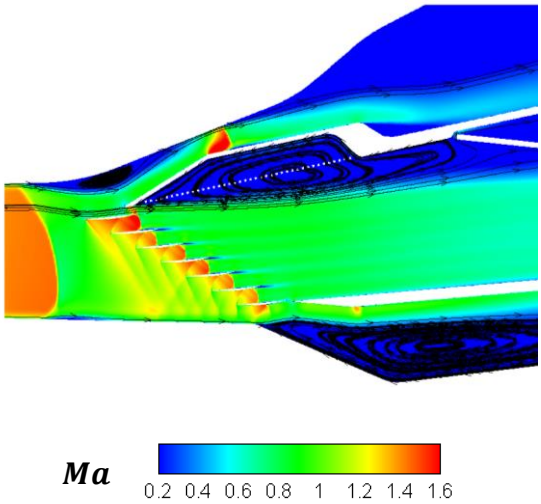

(c) Mach counter and streamlines (CFD)

Figure B.14 Oil flow results and streamlines by CFD

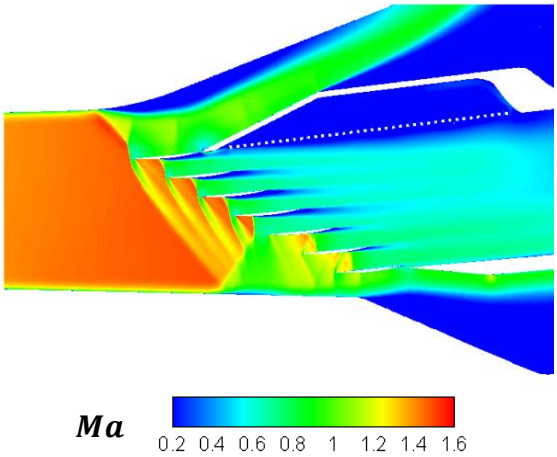

Figure B.15 Adjusting of bypass flow passage

B.4 Functions of Wind Tunnel Components

B.4.1 Pressure Box

Figure B.16 shows the function of current downstream pressure box (c) by comparing with the solid structure (a) and hollow structure without wall (b). In solid structure (a), a strong shock wave appears in the downstream of the cascade from the upper wall to the trailing edge of blade -1. This phenomenon is caused by the narrow passage between the upper wall and blade -3. An oblique shock forms at the leading edge of the pressure box and then is reflected in the narrow passage. It affects the downstream blades and finally forms a large supersonic area. This design will deteriorate the downstream uniformity of the cascade drastically. The designs in (b) and (c) can solve this problem by inducing the high velocity flow into the low speed hollow area and eliminating the shock reflection.

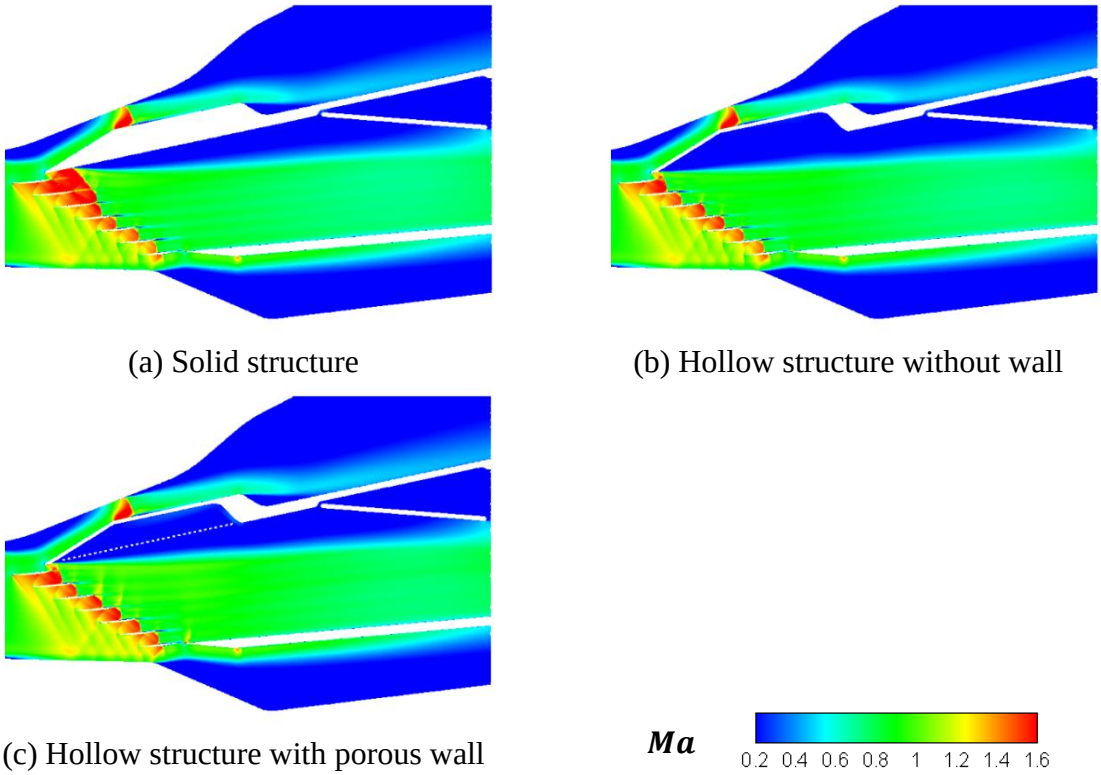

(a) Solid structure

(b) Hollow structure without wall

(c) Hollow structure with porous wall

Figure B.16 Influence of pressure box design on flow field

B.4.2 Throttle Valve

Figure B.17 shows the function of downstream throttle valve adjustment. When the throat valve closes from -4.5° to -6°, the downstream Mach number near the throat valve become smaller with pressure increasing. This back pressure increasing will propagates to the cascade outlet and pushes the passages shock moving towards upstream direction. In the unique incidence range of supersonic flow, the upstream flow field of cascade won't change with the opening of throat valve. When the throat valve continues to close, the increasing of back pressure will cause oblique shocks attached to the blade leading edges detach from the blade, and the inlet flow field will change.

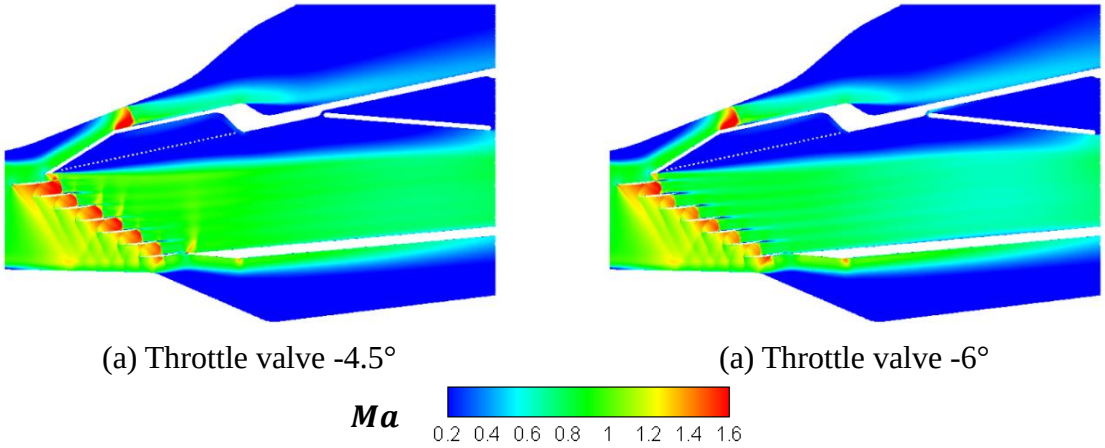

(a) Throttle valve -4.5° (a) Throttle valve -6°

Figure B.17 Influence of throttle on flow field

B.5 Correction of Mach Number at Cascade Inlet

The ratio of total pressure after a normal shock and it before the normal shock wave is defined as the total pressure ratio δ, which can be calculated as eqn.(B.1). The subscripts 1 and 2 mean the parameter before and after the shock wave.

$$\delta = \frac{P_2^*}{P_1^*} = \frac{\left[\frac{(\gamma+1)\times Ma_1^2}{2+(\gamma-1)\times Ma_1^2}\right]^{\frac{\gamma}{\gamma-1}}}{\left[\frac{2\gamma}{\gamma+1}\times Ma_1^2 - \frac{\gamma-1}{\gamma+1}\right]^{\frac{1}{\gamma-1}}} \tag{B.1}$$

In current experiment, the Mach number before the normal shock wave is about 1.4. By substituting 1.4 into eqn.(B.1), total pressure ratio is calculated as 0.9582, which indicates that the total pressure loss caused by the normal shock is about 4.18%.

As we used the total pressure P_1^* in settling chamber and cascade inlet static pressure P_{in} to ensure the Mach number to be 1.2. By using the correct total pressure P_2^* before the cascade, the Mach number is corrected to 1.167. The later CFD calculation is conducted by matching the Mach number at measuring point to 1.167 and pressure coefficient calculation uses same definition as the experiment.

B.6 Summary

In this chapter, details of the global flow field inside the wind tunnel has been clarified. The following conclusions can be obtained.

(1) With current wind tunnel structure, a normal shock wave exits in the rear of the nozzle. The supersonic inlet of the cascade is realized by the expansion wave located at the suction side of blade -3. It helps forming the downstream periodic inlet flow. The uniformity of the cascade was confirmed to be satisfactory for three central blades.

(2) The effective flow areas in the bypasses are of great importance for adjusting the flow field of test section. Besides, the function of pressure box and throat valve was illustrated.